Influence of Confined Geometry on Anisotropic Soft Matter

A Thesis Submitted to the
Mangalore University

For the Degree of

DOCTOR OF PHILOSOPHY

in

PHYSICS

by

Vijay Kumar. M

Centre for Nano and Soft Matter Sciences
Bangalore – 560 013
India

April 2015

Influence of Confined Geometry on Anisotropic Soft Matter

Thesis

Submitted to the Mangalore University
for the award of Degree of

DOCTOR OF PHILOSOPHY

in

Physics

by

Vijay Kumar. M

Under the Supervision of

Dr. S. Krishna Prasad

Centre for Nano and Soft Matter Sciences
Bangalore – 560 013
India

April 2015

Dedicated

to

my father, mother and sisters

Though things diverse from diverse sages' lips we learn,

' Tis wisdom's part in each the true thing to discern.

by

Thiruvalluvar

Declaration

I hereby declare that the entire work embodied in this thesis titled *"**Influence of Confined Geometry on Anisotropic Soft Matter**"* has been carried out by me at Centre for Nano and Soft Matter Sciences, Bangalore, India, under the supervision of ***Dr. S. Krishna Prasad*** and that it has not been submitted elsewhere for the award of any Degree, Diploma, Associateship or any other similar title of any other university or institution.

Place: Bangalore (Vijay Kumar. M)

Date:

Certificate

I hereby certify that the thesis titled ***"Influence of Confined Geometry on Anisotropic Soft Matter"*** is a bonafide record of research work carried out by ***Mr. Vijay Kumar. M*** at Centre for Nano and Soft Matter Sciences, Bangalore, India, under my supervision and that it has not been submitted elsewhere for the award of any Degree, Diploma, Associateship or any other similar title of any other university or institution.

Place: Bangalore
Date:

Dr. S. Krishna Prasad
(Research Supervisor)

Acknowledgements

I would like to express my profound sense of gratitude to my research supervisor Dr. S. Krishna Prasad for giving me the privilege to conduct this Ph.D work under his supervision. I am deeply indebted to him for his guidance and help through the years.

I would like to express my sincere thanks to Dr. D. S Shankar Rao for helping and teaching me in all my experiments with more patience. I specially thank Dr. D. S Shankar Rao for all the help rendered during the preparation of this thesis. I profusely thank Dr. Geetha G. Nair and Prof. K. S. Krishnamurthy for their valuable suggestions and interest in the progress of my research work.

I am extremely grateful to Dr. D. S. Shankar Rao for all the help especially for his meticulous proof reading of this thesis.

My thanks are due to Dr. C. V. Yelamaggad and Dr. Uma S. Hiremath for helping me in many ways especially in matters related to chemistry and providing me compounds to carry out experiments.

I am grateful to Prof. G.U. Kulkarni, Director, Centre for Nano and Soft Matter Sciences for all his support in the final stages of my Ph.D thesis submission.

I am grateful to Prof. K. A. Suresh, former Director, for all his support during all these years. I would also like to thank Dr. Praveer Asthana, Acting Director, Centre for Nano and Soft Matter Sciences for all his support and help throughout.

My special thanks to Mr. Subodh M. Gulvadi, Administrative Officer and Mr. Vivek Dubey, Mrs Netravathi, Mr K.R. Shankar, Mr. Jayaram and Mr. Manjunath for their whole hearted support. I also thank Dr. Sanjay Varshney and Mrs. Sandhya Hombal for all their help. My special thanks to Mr.V. Jayaprakash, Mr. Samuel Hebich, Mr. D. G. Prahlad and Mr. Ningappa Kadimani, Mr. Kumar and other support staff for their assistance and on day to day matters.

My sincere thanks to Prof. K. M. Balakrishna, Prof. S. M. Dharmaprakash, and Prof. K. B. Vijaya Kumar Department of Physics, Mangalore University for all their guidance and help in official matters of University.

My thanks are due to Dr. V. Jayalakshmi, Dr. S. Sridevi, Dr. R. Bhargavi, Dr. Prasad N. Bapat, and Dr. Pramod Tadapatri for being extremely supportive all these years.

I express my heartfelt gratitude to all my lab mates Mrs. P. Srividya, Ms. P. Lakshmi Madhuri, Ms. S. Vimala, Mr. B. Kamaliya, Ms. T. Shilpa and Mrs. Usha for extending their full cooperation during this work. I am also extremely thankful to all my research colleagues Dr. N. G. Nagaveni, Ms. Kayathri, Dr. Rashmi Prabhu, Mrs. Shilpa Harish, Ms. R. Rajalakshmi, Mr. Nagaiah Kambala, Ms. H. N. Gayathri, Ms. M. Monika, Mr. B. N. Veerabhadra Swamy, Mr. K. Brahmaiah, Mr. Chandan Kumar and Mr. Arup Sarkar, Ms. Priya Madhuri, Dr. Nani Babu Palakurthy and Mr. Sachin for making my stay memorable.

I would like to specially thank my hostel mates Chandhan Kumar and Arup for their cooperation and support for making stay memorable.

I gratefully acknowledge the travel support provided by Dep. of Science and Technology, Govt. of India enabling me to participate in 25th International Liquid Crystals Conference-2014 at Dublin, Ireland.

I specially thank my sisters Mrs. M. Nithya and Mrs. M. Soosai Theresh for their help during all my studies. I also want thank Mr. Soosai Raj and my brothers Mr. R. Ragul, Mr. R. Ramesh, Mr. R. Mohan and Mr. G. Thangam.

Finally I would like to thank my friends Mr. P. Rajiv Gandhi, Mr. Arputharaj, Mr. Manokar, Mr. M. Tamil Arasan, Mr. A. Manickam and Dr. P. Indra Devi for their support and encouragement.

Vijay Kumar. M

Contents

Overview

Chapter-1

1. Introduction

1.1 Soft matter

Soft matter is a subfield of condensed matter, comprising a variety of physical states that are easily deformed by thermal stresses or thermal fluctuations [1-3]. Systems classified under this category include liquid crystals, colloids, polymers, foams, gels, biological materials, etc. An important common feature shared by these materials is that the underlying physical behaviours have an energy scale comparable with room temperature thermal energy, with the quantum aspects being unimportant. Bringing in a further dimension, a*nisotropic soft matter* exhibit anisotropy in the physical properties such as electrical, optical, dielectric, magnetic and mechanical etc. Soft matter (SM) self-organize into *mesoscopic* structures much larger than the microscopic scale (the arrangement of atoms and molecules), and yet much smaller than the macroscopic (overall) scale of the material. As a consequence of this, it is often difficult, in comparison to the hard condensed matter, to predict their behaviour from the basic constituents. For example, the overall mechanical stiffness of the foam emerges from the combined interactions of the constituent bubbles.

The importance of SM cannot be over emphasized owing to their wide ranging presence such as structural and packaging materials, foams and adhesives, detergents and cosmetics, paints, food additives, lubricants and fuel additives, rubber in tyres, as well as in the bio-world such as blood, muscle, milk, yogurt, jello. For example, liquid crystals (LC), an exemplary category of soft matter, being orientationally ordered fluid with or without positional order in less than 3 dimensions, hold attractions owing to their basic uniqueness and also as technologically important materials in display devices (LCDs) [4]. On the other hand, plastic crystals (PC) are positionally ordered in all the three dimensions, but are orientationally disordered [5]. Despite such a diversity, many of the properties of SM have common physicochemical origins, owing to a large number of internal degrees of freedom, weak interactions between structural elements, a delicate balance between entropic and enthalpy contributions to the free energy, etc. In addition to presenting the above mentioned features, and thus being of interest in their own right, the studies on SM have also revived certain classical fields of physics such as fluids and elasticity.

As to be seen in a later section, subjecting soft matter to externally imposed length scales has lead to interesting effects. Let us consider two examples, foams and living polymers. Conventional foams and foamed gels present a variety of relevant properties that make them suitable for use in the oil and gas sector. For example, the evolution of foamed gel as a function of aging time subsequent to placement in porous media has been investigated [6]. This is significant because after foamed gel placement in porous media, the pore level configuration of the gelled lamellar structure determines the fluid diverting performance of mature foamed gel barriers. The second example that may be mentioned is that of dilute solutions of living polymers of rigid or flexible macromolecules, confined between two solid repulsive walls. When the confined system is taken to be at equilibrium with an external reservoir the living polymers behave similarly to a polydisperse solution of unbreakable chains. However for closed gaps the behaviour is quite different from a classical polymer solution because the worm-like micelles can adapt their intrinsic polydispersity in order to release the confinement constraint. In particular, for rigid living polymers this leads to a divergence of the average chain-length in the limit of strong confinement, as well as to a non-monotonic behaviour of the pressure acting on the walls [7].

In the work to be described in this thesis, the influence of such restricted geometries on the behaviour of two kinds of soft matter exhibiting anisotropy in certain physical properties have been investigated. Both the chosen classes of materials occur as a consequence of the multi-step melting process of certain (mostly) organic materials. The aim of the work is to investigate how the external imposition of the length scale also has a direction dependent influence on the structure and physical properties of the medium. To provide a background for the results to be described in subsequent chapters we provide below a summary of the structure and classification of these two classes of anisotropic soft matter.

Part A: Anisotropic Soft Matter

1.2 Liquid crystals

Liquid crystals, as the name suggests, are states of matter in which the degree of ordering is in between the three dimensionally ordered solid and the isotropic liquid. Similar to crystals, these intermediate phases (also known as mesophases) exhibit anisotropy in their optical, magnetic and electrical properties. At the same time they possess some of the mechanical properties of a fluid, e.g., inability to support shear. Exhibited mostly by organic materials, these mesophases appear owing to either the action of temperature (thermotropic liquid crystals) or the action of a suitable solvent (lyotropic liquid crystals). A detailed account of the structure and physical properties may be found in several monographs available in the literature [8-12]. Due to the unique combination of structure and fluidity, liquid crystals (LC) have gained popularity not only as exemplary materials in soft matter, but are technologically important, owing to the huge success as portable flat panel display devices, which have become ubiquitous today.

The constituents that give rise to thermotropic LCs are elongated rod-like (calamitic) or disk-like (discotic) molecules (In recent times banana–shaped LCs are emerging as the third class [13]). The length of the molecules is typically a couple of nanometres. The ratio of the length to the diameter of the rod-like molecules or the ratio of the diameter to the thickness of the disk-like molecules being about 5 or larger, is a necessary but not sufficient condition for the observation of thermotropic mesomorphism. In the crystalline form, the system possesses both three-dimensional positional order as well as orientational order of the molecules, whereas the isotropic liquid state lacks both such orders. The combination of orientational order plus positional order in one or two dimensions forms the basis to define the 40-odd liquid crystal phases discovered till date.

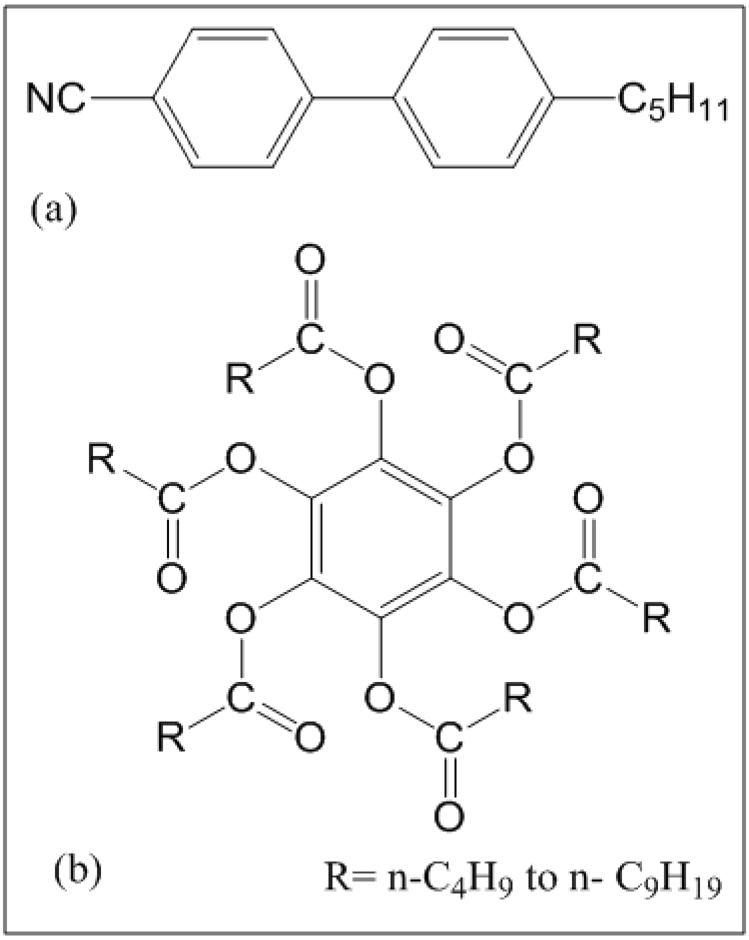

Figure1.1: Molecular structures of (a) rod-like (4’-n-pentyl-4- cyano-biphenyl, 5CB), and (b) disc-like (benzene-hexa-n-alkanoates) liquid crystals.

Figure 1.1(a) shows the structure of a simple and well known calamatic liquid crystal molecule, 4’-n-pentyl-4- cyano-biphenyl (5CB for short). It consists of a biphenyl moiety as the rigid core, and a flexible tail in the form of a hydrocarbon chain. With very few exceptions the presence of a rigid part and a flexible part seem to be necessary for a molecule to exhibit liquid crystallanity. This can be understood in terms of the argument that if the molecule is completely flexible, it will not favour orientational order, and if completely rigid, it will transform directly between the crystalline and isotropic phases. Thus the design of a mesogenic molecule requires a judicious balance of the rigid and flexible parts. While in the frozen form the molecules do not have a cylindrical shape (the dimensions of length, breadth and thickness are different), for all practical purposes they can be regarded as a cylinder, owing to the fact in the liquid crystalline state, they possess a fast rotation – on the time scales of 10^{-9} s – around the long molecular axis. The space/time averaged direction of orientation of all the molecules is defined by a parameter known as the director, and denoted by the symbol $\vec{\boldsymbol{n}}$. Further, unless under special circumstances, the LC phases do not exhibit ferroelectricity along $\vec{\boldsymbol{n}}$**,** and hence the director is apolar, i.e., $\vec{\boldsymbol{n}} = -\vec{\boldsymbol{n}}$. This is true even if the molecule has a permanent dipole moment, such as the cyano (CN) group of 5CB. In this case, the dipole has equal probability of pointing up or down. Figure 1.1(b) depicts a typical discotic liquid crystal molecule (benzene-hexa-n-alkanoates, for shortly called as BHn-alkanoates), showing the usual components of a rigid core whose periphery connects to multiple (3 or more) flexible tails [14]. The proposed research work plans to concentrate on thermotropic liquid crystals of the calamitic type and therefore we describe this category in a little more detail here.

1.2.1 Classification of thermotropic liquid crystals

Friedel [15], classified thermotropic liquid crystals of rod-like molecules broadly into three types: *nematic, cholesteric* and *smectic phases.*

Nematic phase

The nematic (N) phase has long-range orientational order, but no long- range translational order (Figure 1.2 (a)). The molecules are spontaneously oriented with their long axes approximately parallel to the director $\vec{\boldsymbol{n}}$. Having only orientational order, the N phase possesses ∞-fold rotational symmetry around the director and a three-dimensional translational symmetry. As mentioned already, the phase also has the so-called nematic symmetry, i.e. its physical properties remain unchanged under the inversion of the nematic director ($\vec{n} = -\vec{n}$). However, the preferred direction usually varies from point to point in the medium, but a homogeneously aligned specimen is optically uniaxial and strongly birefringent. Although there have been reports of the observation of the biaxial nematic phase in a low molar mass thermotropic system [16] its existence is yet to be established unambiguously.

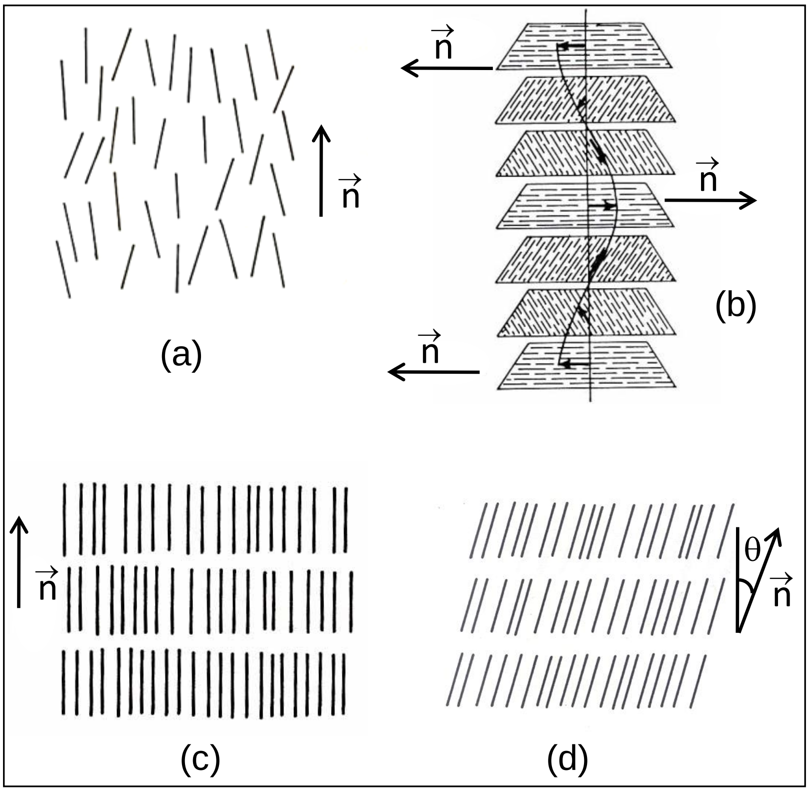

Figure 1.2: Schematic representation of the molecular arrangement in various liquid crystalline phase: (a) nematic, (b) cholesteric, (c) smectic A and (d) smectic C.

Cholesteric phase

The cholesteric mesophase is the chiral version of the nematic phase, observed in materials with optically active molecules. [*The name cholesteric, which is often given to chiral nematics, has a historical origin: the first chiral nematic liquid crystals were derivatives of the naturally occurring chiral material, viz., cholesterol*.] As a result of the chirality, the structure has a screw axis superimposed normal to the preferred molecular direction (Figure 1.2(b)). However, a racemic mixture (of right- and left- handed chiral molecules) will have a helix of infinite pitch that corresponds to the true nematic. For certain pure compounds, such a pitch-compensation also occur at a certain temperature [17]. The spiral arrangement of the molecules in the cholesteric mesophase is responsible for its unique optical properties [18], viz., selective reflection of circularly polarized light and a rotatory power about thousand times greater than that of an ordinary optically active substance.

Smectic phase

A smectic phase is characterized by a layered structure in addition to the orientational order of the nematic phase [19]. Depending on the molecular arrangements within the layer and the extent of inter-layer correlations smectic mesophases are classified into different types [20]. In the following, we describe the structures of the smectic phases commonly encountered, viz., smectic A, smectic C and its chiral modification, smectic C*.

Smectic A

In the smectic A (SmA) phase the average orientation of the molecules is normal to the layer planes with their centres irregularly spaced within each layer in a “liquid –like” fashion (Figure 1.2(c)). In fact, this fluidity of the layer is an essential characteristic of all smectic phases. A more rigorous way to treat the layering arrangement is to consider a one-dimensional mass density wave [21]. In the case of the SmA phase the wave vector of this mass density wave is parallel to the director. The inter-layer correlation is not a true long-range order, but exhibits an algebraic decay [22], a feature referred to as quasi-long range order.

Smectic C phase

The smectic C (SmC) phase is the tilted analogue of the SmA phase i.e., the molecules which are upright in SmA, are now tilted with respect to the layer normal (Figure 1.2(d)). However, the tilt breaks the rotational symmetry about the layer normal. Hence the polar angle fluctuations (towards and away from the layer normal) and the azimuthal (at constant polar angle) fluctuations have different energy costs, and consequently their magnitudes are different. This results in the SmC phase to have an optically biaxial character, while the SmA phase is generally optically uniaxial.

Smectic C phase*

If the constituent molecules are optically active then the SmC phase is referred to as chiral smectic C or smectic C* (SmC*) phase. Due to the presence of chirality the azimuthal angle of the tilted molecules precesses from one layer to another giving rise to a helicoidal structure (Figure 1.3(a)).

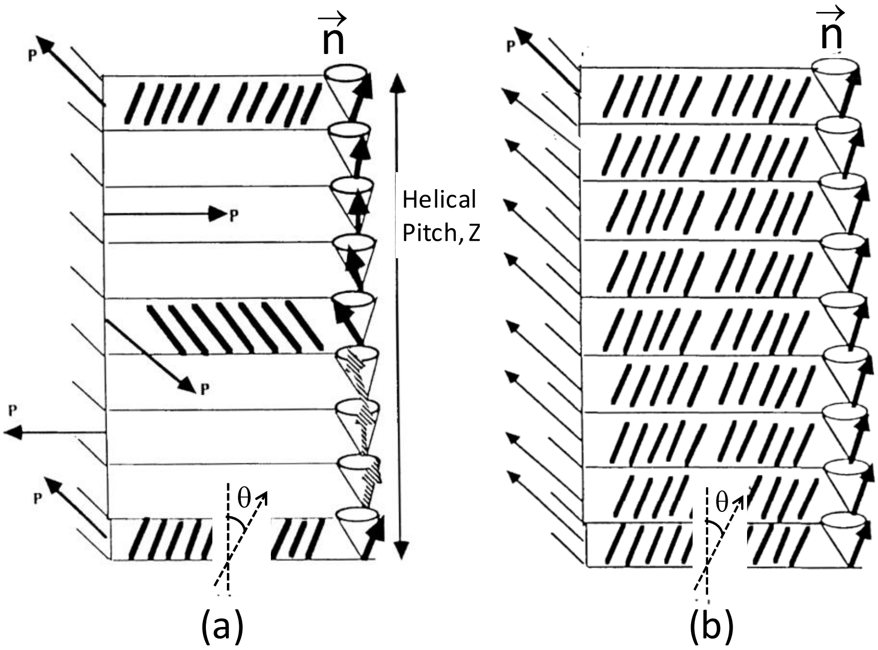

Figure 1.3: Schematic representation depicting (a) helicoidal and (b) unwound structures of the smectic C phase.*

The pitch of the helix is given by 2π/q, where q is the wave vector of the helix. Symmetry arguments demand the SmC* phase to exhibit ferroelectric properties, i.e., each layer shows a non-zero spontaneous polarisation P perpendicular to the direction of the tilt and the layer normal **Z** [23]. However, the presence of the helix averages out the macroscopic polarisation to zero. To obtain a non-zero macroscopic polarisation the helix has to be unwound by an external field, such as electric field or shear or by surface interactions. For a review on the topic see Ref. 24. The structure of an unwound smectic C* phase is shown in Figure 1.3(b).

For materials having nematic and smectic mesophases the typical sequence of phase transitions on cooling the sample is usually Isotropic - N – SmA – SmC – solid. Exceptions to this rule, in which materials exhibit reentrant phases, are known [25-28]. A comment about the physical appearance of these phases: In the isotropic liquid state the molecules can easily move around. The translational viscosity is comparable to that of water. In the nematic phase, the molecules can still diffuse around and the translational viscosity does not change much from that of the isotropic liquid state. For a material in poly-domain SmA phase, the translational viscosity is significantly higher, and the phase behaves like grease. In the solid phase the translational viscosity becomes infinitely large and the molecules (almost) no longer diffuse.

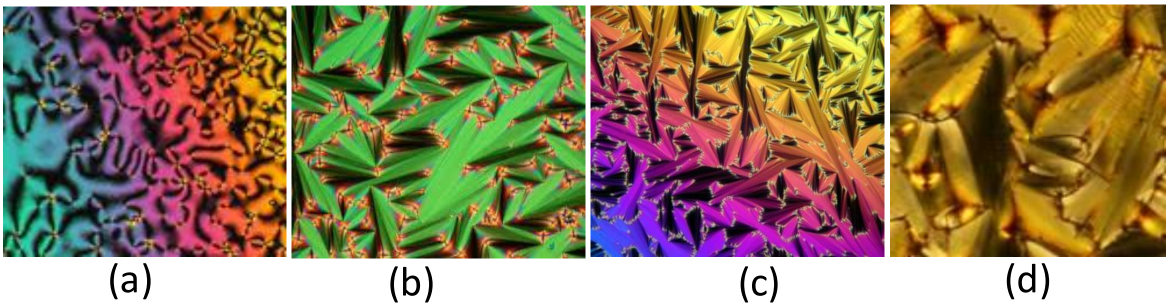

Figure 1.4: Commonly observed textures under a polarizing optical microscope: (a) Schlieren texture in the nematic, (b) fan-shaped texture in the SmA, (c) broken fan-shaped texture in the SmC and striped fan-shaped texture in the SmC phases.*

As stated earlier, the LC phases exhibit anisotropy in their physical properties. The presence of such an anisotropy in the optical properties manifests as a difference in the refractive index value measured along and perpendicular to the director, making the materials birefringent. An important consequence of this feature is the appearance of beautiful and characteristic textures (unique to each phase) when a thin film of the material is observed under a polarizing microscope. Such textures, important from the viewpoint of classifying the phases are shown in Figure 1.4(a-d) for the N, SmA, SmC and SmC* phases [29]. Apart from these, *fluid at least in one-dimension phases*, LC materials also exhibit certain three-dimensional positionally ordered phases possessing certain orientational degrees of freedom.

Since they share some common features with plastic crystals, to be described below, much interest has been generated in studying these phases. Chapter-4 describes an investigation involving such a 3-d ordered phase of LC molecules.

1.3. Plastic Crystals

A plastic crystal state comprises weakly interacting molecules that possess three dimensional positional order and some orientational or conformational degree of freedom. The plastic part of the name is to indicate the mechanical softness of such phases, which resemble waxes in getting easily deformed. If the internal degree of freedom is molecular rotation, the term rotor phase is employed, and if the internal degree of freedom is frozen in a disordered way, the label, orientational glass, is used. The orientational degree of freedom may be an almost free rotation, or it may be jump diffusion between a restricted numbers of possible orientations, as was shown for carbon tetra bromide [30].

1.4 Structural aspects of rotator phases

Some well known materials which exhibit these rotator phases [5, 31, 32] are certain normal alkanes, 1-alcohols and semifluorinated alkanes. n-alkanes are chemical compounds that consist only of hydrogen and carbon atoms and are bonded exclusively by single bonds (i.e., they are saturated compounds) without any cycles (or loops; i.e., cyclic structure). They belong to a homologous series of organic compounds in which the members differ by a constant relative molecular mass of 14. Saturated oils and waxes are examples of larger alkanes where the number of carbons in the carbon backbone is greater than 10. Long chain alkanes with more than 20 carbon atoms exhibit the rotator phases. The structural aspect of these rotator phases are briefly described below. Till date five different rotator phases, labelled R_I to R_V (or R1-R5 in the notation that we employ here), have been identified and characterized.

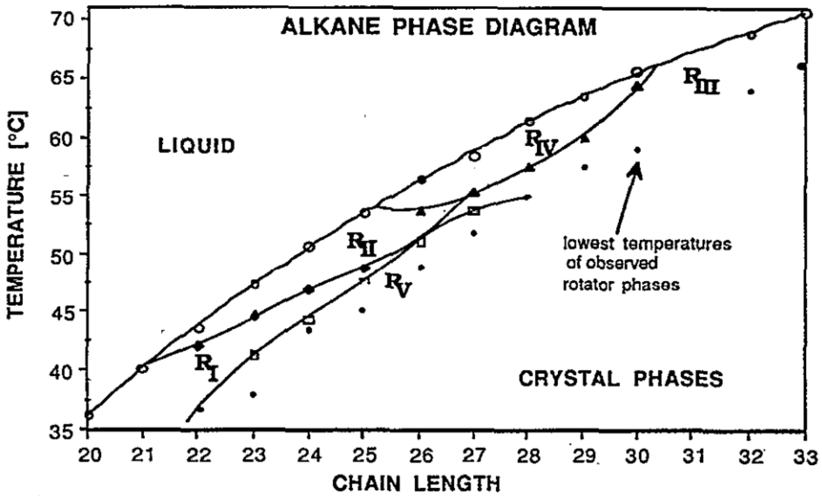

Figure 1.5: Temperature-chain length phase diagram showing the five rotator phases of the normal alkanes C20-30, 32, and 33. The solid dots show the lowest temperatures at which the rotator phase has been observed; (From Sirota et al [5])

Figure 1.5 displays the temperature-chain length phase diagram in the carbon atom range where rotator phases are observed for n-alkanes. Unlike the low-temperature fully crystalline phases, the rotator phases are characterized by relatively large changes in their structural constants as a function of temperature. As they are the most basic organic series and also are the building blocks for surfactants, lipids and liquid crystals, it is imperative to understand the detailed behaviour of normal alkanes. The interest in these phases also arises from the fact that they are representative of all weakly ordered phases in that the interaction energies are weak, in comparison to most solid state systems, and a large number of phases can occur with subtle entropic effects. Further, the rotator phases are well known for their interesting surface crystallization, negative thermal compressibility, anomalous high heat capacity and high thermal expansion properties [33]. Apart from the industrial uses such as in the petroleum and lubricating industry, they have important applications as thermohydraulic microactuators [34].

The distinction between the different rotator phases is made in terms of the lattice distortion ($\mathfrak{D}$), tilt magnitude (ϕ), and its direction [5]. Our interest specially is on three of them, viz., R2, R1 and R5 phases. Among these phases, the R2 phase, displaying the highest symmetry, has a rhombohedral structure with the untilted molecules pointing along the layer normal and an undistorted hexagonal lattice. In the R1 phase the hexagonal lattice is distorted to a rectangular form with untilted molecules. The R5 phase is the same as the R1 phase except that the molecules are tilted by an angle ϕ towards their next-nearest neighbours (NNN). The distortion $\mathfrak{D}$ of the lattice with respect to the hexagonal may be defined as 1-A/B, where A and B are the minor and major axes of an ellipse drawn through the six NNN when viewed along the axis of the chains. Thus, $\mathfrak{D} = 0$, $\phi = 0$ in the R2, $\mathfrak{D} \neq 0$, $\phi = 0$ in the R1 and $\mathfrak{D} \neq 0$, $\phi \neq 0$ in the R5 phase. The parameters $\mathfrak{D}$ and ϕ are used as order parameters for the R2-R1 and R1-R5 transitions respectively. Since $\mathfrak{D} \neq - \mathfrak{D}$, the former transition is described with a cubic term in the order parameter and therefore has to be first order. The latter transition can either be first or second order with the possibility of a tricritical point (TCP) separating the two branches. The transitions between these phases have also been studied in the frame work of Landau theory [35,36] as well as by molecular dynamics simulation [32a]. The molecular relaxation behaviour of the rotator phases has also been investigated [37].

In recent years, examining the behaviour of alkanes in a confined situation has attracted significant attention. These studies [38-41] have employed confining situations having a length scale comparable to the molecular dimensions, or have concentrated on the transition involving the crystalline phase, with the main result being a large supercooling of the crystallization point. The present thesis employs confinement at mesoscopic lengths, and thus enriches the available knowledge.

1.5 Plastic crystals versus liquid crystals

As is clear from the descriptions given above, both liquid crystals and plastic crystals can be considered like a transitional stage between true solids and true liquids. Another common denominator is the simultaneous presence of order and disorder. One of the main differences between these two types of soft matter is revealed in the Xray diffraction patterns. Plastic crystals possess long range positional order and therefore show multiple sharp Bragg reflections. Liquid crystals show no or very few Bragg peaks because the positional order is not truely long range. The anisotropy of the molecular shape is a governing feature in liquid crystals and not in plastic crystals. In this respect one could see them as opposites.

Part B: Confinement

1.6 Introduction to confinement

Materials often reveal new properties under confined situation than in the bulk state [42]. The physical characteristics such as phase transition, the magnitude of the order parameter, and the orientation of the molecules can be substantially affected and new thermodynamic LC phases can be induced [43] or bulk phases may be suppressed [44-45] due to confinement. Understanding the behaviour of finite sized systems is important in many areas of sciences from both theoretical and experimental points of view. In particular, the influence of system-size on phase transitions, a subject of continued interest for more than a century, has received much attention in the past two decades. For example, the effect of confinement on freezing and melting transitions has been extensively studied. These studies have raised fundamental and challenging questions pertaining to the known static and dynamical properties, and answers to them have important implications in many industrial and geophysical operations, like pollution control, mixture separation, catalysis, lubrication, adhesion, tertiary oil recovery, gas field technology, removal of pollutants from ground water and soils, and fabrication of nanomaterials. Molecules confined within narrow pores can exhibit a wide range of physical behavior. The presence of wall forces, competition between fluid-wall and fluid-fluid forces can cause phase transitions not found in the bulk, for example, layering, wetting, commensurate-incommensurate transitions, etc [46-51].

From a conceptual point of view, the differences between the bulk and confined systems arise from the overlap and competition between the typical correlation lengths driving the phase structure, or dynamics, and the finite size of the system. The introduction of a natural length scale to the system by the confining geometry can cause two major effects: the first is the cut-off or finite size effect, owing to which neither the static nor the dynamical correlation length can exceed the maximum pore size, resulting in perhaps the breakdown of scaling and universality. The second is the surface effect, caused by the enhancement in the surface-to-volume ratio due to the additional surface of the confining medium. The two types of anisotropic soft matter considered here are especially suitable for work on confined geometries for a number of reasons. For example,

(i) they exhibit a variety of phases with different degrees of orientational/translational order,
(ii) the involved transitions are second-order or at best weakly first-order,
(iii) they are typical representatives of soft (elastically weak) materials,
(iv) their response to perturbations induced by the confining matrix is pronounced and long ranged,
(v) they do not generally have chemical interactions with the typical host matrix.
(vi) liquid crystals also present strong competition among elastic, surface, and external field forces.

In comparison to studies of restricted geometries on phase transitions in liquid crystals, the measurements on rotator phases are very few. For the case of liquid crystals the confinement of the material has been achieved in several ways. Apart from simply confining the sample in wedge-shaped cell, pre-fabricated geometries such as porous membranes, and the *in-situ* fabricated network confinements employing particles capable of forming hydrogen bonding such as aerosil, etc have also been employed for these studies. In the case of the pre-fabricated systems, the voids in the confining matrix could be highly regular as in the case of membranes like Anopore, Nuclepore, etc. or an irregular network like in the case of aerogels. The geometrically enforced disorder observed in these situations can also be realized by including or “filling” certain particles into the liquid crystal. A popular choice for the particle has been aerosil®: silica spheres of ~ 7 nm diameter whose surfaces are decorated to achieve hydrophilic or hydrophobic interactions which result in *in-situ* created voids for confining the liquid crystalline medium. However, as against the LC materials, plastic crystals pose a challenge for the confinement studies since, unlike LCs the n-alkane molecules cannot be oriented with the application of an external field such as electrical or magnetic.

Certain commercially available matrices that can be employed as prefabricated restricted geometries are shown in figure 1.6. The advantage of such membranes lies in the fact that structures into which the material can be filled, is predetermined. This enables investigations to be carried out in nearly identical confined structures. Among these the Millipore membranes are composed of biologically inert mixture of cellulose acetate and nitrate shown in figure 1.6(e). The available pore size, i.e, diameter of the pore or the cavity that confines the material, ranges from 0.025 to 8 μm. But the drawbacks are that these membranes have a large distribution of the pore size and the cavities are interconnected. Synpor membranes have similar features. The polycarbonate Nuclepore membranes have a contrasting nature shown in figure 1.6(f). They are manufactured using two-stage track etching process. After bombardment with α-particles the damaged radiation tracks are chemically etched to obtain the desired pore size. These membranes are available as disks of 4.7 cm diameter and thickness of 10 μm with a variety of pore sizes ranging from 30 nm upto a few microns diameter. The pore size distribution is relatively narrow with 80% of the pores being within 10% of the mean. The bombardment technique, however, results in the existence of doublets, as well as some interconnection of the pores. Further the relatively small thickness (10 μm) of the Nuclepore membrane is not conducive for scattering measurements with conventional Xray apparatus. The polytetrafluoroethylene or PTFE is a synthetic fluoropolymer of tetrafluoroethylene based membrane or filter shown in figure 1.6(g). The available pore size ranges from 0.2μm to 0.45μm with 85% porosity. But the drawbacks are that these membranes have a very large distribution of the pore size and the cavities are interconnected.

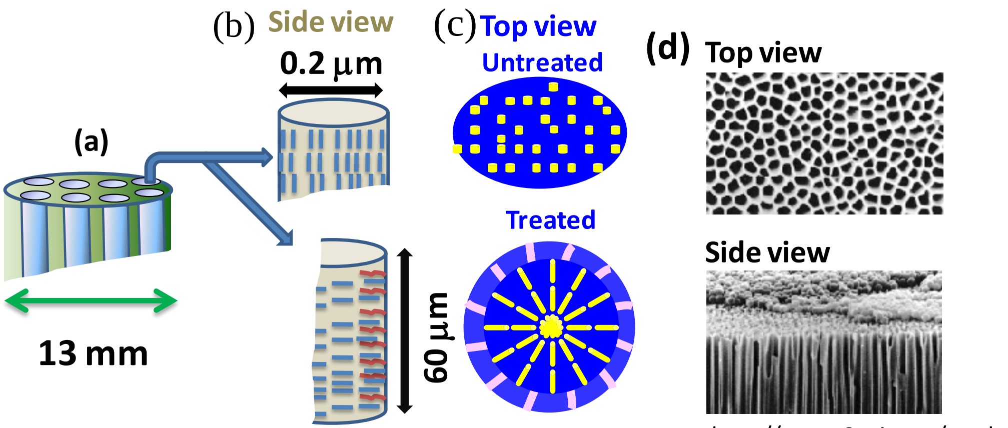

http://www.2spi.com/catalog/spec_prep/filter2.shtml

(e) Millipore (f) Nuclepore (g) PTFE

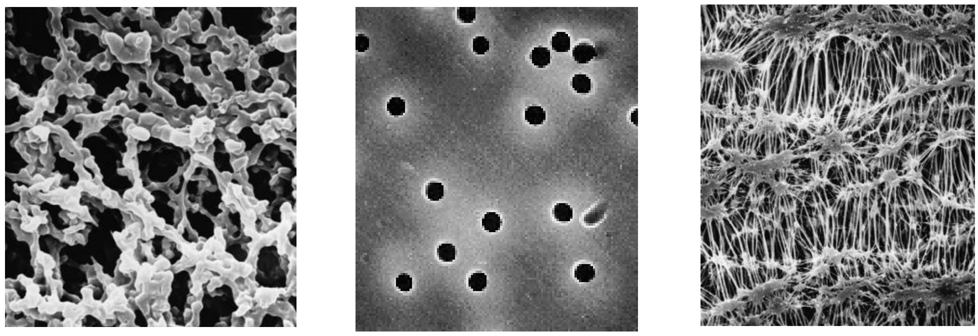

http://www.merckmillipore.com/ http://www.2spi.com/ http://www.merckmillipore.com/

Figure 1.6: (a-c) Schematic side and top view of the Anopore without and with surface treatment. Microscopy images of the different commercially available membranes: (d) Anopore (e) Millipore, (f) Nuclepore and (g) Polytetrafluoroethylene or PTFE.

The Anopore membranes, on the other hand, are made from an inorganic aluminium oxide matrix using an electrochemical anodizing process. The anodizing voltage controls the pore size. Since the process is electrochemical, conditions can be precisely controlled and a reproducible pore structure with narrow pore size distribution and high pore density is obtained. The cavity wall is smooth compared to that of Nuclepore (where it is corrugated because of etching) and hence has the capability to withstand a variety of surface treatments. Microscopy images of an Anopore membrane are shown in figure 1.6(d). The cross-section shows uniform cylindrical channels despite the 'honeycomb' nature of the surface. These membranes are available as disks of diameter 13 mm with a pore size 200 nm, porosity of 50% and a pore density of 10^9 cm^{-2}. In contrast, Nuclepore membranes have a porosity that is a factor of three less than that of Anopore but with a pore density that is almost ten times lower. To sum up the Anopore membranes having highly parallel cylindrical pores with narrow pore size distributions, a smoother cavity surface (permitting chemical treatments) and with large surface to volume ratio are quite attractive for physical studies, especially the anisotropic properties of the two kinds of soft matter chosen here.

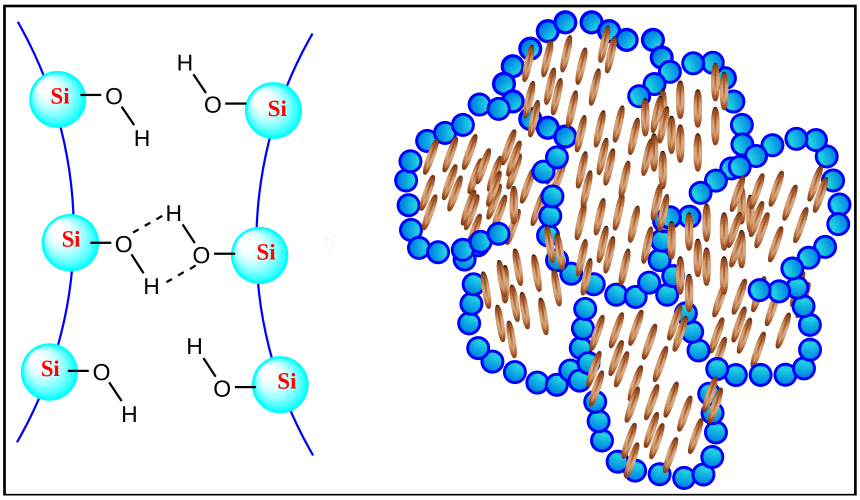

Figure 1.7: Schematic of the network formation of aerosil spheres owing to the hydrogen bonding between the particles (left) and confinement of the rod-like anisotropic soft matter with orientational order (right).

In the case of *in-situ* created geometry, matrices are formed by mixing the aeorsil particle into the organic materials which need to be confined. The advantage of the aerosil network is that the random disorder can be controlled and fine tuned by simply varying the concentration of the silica particles. The fragile hydrogen bond network (see Figure 1.7) that results from the interactions between the particles permits the disorder to be created *in situ*, allowing the influence of the quenched randomness on various phase transitions to be examined. The advantage of the aerosil network is that the random disorder can be controlled and fine-tuned by simply varying the concentration of the silica particles. Further the surfaces of the particles are decorated to achieve hydrophilic or hydrophobic interactions, details of which are discussed in Chapter-3.

1.7 Scope of this thesis

A brief description of the contents of the remaining chapters outlining the essential results is provided in this section.

Chapter-2: Confinement-Driven Weakening of the Rotator Phase Transitions in an Alkane

This chapter describes calorimetric and Xray diffraction measurements in the R1, R2, and R5 rotator phases of a long chain alkane (n-tetracosane, $C_{24}H_{50}$) in its bulk form and when confined to porous matrices (PTFE and Anopore) of two different length scales. Probing the order within and normal to the layers, drastic weakening of the R2-R1 and R1-R5 transitions is seen in the Anopore case having a mesoscopic length scale (200 nm), whereas the effect is milder with PTFE having a wider pore size. The effect on the Anopore confined situation is to such an extent that it results in the first observation of a confinement-driven second order transition in these systems. A significant reduction of the temperature range of the R1 phase is also seen in the Anopore case, a feature argued to cause the change in the order of the transition. Comparisons are also made on the recent prediction of such a point in a Landau model. These findings, while paving a new means of realizing a tricritical point, help in a better understanding of finite size effects in alkanes.

Chapter-3: Influence of Quenched Disorder Created by Nanosilica Network on Phase Transitions in Tetracosane

This chapter is on the detailed calorimetric measurements on composites of n-tetracosane, doped with nanosilica aerosil particles decorated with a corona of hydrophobic/hydrophilic nature. The weakly perturbing random field created by the addition of the aerosil particles has the general effect of weakening all the transitions to, and between, the three different rotator phases that the pure alkane exhibits. One of highlights of the studies is that the strong first order transitions of the pure alkane, viz., from the isotropic liquid to hexagonal rotator phase (Iso–R2), and tilted monoclinic rotator phase to the crystalline phase (R5–Cr), are accompanied by a much weaker supplementary peak at lower temperatures. In analogy with observations made in aerosil composites of liquid crystalline systems, and additionally with information from preliminary Xray diffraction measurements on the currently studied materials, it is reasoned that the subsidiary peaks are nothing but the transformations between the same phases as the corresponding main peaks due to the bulk of the material, but occurring in the vicinity of the surface of the aerosil particles. The nature of the corona of the aerosil particles also seems to play an important role. For the bulk transitions, the reduction in the transition enthalpy is higher for the composites with the hydrophilic particles, than those with hydrophobic particles; the opposite is true for the surface transitions. The data also suggest that the lowering of the transition temperature of the surface transition with respect to its bulk counterpart is more for the hydrophobic composites than the hydrophilic ones. We provide an explanation for these features based on the surface interactions between the particles and tetracosane molecules, and also the strength of the gel network. This chapter also describes the results of rheological measurements of the aerosil composites.

Chapter-4: Competition between Anisometric and Aliphatic Entities: An Unusual Phase Sequence with Induction of a Phase in an n-Alkane – Liquid Crystal Binary System

This chapter embodies a detailed study of the calorimetric and Xray investigations on a binary system of tetracosane and a liquid crystal (butyloxybenzilidene-octylaniline, or BBOA). This work demonstrates two important features arising out of introducing a liquid-crystalline (LC) compound into the rotator phase matrix and the consequent competition between the anisometric segments of the LC moieties and the aliphatic units. First, we show that the change in the structural character of the mixed medium depends on which of the entities forms the minority concentration: in the case of this being the alkane, the minority entities are nano-confined between the layers of the majority LC molecules. In contrast, if the LC molecules are present in a small concentration, then the layered structure merely gets roughened without any inter-layer confinement. The second and more significant result is the induction of a rotator phase at low LC concentrations that leads to an unusual phase sequence not reported hitherto. A Landau model is also presented that explains some of the observed features.

Chapter-5: Comparative Studies of the Nano-Composites of Strongly/Weakly Polar Liquid Lrystals Doped with Carbon Nanotubes

This chapter describes the results of dielectric and conductivity measurements on a composite of carbon nanotubes and a liquid crystal possessing dual frequency switching characteristics. The conductivity increases by two orders of magnitude with respect to that for the host liquid crystal, and achieves negligible temperature dependence. The frequency dependence of the ac conductivity is explained by the extended pair approximation model, although the exponent is slightly higher than generally seen. We demonstrate that the current through the sample can be field-driven between the two anisotropic values (170:1) by simply changing the frequency of the applied voltage, and exhibiting at least a millisecond response. The chapter also presents a comparison in the dielectric and conductivity behaviour when the polarity of the host LC is substantially changed.

Chapter-6: Experimental Studies on Composites of Gold Nano-Particle/Weakly Polar Nematic Liquid Crystal in bulk and confined forms

This chapter deals with calorimetric and dielectric investigations on a pure nematic liquid crystal and its composites comprising Gold nanoparticles (GNPs). Calorimetric measurements show that the inclusion of GNP has a strong influence on the isotropic–nematic transition temperature as well its first order character in terms of the transition entropy. The absolute value of conductivity increases by two-three orders of magnitude with respect to that for the host liquid crystal and its concentration dependence is demonstrated to be described by the percolation scaling law generally observed in composites of metal particles and polymers. The frequency dependence of the ac conductivity exhibits a critical frequency that is concentration-dependent, but the exponents obtained defy Jonscher's Universal Response principle. A surprising feature is the observation of a substantial increase in permittivity and their anisotropy values with faster director relaxation in the presence GNP. We provide an explanation for this antagonistic behaviour in terms of the alignment of the liquid crystal molecules in the vicinity of GNP, and the importance of the weak polarity of the liquid crystal used. The second part of the Chapter looks at the influence of embedding the LC-GNP composite in a restricted geometry created by aerosil particles. The inclusion of aerosil particles creating a gel network, albeit being non-conducting, surprisingly enhances the already high conductivity of the LC-GNP material. The nature of the aerosil corona (hydrophobic/hydrophilic) also controls the behavior. We argue that these features are caused by the amelioration of the percolation network of GNPs through the primary gel network of the hydrogen bonding aerosil particles. The concept can be generalized for a variety of systems wherein metal nanoparticles are imbibed in an insulating matrix.

Chapter-7: Confinement Studies on a Room Temperature Ferroelectric Liquid Crystal

This final chapter is on the results of X-ray, linear and non-linear dielectric constant measurements on a room temperature ferroelectric liquid crystalline phase in its bulk form and upon confinement in an Anopore membrane. The used material exhibits smectic C* (SmC*) helical pitch of ~ 200 nm, which is comparable to the pore dimension of the membrane. Xray measurements show several interesting results including unusually strong harmonic reflections, substantial broadening of the peak profile, correlation length smaller than the pore diameter, etc. The data suggest that the SmA–SmC* transition could be very close to a tricritical point in the bulk and moving away from it upon confinement. The dielectric studies show that confinement accelerates the relaxation dynamics of both the soft and the Goldstone modes, although with a reduced strength. The non-linear component of the dielectric constant exhibits qualitatively different thermal behaviour in the bulk and Anopore samples.

1.8 List of publications

The following is the list of publication resulting from the work carried out by the candidate, and included in the thesis:

1. K. Bhavesh, **M. Vijay Kumar**, C.V. Yelamaggad and S. Krishna Prasad, Enhancement of electrical conductivity of a liquid crystal-gold nanoparticle composite by a gel network of aerosil particles, *Appl. Phys. Lett.,**106**, 083110-5* (2015).

2. **M. Vijay Kumar**, S. Krishna Prasad, D.S. Shankar Rao and P.K. Mukherjee, Competition between anisometric and aliphatic entities: Induction of a new phase in a n-alkane – liquid crystal binary system, *Langmuir*, **30**, 4465–4473 (2014).

3. S. Krishna Prasad, **M. Vijay Kumar**, T. Shilpa and C. V. Yelamaggad, Enhancement of electrical conductivity, dielectric anisotropy and director relaxation frequency in composites of gold nanoparticle and a weakly polar nematic liquid crystal, *RSC Advances*, **4**, 4453-4462 (2014).

4. S. Krishna Prasad, **M. Vijay Kumar**, C.V. Yelamaggad, Dual frequency conductivity switching in a carbon nanotube/liquid crystal composite, *Carbon*, **59**, 512-517 (2013).

5. **M. Vijay Kumar** and S. Krishna Prasad, Composites of single walled carbon nanotubes and liquid crystals as switchable conductors, *Nanosystems: Physics, Chemistry, Mathematics*, **4**, 425–429 (2013).

6. **M. Vijay Kumar**, S. Krishna Prasad, D.S. Shankar Rao & E.P. Pozhidaev Confinement driven effects in a room temperature ferroelectric liquid crystal: X-ray, linear and non-linear dielectric investigations, *Phase Transitions*, **86**, 323–338 (2013).

7. **M. Vijay Kumar** and S. Krishna Prasad, Influence of quenched disorder created by nanosilica network on phase transitions in tetracosane, *RSC Advances*, **2**, 8531–8538 (2012).

8. **M. Vijay Kumar**, S. Krishna Prasad, and D.S. Shankar Rao, Confinement-Driven Weakening of the Rotator Phase Transitions in an Alkane through a Possible Tricritical Point, *Langmuir*, **26**, 18362–18368 (2010).

In addition to the above publications, the candidate is also an author to the following articles which are not discussed in the thesis:

1. **M. Vijay Kumar**, R. Bhargavi, G.G. Nair and S. Krishna Prasad, *Manuscript in preparation*.

2. **M. Vijay Kumar**, S. Krishna Prasad, Y. Marinov, L. Todorova, A.G.Petrov, Flexo-Dielectro-Optical Spectroscopy as a Method of Studying Nanostructured Nematic Liquid Crystals**.** *Mol. Cryst. Liq. Cryst., (in Press).*

3. D.S. Shankar Rao, **M. Vijay Kumar**, S. Krishna Prasad, Uma S. Hiremath, M. Sarvamangala and S. Basavaraja, Novel columnar–calamitic phase sequences in a binary system of bent-core and rod-like mesogens, *J. Mater. Chem. C,* **1**, 7488–7497 (2013).

4. K.S. Krishnamurthy, Pramoda Kumar and **M. Vijay Kumar**, Polarity-sensitive transient patterned state in a twisted nematic liquid crystal driven by very low frequency fields, *Phys. Rev. E.,* **87**, 022504-11 (*2013*).

5. M. Sarvamangala, **M. Vijay Kumar**, S.M. Khened, S. Basavaraja, D.S. Shankar Rao and S. Krishna Prasad, Anomalous dielectric behavior in the nematic and isotropic phases of a strongly polar–weakly polar binary system, *Phase Transitions,* **86**, 454–462 (2013).

The results described in chapter 2, 5, 6 and 7 were presented by the candidate at the following international/national conferences:

1. ***Oral presentation***, “Enhancement of electrical conductivity, dielectric anisotropy and director relaxation frequency in composites of gold nano -particle and a weakly polar nematic liquid crystal”, at 21th National Conference on Liquid Crystals-2014, Nov 10-12, 2014, Kanpur, India.

2. ***Oral presentation***, “Enhancement of electrical conductivity, dielectric anisotropy and director relaxation frequency in composites of gold nano -particle and a weakly polar nematic liquid crystal”, at 25th International Liquid Crystal Conference-2014, 29 June – 4 July, 2014, Dublin, Ireland.

3. ***Poster presentation***, “Novel columnar–calamitic phase sequences in a binary system of bent-core and rod-like mesogens”, at 25th International Liquid Crystal Conference-2014, 29 June – 4 July, 2014, Dublin, Ireland.

4. ***Oral presentation***, “Composites of single walled carbon nanotubes and liquid crystals as switchable conductors”, at IUPAC–Sponsored International Symposium on Macro- and Supramolecular Architechures and Materails: Nano System and Apllications, MAM-2012, Nov 21-25, 2012, Thrichencode, Tamilnadu, India.

5. ***Poster presentation***, “Confinement driven effects in a room temperature ferroelectric liquid crystal: X-ray, linear and non-linear dielectric investigations”, 18th National Conference on Liquid Crystals-2011, Nov 15-17, 2011, Itanagar, India.

6. ***Poster presentation***, “Confinement-driven weakening of the rotator phase transitions in an alkane through a possible tricritical point”, 17th National Conference on Liquid Crystals-2010, Nov 16-18, 2010, Surat, India.

1.9. References

1. I. Hamley, *Introduction to Soft Matter* (2nd edn), John Wiley, Chichester (2000).
2. R.A.L. Jones, *Soft Condensed Matter*, Oxford University Press, Oxford (2002).
3. P.G. de Gennes, Soft Matter, *Nobel Lecture* (1991), http://www.nobelprize.org/nobel_prizes/physics/laureates/1991/gennes-lecture.pdf.
4. R.H. Chen, *Liquid Crystal Displays: Fundamental Physics and Technology*, John Wiley (2011); P. Yeh and C. Gu, *Optics of Liquid Crystal Displays*, John. Wiley & Sons (2010).
5. See e.g., the seminal paper, E.B. Sirota, H.E. King, D.M. Singer, and H.H. Shao, *J. Cherm. Phys.* **98**, 5809 (1993).
6. L. Romero-Zeron and A. Kantzas, *J. Canad. Petr.*, **45**, 11 (2006).
7. V. Schmitt, F. Lequeux, C. Marques *J. de Phys. II*, **3**, 891 (1993); also see P.A. Hassan, J. Narayanan and C. Manohar, *Curr. Sci*. **80**, 980 (2001).
8. S. Chandrasekhar, *Liquid Crystals*, (2nd edn), Cambridge University Press, New York (1997).
9. P.G. de Gennes and J. Prost, *The Physics of Liquid Crystal*, Oxford University Press, New York, (1993)
10. P.J. Collings and M. Hird, *Introduction to Liquid Crystals, Chemistry and Physics*, Taylor & Francis, London (1997).

11. A. Jákli, and A. Saupe, *One-and Two-Dimensional Fluids: Properties of Smectic, Lamellar and Columnar Liquid Crystals*, Taylor and Francis (2006).
12. L.M. Blinov, *Structure and Properties of Liquid Crystals*, Springer, London, New York (2011).
13. A. Ramamoorthy (Ed.): *Thermotropic Liquid Crystals: Recent Advances*, Springer Netherlands (2007); R.A. Reddy and C. Tschierske, *J. Mater. Chem.*, **16**, 907 (2006).
14. S. Chandrasekhar, B.K. Sadashiva and K.A. Suresh, *Pramana*, **9**, 471 (1977).
15. G. Friedel, *Ann. Physique*, **18**, 273 (1922).
16. For summary on the attempts and present status, See e.g., C. Tschierske and D.J. Photinos, *J. Mater. Chem.*, **20**, 4263 (2010).
17. S.T. Lagerwall, B. Otterholm and K. Skarp, *Mol. Cryst. Liq. Cryst.*, **152**, 503 (1987).
18. See e.g., F.D. Saeva, in *Liquid Crystals, the Fourth State of Matter*, ed. F. D. Saeva, Marcel Dekker, New York, 249 (1979).
19. J. Prost, *Adv. Phys*., **33**, 1 (1984) and references therein.
20. P.S. Pershan, *Structure of Liquid Crystal Phases*, Singapore: World Scientific Lecture Series (1988).
21. K.K. Kobayashi, *Phys. Lett.*, **31A**, 125 (1970); W. L. McMillan, *Phys. Rev. A*, **4**, 1238 (1971); P.G. de Gennes, *Solid State Commun.*, **10**, 753 (1972).
22. J.A. Nielsen, J.D. Litster, R.J. Birgeneau, M. Kaplan, C.R. Safinya, A.L. Andersen and B. Mathiesen, *Phys. Rev. B*, **22**, 312 (1980).
23. R.B. Meyer, L. Liebert, L. Strzelecki and P. Keller, *J. Phys. (Paris)*, **36,** 69 (1975); R.B. Meyer, *Mol. Cryst. Liq. Cryst*., **40**, 33 (1977).
24. S.T. Lagerwall, *Ferroelectric and Antiferroelectric Liquid Crystals*, Germany: Wiley-VCH (1999); I. Muševic, R. Blinc and B. Zekš, *The Physics of Ferroelectric and Antiferroelectric Liquid Crystals*, (World Scientific, Singapore) (2000).
25. P.E. Cladis, *Phys. Rev. Lett.*, **35**, 48 (1975); P.E. Cladis, in *Physical Properties of Liquid Crystals*, Eds. D. Demus and J. Goodby, G. W. Gray, V. Vill, H.W. Spiess, John Wiley & Sons, Wiley-VCH,(Weinheim (1999).
26. N.V. Madhusudana, B.K. Sadashiva and K.P. L. Moodithaya, *Curr. Sci*, **48**, 613 (1979); F. Hardouin, G. Sigaud , M.F. Achard and H. Gasparoux, *Phys. Lett.* **71A**, 347 (1979).
27. P.E. Cladis, R.K. Bogardus, W.B. Daniels, and G.N. Taylor, *Phys. Rev. Lett.*, **39**, 720 (1977).

28. D.S.S. Rao, S.K. Prasad, S. Chandrasekhar, S. Mery, and R. Shashidhar, *Mol. Cryst. Liq. Cryst.*, **292**, 301 (1997); D.S.S. Rao, S. K. Prasad, V. N. Raja, C.V. Yelamaggad, and S.A. Nagamani, *Phys. Rev. Lett.*, **87**, 085504 (2001); C.V. Yelamaggad, V.P. Tamilenthi, D.S.S. Rao, G.G. Nair, and S.K. Prasad, *J. Mater. Chem.* **19**, 2906 (2009); J.O. Indekeu and A. Nihat Berker, *Phys. Rev. A*, **33**, 1158 (1986).
29. I. Dierking, *Textures of Liquid Crystals*, Wiley-VCH, Weinheim (2003); I.-C. Khoo, *Liquid Crystals*, Wiley-VCH, Weinheim (2007); S.V. Pasechnik, V.G. Chigrinov, and D.V. Shmeliova, *Liquid Crystals: Viscous and Elastic Properties*, Wiley-VCH, Weinheim (2009); J.W. Goodby , P.J. Collings , T. Kato , C. Tschierske , H. Gleeson, P. Raynes (Eds.), *Handbook of Liquid Crystals*, **Vol 8**, 2nd ed, Wiley-VCH, Weinheim (2014).
30. J.C. W. Folmer, R.L. Withers, T.R. Welberry, and J.D. Martin. *Phys. Rev. B*, **77**, 144205 (2008).
31. A. Müller, *Proc. R. Soc. London, Ser. A*, **138**, 514 (1932).
32. (a) M. C. Shih, T. M. Bohanon, J. M. Mikrut, P. Zschack and P. Dutta, *Phys. Rev. A*, **45**, 5734 (1992); (b) R. Berwanger, A. Henschel, K. Knorr, P. Huber, and R. Pelster, *Phys. Rev. B*, **79**, 125442 (2009); (c) N. Wentzel and S.T. Milner, *J. Chem. Phys.*, **132**, 044901 (2010).
33. E.B. Sirota, and H.E. King, *Science*, **281**, 143 (1998).
34. M. Lehto, J. Schweitz and G. Thornell, *J. Microelectromech. Syst.*, **16**, 728 (2007).
35. P.K. Mukherjee and M. Deutsch, *Phys. Rev. B*, **60**, 3154 (1999).
36. P.K. Mukherjee, *J. Chem. Phys.*, **134**, 224502 (2011).
37. L.P. Singh, S.S.N. Murthy and G. Singh, *J. Chem. Phys*. **128**, 024702 (2008).
38. L.D. Gelb, K.E. Gubbins, R. Radhakrishnan, and M. Sliwinska-Bartkowiak, *Rep. Prog. Phys.* **62**, 1573 (1999).
39. A. Henschel, T. Hofmann, P. Huber and K. Knorr, *Phys. Rev. E*, **75**, 021607 (2007); P. Huber, D. Wallacher, J. Albers and K. Knorr, *Euro. Phys. Lett.*, **65**, 351 (2004).
40. K. Jiang, B. Xie, D. Fu, F. Luo, G. Liu,Y. Su and D. Wang, *J. Phys. Chem. B*, **114**, 1388 (2010).
41. U. Zammit, M. Marinelli, F. Mercuri and S. Paoloni, *J. Phys. Chem B.*, **114**, 8134 (2010).
42. J. Klein and E. Kumacheva, *Science*, **269**, 816 (1995); P. Huber, J. *Phys.: Condens. Matter*, **27**, 103102 (2015); G.P. Crawford and S. Zumer (Ed.): For an excellent

collection of review articles in the field of liquid crystals, See *Liquid Crystals in Complex Geometries*, Taylor & Francis, London (1996).

43. B. Jacobsen, K. Saunders, L. Radzihovsky, and J. Toner, *Phys. Rev. Lett.*, **83**, 1363 (1999); L. Radzihovsky and J. Toner, *Phys .Rev. B*, **60**, 206 (1999).
44. G.S. Iannacchione, G.P. Crawford, S. Žumer, J.W. Doane, and D. Finotello, *Phys. Rev. Lett.*, **71**, 2595 (1993).
45. M. Ravnik, J. Fukuda, J. M. Yeomansa and S. Žumer, *Soft Matter*, **7**, 10144 (2011); L. Corvazier and Y.Zhao, *Liq. Cryst.*, **27**, 137 (2000).
46. R. Bergman and Swenson, *J. Nature*, **403**, 283 (2000).
47. R. Radhakrishnan, K.E. Gubbins and M. Sliwinska-Bartkowiak, *Phys. Rev. Lett.*, **89**, 076101 (2002).
48. K. Binder, *Ann. Rev. Mat. Res.*, **38**, 123 (2008).
49. J.K. Perron, M.O. Kimball, K.P. Mooney and F.M. Gasparini, *Nature Physics*, **6**, 499 (2010); A.M. Kahn and G. Ahlers, *Phys. Rev. Lett.*, **74**, 944 (1995).
50. S.K. Singh, A. Sinha, G. Deo, J.K. Singh, *J. Phys. Chem. C*, **113**, 7170 (2009).
51. H.K. Christenson, *J. Phys.: Condens. Matter.*, **13**, 95 (2001).

Chapter-2

Confinement-Driven Weakening of the Rotator Phase Transitions in an Alkane

Overview

This chapter describes calorimetric and Xray diffraction measurements in the R1, R2, and R5 rotator phases of a long chain alkane (n-tetracosane) in its bulk form and when confined to porous matrices (PTFE and Anopore) of two different length scales. Probing the order within and normal to the layers, drastic weakening of the R2-R1 and R1-R5 transitions is seen in the Anopore case having a mesoscopic length scale (200 nm), whereas the effect is milder with PTFE having a wider pore size. The effect on the Anopore confined situation is to such an extent that it results in the first observation of a confinement-driven second order transition in these systems. A significant reduction of the temperature range of the R1 phase is also seen in the Anopore case, a feature argued to cause the change in the order of the transition. Comparisons are also made on the recent prediction of such a point in a Landau model. These findings, while paving a new means of realizing a tricritical point, will lead to better understanding of finite size effects in alkanes.

The results are published in:

M. Vijay Kumar, S. Krishna Prasad and D. S. Shankar Rao, Confinement-Driven Weakening of the Rotator Phase Transitions in an Alkane through a Possible Tricritical Point, *Langmuir*, **26**, 18362–18368 (2010).

2.1 Introduction

Normal alkanes, in their pure form as well as their mixtures have been studied extensively, especially during the last twenty years or so [1-3]. The interest is from both the technological and pure-science points of view. They form the basic building blocks for a variety of soft matter systems such as lipids, surfactants, liquid crystals, polymers, to name a few. For the basic sciences, *n*-alkanes form simple and convenient model systems, understanding of which can help unravel of far more complex situations, like in polymers and biomembranes [4]. Alkanes are the main constituents of mineral oil and thus for the petroleum industry, a thorough understanding of their structural and thermodynamic properties is of vital importance. These substances are also considered to be the preferred tunable phase change materials for solar energy storage [5-7], cooling of power electronic devices [8], energy-saving [9] and solar absorption cooling systems [10].

In certain *n*-alkanes, C_nH_{2n+2} (hereafter denoted simply as C_n), 1-alcohols and semi-fluorinated alkanes, the polymorphic nature of the phase sequence in the standard crystalline state is further enriched by the existence of mesostate/s that occur between the truly crystalline phase and the liquid phase. As early as in 1932, Müller [11] presented X-ray evidence to show the existence of a phase between the crystalline and the liquid phase of some paraffins, in which the alkane molecules possess 3-d positional order, but exhibit more or less free rotation about their axes, and hence the name *rotator phase*. The phase was proposed to have a layered structure wherein the aliphatic chains are hexagonally packed with their long axes perpendicular to the layer planes. Subsequent efforts have put these concepts on a firmer basis [12, 13]. Extensive research over the years has resulted in the identification of different rotator phases. The existence and nature of a specific rotator phase could depend on, apart from the thermodynamic parameters – temperature and pressure – parameters such as the parity of *n*, the number of carbon atoms in the chain. This may not be surprising as individual molecules have different symmetries for the odd and even parity cases: a mirror plane for the odd (mm2 class) and a centre of inversion for the even (2/m class).

2.2 Classification of rotator phases

Up to now five different rotator phases – labeled simply as R1 to R5 [13] – have been reported which differ in their symmetries, in-plane molecular packing, layering sequence, and the magnitude of molecular tilt with respect to the layer normal. A common feature is, of course, that all these phases consist of layered structures with three-dimensional crystalline order of the molecular centers, but no long-range orientational order. It is this orientational melting but an intact positional order that these phases are known for, and in this aspect they have some similarities with the plastic phases such as the Crystal B (CrB) observed in liquid crystalline systems [14]. The classification of the phases considers three parameters, namely, the lattice distortion ($\mathcal{D}$), tilt magnitude (θ) and distortion direction (ϕ_d) as order parameters. Table 2.1 lists a summary of this classification scheme [13].

Table 2.1: Summary of the magnitude of the lattice distortion ($\mathcal{D}$), molecular tilt (θ), distortion direction (ϕ_d) and direction of tilt (ϕ_t) in different rotator phases.

Phase	$\mathcal{D}$	θ	ϕ_d **and** ϕ_t
R_{IV}	small	> 0	0
R_{III}	small	> 0	> 0
R_{II}	0	0	
R_{I}	large	0	
R_{V}	large	> 0	0

In the following we look at the application of this scheme for distinguishing between the different phases, for which we now define the three order parameters mentioned above. We begin with considering the ordering in the most symmetric of these phases, namely, the R2 phase. This phase exhibits a hexagonal packing of the upright chains. Thus the hexagonal ordering (of the molecules projected on to the layer plane) is that of an undistorted (with respect to hexagonal), non-tilted lattice, and is taken to be the basis for the classification of the other phases. Therefore, the lattice distortion ($\mathfrak{D}$) defined as $\mathfrak{D} = 1-(A/B)$, where A and B are the minor and major axes of an ellipse drawn through the six neighbours when viewed along the long axis of the molecule. For systems with a finite distortion, the distortion direction is indicated by the angle ϕ_d. Thus, $\mathfrak{D}=0$ and $\phi_d = 0$ in the hexagonal phase. If the molecules get tilted with respect to the layer normal the tilt is represented by a polar angle (θ, also generally referred to as the molecular tilt) and an azimuthal angle ϕ_t. These features are schematically shown in Figure 2.1

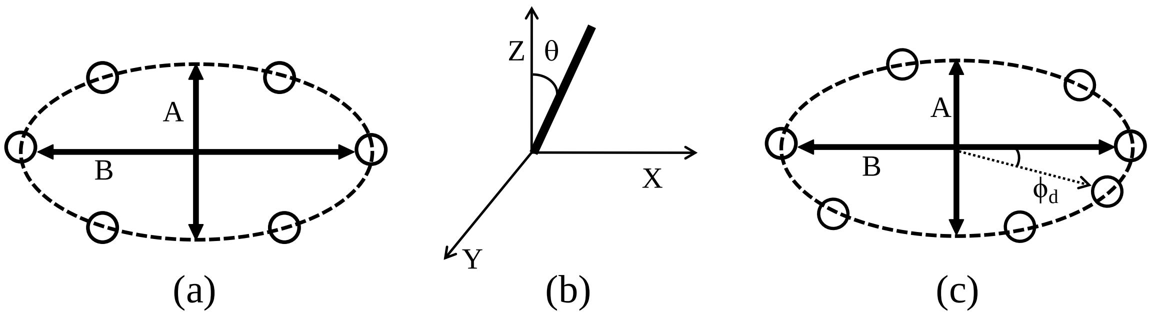

(a) (b) (c)

Figure 2.1: Schematic illustration to define (a) the lattice distortion $\mathfrak{D}$ (=1-A/B), *in the case of an orthorhombic lattice represented by the minor (A) and major (B) axes of the ellipse formed by the locus of the projected long axes of six nearest neighbour alkane molecules A=B, corresponds to a hexagonal lattice. Panel (b) shows the side view of the layers (XY plane) to depict the tilt (θ) of the molecules with respect to the layer normal (Z) direction. The case of an oblique distortion characterized by the distortion angle* ϕ_d *is depicted in panel (c).*

2.3 Orthogonal and tilted rotator phases

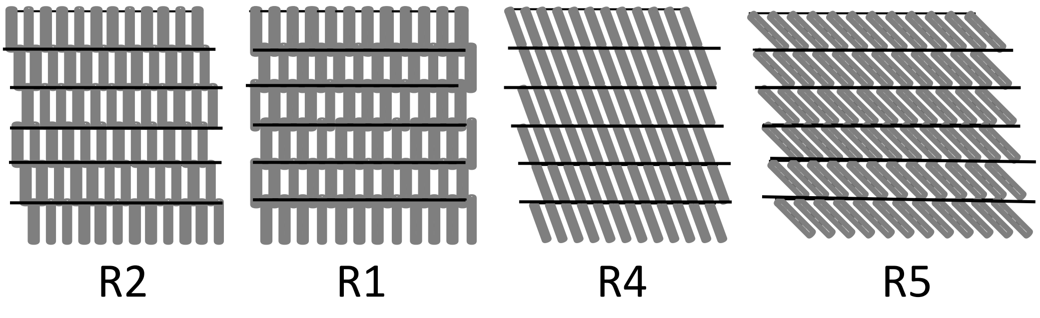

Figure 2.2: A cross-sectional view of the molecular arrangement in the different rotator phases.

A schematic view showing the stacking of the molecules in the layers of the different phases is given in Figure 2.2. The R1 and R2 phases are orthogonal phases with the molecules pointing along the layer normal whereas in the of R3, R4 and R5 phases there is a finite tilt of the molecules about the layer normal direction and thus these three phases are tilted phases. The R2 phase has a rhombohedral structure with a ABC trilayer stacking. Thus the molecules in adjacent layers are over interstitials sites. Lowering the symmetry of this phase the hexagon can get distorted resulting in the R1 phase with a rectangular lattice having AB…AB bilayer stacking as the molecules are placed, on an average, halfway between two nearest neighbours of the adjacent layers. So $\mathfrak{D} \neq 0$ and ϕ_t, $\phi_d = 0$ in the R1 phase. In R3 phase, the directions of the molecular tilt and lattice distortion are not along any particular symmetry direction relative to the lattice and the structure is triclinic. The lattice distortion is small and the azimuthal direction of tilt is in between the next-nearest neighbour (NNN) and the nearest neighbour direction (NN). The R4 phase is nearly hexagonal lattice with end to end monolayer AA with the tilt in a direction between nearest neighbors (NN). Finally, in the R5 phase, the distortion and stacking are similar to R1 phase except that the molecules are tilted between NNN. Thus, $\mathfrak{D}$ and ϕ_t are very large with $\phi_d = 0$. Some of these features are reflected in highly ordered liquid crystalline structures, gel phases of phospholipids, and Langmuir monolayer systems [15]. Figure 2.3 [13a] shows the rich phase diagram that can be obtained with subtle variations of the length and parity of the alkane family.

With such an intricate behaviour, the need arises to investigate the influence of confined geometry on the phase/phase transition of these long-range correlated systems. As indicated in the Chapter-1, the behavior in nano-confinement situations is of significant interest, since the new physics resulting from finite-size effects, reduced dimensionality, surface forces, etc., can help in a better understanding of the various thermo physical and interfacial phenomena, having implications in many industrial and geophysical operations, apart from contributing to the field of transitions among ordered phases [16]. It is also interesting to note that molecular simulations have brought out very well certain experimentally observed features [17-19]. The rotator phases are well-known for their interesting surface crystallization behaviour, negative thermal compressibility, anomalous high heat capacity, and high thermal expansion properties [13, 20]. Apart from the industrial uses in the petroleum and lubricating industry, they have important applications as thermohydraulic microactuators [21].

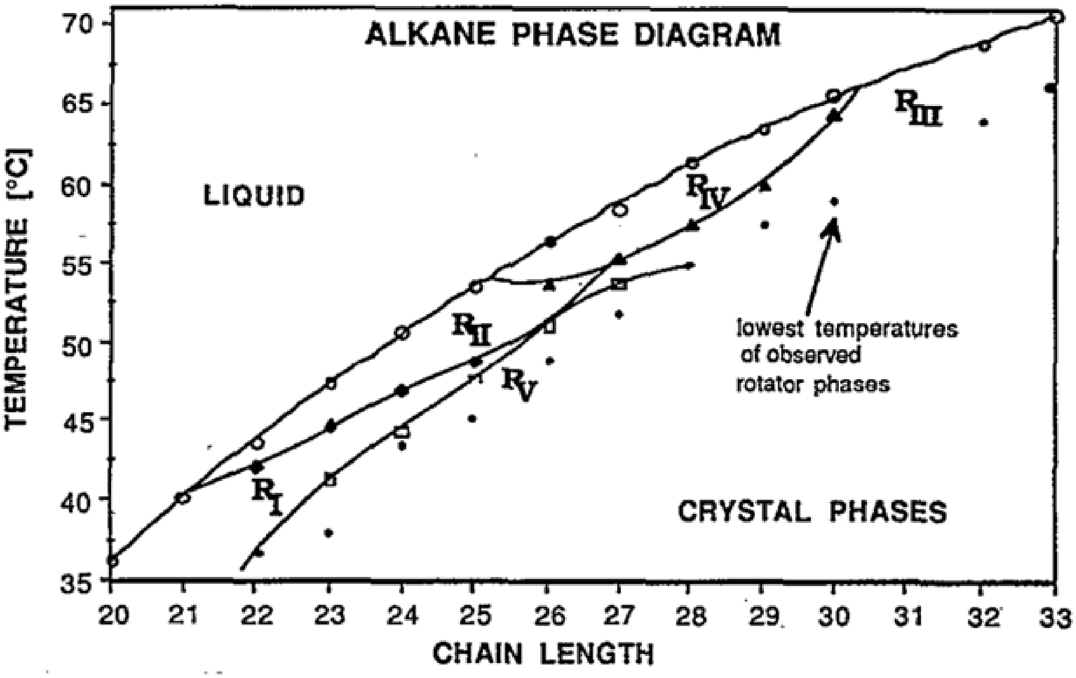

Figure 2.3: Phase diagram showing the five rotator phases of the normal alkanes C20-30, 32, and 33. The solid dots show the lowest temperatures at which the rotator phase has been observed (From. Ref. 13a).

From phase transition point of view, confinement of the material has been seen to affect the nature of the phase transitions like gas–liquid transformation (capillary condensation), liquid–liquid and freezing/melting transitions, different solid-solid transition, and also influence phenomena such as supercooling and surface (or interface) freezing of monolayers [22]. As already mentioned in Chpter-1, these studies [16, 23, 24] have employed confining situations with a length scale comparable to the molecular dimensions, or have concentrated on the transition involving the crystalline phase, with the attractive result, from the viewpoint of present studies, being a large supercooling of the crystallization point.

In this chapter, we demonstrate that confinement on the mesoscopic length scale has dramatic effects on the transitions involving rotator phases, by probing the ordering within and normal to the layers. We observe unique weakening of the transitions, especially that between the R1 and R5 phases, the extent of which is dependent on the magnitude of the length scale. Together with the lattice distortion parameter, we look at the order parameter behavior and show that confinement could be a strong possibility to realize the TCP on the R1-R5 boundary, a feature that is significant in view of the recent theoretical prediction [25] of such a point, albeit in the pressure-temperature plane.

2.4 Material

The material chosen for the present study is n-tetracosane ($C_{24}H_{50}$ or C_{24} for short). It exhibits R1, R2 and R5 rotator phases between isotropic (Iso) and crystalline (Cr) states. The molecular structure and phase sequence of this compound are shown in Figure 2.4.

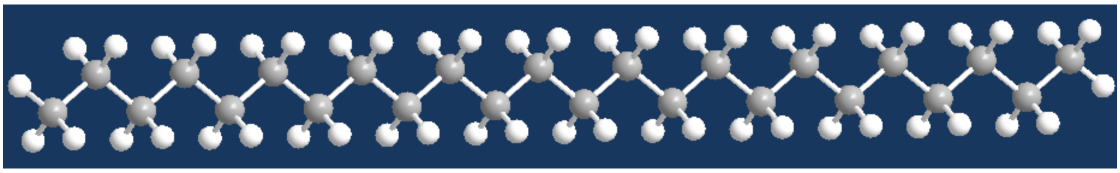

Iso 49.8 °C **R2** 46.7 °C **R1** 44.1 °C **R5** 42.6 °C **Cr**

Figure 2.4: The molecular structure and phase sequence of tetracosane

2.4.1 Sample filling into Anopore and PTFE membranes

Experiments have been performed in the bulk and two confining matrices, namely Anopore and PTFE. Recalling some of the details of these two membranes given in Chapter-1, it is to be noted that the Anopore membrane is of 60 μm thickness with 200 nm pore dimension while the PTFE membrane has a thickness 100 μm and a pore dimension of 450 nm (Both porous matrices were obtained from Whatman, USA). While the individual porous channels are completely isolated in the case of Anopore, there is substantial connectivity in the case of PTFE membrane (see Figure 2.5). The cavity surfaces of Anopore are naturally hydrophilic while those of PTFE are hydrophobic or hydrophilic.

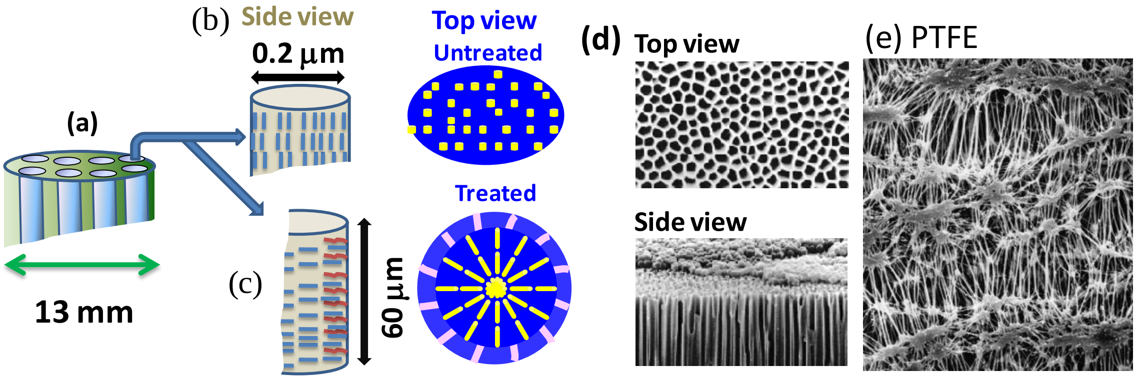

Figure 2.5: (a) Schematic representation of the channels in an Anopore membrane. Illustration of the possible molecular arrangement inside a single pore in the (b) untreated and (c) palmitic acid treated membrane. The images provided in (d) are the SEM (scanning electron microscope) pictures of these two situations (http://www.2spi.com/); especially note the regularity of the channels. (e) SEM image of a PTFE membrane (http://www.merckmillipore.com/) displaying the irregularly arranged channels.

For sample filling, a procedure reported earlier for liquid crystalline (LC) materials [See e.g., Ref. 26] was followed. Before usage, the Anopore membrane was kept in vacuum for 15 hours at 300°C to remove any residual gas. For filling the sample, the membrane (Anopore/PTFE) was heated to a temperature slightly higher than the isotropic-R2 value. The experiments required two different molecular alignment directions. For the case wherein the molecules had to be in the plane of the membrane, the Anopore matrix was treated with a 2 wt% solution of long chain acid (palmitic acid, $C_{15}H_{31}COOH$) in methanol, a procedure known to induce the required alignment [27]. The membrane was dipped in palmitic acid solution for approximately 30 minutes, taken out and quickly pressed with filter paper in order to remove the extra solvent on both sides of the membrane. It was then placed in an oven at 60°C for an hour to evaporate and remove the solvent completely. The acid head group of palmitic acid binds chemically to the Anopore surfaces and the aliphatic chains form a compact array perpendicular to the cavity wall. Now, the Anopore membrane becomes hydrophobic in nature after the surface treatment. After this, the C24 sample was kept on the top surface of the membranes and the temperature was maintained a few °C above the isotropic for 1 hour to ensure complete filling by capillary action. The excess sample left on the surfaces was then removed by pressing between filter papers. In the membrane with such a chemical modification of the surface, strong scattering of light was observed upon filling the sample. More importantly, the modification induces an orientation such that the molecules are normal to the pore walls. This may lead to planar-radial, planar-polar, escaped radial or planar bipolar configuration of the molecular orientation. In the case of untreated Anopore, the molecules have the tendency to align along the pore axis, a configuration ideally suited to study the in-plane correlations. When the sample is filled into the untreated membrane it becomes quite transparent due to the matching of the refractive indices of the membrane and the sample, a feature used as a confirmatory test for the molecular orientation along the axes of the pores.

2.5 Measurements

2.5.1 Differential Scanning Calorimeter

Differential scanning calorimetric (DSC) scans were taken with the help of a calorimeter based on the principle of power compensation (Perkin-Elmer, Model- Pyris Diamond DSC). The sample and reference chamber of the DSC were maintained under nitrogen environment during the scan. The bulk sample in powder form or the two confined samples as properly cut pieces of the filled membranes were taken in 50 μl Aluminum cups. An empty Aluminum cup of approximately the same bare weight as the sample cup served as the reference cup to take care of the background variation of the enthalpy and specific heat contributions by the sample chamber.

2.5.2 High Resolution Xray diffraction apparatus

Xray measurements were performed using the PANalytical X’Pert PRO MP X-ray diffractometer schematically shown in figure 2.6. It consists of a focusing elliptical mirror and a fast high resolution detector (PIXCEL). The sealed – tube X-ray source was operated at 45 KV and 30 mA, and CuK$_\alpha$ radiation (wavelength: 0.15418 nm) was employed for the measurements. The operating setup parameters like 2θ range, step size, exposure time were controlled by Data collector software. The bulk sample was filled in a Lindeman capillary of 1mm diameter in the isotropic state, and the membranes for the confined cases were mounted on a holder with proper entry and exit holes such that the sample did not come in contact with the holder surface. The holder/capillary was in turn placed in the Mettler hotstage for controlling the temperature. The Mettler temperature programmer was controlled by computer.

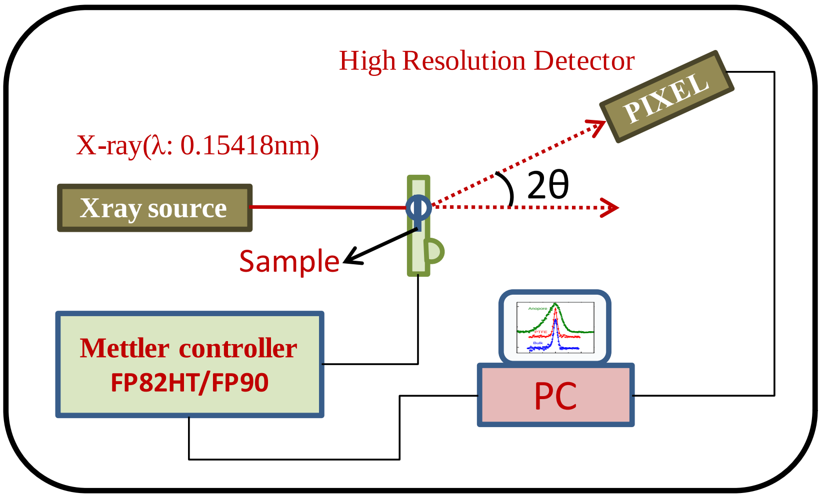

Figure 2.6: Schematic diagram of the Xray diffraction apparatus

2.6 Results and Discussion

2.6.1 Differential Scanning Calorimetric Measurements

Figure 2.7 shows the DSC scans obtained at a rate of 1^{o} C/min for the bulk and the two confined cases. The scans for the confined samples look qualitatively similar, and therefore, their phase sequence may be assumed to be the same as that for the bulk sample, a feature indeed confirmed by X-ray studies, to be discussed later. The first salient feature seen in the DSC scans is the broadening of the transitions upon confinement, with the magnitude being different for different transitions and also dependent on the length scale of confinement. For the Iso-R2 transition, the width of the thermal anomaly gets doubled for both PTFE and Anopore samples, whereas the transition to the crystal phase is significantly wider for the Anopore case only. The widening of the transition when the material is confined to narrow pores is quite well known [28], especially in liquid crystals [29-37]. Also seen is the fact that the crystallization point is lowered for the Anopore sample, a behavior in agreement with the strong supercooling seen in the case of very small length scale confinements [38].

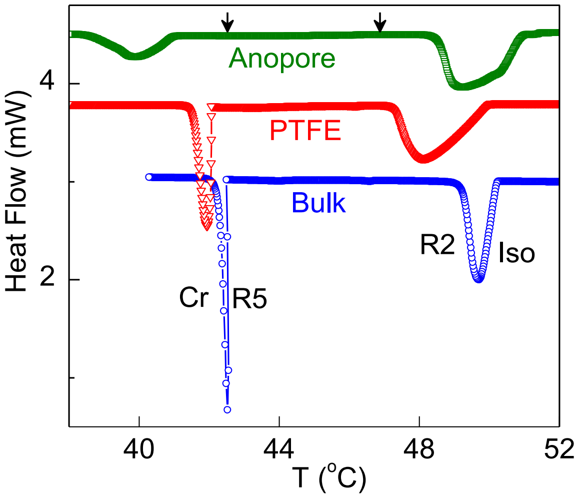

Figure 2.7: Differential scanning calorimetric scan for the Bulk, PTFE and Anopore confined samples. While the high temperature peak corresponds to the Iso-R2 transition, the low temperature one is associated with the crystallization process from the R5 phase. Since the R2-R1 and R1-R5 transitions are too weak to be seen on the scale shown, the temperature range between the two vertical arrows is shown on an enlarged scale in Figure 2.8.

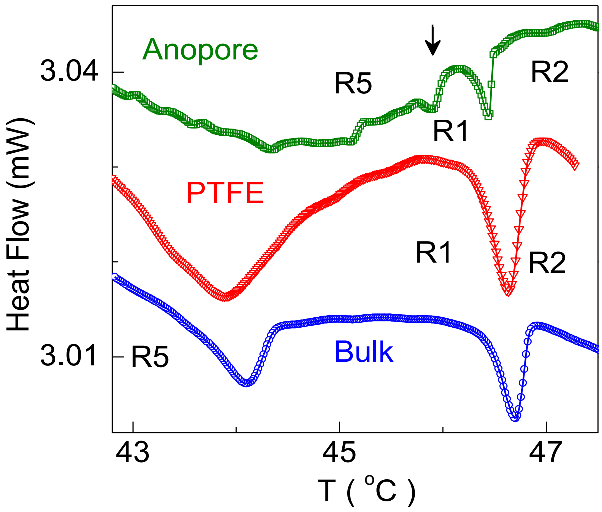

Figure 2.8: An enlarged view of the calorimetric scans in the region of the R2-R1 and R1-R5 transitions. The thermal signatures become extremely weak for the Anopore case, with the change across R1-R5 being barely visible (marked by an arrow). For convenience of presentation, the data for PTFE and Anopore scans have been given an arbitrary vertical shift.

More important, from the viewpoint of the present studies, are the data across R2-R1 and R1-R5 transitions, shown in Figure 2.8. Here a dramatic weakening of the thermal signatures for the Anopore sample has been observed, so much so that the R1-R5 transformation is barely visible, and the range of R1 phase significantly diminished. The transition temperatures as obtained from the peak points of the DSC scans for the bulk and confined situations are given in Table 2.2. The transition enthalpies also corroborate these features: since the exact amount of the sample could not be obtained in the confined case, the ΔH values were normalized by that for the Iso-R2 transition. With this, the enthalpy values (in J/g) across the R2-R1 and R1-R5 transitions are 0.64, 0.85 for the bulk; 0.4, 0.59 for PTFE; 0.06, ~0 for Anopore.

Table 2.2: Transition temperatures (^oC) for the different transitions in the bulk and the two confined situations. The enthalpy (J/g) across Iso-R2 and R5-Cr transitions are given within the squared brackets.

Sample	Iso-R2	R2-R1	R1-R5	R5-Cr
Bulk	49.8 [69]	46.7	44.1	42.6 [31]
PTFE	48.6 [44]	46.6	43.9	42.4 [19]
Anopore	49.6 [26]	46.4	45.9	40.2 [8]

It may be recalled that the R2-R1 transition is associated with restacking from ABC to ABAB type packing and also accompanied by lattice distortion. Therefore, the enthalpy of this transition should not be zero. On the other hand, the R1-R5 transition has only the tilt angle change without any restacking and distortion, so its transition enthalpy is not expected to be higher than that for R2-R1 transformation. However, the large specific heat change for the R1-R5 calculation of the transition, especially on the lower temperature side, could lead to a slightly erroneous calculation of the transition enthalpy for this transition in comparison to that for the R2-R1 transition. Thus, it appears that the confinement has a much stronger effect on the R1-R5 transition, as compared to the R2-R1 transition, with the data for the Anopore sample suggesting a possible second order R1-R5 transition.

2.6.2 Influence of confinement on the transition temperature

As seen from Table 2.2 the general trend that is observed is that confinement lowers the transition temperature as well as the transition enthalpy. In this section we look at the implication of such a feature noted in other condensed matter systems also [39]. Observing such behaviour for the nematic-isotropic transition, Dadman and Muthukumar [29] provided an explanation on the basis of surface anchoring and finite size effects. According to this argument small finite clusters undergo the transition at a temperature lower than that in the bulk owing to the fact that clusters (or domains) could be poorly correlated. The curved pore surface facilitates breakdown of the long-range positional order. The formation of small crystals was first described by Gibbs [40], and the related theory for the effect of curvature on the vapour pressure of liquid droplets was derived by Thomson [41]. For the melting of solids in confined pores, the quantitative dependence of the melting point depression ΔT_m (= T_m – T_m(pore)) on the pore radius is obtained using the Clausius–Clapeyron equation to give the vapour pressure as a function of temperature, and the Kelvin equation to correlate this vapour pressure with the pore radius. Thus, for a cylindrical pore of radius R, the expression, often called the Gibbs-Thomson equation, is given by [42]

$$\Delta T_m = \frac{2T_m\sigma_{sl}}{\Delta H_m \rho R} \tag{2.1}$$

Here σ_{sl} is the average interface surface energy tension between the solid and liquid phases, ΔH_m is the bulk enthalpy of melting and ρ is the mass density of the sample. This expression can be employed to estimate either σ_{sl}, or using known value of σ_{sl} to compare with the experimentally determined depression in the transition temperature when the material is confined in porous media. Owing to the fact that the pores are regular and well defined for Anopore membrane we calculate σ_{sl} for that case. Substituting the values for the strongest transition (Iso-R2) shown in Table 2.2, and using ρ to be 797 Kg/m^3, we obtain σ_{sl} to be 4 mJ/m^2. This value is a factor of 4 smaller compared to that obtained for the melting (crystal-isotropic) of a shorter alkane, n-Heptane [43], but is in the same range as those for the orientational melting and two-dimensional melting transitions of a liquid crystal [36]. A similar calculation done for the PTFE case yields an order of magnitude higher σ_{sl}. This feature is in general agreement with the trend seen by McKenna [43] that σ_{sl} increases for wider pores. However, the possibility of the two important differences between the Anopore and PTFE membranes, viz., interconnectivity of pores and hydrophobic nature of the latter influencing the values cannot be ruled out.

2.6.3 Xray measurements

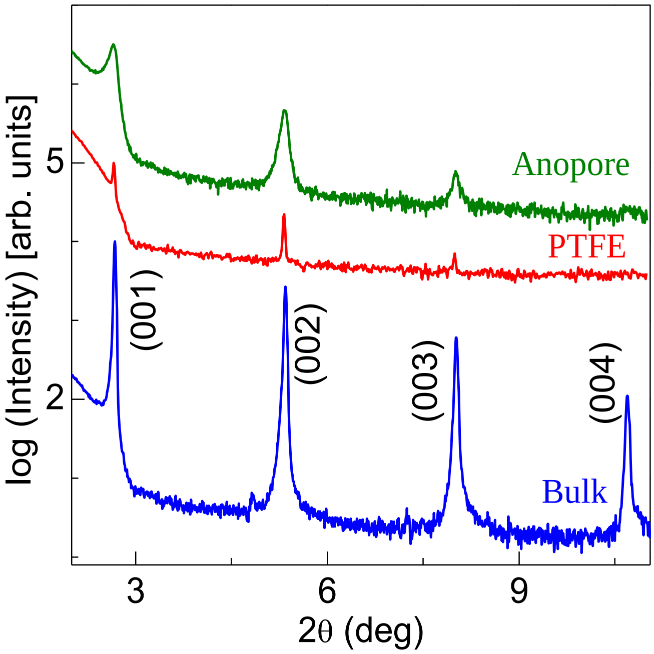

Figure 2.9: Representative Xray scans in the R2 phase for the bulk and the two confined systems, exhibiting the harmonics of the fundamental peak (indexed as 00l peaks, where l =1 to 4), characteristic of the plastic nature of the phase. Note that this character is retained in the confined cases as well, although the intensities diminish.

Xray measurements were carried out in the 2θ range of 1-30° covering the low as well as wide angle scattering from the sample. The raw X-ray diffraction profiles in the low angle region shown in Figure 2.9 for bulk, Anopore and PTFE samples feature the strong higher harmonics of the fundamental periodicity associated with the well ordered layering characteristic of the plastic nature of the R2 phase even in the confined cases. However, the effect of confinement becomes evident when the data are viewed on an enlarged scale (see Figure 2.10). While the scan for PTFE is virtually as sharp as that for the bulk, the reduced length scale of the Anopore broadens the peak substantially.

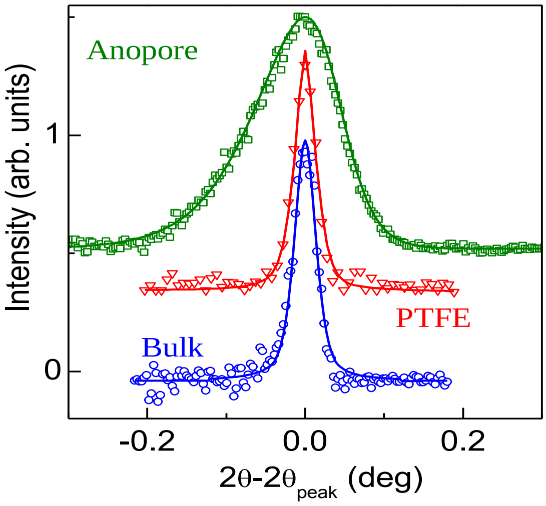

Figure 2.10: The background-subtracted fundamental peak on the reduced diffraction angle scale, for the three sample scenarios. Especially to be noted is the substantial broadening of the profile for the Anopore confined material. The lines are fits to a Lorentzian expression, albeit asymmetric in the case of Anopore sample.

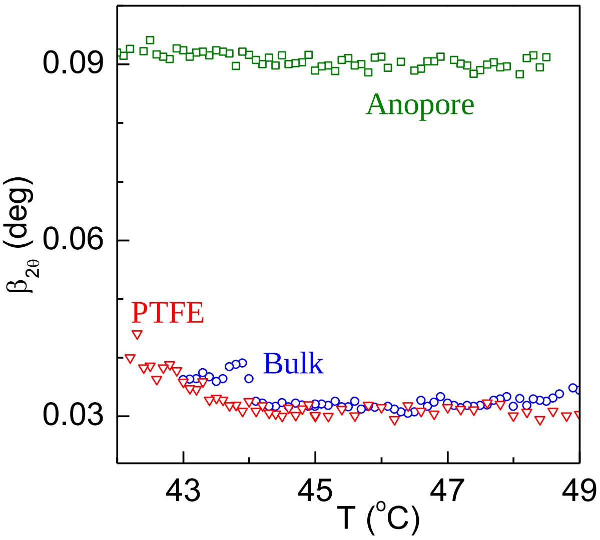

Figure 2.11: Temperature dependence of $\beta_{2\theta}$ *the full-width-at-half-maximum data for the bulk and confined cases. Notice that the values for the bulk and PTFE cases are comparable, whereas the Anopore sample has a much larger FWHM.*

A Lorentzian expression with a suitable background term describes the profiles well in all the cases, except that an asymmetric shape factor had to be included for the Anopore case, due to the intensity contribution from the membrane material. $\beta_{2\theta}$, the full width of the peak (FWHM) obtained by the fitting process, shows in a striking fashion the difference between especially the PTFE and Anopore cases (see Figure 2.11). While the data for the former essentially lie on those for the bulk sample, the Anopore sample exhibits a remarkable increase (factor of 3), a feature that is true in all the three rotator phases. Such a peak broadening, when the material is confined in Anopore membranes, recently reported [36] for the fluid (SmA) and plastic (CrB) layered phases of a liquid crystalline material, is not known for any alkane. From such line broadening, the average length scale of the structure (ξ_s) can be calculated by using the Debye-Scherrer expression,

$$\xi_s = \frac{0.89 \times \lambda}{\beta_{2\theta} \times \cos\theta_{peak}} \tag{2.2}$$

Here λ is the wavelength of the Xray beam. The measured $\beta_{2\theta}$ values were corrected for the structural broadening by using $\beta_{2\theta} = (\beta^2_{2\theta:meas} - \beta^2_{2\theta:std})^{1/2}$. Here the FWHM value for the bulk was used as $\beta_{2\theta:std}$. The calculated ξ_s values are 510 nm for both the bulk and PTFE cases but are much lower (190 nm) for the Anopore sample, clearly showing the finite-size effects. It may be noted that the ξ_s values in the two confining cases are comparable to their pore sizes. Since the ξ_s value for the bulk, which can be taken as the instrumental-resolution limit, is the same for the PTFE case suggests that experiments with a higher instrumental resolution would be required to bring out the differences between the bulk and PTFE situations. It should however be borne in mind that the nature of the channels is different for the Anopore and PTFE membranes: while the former has regular isolated channels, PTFE has irregular channels, which are interconnected as well. Further, the surface of the pores is hydrophilic for Anopore but hydrophobic for PTFE. Obviously, the reduced correlation length means decreased interlayer correlation, a feature suggested [20] to affect the order of the R1-R5 transition. We shall return to this point.

Features similar to those in the low angle reflection are observed for the wide angle reflection, which is associated with the intermolecular separation within the layers and maps the ordering within the layers. The wide angle profiles, in fact, confirm the structures of the rotator phases in the confined samples also with a single peak in the R2 phase (figure 2.12(a)) and split peaks in the R1 (figure 2.12(b)) and R5 (figure 2.12(c)) phases. The existence of a single peak in the R2 phase and two peaks in the other two phases is indeed expected. This is owing to the fact that the hexagonal structure of the R2 phase can be described by a single lattice parameter. Such a perfect hexagonal symmetry is broken in the two other structures, requiring an additional lattice dimension [13]. The widening of the profiles for the Anopore shows that not only the interlayer correlation but even the in-plane ordering gets diminished.

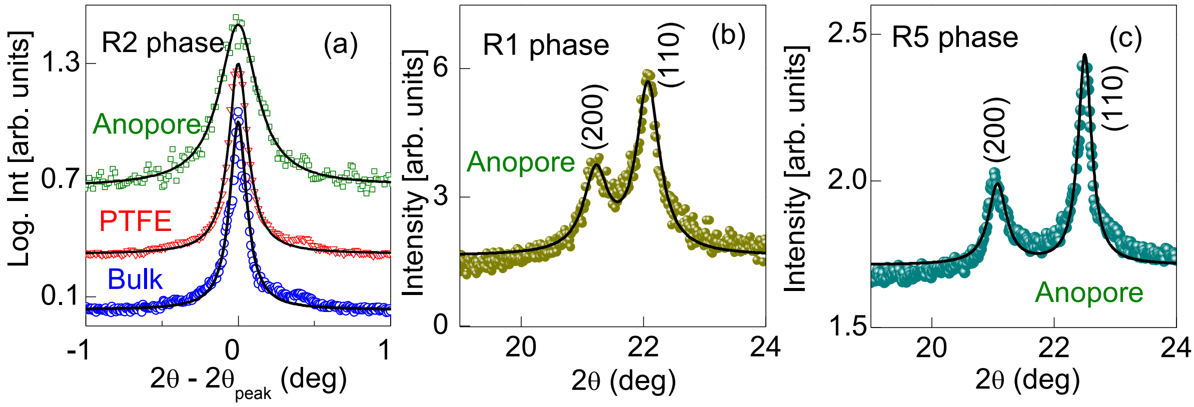

Figure 2.12: (a) Wide angle Xray scans in the R2 phase of the bulk and confined samples. The lines represent fits to a Lorentzian expression. Notice that just as the low angle scan, the Anopore profile has a substantial broadening compared to the other two cases;(b) and (c) show the profiles in the R1 and R5 phases of the Anopore confined sample; the twin peaks can be indexed as 200 and 110. The solid line depicts the sum of two Lorentzian expressions.

The central results of this study are shown in Figure 2.13(a), which display the temperature dependence of the d-spacing corresponding to the layer thickness [44]. The layer spacing has weak temperature dependence in the orthogonal (R2 and R1) phases and a strong decrease upon transformation to the R5 phase. The surprising result is that such a change manifests as a precipitous drop for the bulk but a very gradual one for the Anopore sample, with the PTFE case having an intermediate situation. The first derivative of d with temperature, δd/δT, which may be taken as a measure of the one-dimensional thermal expansion, shows the differences among the three sample situations in an even more dramatic fashion (see in Figure 2.13(b)); the height of the peak is maximum for the bulk and least for the Anopore sample, mimicking scenarios seen for systems exhibiting a critical/tricritical point. The tilting of the molecules is the major change upon entering the R5 from the R1 phase. Assuming a rigid rodlike situation (schematically shown in Figure 2.14), the tilt can be calculated as cos θ = d_{R5}/d_{R1} (d_{R1} is the d value at T_{C2}, the R5-R1 transition temperature). The bulk as well as the PTFE samples exhibit a jump in θ at T_{C2} and stronger temperature dependence in the R5 phase. In contrast, the Anopore case has a continuous and weaker growth in θ (Figure 2.14), establishing that the transition is second order.

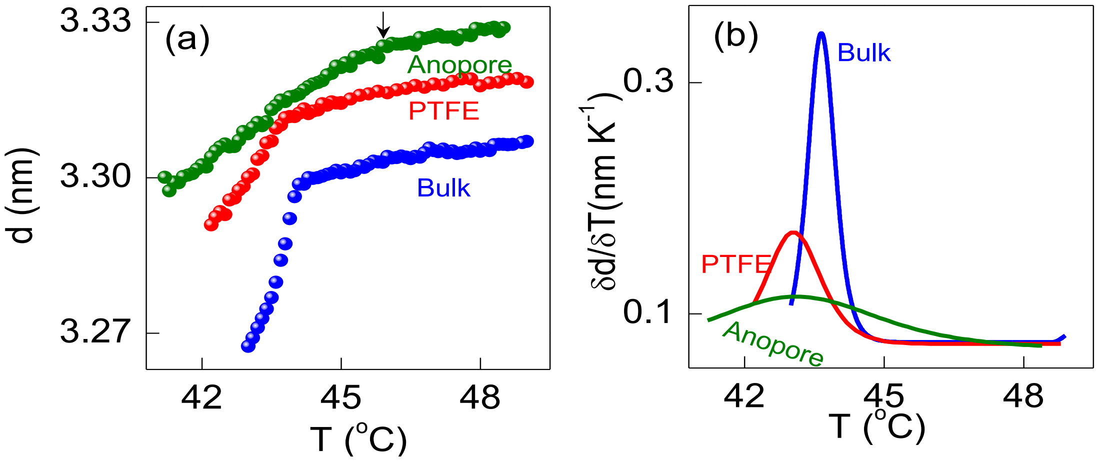

Figure 2.13: (a) Thermal variation of the layer spacing d in the bulk and confined situations. (For better presentation, the PTFE data set has been given vertical shift of -0.005 nm). The abrupt lowering of d for the bulk and PTFE samples marks the onset of R1-R5 transition. In contrast, the Anopore sample shows a gradual decrease below the temperature marked with an arrow. (b) The first derivative of d with temperature displaying the feature that the effect of confinement in Anopore is very drastic.

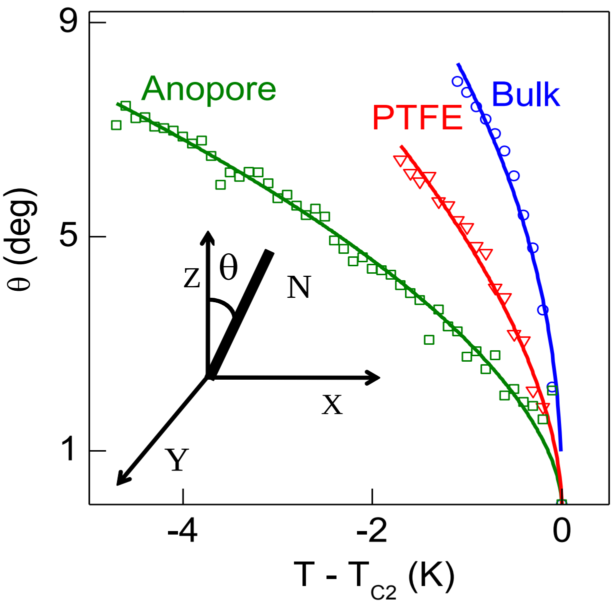

Figure 2.14: Temperature dependence of the calculated tilt angle (θ) in the R5 phase (T_{C2} is the R1-R5 transition temperature). The Anopore case has a weaker growth, and a smaller limiting value of the tilt angle. The solid line is merely guide to the eye for the bulk and PTFE sets, but represents a power law fit for the Anopore sample. The inset shows a schematic representation of the tilting (by θ) of the alkane molecule (thick bar N) with respect to the layer normal (z direction), with the plane xy defining the layer.

Thermodynamic [45] and structural [13a] aspects were studied in detail by Sirota and co-workers to investigate at atmospheric pressure, the order of the transitions between the R2, R1, and R5 phases. The structural work has been extended to high pressure also [13b]. In the following, we summarize these results (also see Mukherjee and Deutsch, Ref. 25).

a) The R1-R2 transition was found to be of first order, with a discontinuous jump in the order parameter.

b) On the other hand, the situation regarding the order of the R1-R5 transition was somewhat ambiguous. While the X-ray data suggested a discontinuity at the transition of the relevant order parameter indicating a first-order transition, the authors [13a] mention that the limited resolution of the measurements could not exclude a continuous (second order) transition.

c) In the calorimetric work [45] an emphatic statement that the absence of a sharp peak in the heat capacity suggesting the transition to be in fact second order, is followed by a rider that the narrow temperature ranges of the R5 phase make the features difficult to interpret, and even if this transition has a small first-order component, it appears to be predominantly second order in character.

d) The pressure measurements, however, suggested that the R1-R5 phase transition changes from first to second order as the pressure is increased. However, a recent photopyroelectric calorimetric work [20] has shown that in a bulk sample of n-tetracosane (the compound studied here) the R1-R5 transition is unambiguously first order, with a clear hysteresis. In fact, the basis on which Sirota et al [45] considered the absence of a sharp peak as the evidence of a second order transition itself has been questioned [20].

In view of these observations, it is interesting to note that a recent Landau analysis indeed predicts the possibility of a tricritical point (TCP) on the R1-R5 phase boundary, although in the pressure-temperature plane [25]. The model having parallels to the well known analysis for TCP scenarios for the orthogonal smectic A-tilted smectic C transition of LC materials [46], considers the free energy of the system to be expanded in terms of dual order parameters, the tilt angle θ and the lattice distortion $\mathfrak{D}$, and a coupling between them. It is given by [25]

$$F = F_1(\mathfrak{D}_o) + \frac{1}{2}u(\mathfrak{D} - \mathfrak{D}_o)^2 + \frac{1}{2}\alpha\theta^2 + \frac{1}{4}\beta\theta^4 + \frac{1}{6}\delta\phi^6 + \gamma\mathfrak{D}\theta^2 + \frac{\eta}{2}\mathfrak{D}^2\theta^2 \qquad (2.3)$$

Here F_1 is the free energy density of the R1 phase, $\mathfrak{D}_o$ is the lattice distortion parameter at the transition, u is the inverse response function of the R1 phase, α, β and δ are the usual Landau coefficients and γ and η coefficients coupling the two order parameters. When the coupling between θ and $\mathfrak{D}$ is strong, the R1-R5 transition is first order but second order otherwise. Thus to understand the behaviour of θ with confinement, it is necessary to determine the temperature variation of the intermolecular separation 'D' in the layer plane, and consequently $\mathfrak{D}$ using the wide angle scans, such as shown in Figure 2.15.

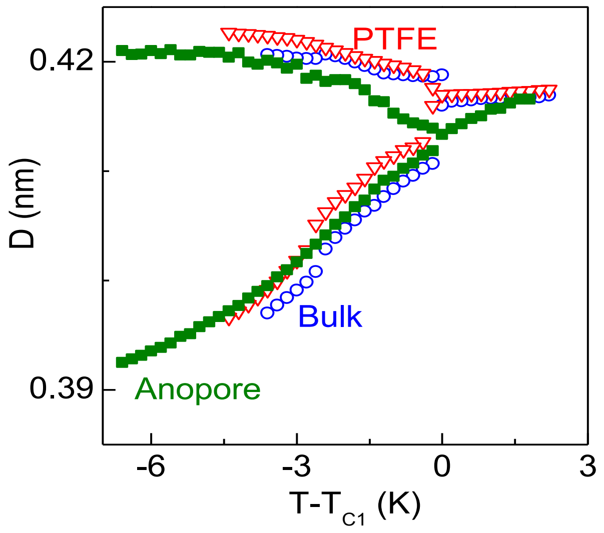

Figure 2.15: Variation of the inter-molecular spacing D*, obtained from the wide-angle scans, in the bulk (circles), PTFE (triangles) and Anopore (squares) samples, as a function of reduced temperature;* T_{C1} *is the R2-R1 transition temperature.*

In terms of the experimental parameters, $\mathfrak{D}$ is defined as $\sqrt{3} - A/B$, where A and B are the lattice dimensions; thus $\mathfrak{D} = 0$ in the R2 phase. The thermal variation of D and $\mathfrak{D}$ for the three cases, are depicted in Figure 2.15 and 2.16 (a) respectively. The breaking of the perfect hexagonal symmetry of the R2 phase results in a twin peak profile in the R1 and R5 phases, causing a splitting in the D values. In all the cases, there is a step-like change in D, and a jump in $\mathfrak{D}$ from a value of ~0, at T_{C1}, the R2-R1 transition temperature, but the magnitude of the jump depends upon confinement and its extent. The lattice area also displays concomitant changes (see Figure 2.16 (b)). In comparison to the value for the bulk case, the jump in $\mathfrak{D}$ at T_{C1} is about 20% smaller for PTFE and factor of 4 smaller for Anopore sample. The Landau model mentioned above, predicts that at T_{C1}, $\mathfrak{D}$ should jump by 2b/3c, and ΔH would change as $\mathfrak{D}^2$. Considering that ΔH reduces by 38% and a factor of ~ 13 for PTFE and Anopore respectively, the data here are in fair agreement with the expectations of the theory. For the R1-R5 transformation, the nature of the transition depends, as stated above, on the coupling between θ and $\mathfrak{D}$. Specifically, if the coupling is weak, the Landau model predicts that $\theta \sim (T_{C2}-T)^{1/2}$, typical of a mean field second order transition.

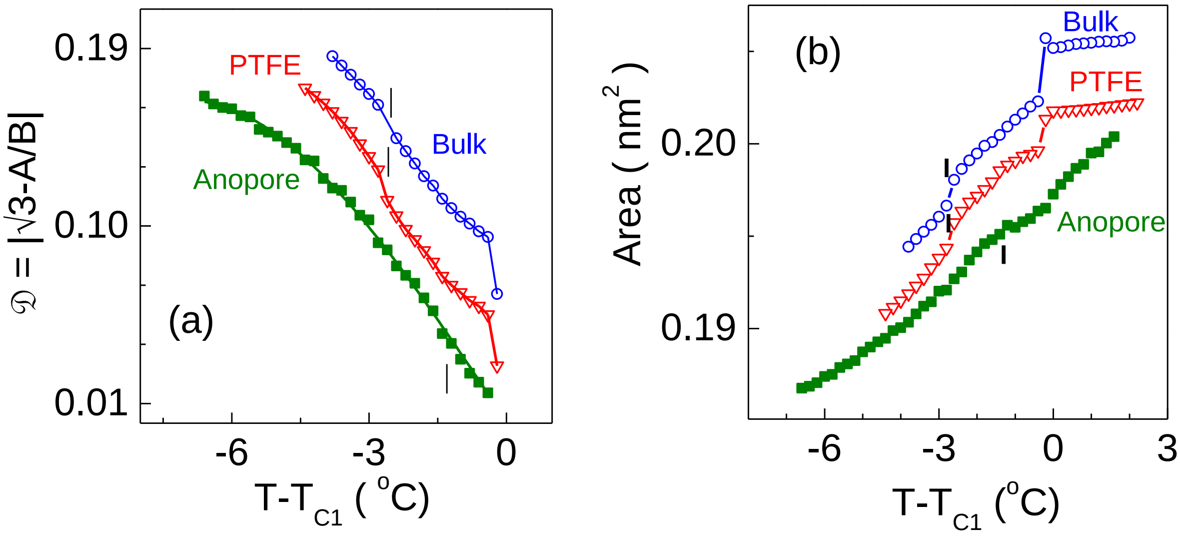

Figure 2.16: The thermal variation of (a) the extracted distortion parameter $\mathfrak{D}$ and (b) the area of the lattice exhibiting discernable jumps at both R2-R1 and R1-R5 transitions only for the bulk and PTFE samples. T_{C1} represents the R2-R1 transition temperature, and the vertical lines, the R1-R5 transition point. (For better presentation, the PTFE and bulk data have been vertically shifted up by 0.02 and 0.05 for distortion set and 0.01 and 0.05 nm^2 for area set respectively).

As indeed seen in Figure 2.16 (a), in the R5 phase, the temperature dependence of $\mathfrak{D}$ is much smaller for Anopore sample (the slopes are -0.025/K, -0.026/K and -0.017/K for bulk, PTFE and Anopore samples) suggesting that the coupling is weaker perhaps due to the reduction in the temperature range of the intermediate (R1) phase. Since the bulk and PTFE data exhibit a jump in θ at T_{C2}, the Anopore data were fit to a power law of the type,

$$\theta = \theta_o \ (T_{C2} - T)^x \tag{2.4}$$

The fitting is shown as solid line in Figure 2.14 and yields an exponent x = 0.58±0.01, a value not very different from the mean field prediction of 0.5. The small discrepancy between the theory and the experimental value could be due to the additional strain fields introduced by the curvature of the pore, a feature not in the theory. Thus the first order R1-R5 transition of the bulk is driven to become a second order one by confinement, i.e., simply by controlling the length scale of the structure. This observation, therefore, presents the possibility of realizing a tricritical point by tuning the length scale of confinement. From a phase transition point of view, the weakening of the R1-R5 transition upon confinement could be arising because of two reasons. First, the interlayer correlation that gets reduced in the Anopore case possibly decreases the coupling between the lattice distortion and the tilting, resulting in such a weakening. The second reason could in fact be a concomitant effect of the first one. Zammit et al [20] showed that the hysteresis associated with this transition becomes smaller when the temperature range of the R1 phase (intermediate between R2 and R5 phases) is reduced. The present studies bring out the feature that confinement in Anopore definitely reduces the temperature range of the R1 phase. Consequently, the R1-R5 transition which has a first order character in the bulk (as also established by Zammit et al [20]), changes over to a second order one upon confinement in Anopore membrane [47]. Examples of the order of the transition changing when the temperature range of the intermediate is reduced are commonly found in liquid crystals [48]. For instance, with the isotropic-nematic-smectic A sequence, as the range of the nematic phase is shrunk the order of the nematic-smectic A transition changes from second to first order. However, the discrepancy that the change in the order of the transition is reversed in the two cases upon reduction of the range of the intermediate phase remains unclear.

A possible molecular level reason for change in the order of the transition could be the following, seen in the light of an argument by Ocko et al [49]. In the rotator phases there are substantial numbers of gauche-bond defects predominantly near the chain ends. When averaged over their individual configurations, these gauche defects will result in larger effective widths at the ends of the molecules as compared to that at their centers, consequent to which there will be a reduction of the lengthwise overlap of the adjacent segments. In such situations a tilting of the molecule is favoured, and is suggested to be the cause for the appearance of tilted phases for longer alkanes. Applying this argument to the present scenario, we can imagine that owing to the restricted length scale to which the correlations can grow, the disorder of the chain segments is substantial upon confinement, creating a situation favourable for the stabilization of the tilted phase. Therefore upon confinement (Anopore case here) the tilted phase occurs at a much higher temperature, and also exists over a larger range of temperatures. The presence of disorder also weakens the strength of the transition, causing the first order character to change to a second order one. Measurements to determine the conformation of the molecules in the confined situations will support these postulations.

2.7 Summary

We have performed calorimetric and X-ray measurements in the R1, R2, and R5 rotator phases of a long chain alkane and probed the order within and normal to the layers, in the bulk, and in confining matrices of two different length scales. In the matrix having the shorter length scale, there is a substantial weakening of both the R2 - R1 and R1 - R5 transitions. The effect on the latter is so drastic that the transition which is first order in the bulk is driven to second order upon confinement. This observation provides a new method of achieving a tricritical point in such systems.

2.8 References

1. D.M. Small, *The Physical Chemistry of Lipids: From Alkane to Phospholipids* Plenum, New York (1986).
2. M. Dirand, M. Bouroukba, V. Chevallier, and D. Petitjean, E. Behar and V. Ruffier-Meray, *J. Chem. Eng. Data*, **47**, 115 (2002).
3. N. Maeda, *Phase transitions of long-chain n-alkanes at interfaces: Implications to bulk phase transitions of hydrocarbons*, LAP LAMBERT Academic Publishing, (2010).
4. See e.g., A. Raudino, M.G. Sarpietro, and M. Pannuzzo, *J. Pharm Bioallied Sci*., **3**, 15 (2011).
5. L.M. Bal, S. Satya, S.N. Naik and V. Meda, *Renewable Sustainable Energy Rev.*, **15**, 876 (2011).
6. S. Sinha-Ray, R.P. Sahu and A.L. Yarin, *Soft matter*, **7**, 8823 (2011).
7. S. Khare, M. Dell'Amico, C. Knight and S. McGarry, *Solar Energy Materials & Solar Cells*, **107**, 20 (2012).
8. R. Sabbah, M.M. Farid and S. Al-Hallaj, *Appl. Therm. Eng.*, **29,** 445 (2009).
9. F. Kuznik, D. David, K. Johannes and J.J. Roux, *Renewable Sustainable Energy Rev.*, **15**, 379 (2011).
10. L. Agyarko and G.A. Mansoori, *Conference Proceedings of the AIChE Spring Meeting and 7th Global Congress on Process Safety*, Chicago (2011).
11. A. Müller, *Proc. R. Soc. London Ser. A* **138**, 514 (1932); also see J.D. Bernal, *Z. Krist.*, **83**, 153 (1932).
12. K. Larsson, *Nature*, **213**, 383 (1967); G. Ungar and N. Masic, *J. Phys. Chem*., **89**, 1036 (1985); J. Doucet, I. Denicolo, and A. Craievich, *J. Chem. Phys.*, **75**, 1523 (1981).
13. (a). E.B. Sirota, H.E. King, D.M. Singer and H.H. Shao, *J. Chem. Phys*. **98**, 5809 (1993); (b). E.B. Sirota, D.M. Singer and H.E. King, *J. Chem. Phys.*, **100**, 1542 (1994); (c). E.B. Sirota, *Langmuir*, **13**, 3849 (1997).
14. See, e.g., P.S. Pershan, Structure of Liquid Crystal Phases, *World Scientific* Singapore (1988).
15. V.M. Kaganer, H. Mohwald and P. Dutta, *Rev. Mod. Phys.*, **71**,779 (1999).

16. L.D. Gelb, K.E. Gubbins, R. Radhakrishnan, and M. Sliwinska-Bartkowiak, *Rep. Prog. Phys.* **62**, 1573 (1999).
17. J. Ryckaert, I.R. McDonald and M. L. Klein *Mol. Phys.,* **67**, 957 (1989).
18. A. Marbeuf and R. Brown, *J. Chem. Phys*., **124**, 054901 (2006).
19. N. Wentzel and S. T. Milner, *J. Chem. Phys.,* **132**, 044901 (2010).
20. U. Zammit, M. Marinelli, F. Mercuri and S. Paoloni, *J. Phys. Chem B*. **114**, 8134 (2010).
21. M. Lehto, J. Schweitz and G. Thornell, *J. Microelectromech. Syst.,* **16**, 728 (2007).
22. C. Alba-Simionesco, B. Coasne, G. Dosseh, G. Dudziak, K.E. Gubbins, R. Radhakrishnan and M. Sliwinska-Bartkowiak, *J. Phys.: Condens. Matter,* **18**, 15 (2006).
23. A. Henschel, T. Hofmann, P. Huber and K. Knorr, *Phys. Rev. E.,* **75**, 021607 (2007).
24. K. Jiang, B. Xie, D. Fu, F. Luo, G. Liu,Y. Su and D. Wang., *J. Phys. Chem. B.*, 114, 1388 (2010).
25. P.K. Mukherjee, *J. Phys. Chem. B.,* **114**, 5700 (2010); For an early treatment of this model see P.K. Mukherjee and M. Deutsch, *Phys. Rev. B.,* **60**, 3154 (1999).
26. C.V. Lobo, S. Krishna Prasad and D.S. Shankar Rao, *Phys. Rev. E.,* **69**, 051706 (2004); S. Krishna Prasad, S. Sridevi and D.S. Shankar Rao, *J. Phys. Chem. B* **114,** 7474 (2010).
27. See, e.g., G.P. Grawford and S. Zumer, *For excellent collection of review articles in this field, Liquid Crystals in Complex Geometries*, Eds., Taylor & Francis, London (1996); S.A. Rózanski, F. Kremer, H. Groothues and R. Stannarius, *Mol. Cryst. Liq. Cryst*. **303**, 319 (1997).
28. See e.g., D. Wilms, A. Winkler, P. Virnau, and K. Binder, *Phys. Rev. Lett*. **105**, 045701 (2010).
29. M.D. Dadman and M. Muthukumar, *J. Chem. Phys.,* **98**, 4850 (1993).
30. G.S. Iannacchione, G.P. Grawford and S. Zumer, J.W. Doane and D. Finotello, *Phys. Rev. Lett.*, **71,** 2595 (1993).
31. S.A. Rozanski, R. Stannarius, H. Groothues, and F. Kremer, *Liq. Cryst.,* **20**, 59 (1996).
32. Ch. Cramer, Th. Cramer, F. Kremer, and R. Stannarius, *J. Chem. Phys.,* **106** 3730 (1997).
33. K.L. Sandhya, Geetha G. Nair, S. Krishna Prasad and A. Khandelwal, *Liq.Cryst.,* **28**, 1847(2001).

34. G. Sinha, J. Leys, C. Glorieux, and J. Thoen, *Phys. Rev. E,* **72**, 051710 (2005).
35. F.M. Aliev, Z. Nazario and G.P. Sinha. *J. noncryst. Solids,* **305**, 218 (2002).
36. S. Krishna Prasad, S. Sridevi and D. S. Shankar Rao, *J. Phys. Chem. B.,* **114**, 7474 (2010).
37. C. Grigoriadis, H. Duran, M. Steinhart, M. Kappl, H.J. Butt and G. Floudas, *ACS Nano,* **5**, 9208 (2011).
38. P. Huber, D. Wallacher, J. Albers and K. Knorr, *Europhys. Lett.* **65**, 351 (2004).
39. H.K. Christenson, *J. Phys.: Condens. Matter,* **13,** 95 (2001).
40. J.W. Gibbs, *Collected works*, Vol.**1**, Yale University Press, New Haven (1928).
41. W.Thomson (Lord Kelvin), *Philos. Mag.,* **42**, 448 (1871).
42. F.M. Aliev and N. Breganov, *Sov. Phys. JETP,* **68**, 70 (1989).
43. C.L. Jackson and G.B. McKenna, *J. Chern. Phys.,* **93**, 12 (1990).
44. There is nearly a 10% increase in the spacing (in the R2 phase) upon Anopore confinement. Such an increase is known in smectic systems and associated with a slight stretching of the alkyl chains caused by the larger surface interaction created by the higher surface to volume ratio of the membranes, See, e.g., Ref 26.
45. E.B. Sirota, D.M. Singer, *J. Chem. Phys.,* **101**, 10873 (1994).
46. H.Y. Liu, C.C. Huang, Ch. Bahr and G. Heppke. *Phys. Rev. Lett*., **61,** 345 (1988); R. Shashidhar, B.R. Ratna, G.G. Nair and S. Krishna Prasad, *Phys. Rev. Lett.,* **61**, 547 (1988).
47. A caveat regarding the R1-R5 transition is the following: While the tilt order parameter is the same, one difference between the smectic-A-smectic-C and R1-R5 transitions is that in the former case the layers are 2D liquids and the azimuthal direction is a locally continuous variable while in the latter there are only three inequivalent directions since the lattice already has crystalline order.
48. See, e.g., S. Chandrasekhar, Liquid Crystals; Cambridge University Press: Cambridge (1992).
49. B.M. Ocko, X.Z. Wu, E.B. Sirota, S.K. Sinha, O. Gang and M. Deutsch, *Phys. Rev. E,* **55**, 3164 (1997).

Chapter-3

Influence of quenched disorder created by nanosilica network on phase transitions in tetracosane

Overview

This chapter describes detailed calorimetric measurements on composites of a long chain n-alkane, tetracosane, doped with nanosilica aerosil particles decorated with a corona of hydrophobic/hydrophilic nature. The weakly perturbing random field created by the addition of the aerosil particles has the general effect of weakening all the transitions to, and between, the three different rotator phases that the pure alkane exhibits. One of highlights of the studies is that the strong first order transitions of the pure alkane, viz., from the isotropic liquid to hexagonal rotator phase (Iso–R2), and tilted monoclinic rotator phase to the crystalline phase (R5–Cr), are accompanied by a much weaker supplementary peak at lower temperatures. In analogy with observations made in aerosil composites of liquid crystalline systems, and additionally with information from preliminary Xray diffraction measurements on the currently studied materials, it is reasoned that the subsidiary peaks are nothing but the transformations between the same phases as the corresponding main peaks due to the bulk of the material, but occurring in the vicinity of the surface of the aerosil particles. The nature of the corona of the aerosil particles also seems to play an important role. For the bulk transitions, the reduction in the transition enthalpy is higher for the composites with the hydrophilic particles, than those with hydrophobic particles; the opposite is true for the surface transitions. The data also suggest that the lowering of the transition temperature of the surface transition with respect to its bulk counterpart is more for the hydrophobic composites than the hydrophilic ones. We provide an explanation for these features based on the surface interactions between the particles and tetracosane molecules, and also the strength of the gel network. This chapter also describes the results of rheological measurements of the aerosil composites.

The results are published in:

M. Vijay Kumar and S. Krishna Prasad, Influence of quenched disorder created by nanosilica network on phase transitions in tetracosane, *RSC Advances*, **2**, 8531–8538 (*2012*).

3.1 Introduction

In the previous Chapter we discussed the influence of the pre-fabricated confinement on the phase behaviour of n-tetracosane. As indicated earlier such a geometrical restriction can also be imposed by creating a network of nanoparticles which form *voids* into which the soft matter gets confined. Such "*in-situ"* created porous media also creates the disorder in the bulk medium. Aerosil®, a fumed silica spherical particle of ~ 7 nm diameter, as the nanoparticle, has been extensively employed for this purpose, especially with liquid crystalline material as the soft matter component [1]. The following comments are based on these studies which have focussed on the disorder created by the aerosil [2]. In these systems the disorder can be usefully described as a random local field that is conjugate to the order parameter. To state differently, the aerosil particles induce random field-like disorder through random surface interactions. A liquid crystal (LC) is perturbed with weak to intermediate strength quenched disorder when aerosil particles are introduced. When dispersed in LC, hydrogen bonds form between the aerosil particles (a feature to be discussed later) creating a low density gel, the structure of which, on very long length scales, exhibits fractal correlations [3]. The gel itself has no particular correlations commensurate with the wave vector of the smectic and hence is considered to be effectively random. The advantage of the aerosil-soft matter systems over other induced-disorder systems is that the amount of disorder can be conveniently tuned by varying the particle concentration. The dispersion of aerosil spheres in LC can be viewed as introducing a random distribution of surfaces. The resulting interaction between the LC and the particle surface leads to two primary effects altering the orientational order. First, there is a surface induced order that decays with distance from the surface and yields a local paranematic like state. The magnitude of this "field" effect is fixed by the intrinsic properties of the surface and the liquid crystal; increasing the silica density only increases its extent. Second, there is an elastic strain arising from competing surface interactions, whose magnitude, as it involves many surfaces, is likely to increase with silica density. Above a critical density the latter effect presumably dominates [4].

First order transitions with quenched random disorder (QRD) have additional considerations than continuous transitions due to the possibility of two-phase coexistence (hence interfaces between ordered and disordered regions), intrinsically finite correlation length at the transition, and hysteresis effects. This has made the experimental and theoretical studies of QRD effects at first-order transitions much more challenging. Although the random-field model is the same starting point, first-order transitions have the added complication of an energy penalty for the formation of interfaces between coexisting phases [5]. In this view, the QRD effect present as a random-field in each domain randomly shifts the transition temperature of each domain thus smearing the overall transition. A recent theoretical study applied renormalization group analysis to the ordering of nematics with QRD and concluded that such systems belong to Random-Anisotropy (RA) Heisenberg class [6]. These studies are highly relevant to the present studies on an n-alkane material exhibiting rotator phases. First the rotator phases are layered phases just as the smectic phase employed in LC-aerosil studies. Secondly, some of the transitions involved are quite strong first order in character. Prior to the present study there had been only one investigation on the influence of aerosil particles on alkanes exhibiting rotator phases [7]; this work particularly dealt with the specific heat behaviour of the material.

This chapter describes the influence of quenched disorder created by nanosilica network on phase transitions in n-tetracosane. Employing structural (XRD) and thermal (DSC) probes, the investigations also compare and contrast the influence of the nature of corona that decorates the aerosil particles, viz., hydrophobic vs. hydrophilic. The gel strength as an additional variable has been realized by varying the concentration of the hydrophilic particles through the soft gel to strong gel regime.

3.2. Experimental

3.2.1 Materials

Details of the long chain n-alkane, tetracosane ($C_{24}H_{50}$), used as the host in this study, have already been given in Chapter-2. This material was chosen so as to compare the influence of the two types of confinement on the rotator phases, viz., the pre-fabricated geometry discussed in the previous chapter and QRD which will be described here. To achieve the quenched disorder, two types of nanosilica particles (Aerosil®) were employed, both from Degussa Corporation (provided as a gift by Mr Vikas Rane of d-hindia Ltd, Mumbai). One of them is hydrophilic (Aerosil A- 300) and the other hydrophobic (Aerosil R812) with the specific surface area being 300 ± 30 and 260 ± 30 m^2/g respectively. In both the cases, the primary particle is spherical in shape, with an average diameter of 7 nm. In the following we give a brief description about aerosil particles, the information being taken from Technical Bulletin No. 11, Fine Particles on *Basic Characteristics of AEROSIL* by Degussa Corporation. The particles represent fumed, highly dispersed, amorphous, pulverulent synthetic silica.

3.2.2 Preparation of the aerosil fumed silica

The aerosil silica particles are synthesised on industrial scales using the method of continuous flame hydrolysis of silicon tetrachloride ($SiCl_4$). During this process, $SiCl_4$ is converted to the gas phase which then reacts spontaneously and quantitatively in an oxy-hydrogen flame with the intermediately-formed water to produce the desired silicon dioxide. The associated chemical reaction is $2H_2 + O_2 + SiCl_4 \rightarrow SiO_2 + 4HCl$. By varying the concentration of the co-reactants, the flame temperature, and the dwell time of the silica in the combustion chamber, it is possible to influence the particle size, the particle size distribution, the specific surface, and the surface properties within wide boundaries. The basic particle produced after this treatment is hydrophilic. Using proper surface chemistry it is possible to change this nature to hydrophobic. The number of silanol groups of the hydrophilic particle is reduced during the treatment by about 30 % of the initial value.

3.2.3 In-situ created Aerosil gels

The fumed silica obtained from the above process can form densely packed suspension in which the silica occupies 2 to 3% of the volume.

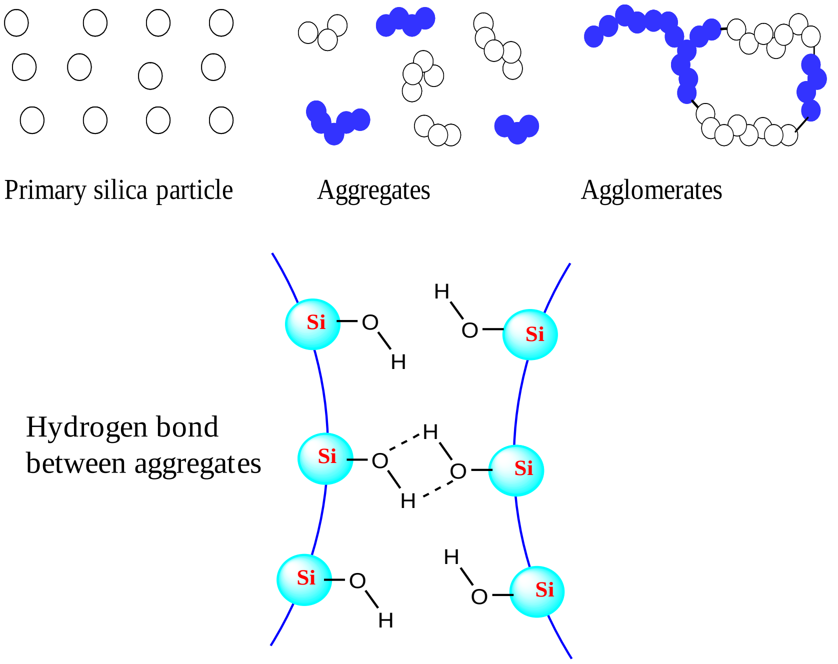

Figure 3.1: Building principle of solid framework of fumed silica depicting the formation of hydrogen bonds between aggregates (from Ref .9)

The particles of the precipitated silica are characterized by extended caves, whereas fumed silica forms irregularly branched strings. Figure 3.1 shows the building principle of fumed silica [9]. The spherical primary particles form aggregates via Si-O-Si moieties. The SiOH groups on the surface of these aggregates can form hydrogen bonds between different particles which lead to the formation of agglomerates. Compared with covalent bonds the energy of the hydrogen bonds is relatively small so that they can be broken by mechanical interaction but subsequently available for the formation of new bonds with a different spatial arrangement of the aggregates. Specifically, when dispersed in an organic medium, aerosil particles comprising three to four lightly fused spheres and having a mean radius of gyration of ~ 24 nm [3] will attach to each other and form a gel by diffusion-limited aggregation process. A typical gel formed this way is generally called thixotropic, because of its ability to break easily, caused by the weak nature of hydrogen bonded silica chains. A cartoon representing the situation of the layer structure of liquid crystalline smectic phase being embedded in an aerosil network, relevant from the viewpoint of layered rotator phases, is depicted in Figure 3.2

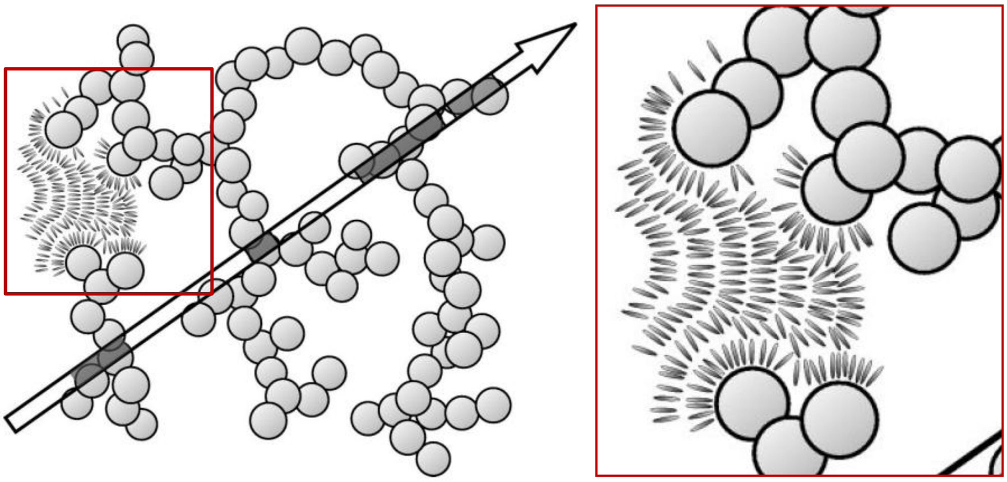

Figure 3.2: Left: Schematic representation of an aerosil liquid crystal gel formed by diffusion limited aggregation process, with the circles depicting aerosil particles, and the short lines, the liquid crystalline molecules. Open and shaded parts of arrow show void and solid chords, respectively (from ref. 10). Right: Enlarged view in the vicinity of a particle showing the tendency of the liquid crystalline molecules to be normal to the particle surface.

3.2.4 Preparation of composites

The composites of tetracosane with aerosil were prepared using mechanical mixing as well as solvent mixing procedures, similar to protocols reported for liquid crystalline materials [3,11], and summarized below. First, aerosil was degassed or dried under vacuum for 15 hours at 300°C to remove any adsorbed water. For the physical mixing method, since the quantity of the sample required was quite small (~15 mg), the possibility of inhomogeneous mixing was drastically reduced. Appropriately weighed aerosil and LC materials were physically stirred while maintaining the temperature of the system at 5 ^{o}C above the isotropic-R2 transition temperature. In the solvent mixing method, the weighed aerosil was added to C24 dissolved in pure methanol. The whole mixture was sonicated for 30 minutes at room temperature to obtain a good dispersion of the aerosil in the medium. Subsequently, while keeping the temperature at 60^{o}C the solvent was allowed to evaporate slowly over a period of 15 hours. The composite thus prepared was used immediately after the preparation. In this study the aerosil mixtures are characterized in terms of the dimensionless ratio $\rho = m_a/m_{C24}$, where m_a is the mass of aerosil and m_{C24} is the mass of tetracosane. Investigations have been carried out on mixtures with ρ = 0.03, 0.06, and 0.10 (hydrophilic / hydrophobic) as well as on pure C24. The results on a representative composite showed no differences in the behaviour of the materials prepared by the two methods of preparation.

3.3 Methods

The differential scanning calorimetric measurements were performed by using a Perkin Elmer DSC (Model- Pyris Diamond DSC), while keeping the sample in an inert (nitrogen) atmosphere. Structural measurements were performed using PANalytical X'Pert PRO MP Xray diffractometer [12]. The details of these two apparatus are already given in Chapter-2. As stated earlier the aerosil mixtures form organogels. Owing to the high viscosity of the gels the material could not be filled into the glass capillaries (normally used for Xray measurements). For this reason the sample was sandwiched between two Kapton® strips. Kapton is a polyimide film developed by Dupont and commercially available. It remains stable across a wide range of temperatures, from −269 to +400 °C. From the viewpoint of present studies, high mechanical, thermal stability and high transmittance to Xrays make it the preferred material. It is also relatively insensitive to radiation damage [13]. Rheological measurements were performed using the AR-G2 Rheometer (TA Instruments) by employing parallel plate geometry of 8mm diameter and a geometry gap of 800μm. Temperature of the samples is controlled by using a built-in Peltier temperature controller. The apparatus is schematically shown in Figure 3.3.

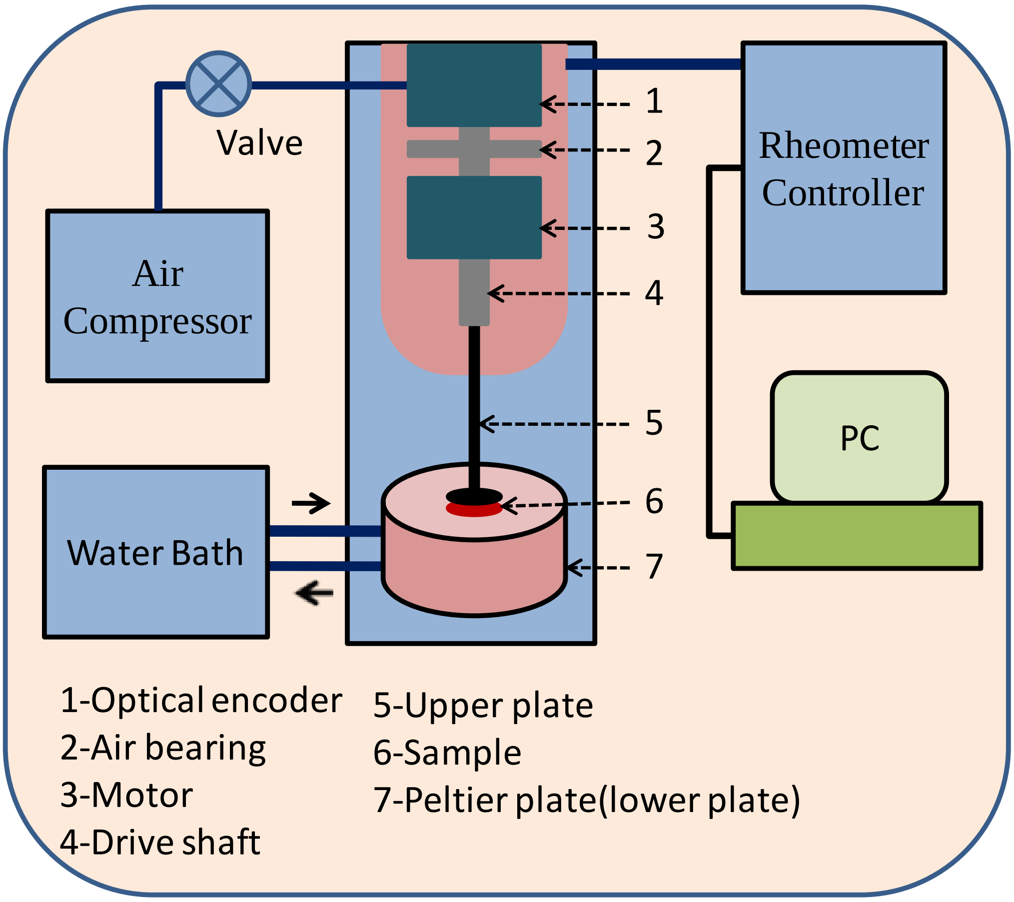

Figure 3.3: Schematic diagram of AR-G2 Rheometer.

3.4 Results and Discussion

3.4.1. Isotropic-R2 transition

The DSC profiles obtained at a rate of 1^{o}C/min in the heating and cooling modes in the vicinity of the Iso-R2 transition for pure C24 and the composites are shown in Figure 3.4. The pure alkane exhibits a single peak (see Figure 3.4a) in both the modes, although with a sizeable hysteresis between the heating and cooling scans, a feature expected for strong first order transitions. In contrast, the aerosil composites, even at the lowest concentration studied here, exhibit an additional, albeit much weaker, thermal anomaly (see Figures 3.4b-d) at temperatures just below the main peak, more clearly seen on an expanded scale, as in Figure

3.5. The appearance of the second peak in both specific heat and DSC profiles, absent in the pure material, has been known for low concentration LC-aerosil composites exhibiting the nematic-isotropic transition [See e.g., Refs. 4, 11, 14 and 15].

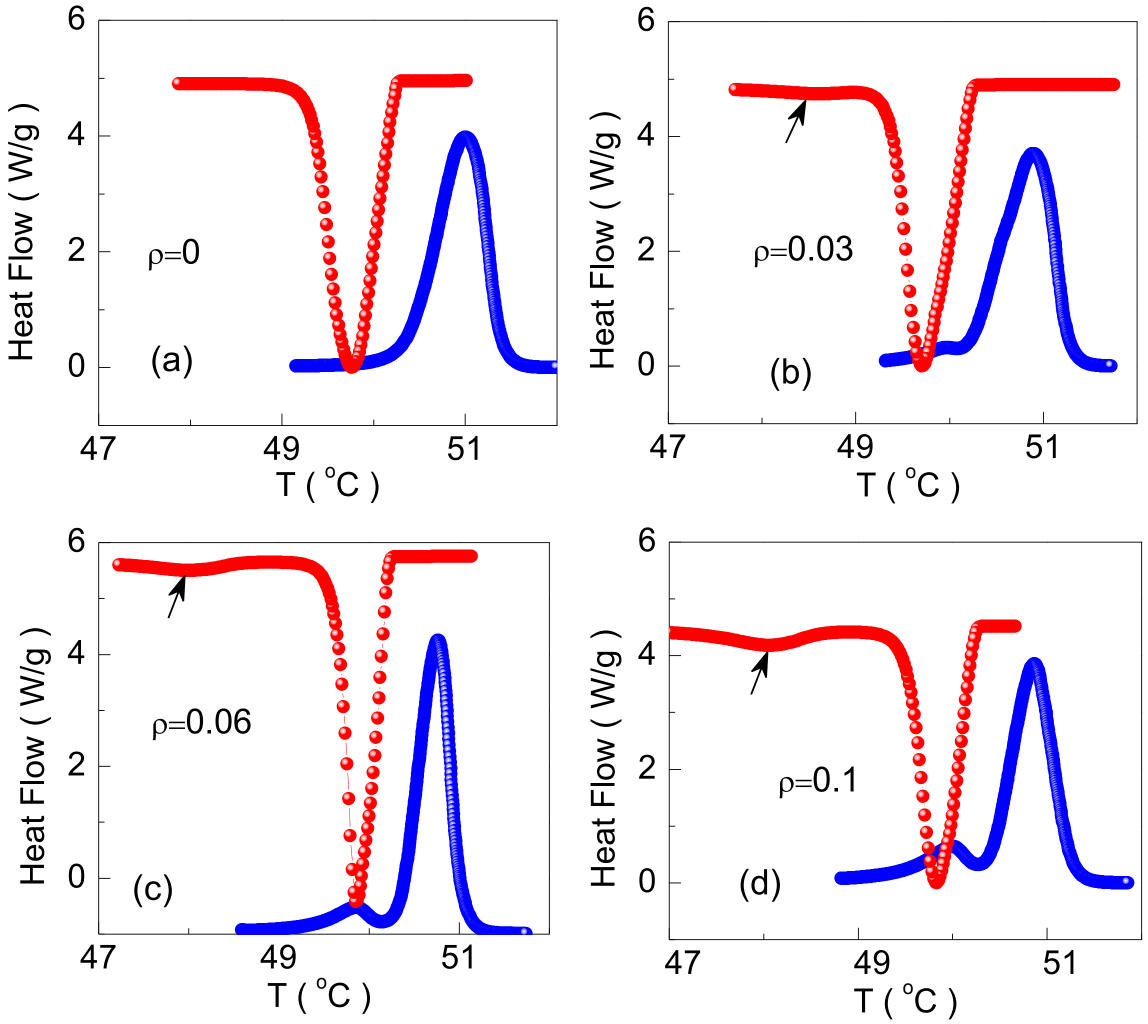

Figure 3.4: Differential scanning calorimeter (DSC) profiles obtained in the vicinity of the Iso-R2 transition in the heating (blue circles) and cooling (red circles) modes at a rate of 1°C/min for the (a) pure C24, and the hydrophobic composites with ρ of (b) 0.03, (c) 0.06 and (d) 0.1. The arrows on the cooling mode data indicate the appearance of an additional peak, which is designated as R2-X transition.

The double-peak profile has also been recently observed in heat capacity data for hydrophilic aerosil-C24 mixtures [7]. However, as will be discussed in a later section, the nature of the aerosil particle – hydrophilic/hydrophobic – results in certain important differences in the behaviour of the system. So the present investigations have concentrated on the mixtures formed with hydrophobic particles since (i) the chemical nature of the tips of the decorations (methyl groups) and the host alkane are the same, and thus the phase transitions in the composites can be expected to be significantly influenced, and (ii) some data on the effect of hydrophilic aerosil particles have already been reported [7], and thus a comparison between the relative influence of hydrophobic and hydrophilic particles is possible. It is clear from Figure 3.5 that the magnitude of ρ has a larger influence on the weaker low temperature peak (referred to as R2-X) than on the high temperature peak (Iso-R2). The Iso-R2 shows, concomitant with the appearance of R2-X, a slight increase initially in the peak height, but with further increase in ρ, registers a drop. In contrast, the peak height of R2-X increases by a factor of ~ 6 for ρ = 0.1, from its negligible strength for ρ = 0.03. Table 3.1 and Figure 3.6 present the peak temperatures and the transition enthalpy in the heating as well as cooling modes for both Iso-R2 and R2-X transformations. With concentration, the peak temperature of the Iso-R2 transition hardly changes (within the error of 0.1 ^{o}C in the measurement) for either of the modes.

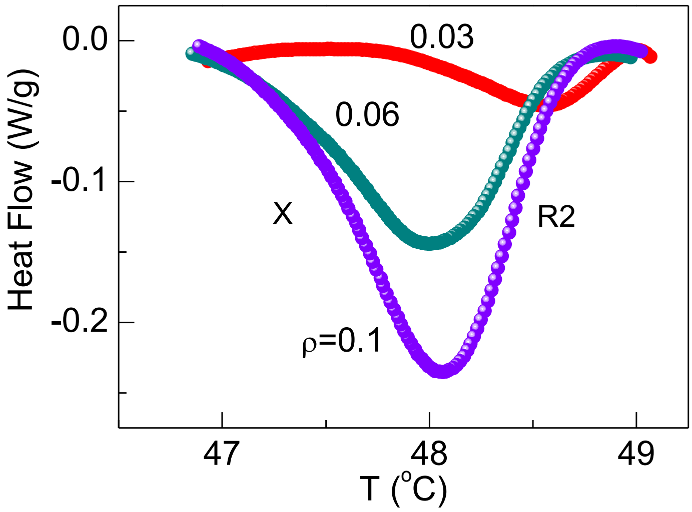

Figure 3.5: DSC profiles shown on an enlarged scale in the vicinity of the R2-X transition observed for the three hydrophobic composites, the concentrations (ρ) of which are indicated against each curve. Note that the strength of the transition increases as ρ increases.

Table 3.1: Transition temperatures (in ^oC) and the associated enthalpy (in J/g, shown enclosed in parenthesis) across the Iso-R2 and R2-X transitions for pure C24 and three hydrophobic composites.

ρ	Iso-R2		R2-X	
	Heating	**Cooling**	**Heating**	**Cooling**
0	51.00 [157.0]	49.76 [159.6]	--	--
0.03	50.90 [132.7]	49.72 [139.4]	49.97 [0.88]	48.61 [0.72]
0.06	50.76 [124.1]	49.89 [120.9]	49.86 [7.53]	48.00 [7.71]
0.1	50.87 [104.8]	49.84 [106.2]	50.18 [11.4]	48.07 [11.09]

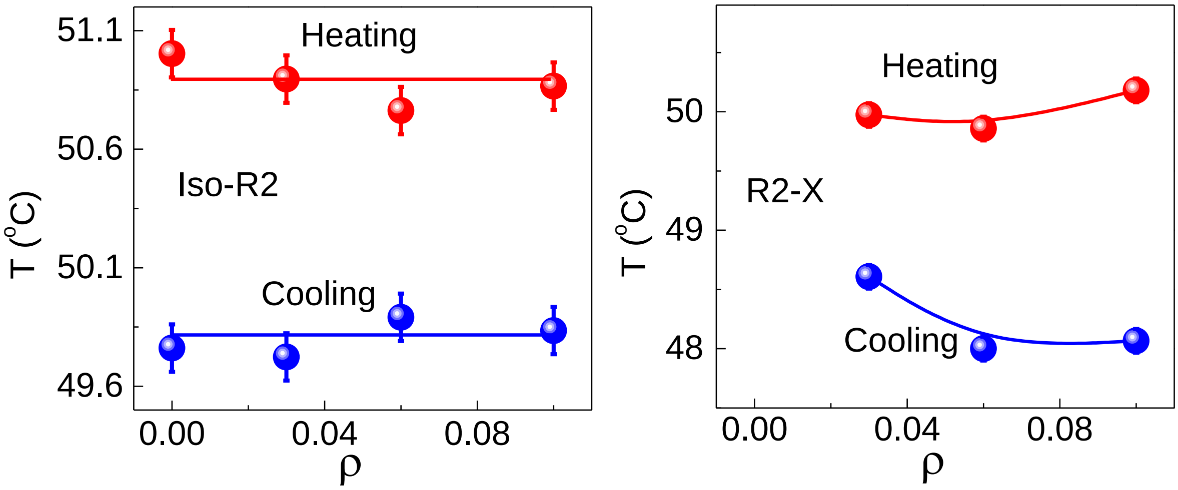

Figure 3.6: ρ-dependence of the transition temperature for the Iso-R2 (left panel) and R2-X (right panel) transitions in the hydrophobic system. Notice that the scale for the right panel is a factor of 3 larger than that for the left panel. Within the error of the measurement, there is hardly any concentration dependence for the Iso-R2 transition, but substantial variation for the R2-X transition. [The error bar for the right panel data is roughly the same size as that of the symbols].

It may be recalled here that composites of aerosil with LC (for this aspect we consider specifically alkyl/alkoxy cyanobiphenyls only; the case with a non-polar LC will be discussed later in section 3.4.4) do exhibit a clear, albeit weak, concentration dependence of the N-I transition temperature over the range of aerosil density (ρ) studied here [See e.g., Ref. 14]. On the other hand, the peak temperature of R2-X is very weakly dependent on ρ in the heating mode, but strongly so in the cooling mode, resulting in an enhanced range of 1.75 °C for the intermediate region, before the R2-X transition sets in. However, even for ρ =0.1, the ratio of the peak heights of the R2-X to Iso-R2 transitions is only about 0.07, whereas in the LC cases, the two peaks would have comparable height [3]. The feature that the magnitude of the hysteresis, which can be taken to be a measure of the first order character of the transition, is hardly affected for the Iso-R2 but increases for the R2-X, should be suggesting that the thermal strength of the transition is influenced similarly.

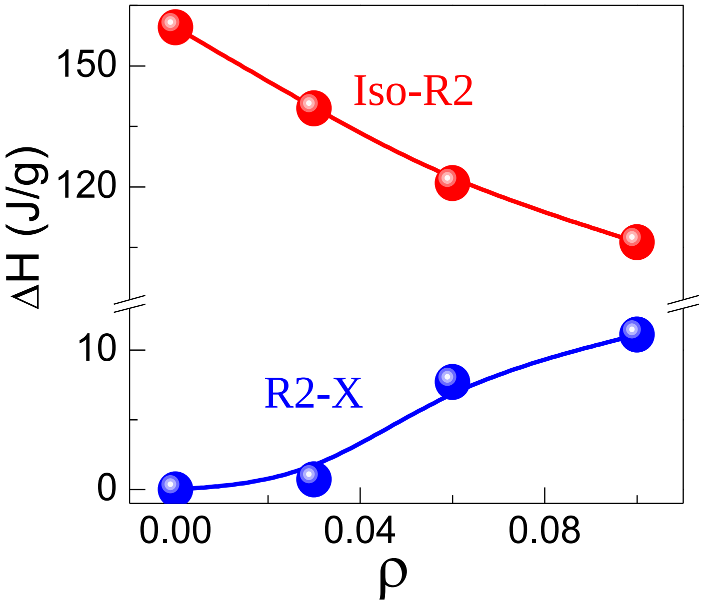

Figure 3.7: Concentration dependence of the transition enthalpies for the Iso-R2 and R2-X transitions in the hydrophobic system, exhibiting a slight (~50%) decrease for the former and a large (~ an order of magnitude) increase for the latter set.

However, the transition enthalpy ΔH (calculated from the area under the peaks) dependence on ρ, as displayed in Figure 3.7, and tabulated in Table 3.2, shows that the Iso-R2 transition exhibits a 50% lowering in the value from ρ = 0 to 0.1, whereas the value for the R2-X transition grows by an order of magnitude (see Figure 3.7). Before discussing the possible causes for the appearance of R2-X and its ρ-dependence, let us compare these results with those obtained for composites having hydrophilic aerosil particles.

Table 3.2: Transition temperatures (in ^{o}C) and the associated enthalpy (in J/g, shown enclosed in parenthesis) in the cooling mode across the R2-R1 and R1-R5 and R5-Cr transitions. For the hydrophobic composites the former transition is labelled in the text as X-R1. The data for the additional peak (Cr-X2) seen below crystallization in the composites are also given. ^{a} Owing to the weakness of the transition, as well as the strong temperature dependence of the background, enthalpy values are not given.

ρ	R2-R1/X-R1	R1-R5	R5-Cr	Cr-X2
0	46.65 [0.67]	44.05 [0.86]	41.96 [92.4]	--
0.03	46.62 [0.41]	44.05 [a]	42.49 [66.3]	38.28 [0.09]
0.06	46.64 [0.40]	44.09 [a]	41.8 [61.5]	38.41 [1.27]
0.1	46.67 [0.30]	44.09 [a]	41.98 [58.5]	38.63 [2.10]

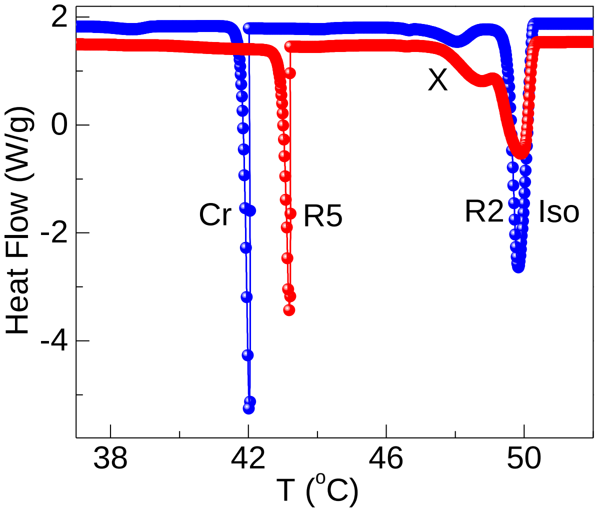

Figure 3.8: Diagram comparing the DSC scans obtained for the ρ = 0.1 composites with hydrophobic (blue circles) and hydrophilic (red circles) particles. All the transitions are weaker for the hydrophilic material.

The scans are shown in Figure 3.8 for the two different composites consisting of the same amount of aerosil (ρ = 0.1), but with hydrophobic and hydrophilic corona. Both the composites exhibit the double peak profile, but the one with hydrophilic particles has considerably weaker transitions. Further, while the Iso-R2 transition temperatures are comparable between the two types, the R2-X transition occurs at a slightly lower temperature for the system with hydrophobic particles. The transition enthalpies are also lower for the hydrophilic case, being as much as a factor of 2 for the R2-X transition.

Possible causes for the double peak profile

In the following we explore the possible reason for the appearance of the two peaks (Iso-R2 and R2-X) peaks in the composites. In analogy with the arguments made for the LC-aerosil composites, the observed double peak profile here can be viewed in terms of a surface transition separated from a bulk transition [7]. The bulk transition is caused by molecules which are away from the aerosil surfaces so as not to be influenced by the particles. The second transition, which in the present case as well as for LC materials occurs at a lower temperature than the bulk one, is due to the molecules which are attached to, or in the "catchment" region of the particles. The alkane molecules in the immediate vicinity can bind to the particle with an orientation that is locally perpendicular to the aerosil surface creating a region of disorder in comparison to the ordering that gets developed in the region of *bulk* molecules. A reduction in the ordering for the *surface* molecules, would thus lower the transition temperature (In the LC case, when the surface induces a higher order, an increase in transition temperature has been observed, see e.g., Ref. 16).

If the situation is such that the surface effect is weak, then one expects a mere broadening of the bulk peak. If the aerosil surface effects become strong, then there can be a bifurcation of the temperature at which the bulk and the surface molecules undergo the transition resulting in doubling of the peaks. If this argument is true then with increasing concentration of aerosil particles, the strength of the bulk transition should decrease and that due to the surface particles must increase. This is indeed observed in the experiments. Therefore the R2-X transition is nothing but the Iso-R2 transition happening at the aerosil surface. This view is further corroborated by preliminary Xray studies which show that the scattering profile, and thus the structure, remains the same on either side of the R2-X transition (see Figure 3.9). Let us recall that the ratio of the DSC peak heights of the surface and bulk transitions is much smaller in the present case as compared to the LC case. This perhaps should be expected since in the LC case, the ordered phase (nematic) is also a fluid. Therefore the surface effects can be expected to extend to regions farther from the surface, increasing the number of molecules which get influenced. In contrast, in the present case, the ordered phase has 3-d positional order which does not favour the surface effect to penetrate deeper resulting in a weaker surface peak.

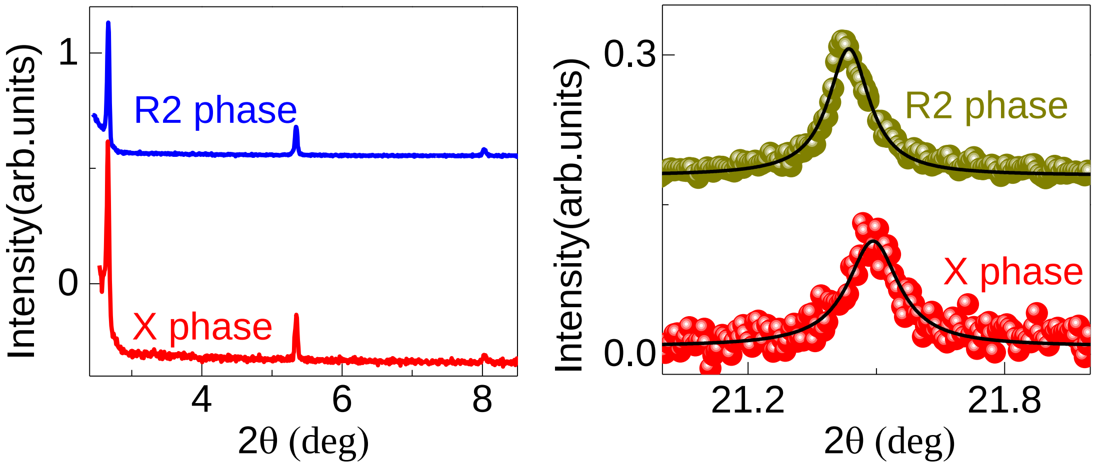

Figure 3.9: Left: Xray diffraction profiles in the R2 and X phases for ρ =0.06 composites. The pattern is essentially identical in the two phases. Right: The wide angle peak for the X phase appears to be overriding a diffuse maximum centred around the same peak wave vector as the sharp peak. This feature is absent in the profile for the R2 phase. It is possible that either the fewer layers which get affected by the surface or the anchoring conditions cause the diffuse background.

The data in Figure 3.8 bring out the differing influences of the nature of the corona on the bulk and surface transitions. Compared to the pure C24 (see Figure 3.4a), the reduction in the strength of the Iso-R2 (bulk) transition is more for the hydrophilic composite. However, the surface induced transition is also weaker for this system. In other words, the effect on the bulk part is more for the hydrophilic case, and the effect due to the surface is stronger for the hydrophobic. Now let us look at a probable reason for such a difference. For this purpose, let us consider the essential difference between the surfaces of the two kinds of particles, by taking into account the information provided in the Technical Bulletin no. 11 of Degussa AG, mentioned above. The continuous flame hydrolysis process results in fumed nanosilica particles which are hydrophilic in nature due to the presence of silanol (Si-OH) groups at the surface. The surface chemistry which is thus dominated by the silanol groups is the main feature of these particles. The presence of such groups gives rise to hydrogen bonding through which a particle can bond (hydrogen or H- bridge) with its neighbor or with another molecule. The probability of finding a suitable neighbor particle for the purpose of forming an H bridge increases with the fineness of the particle. In other words, as the diameter of the particle decreases the number of free OH groups decreases. For the hydrophilic aerosil studied here (A-300) this density is in the range of 2.5 free OH groups/nm^2. The hydrogen bonding, in fact, is responsible for the hydrophilic character as it easily binds with water. The good chemical reacting nature of these silanol groups provides a pathway to convert the surface from hydrophilic to hydrophobic type. To achieve hydrophobic aerosils, the silanol groups of freshly produced hydrophilic silica are made to react with molecules like hexamethyldisiloxane (for R812, the hydrophobic aerosil used here) resulting in the formation of Si-O-Si $(CH_3)_3$ units, and consequently the material acquires a hydrophobic character. The chemical treatment substitutes only 70% of the silanol units with the result that 30% of free Si-OH sites remain. From the point of view of the current studies, the presence of these free silanols, as well the large number of methyl units attached to the particle, are of significance.

An important character of the hydrophilic aerosils is their ability to gelate liquids, owing to the capability of the particles to H-bond among themselves creating a fragile network. At low concentration of the aerosil, this network is not so strong and deforms easily under external stress, resulting in soft gels. At higher concentrations, the structure becomes rigid, giving rise to stiff gels. These features manifest to enhance the viscosity of the system by orders of magnitude. In the present study, we could visually observe the enhancement of the viscosity in the isotropic phase of composites of both types of aerosils. This indicates that in the hydrophobic case, even the reduced number of silanol groups is sufficient to create a gel-like situation. In fact, rheological measurements [to be discussed in section 3.5] show that the composites with either type of particles form gels, showing that even though only a fraction of silanol groups are left over they help in gelation of the hydrophobic system. However, the hydrophilic gel is very strong having a storage modulus which is 7 orders of magnitude higher than that for the hydrophobic composite. Obviously the strength of the gel alone cannot account for the effect on both the bulk and surface parts seen in the calorimetric data (Figures 3.4 and 3.5).

The nature and strength of anchoring of the C_{24} molecules on the two different types of silica surfaces are employed in the following to explain the experimental features. The SiO surface is known to disorder the LC molecules which are in its vicinity [17]. Owing to the large surface to volume ratio, the aerosils can be expected to amplify this disordering effect. Indeed, in the case of LC, various studies have shown that the presence of aerosils disorders the liquid crystalline phase [3, 11, 18-22]. Evidence was reported [11] of a clear acceleration of the relaxation frequency associated with motion of the molecules about the short molecular axis, in composites of aerosils with a weakly polar molecule, attributing it to the disorder caused by the particles. It should be mentioned that in these LC systems, the molecules are polar, and in majority of the cases strongly so, in contrast to the entirely nonpolar C24 molecule. At the end of this section, we will compare and contrast the behavior of the LC molecules which are strongly polar, like the cyano biphenyls, and those which are hardly polar, such as materials known as nO.m. To understand the different behavior of the LC and alkane systems, it should be recalled that unlike in the case of A-300 aerosils, R812 particles have a short methyl group protruding out of the silica surface. Therefore the C24 molecules find a favorable situation, through van der Waals forces, to lie parallel to these hydrophobic groups, a condition which mimics a stronger anchoring normal to the aerosil surfaces. Owing to the predominantly spherical shape of the aerosil particles, this creates a hedgehog type of arrangement of the C24 molecules around the particle. This situation is schematically shown in Figure 3.10. Now, if the system undergoes the transition from the Iso to the R2 phase at the same temperature at the surface as well as in the bulk regions, then the disordering effect of the surface would create a number of defect centres near the aerosil surface, which may be energetically not favorable.

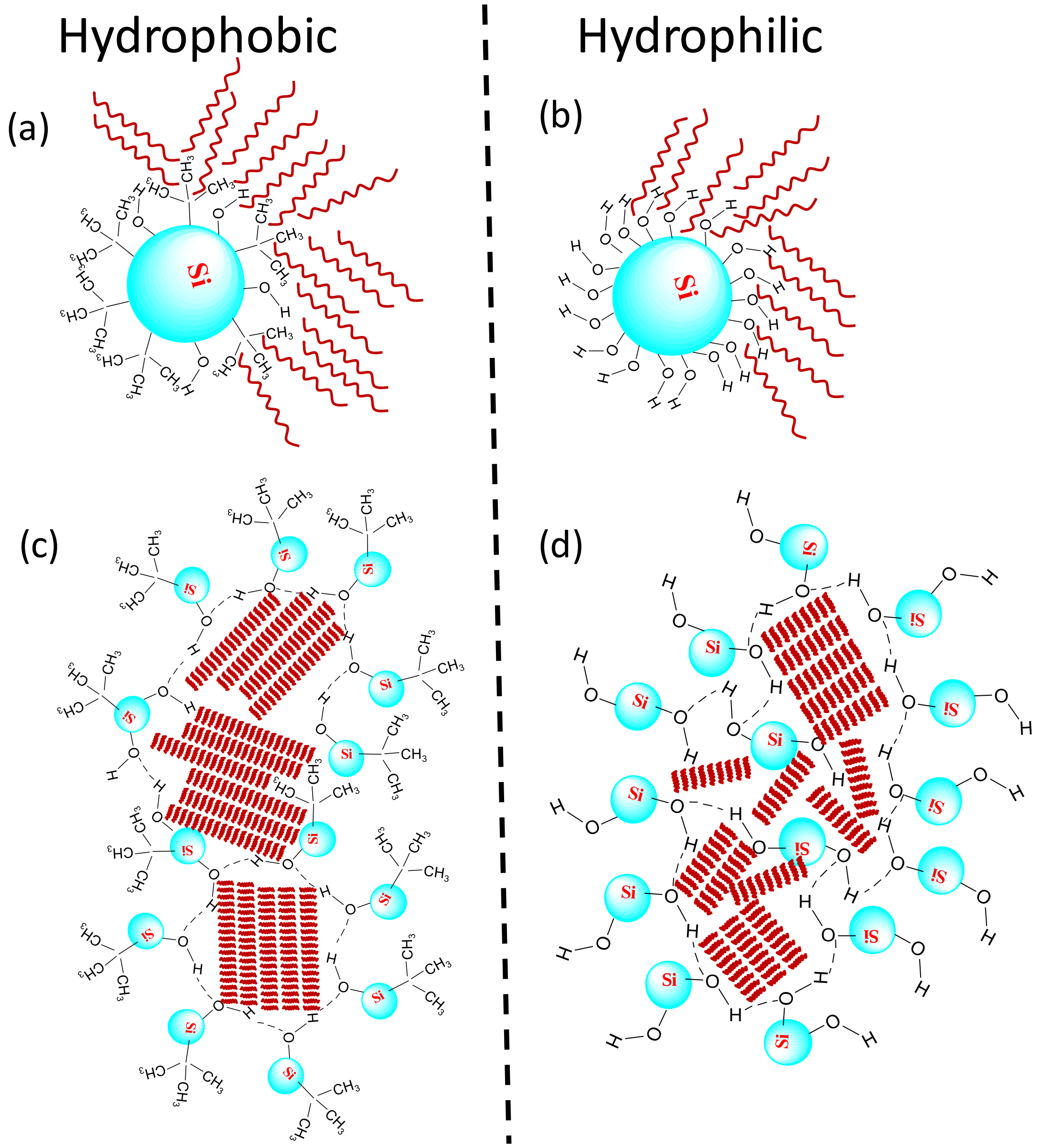

Figure 3.10: Schematic diagram depicting the chemistry of the surface of the aerosil (Si) particles with (a) hydrophobic and (b) hydrophilic corona. The former with its smaller number of free OH groups forms a much looser network (larger enclosure size) than the latter, as shown in (c) and (d). The red lines represent the C24 molecules.

An escape route available for the sample is to have a separate surface transition occurring at a different temperature than the bulk one. If the surface enhances the ordering of the system, then the transition would take place at a temperature higher than the bulk [21,23]. In contrast, since the aerosil surface causes a disorder in the system, the surface transition occurs at a temperature lower than that of the bulk. The gelation process creates bounding surfaces for the C24 molecules to be enclosed. The dimension ξ of such *enclosures* could then mimic situations of finite sized systems. The reduction in the strength of the bulk transitions can be expected to be dependent on ξ. The smaller storage modulus for the hydrophobic composite means a weaker gel or a looser network defining a much larger sized enclosure (larger ξ) than in the hydrophilic composite. This explains the stronger influence on the bulk transitions in the hydrophilic case. On the other hand, owing to the domination of van der Waals attraction between the methyl groups on the surface and the tetracosane molecules in the vicinity of the particle the surface forces become stronger for the hydrophobic case, resulting in an enhanced strength of the surface transitions.

3.4.2 R2-R1 and R1-R5 transitions

The calorimetric profiles across the R2-R1 (labeled X-R1 for the composites) and R1-R5 transitions are presented in Figure 3.11 for pure C24 and the three different hydrophobic composites. Both the transitions, which are quite strong for the pure compound, systematically weaken for the composites. The effect appears to be more on the R1-R5 transition, which appears just as a step-like change for the $\rho = 0.1$ mixture. Recalling that this transition is first order for pure C24, albeit weakly, the step-like change for the $\rho = 0.1$ composite indicates a crossover from first order to a second order transformation. As Figure 3.12 shows, the effect is more on the hydrophilic composite than on the hydrophobic one. As described in the previous chapter C24 when confined in the Anopore membrane undergoes such a drastic weakening of the R1-R5 transition so as to suggest that the transition is indeed second order and lying in the vicinity of a tricritical point.

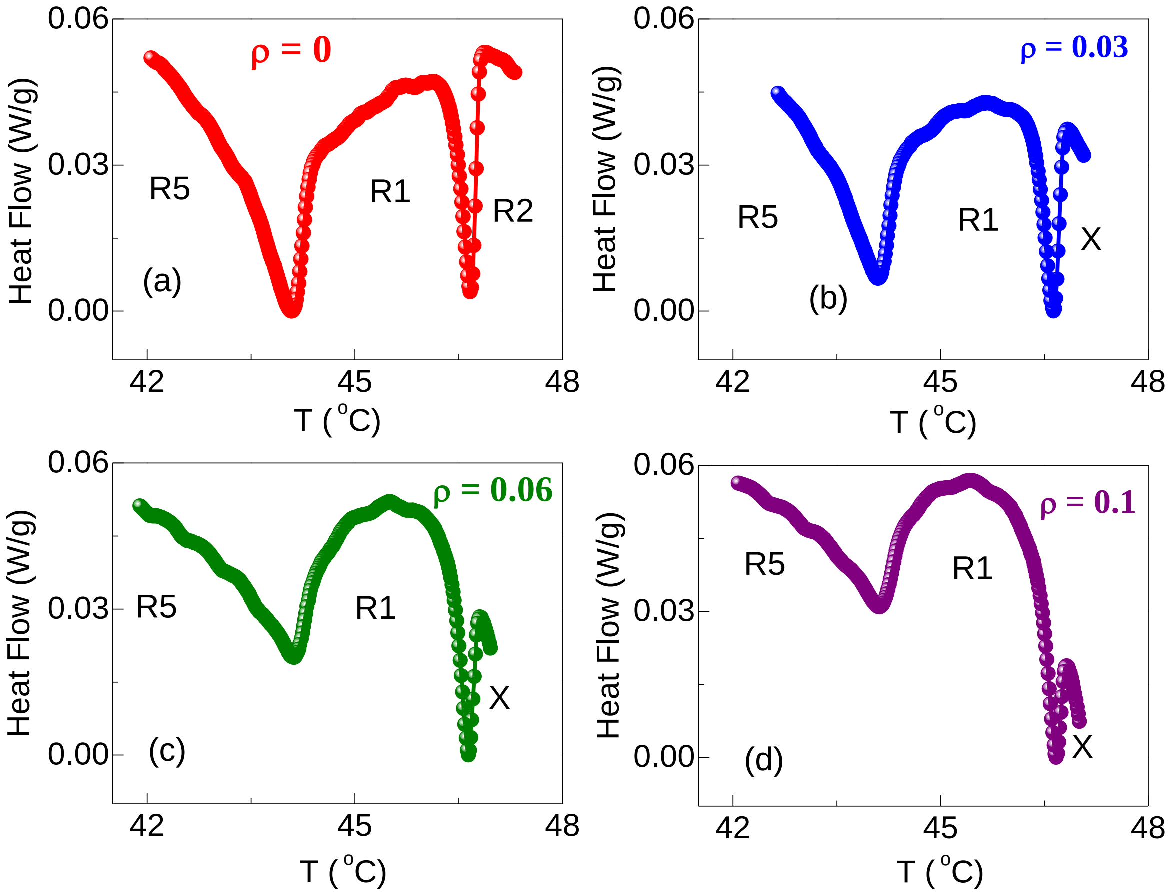

Figure 3.11: DSC profiles for (a) the pure C24 and (b,c,d) the three hydrophobic composites in the vicinity of the R2-R1 (X-R1 for the composites) and R1-R5 transitions. The significant weakening of both the transitions with increasing ρ *is clearly seen.*

Our Xray studies also indicate that across the R1-R5 transition, pure C24 exhibits a step-like variation in $\mathfrak{D}$, whereas the $\rho = 0.1$ material shows a continuous variation. As discussed in Chapter-2, this transition is driven first order due to the coupling between θ and $\mathfrak{D}$. Thus the continuous variation of $\mathfrak{D}$ perhaps results in a second order transition for the composite. Owing to the strong temperature dependence of the background signal (especially for the composites) on the low temperature side of the R1-R5 transition, a precise determination of the transition enthalpy for this case is difficult. The transition enthalpy data for the R2-R1 transition is, as shown in Table 3.2, on the lines of what was observed for the

Iso-R2 transition, diminishing in magnitude with increasing ρ value. Likewise, the transition temperature is hardly affected by the presence of aerosil.

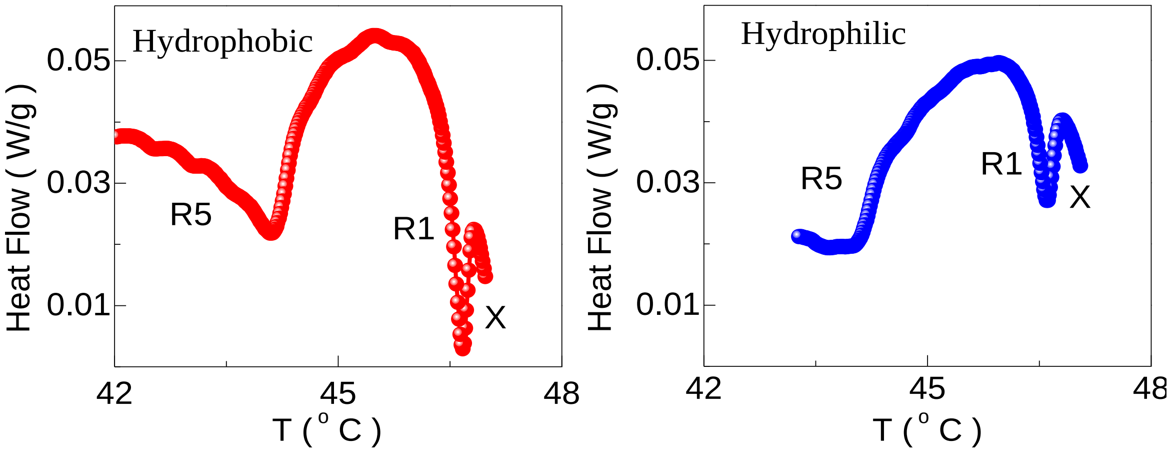

Figure 3.12: Comparison of the profiles obtained for the ρ = 0.1 concentration composites with hydrophobic (right panel) and hydrophilic (left panel) particles. The system with latter type of particles exhibits much weaker transitions

3.4.3 R5-Crystal transition

We, now describe the features observed for the transition involving the true crystallization of the sample, viz., from the R5 to the crystal (Cr) phase. The DSC profiles obtained in the vicinity of the R5-Cr transition are shown in Figure 3.13a for the pure sample and the composites. There is a slight weakening of the peak with increasing ρ.

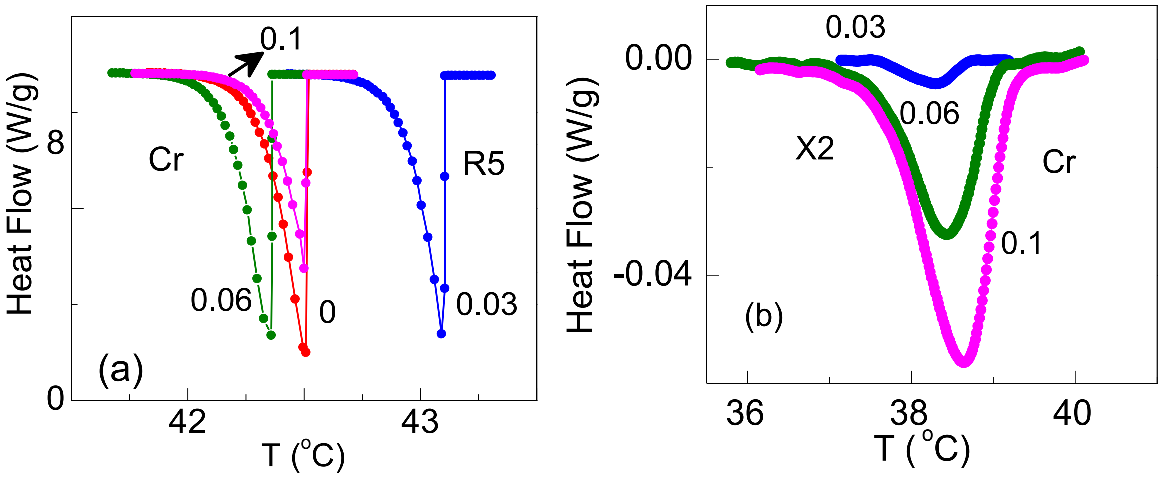

Figure 3.13: (a) DSC profiles across the R5-Cr transition for the pure compound and the three hydrophobic composites with concentrations indicated against each profile. The secondary peak seen at a lower temperature for the composites is displayed in panel (b).

More interestingly, while a single peak is seen for the pure compound, the composites exhibit an additional peak at a lower temperature (see Figure 3.13b), whose strength increases as the concentration of aerosil increases, a feature reminiscent of the behavior near the Iso-R2 transition. This additional transformation is labeled as Cr-X2 transition. Just as in the R2-X case, Xray measurements show no difference in the diffraction patterns taken at temperatures above and below this transition, providing a strong indication that this second peak must be the R5-Cr transition occurring in the vicinity of the aerosil particles, a surprising feature considering the fact that the transformation is between three dimensionally positional ordered phases. In fact, this appears to be the first observation of such a transformation. Again, the hydrophilic system has a weaker Cr-X2 signature than the corresponding hydrophobic composite.

Two general observations can be made concerning the results described above. Firstly, the peak doubling is seen only for the strong first order transformations, perhaps indicating a correlation with the presence of orders/disorders of different magnitudes coexisting in the *surface* and bulk regions. This point should be viewed with a caveat. Enthalpy-wise the secondary peaks, present only in the composites, are much weaker than those associated with the bulk: for example, in the case of the highest aerosil concentration composite, the R2-X transition has a transition enthalpy which is only ~ 7% as that of the Iso-R2 transition. If such secondary peaks do exist for the R2-R1 and R1-R5 transitions, the already low enthalpy of the bulk transitions would preclude the feature from being seen. Secondly, preliminary Xray diffraction measurements do not show any peak broadening in the rotator phases; a feature that was observed for the Anopore confined sample reported in Chapter-2. Further, the aerosil composites of even the highest concentration studied have only a slight lowering in the magnitude of the decrease in the layer spacing seen across the R1-R5 transition. In contrast, the Anopore confined sample exhibited a substantial smearing of the transition. Thus the DSC data and Xray observations are in mutual agreement and also fall in line with the features seen for the Anopore-confined sample. It may be mentioned that (i) in the Anopore-confined case, the Xray peak broadening, determined using Debye-Scherrer expression, corresponded to a correlation length of 190 nm (comparable to the diameter of the Anopore), and (ii) the resolution of the Xray apparatus used for these purposes is in the range of 400-500 nm. Thus the non-broadening of the peaks in the aerosil cases, suggests that the diameter of the pore (created by the aerosil network, in which C24 molecules get confined) may not be less than about 500 nm. This value is higher than what has been reported for the isotropic-smectic A phase transition of LC-aerosil composites [25]. It is possible that three dimensional positional ordering of the rotator phases studied here, as against the one-dimensional ordering in the case of the smectic A phase is responsible for this difference. It is also possible that the 2-d fluid nature of the smectic A phase, which increases the intensity contribution to the wings of the profile forcing the usage of a slightly different expression for the calculation of the correlation length, is the influencing factor. However, the main point that we would like to emphasize is that the aerosil composites provide a continuously variable tool – the concentration of the particles – to control the nature of the R1-R5 transition, a detailed inspection of which is a problem for the future.

3.4.4 Nature of the soft matter and interaction with aerosil particles

In the comparisons that we made in the earlier sections between the behaviour observed for the LC-aerosil and alkane-aerosil composites, the LC considered are, as Zammit et.al [26] also have done, the most well studied alkyl/alkoxy cyanobiphenyls (labeled as LC1 in the following discussion). A special feature of these materials is that the molecules are asymmetric as one terminal has an aliphatic tail, and thus non-polar whereas the other terminal is the nitrile group, which is highly polar. In fact, a few studies have been performed [27] on the composites of aerosil with a liquid crystal that has an alkyl chain at both ends of the molecule (4O.8 and 7O.4, referred to as LC2 here), unlike LC1. The ability of the cyano group of LC1 to form a hydrogen bond with the siloyl group of aerosils, can alter the strength, and thus, the extent of the "surface-affected" region. For this purpose let us compare the thermal features such as the nematic-isotropic transition temperature (T_{NI}) and the associated height of the thermal peak (P_{cal}) upon adding aerosil to LC1 and LC2 materials. Let us consider, for example, systems with an aerosil density of ~ 0.1 g/cm^3. LC1 materials always have *Pcal* of the surface and bulk transitions comparable [3, 26] and the shift in T_{NI}, quite small (~ 0.2 K). Weaker surface peaks and larger shift in T_{NI} have been reported for LC2 materials [27]. This suggests that the nucleation corresponding to the lower temperature peak in the LC2 material occurring with a larger shift T_{NI} in is weaker owing to the strong strain developed in the medium. This is true of the rotator phase system studied here as well. Since the terminal entities (aliphatic groups) that interact with the aerosil surface are identical in the LC2 systems and n-tetracosane, the observed features may be taken to suggest that the surface strain proliferates much more slowly in these cases than in the differently terminated LC1 materials. The larger extent of proliferation thus leaves less number of "remaining" molecules to undergo nucleation, thereby reducing the thermal strength of the low temperature peak. It is also possible that the proliferation is further slowed by reducing the hydrophilicity of the aerosil particles. In understanding these results it must be borne in mind that the hydrogen bonding between the LC1 molecules and the aerosil may play an important role vis-à-vis the van der Waal interaction in the case of LC2 and tetracosane. This has to be further probed with molecules having different chemical structure. Another difference found between the LC1 system [26] and the presently studied tetracosane is the hysteresis of the high and low temperature peaks. The magnitudes are much larger in the present case. Any explanation to account for this behaviour should consider that the strain induced deformation, once created needs a much larger energy to destroy it.

3.5 Rheological behaviour

In this section we discuss the mechanical properties in the R2 phase of pure C24 and representative composites with hydrophilic aerosil. First, the strain and frequency dependent dynamic rheological measurements in the linear regime are described, and then the non-linear aspects are mentioned. We begin with a brief introduction to rheology [28]. In rheology, elasticity is the ability of a material to store deformational energy, and can be viewed as the capacity of a material to regain its original shape after being deformed. Viscosity is a measure of the ability of a material to resist flow, and reflects dissipation of deformational energy through flow. Material will respond to an applied force by exhibiting either elastic or viscous behaviour, or more commonly, a combination of both mechanisms. The combined behaviour is termed viscoelasticity. In these studies, the deformational force is expressed as the stress, or force per unit area, and the degree of deformation of the material is referred to as the strain. Strain may also be expressed as sample displacement (after deformation) relative to pre-deformation sample dimensions. In the present study, we concentrate on dynamic rheological measurements wherein the strain and stress are time dependent, varying in a sinusoidal manner. Thus, the applied sinusoidal strain is given by

$$\gamma = \gamma_o \sin(\omega t) \qquad (3.1)$$

where, ω is the frequency of oscillation and γ_o is the strain amplitude. This results in a sinusoidal stress, phase shifted with respect to the strain by an angle δ, given by,

$$\tau = \tau_o \sin(\omega t + \delta) \qquad (3.2)$$

Dividing eqn. 3.2 by eq. 3.1, the complex modulus G* is obtained.

$$G^* = \frac{\tau}{\gamma} = G' \sin(\omega t) + G'' \cos(\omega t) \qquad (3.3)$$

where,

$$G' = \frac{\gamma_o}{\tau_o} \cos\delta\, , \;\; G'' = \frac{\gamma_o}{\tau_o} \sin\delta \qquad (3.4)$$

Here, G′ is called the storage or elastic modulus, and is indicative of the energy that is stored within the system, characterising the elastic behaviour of the system. The component G″ gives the loss or viscous modulus and is a measure of the energy dissipated per cycle of deformation per unit volume. This characterises the flow behaviour or fluid-like characteristics of the system. For purely elastic material, G′≠0, G″=0, while for purely viscous material, G′=0, G″≠0 and for viscoelastic materials, both the moduli are non-zero. Further, the ratio $\frac{G''}{G'}$ gives the loss tangent (tan δ) which is a measure of the fluidity in the system. For a pure solid (Hookean solid), δ=0, for a pure liquid (Newtonian liquid), δ=1 and for viscoelastic materials, it lies in the range of 0 and 1. We performed measurements with an oscillating strain of either fixed amplitude or fixed frequency applied to the sample, and obtained the system response in terms of the elastic modulus.

3.5.1 Strain amplitude dependence

We begin with the strain amplitude dependence obtained at a constant frequency of 1 rad/s. Figure 3.14 presents the G′ and G″ data for C24, and the two composites ρ =0.06 and 0.1. At the lowest strain the pure compound has characteristics of a solid (G′ > G″), but only marginally so. Even at a modest strain of slightly more than 1% amplitude (γ = 0.01), this feature breaks down, and G′ < G″, a feature typical of liquids. Inclusion of aerosil particles results in two interesting features. Firstly, the absolute magnitude of the two moduli significantly increases, although by different amounts: for ρ = 0.1, G′ enhances by a factor of 22, whereas the loss modulus increases by a much smaller factor (~5). This results in the ratio G′/G″ at equilibrium (here taken to be the value at very low strain amplitudes), increasing substantially; the ratio changes from a meager value of 2 for C24 to 8 for ρ = 0.1 composite.

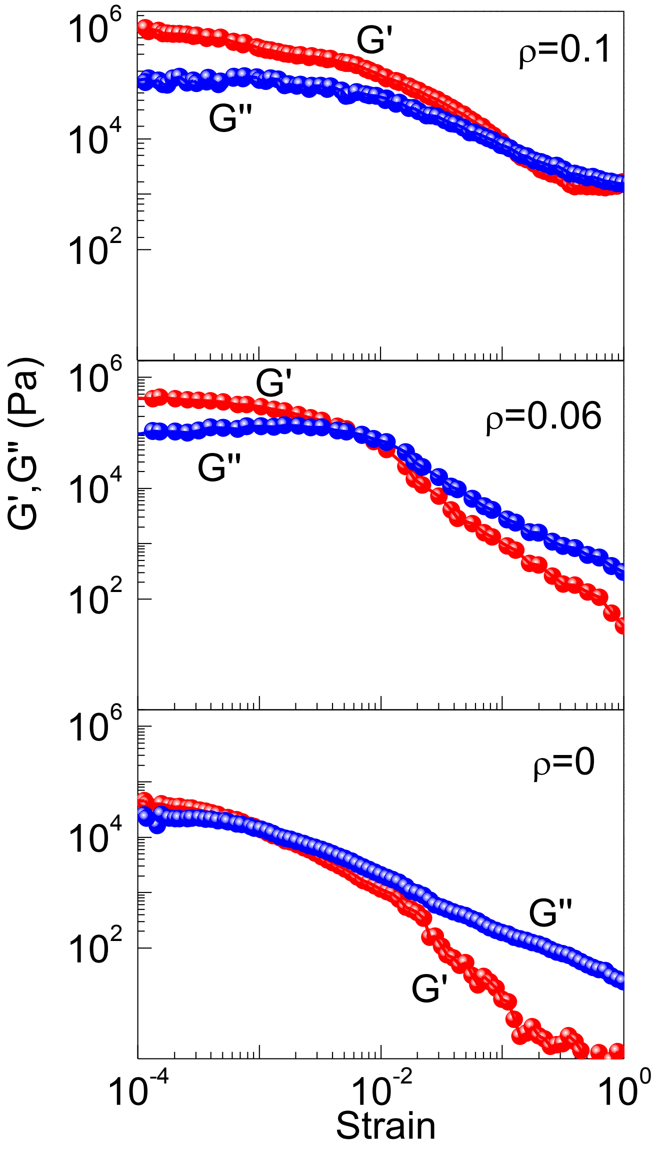

Figure 3.14: *Strain dependence of G′ and G" for pure C24 (ρ= 0) and the hydrophilic aerosil mixtures with ρ=0.06 and ρ=0.1 obtained at T=48^{o}C in the R2 rotator phase (ω =1 rad/s).*

It may be recalled here such large values of G′ as well as G′/G″ are indicative of the material being a strong gel. Secondly, the critical strain γ_c at which there is a crossover from the solid-like (G′ > G″) to the liquid-like (G′ < G″) behaviour, increases by about two orders of magnitude as the aerosil concentration increases from ρ = 0 (pure C24) to 0.1. The strain regime below γ_c is referred to as linear viscoelastic regime (LVR), and the data shows that the LVR regime is maintained up to very high strain impositions by the aerosil network.

3.5.2 Frequency dependence

The oscillation frequency spectra of the moduli obtained by keeping fixed strain amplitude at $\gamma=0.0001$, such that the system is in the LVR region, are shown in Figure 3.15. The observed behaviour is compatible with the strain amplitude-dependence seen in Figure 3.14. While the pure alkane has already a weak dependence of the moduli on the frequency, the composites show a further weakening with the $\rho = 0.1$ composite having a negligible variation over the entire range of frequencies.

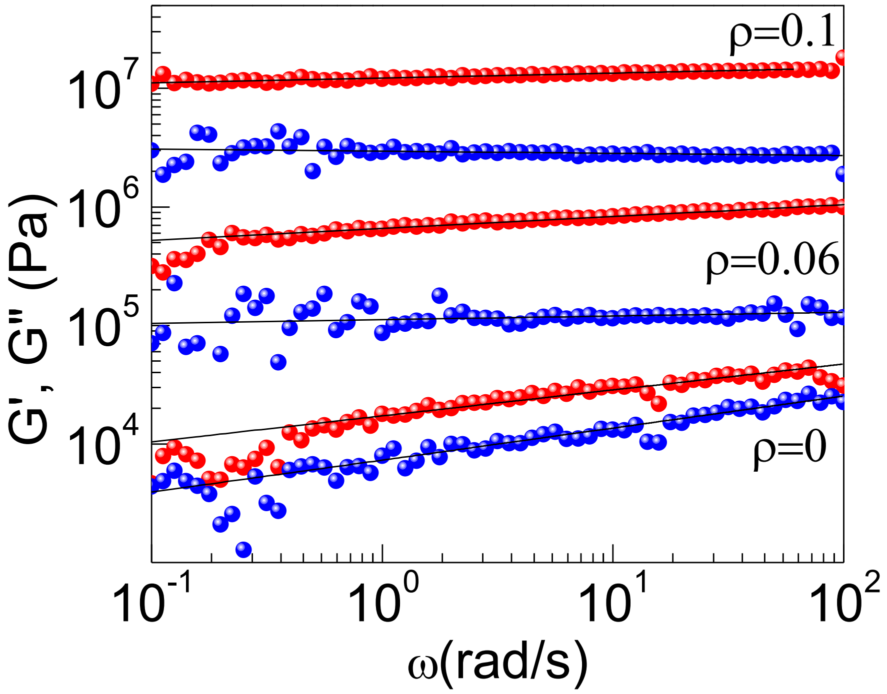

Figure 3.15: *Angular frequency (ω) dependence of the two moduli G' (red circles) and G''(blue circles) obtained with small strain amplitude. Pure has a weak frequency dependency of moduli G' and for the composites it is further weakened.*

Closer inspection of the data shows that there is a slope change in G′ occurring at ~ 0.5 Hz and 0.2 Hz for pure C24 and the $\rho = 0.06$ composite, but no such feature for the higher aerosil concentration composite. This slope change is due to the fact that at lower frequencies (longer time scales) the system would move towards a liquid-like regime, with G′ < G″. The fact that the frequency at which the slope change occurs, moves to lower values means that the system is becoming stiffer, which indeed is the case upon adding aerosil. In other words, the structural relaxation time becomes longer as the aerosil concentration increases. Similar experiments have been performed in composites of aerosil with a smectic A liquid crystal [29]. Prompted by a qualitatively similar behaviour as in this work, we borrow the concept power-law dependence of the storage modulus on the oscillation frequency. Data that are at frequencies above the slope-change point (mentioned above) are considered for the power-law description of the type,

$$G' = G_o\, \omega^{\alpha} \tag{3.5}$$

Here G_o is a lumped term that contains the contribution due to the aerosil gel network and that due to the defect network of tetracosane layers. Detailed temperature-dependent measurements will, in fact, help in separating the two contributions, which is beyond the scope of the present study. The data for pure C24 and the two aerosil composites were fit to eq. (3.5); as seen from Figure 3.15, the fit is quite good. The fitted exponent strongly decreases with increasing aerosil concentration: $\alpha = 0.23 \pm 0.008$, 0.10 ± 0.003 and 0.04 ± 0.001 for $\rho = 0$, 0.06 and 0.1, respectively. Such a feature is indeed seen for the smectic-aerosil composite system mentioned above. It is interesting that the exponent obtained here is comparable for the smectic-aerosil case, but much smaller than that observed for a variety of lamellar systems [30] such as surfactant-based phases, diblock copolymers, and also lyotropic and thermotropic smectics without quenched disorder (i.e., no aerosil content). In the latter type of systems, G' exhibits a square root dependence on ω. It is possible that the presence of hydrogen bonded aerosil further reduces the already weak frequency dependence in the 3-d positionally ordered rotator phase, suggesting that the behaviour may be universal to systems with quenched disorder. Observation of low values assumes importance from the viewpoint of the predictions by Sollich and co-workers [31], whose model provides a unified description of the behaviour in a plethora of complex fluids that includes foams, emulsions, particulate suspensions, and slurries, by bringing in the concept of *soft glassy rheology*. The model argues that the general bases for the observed features are the underlying structural disorder and metastability, and therefore controlled by a single parameter, labelled effective noise temperature α; as $\alpha \to 0$, the system approaches a glass transition. Thus the observation in the present studies that as the aerosil concentration is increased α decreases drastically suggests increasingly glassy dynamics brought about by the quenched disorder. Interestingly, the α value of 0.04 for the present system is smaller than even that for the smectic composite $(\alpha = 0.10)$ with the same aerosil density [29], suggesting that the rotator phase with the quenched disorder is much closer to the glassy state than the smectic.

Complex viscosity

The rheological differentiation between a liquid and a gel can also be conveniently made by determining the complex viscosity η^* using the elastic moduli described above

$$\eta^* = \frac{\left(G'^2 + G''^2\right)^{1/2}}{\omega} \qquad (3.6)$$

The frequency dependence of this complex viscosity is described by a power law

$$\eta^* \propto \omega^{-p} \qquad (3.7)$$

Here values of p close to zero suggest liquid-like behaviour, and if close to 1, a solid-like response [32].

The frequency dependence of complex viscosity is shown for C24 and the two aerosil composites in Figure 3.16. For fitting to eq. (3.7), the dataset over the entire frequency span was considered for $\rho = 0.1$, whereas for $\rho = 0.06$ and 0, it was limited to regions above the slope change point. Eq. (3.7), which on a double logarithmic representation would be a straight line, accounts for the data well in all the cases. The determined p values also exhibit a concentration dependence, with p = 0.76±0.01, 0.899±0.002 and 0.96±0.02, for ρ = 0, 0.06 and 0.10 respectively. These results, while being in agreement with those for well-formed gels [33], establish that the system response from a not-so-solid-like to a definite solid-like behaviour.

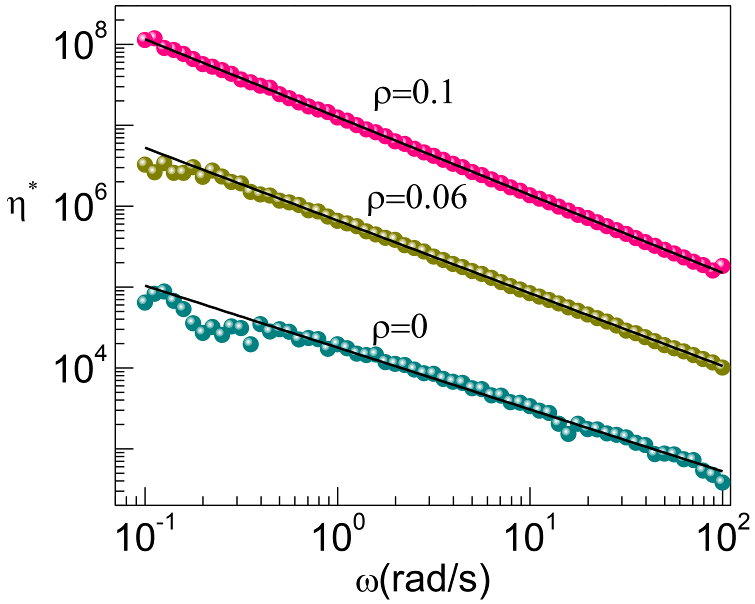

Figure 3.16: *Frequency dependence of the complex viscosity η* determined from oscillatory measurements using equation 3.6. The lines represent fit to equation 3.7. The exponent obtained, being nearly equal to a value of 1, suggests solid-like response of the system seen in well-formed gels.*

3.5.3 Non-linear behavior

Finally, we discuss the behaviour of the aerosil composite in the non-linear rheological regime realized under large strain values, a feature also referred to as Large Amplitude Oscillatory Strain (LAOS) regime. There is an advantage of this type of study wherein the time dependence of the applied probing sinusoidal strain is compared with the stress response from the sample. The raw profile itself bears signatures which help to differentiate not only between a liquid and a gel, but categorize the gels as either soft or hard. Figure 3.17 and 3.18 present exemplary profiles of applied stress and strain curves (See in Figure 3.17 for ρ = 0 and 3.18 for ρ = 0.06) and the corresponding Lissajous representation in an elastic solid, viscous liquid and a viscoeleastic material shown in figure 3.19.

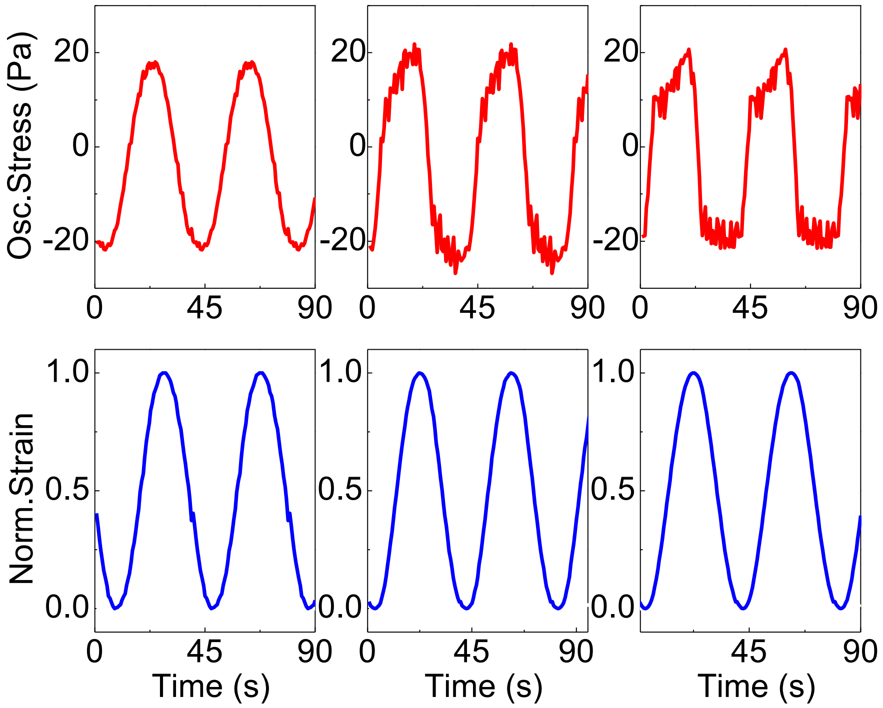

Figure 3.17: Temporal variation of applied strain (lower panels) and stress response (upper panels) ρ =0 at three different strain amplitude (γ_o=0.001, 0.02 and 0.04) with fixed frequency 1rad/s. For better representation, the strain amplitudes are normalized with respect to their maximum peak amplitude (γ_o) of each set.

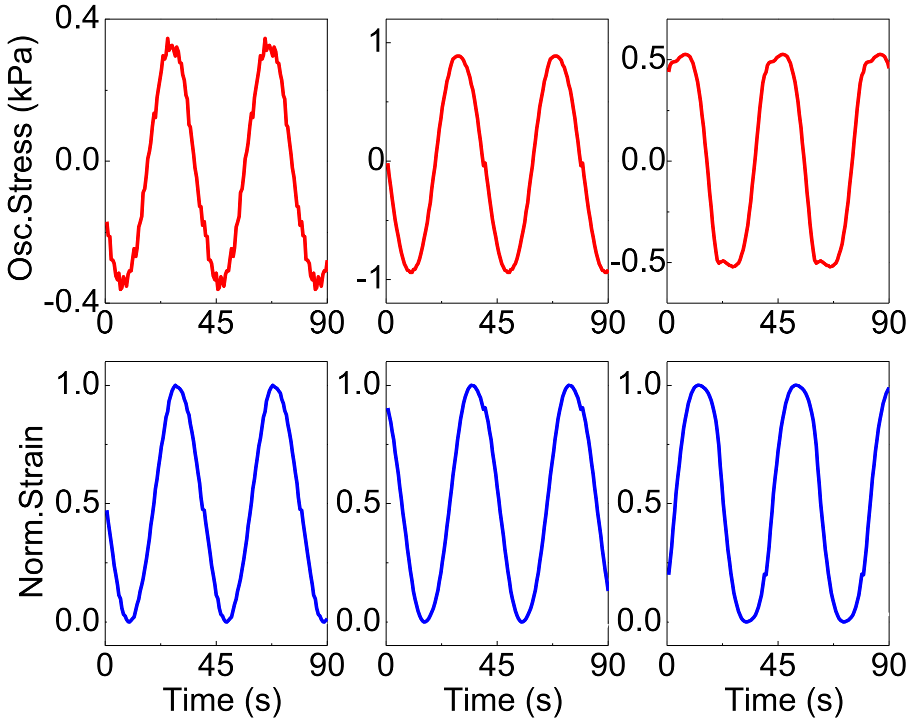

Figure 3.18: Temporal variation of applied strain (lower panels) and stress response (upper panels) for ρ =0.06 at three different strain amplitude (γ_o=0.001, 0.02 and 0.03) with fixed frequency 1rad/s. For better representation, the strain amplitudes are normalized with respect to their maximum peak amplitude (γ_o) of each set.

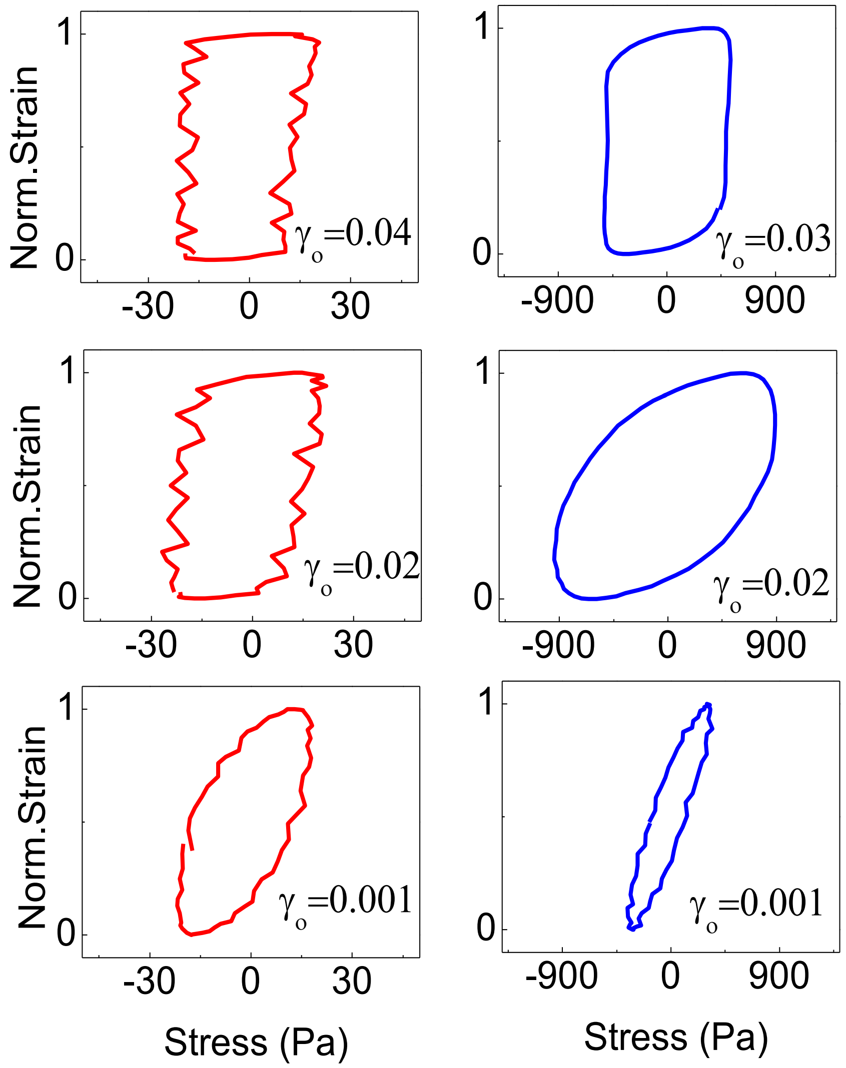

Figure 3.19: Lissajous curves for ρ =0 (left panel) and ρ =0.06 (right panel) composite at three different strain amplitudes at fixed frequency 1rad/s. For better representation, the strain values are normalized with respect to maximum peak amplitude (γ_o) in each set of the data.

As both the elastic as well as viscous response has to be considered, we take the example of a connected spring and a dashpot (Figure 3.20a). The former represents the elastic element, and the latter, the viscous aspect. The time profile of a sinusoidal varying applied strain, and the response in terms of the stress can then be represented as in Figure 3.20(b), (c) and (d) for a purely elastic Hookean solid, purely viscous Newtonian liquid and a viscoelastic system, respectively. To carry the description further, we bring in the analogy with the more familiar electrical response from a pure resistance R, pure capacitor C or a case where both R and C are present. In the electrical scenario, the current response to an applied sine-wave voltage depends on the component in the circuit. In the linear regime, the output will also be sinusoidal with the same frequency, but may have different amplitude and some phase shift. For the resistor, the amplitude will differ depending on the magnitude of the resistance, but there will be no phase shift. This is like the elastic aspect in rheology. If the component is a simple capacitor, then the response would, as for a purely viscous material, exhibit a 90^o phase shift, but no amplitude change. For a RC combination, similar to a viscoelastic material, both parameters would undergo a change. In electrical systems, an often used 2-dimensional parametric representation (on an oscilloscope, for example), referred to as Lissojous figures, would be to plot the input wave against the output wave producing in the general case, an ellipse. The aspect ratio of the resulting ellipse is a function of the phase shift between the input and output, with an aspect ratio of 1 (perfect circle) corresponding to a phase shift of 90^o and an aspect ratio of ∞ (a line) corresponding to a phase shift of 0 or 180 degrees.

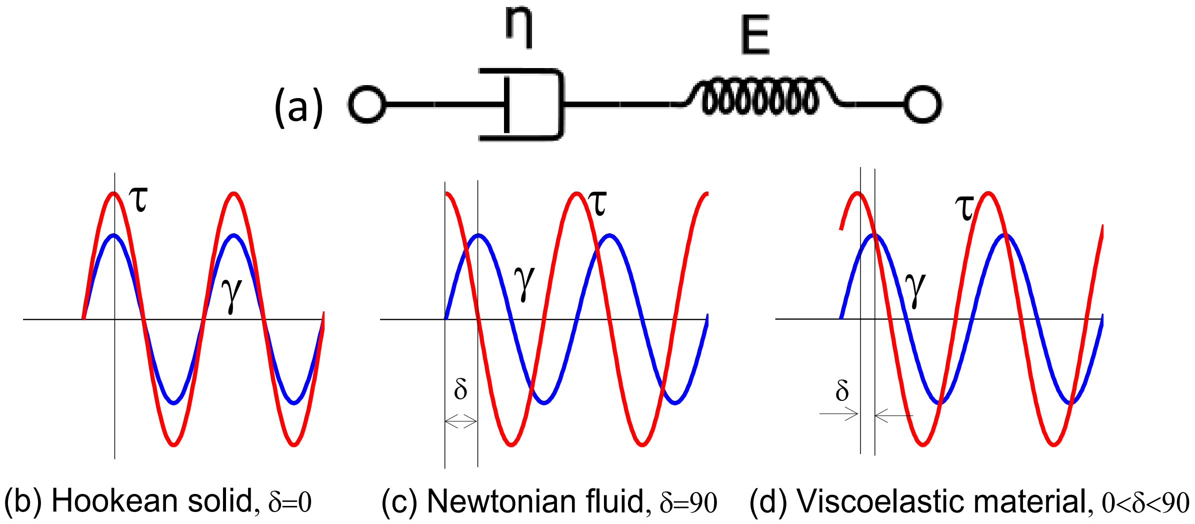

Figure 3.20: (a) Schematic diagram of the viscoelastic system. Here, η and E represents viscosity and elasticity of the system. Variation of phase angle δ for (b) solid where applied strain γ and response function τ are in phase (c) for liquid, γ and τ are out of phase and (d) intermediate for viscoelastic materials (taken from ref. 34).

A similar 2-D representation of Large Amplitude Oscillatory Shear (LAOS) data can be used to characterize nonlinear viscoelastic material responses [35]. In strain controlled

LAOS deformation, the applied strain having the form γ (t) =γ_0 sinωt results in the material stress response τ (t,γ_o,ω) oscillating with the same fundamental period T=2π/ω as the strain, but with a viscoelastic phase shift. In addition, higher harmonic contributions will also be present if the strain is large enough to induce material nonlinearity. Thus, the Lissajous stress σ (t) vs. strain γ (t) representation would be a straight line, a circle, and an ellipse for the purely elastic, purely viscous and viscoelastic response in the linear regime, respectively. The presence of non-linearity will distort the ellipse towards hysteresis loops similar to the case of the electrical response in materials with a spontaneous polarization.

With this background, let us look at the temporal profiles of strain, stress and the corresponding Lissajous representations (see Figures 3.19) in the R2 phase of pure C24 and the ρ = 0.06 aerosil composite obtained with three different strain magnitudes (γ_o), and a fixed frequency of 1rad/s. The used strain amplitudes were γ_o = 0.001, 0.02 and 0.04 for ρ=0 and γ_o = 0.001, 0.02 and 0.03 for ρ=0.06. There is a clear difference between the profiles for the two materials. At the lowest value of γ_o = 0.001, the raw profiles look sinusoidal, and nearly identical although with a smaller phase shift for the composite. The Lissajous curve, however, shows that the loop is more closed up (almost becoming a line) for the composite suggesting that it is more elastic than pure C24. As γ_o is increased the deviation of the response from the sinusoidal profile becomes evident with the stress profile acquiring a *flat top* character for γ_o = 0.02, resulting in the Lissajous curve appearing like a square box. This indicates nonlinear nature of the response. However, it is seen that the nonlinear character reduces for the composite.

In the case of extreme nonlinearity the response curve would become a square wave. This feature forms the basis to quantitatively assess the extent of nonlinearity, by taking into account that the square wave is nothing but a sum of sine waves of the fundamental and its infinite number of harmonics, each with a frequency ω_3, ω_5, ω_7,... ω_n, which is an odd integral number of the fundamental frequency ω_1. Fourier Transform (FT) of the response to extract the different components is a well established procedure for the decomposition [36]. The effect of the non-linearity is clearly brought out by the FT analysis, as random noise, being non-periodic, is efficiently suppressed by the Fourier transform. The FT profiles in the frequency domain are shown in Figures 3.21 (a) and (b) for pure C24 and the ρ =0.06 aerosil composite, respectively.

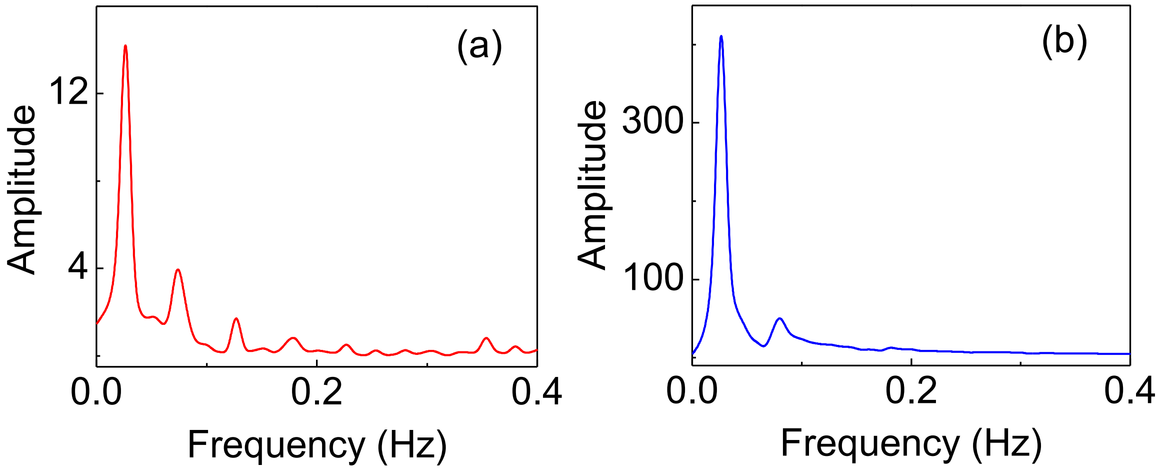

Figure 3.21: The FT profiles in the frequency domains for pure C24 in (a) and the ρ =0.06 aerosil composite in (b), respectively

The spectra display only the fundamental (ω_1) and the third harmonic (ω_3) of the excitation frequency. The amplitude ratio $I\omega_3/I\omega_1$ obtained at the highest strain value, and considered to be a measure of non-linear response, decreases by an order of magnitude from 17% for pure C24 to 1.7% for the composite. This again confirms the dominant elastic character of the composite. Thus, the gelation of the material brought about by the aerosil network makes the system more solid-like. In fact, the shift towards solid-like Lissajous curves upon gelation of C24 is similar to the observation [37] made in triblock polymers, shown in Figure 3.22.

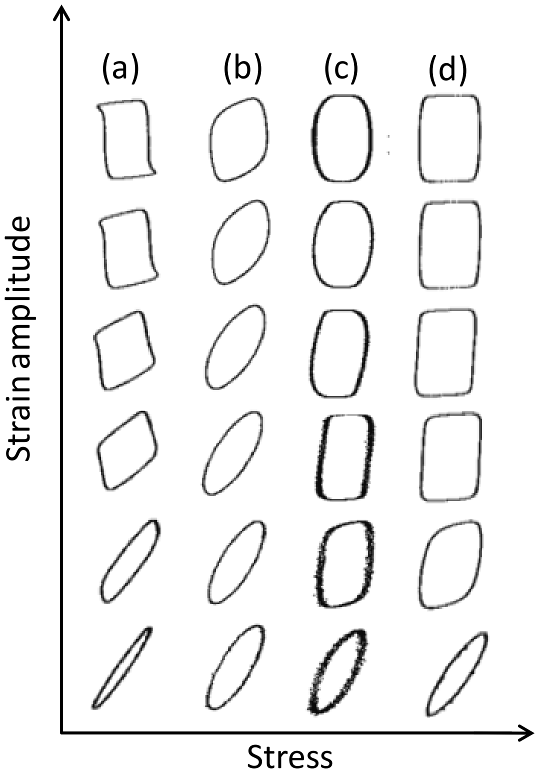

Figure 3.22: The Lissajous curves (stress (y axis) vs. strain (x axis)) of various complex fluids, arranged from small strain amplitude to large strain amplitude at a fixed frequency. (a) Xanthan gum 4% aqueous solution (b) Hyaluronic acid 1% aqueous solution (c) soft gel of PEO-PPO-PEO triblock 20% aqueous solution (d) hard gel of PEO-PPO-PEO triblock 20% aqueous solution[taken from Ref.37].

3.6. Summary

Investigations have been carried out using differential scanning calorimetric measurements on composites of nanosilica aerosil particles with tetracosane, an n-alkane exhibiting different types of rotator phases. The presence of the aerosil particles has the general effect of weakening all the transitions observed in the system. Both the strong first order transitions of the pure alkane, viz., Iso-R2 and R5-Cr, are accompanied by a subsidiary peak, although much weaker. In analogy with observations made in similar composites of liquid crystalline systems, and also with the knowledge of the Xray diffraction measurements on the currently studied materials, it is argued that the subsidiary peaks are nothing but the transformations between the same phases as the corresponding main peaks, but occurring in the vicinity of the aerosil particles. The nature of the corona of the aerosil particles also turns out to have an important influence. For all the transitions seen in the pure material, the reduction in the strength – in terms of transition enthalpy – is higher for the composites with the hydrophilic particles, than those with hydrophobic particles. In contrast, the transitions occurring at the surface are stronger for the hydrophobic systems. Further, the downward temperature shift in the transition temperature of the surface transition with respect to its bulk counterpart is more for the hydrophobic composites than the hydrophilic ones. Employing molecules with different terminal entities, such as an alcohol, can alter the interaction with the corona of the aerosil particles and thus may shed more light on these fine tunable surface-driven phase transformation events. The rheological measurements bring out the features such as gelation, stiffness of the gel, dynamic glassy behavior and large amplitude oscillatory strain (LAOS) upon increasing the concentration of the aerosil with C24.

3.7 References

1. G.S. Iannacchione, *Fluid Phase Equilibria.,* **222-223**, 177 (2004); V. Popa-Nita, I. Gerlic, S. Kralj, *Int. J. Mol. Sci.,* **10**, 3971 (2009).
2. R. Eidenschink and W.H. de Jeu, *Electron. Lett.*, **27**, 1195 (1991)
3. G.S. Iannacchione, C.W. Garland, J.T. Mang, and T.P. Rieker, *Phys. Rev. E,* **58**, 5966 (1998).
4. T. Jin and T.D. Finotello, *Phys. Rev. Lett.*, **86**, 818 (2001).
5. Y. Imry and M. Wortis, *Phys. Rev. B*, **19**, 3580 (1979).
6. D.E. Feldman, *Phys. Rev. Lett*., **84**, 4886 (2000).
7. U. Zammit, M. Marinelli, F. Mercuri, S. Paoloni, *J. Phys. Chem B*, **114**, 8134 (2010).
8. For excellent collection of review articles on confined geometry, see *Liquid Crystals in Complex Geometries,* edited by G. P. Crawford and S. Zumer; Taylor & Francis, London, (1996).
9. M. Kreuzer and R. Eidenschink, *Chapter 15* in Ref. **8**.
10. G.S. Iannacchione, S. Park, C.W. Garland, R.J. Birgeneau and R.L. Leheny, *Phys. Rev. E*, **67**, 011709 (2003).

11. C.V. Lobo, S.K. Prasad, and C.V. Yelamaggad, *J. Phys.: Condens. Matter.*, **18**, 767 (2006); V. Jayalakshmi, G. Geetha Nair and S. K. Prasad, *J. Phys.: Condens. Matter*, **19**, 226213 (2007).
12. S. Krishna Prasad, D.S. Shankar Rao, S. Sridevi, C.V. Lobo, B.R. Ratna, J. Naciri and R. Shashidhar, *Phys. Rev. Lett.*, **102**, 147802-1 (2009).
13. J. Megusar, *J. Nuc. Mat.*, **245,** 185 (1997).
14. A. Roshi, G.S. Iannacchione, P.S. Clegg, and R.J. Birgeneau, *Phys. Rev. E,* **69**, 031703 (2004).
15. S. Aya, Y. Sasaki, F. Araoka, K. Ishikawa, K. Ema, and H. Takezoe, *Phys. Rev. E,* **83**, 061714 (2011).
16. P. Sheng, *Phys. Rev. Lett.,* **37**, 1059 (1976).
17. See e.g., H. Yokoyama, S. Kobayashi and H. Kamei, *Mol. Cryst. Liq. Cryst.,* **99**, 39 (1983).
18. Prasad N. Bapat, D.S. Shankar Rao, S. Krishna Prasad, *Thermochimica Acta,* **495**, 115 (2009).
19. M. Marinelli, A. K. Ghosh, and F. Mercuri, *Phys. Rev. E,* **63**, 061713 (2001).
20. Z. Kutnjak, S. Kralj, and S. Zumer, *Phys. Rev. E,* **66**, 041702 (**2002**); A.V. Zakharov, and J. Thoen, *Phys. Rev. E,* **69**, 011704 (2004).
21. A. Arcioni, C. Bacchiocchi, I. Vecchi, G. Venditti, and C. Zannoni, *Chem. Phys. Lett.,* **396**, 433 (2004)
22. G. Sinha, J. Leys, C. Glorieux and J. Thoen, *Phys. Rev. E,* **72**, 051710 (2005).
23. See e.g., S. Aya, Y. Sasaki, F. Araoka, K. Ema, K. Ishikawa, A.V. Emelyanenko and H. Takezoe, *Phys. Rev. Lett.,* **106**, 117801 (2011).
24. See e.g., P.K. Mukherjee, *J. Phys. Chem. B,* **116**, 1517 (2012) and references therein.
25. M.K. Ramazanoglu, P.S. Clegg, R.J. Birgeneau, C.W. Garland, M.E. Neubert and J. M. Kim, *Phys. Rev. E,* **69**, 061706 (2004).
26. U. Zammit, M. Marinelli, F. Mercuri, and S. Paoloni, *J. Phys. Chem. B,* **113**, 14315 (2009).
27. H. Haga and C.W. Garland, *Liq. Cryst.,* **23**, 645 (1997).
28. See e.g., R.G. Larson, The Structure and Rheology of Complex Fluids, Oxford University Press, Canada, 1999.
29. R. Bandyopadhyay, D. Liang, R.H. Colby, J.L. Harden, and R.L. Leheny, *Phys. Rev. Lett.,* **94**, 107801 (2005).

30. K. Kawasaki and A. Onuki, *Phys. Rev. A*, **42**, 3664 (1990).
31. P. Sollich, F. Lequeux, P. Hébraud, and M.E. Cates, *Phys. Rev. Lett.* **78**, 2020 (1997).
32. C. Silioc, A. Maleki, K. Zhu, A. Kjøniksen, B. Nystrom, *Biomacromolecules*, **8**, 719 (2007).
33. G.G. Nair, S. Krishna Prasad, R. Bhargavi, V. Jayalakshmi, G. Shanker and C.V. Yelamaggad, *J. Phys. Chem. B*, **114**, 697 (2010).
34. S.A. Khan, J.R. Royer, and S. R. Raghavan, *Rheology: Tools and Methods. Aviation Fuels with Improved Fire Safety: A proceeding*, The National Academy of Sciences Chapter **6**, 31 (1997).
35. A.J. Giacomin, and J.M. Dealy; *Large-Amplitude Oscillatory Shear, in Techniques in rheological measurement* A.A. Collyer. London, Elsevier Applied Science, Chapman and Hall, Chapter **4**. (1993).
36. See e.g., M. Wilhelm, *Macromol. Mater. Eng.,* **8,** 287, (2002)
37. K. Hyun, *Progress in Poly. Sci*, **36**, 1697 (2011).

Chapter-4

Competition between Anisometric and Aliphatic Entities: An Unusual Phase Sequence with Induction of a Phase in an n-Alkane – Liquid Crystal Binary System

Overview

In this chapter we demonstrate two important features that arise out of introducing a liquid crystalline (LC) compound into the rotator phase matrix, and the consequent competition between the anisometric segments of the LC moieties, and the aliphatic units. First, we show that the change in the structural character of the mixed medium depends on which of the entities forms the minority concentration: in case of this being the alkane, the two components of the binary system get nanophase segregated, whereas if the LC molecules are in small concentration then the layered structure merely gets roughened without any segregation. The second and more significant result of the calorimetric and Xray experiments, at low LC concentrations, is the induction of a rotator phase that leads to unusual phase sequence, not reported hitherto. Possible scenarios for the molecular arrangement are discussed. A Landau model is also presented that explains some of the observed features.

The results are published in:

M. Vijay Kumar, S. Krishna Prasad, D.S. Shankar Rao and P.K. Mukherjee, *Langmuir*, **30**, 4465–4473 (2014).

4.1 Introduction

The previous chapters described results in systems wherein the confinement occurs at a supramolecular level on length-scales of > 100 nm. The present chapter is about a situation in which the confinement goes down to the nanolevel of individual molecules. The investigations are on a binary system comprising a long chain alkane and a thermotropic liquid crystal. The structural details of the rotator phases exhibited by the alkane used, viz., n-tetracosane have already been discussed in the previous chapters. The motivation for the study was to compare and contrast the influence of plastic phase exhibited by the alkane, which is a simple hydrocarbon- and a liquid crystal molecule that consists of anisometric rigid parts in addition to the aliphatic tail. Therefore, a liquid crystal that exhibits a plastic phase was chosen as the latter entity.

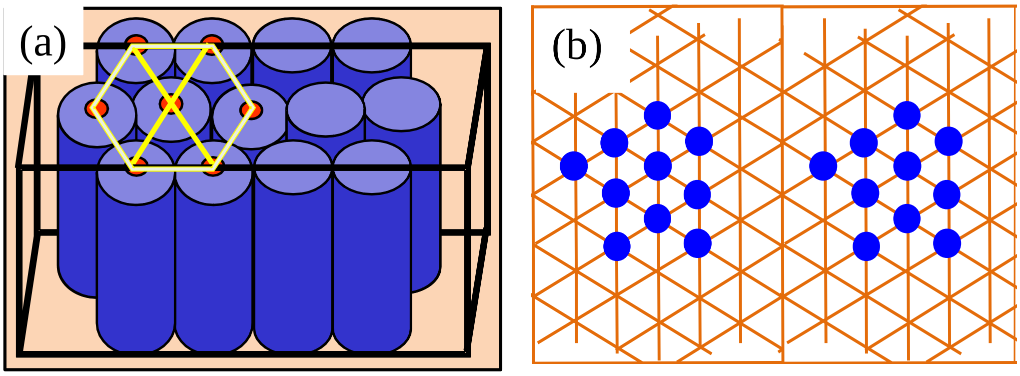

Figure 4.1: Schematic of the molecular arrangement of crystal B (CrB) phase (a) side view and (b) top view.

Here we describe some details of this plastic phase found in anisotropic fluids, specifically thermotropic calamitic liquid crystals (LC). Forming layered structures, the plastic phases of LCs possess three-dimensional translational order with certain orientational degrees of freedom. An example of such a plastic phase is the Crystal B (CrB) phase in which the molecules are upright being positioned along the layer normal and further possessing a six-fold in-layer positional order (and thus similar to the R2 phase of alkanes). A schematic diagram of the molecular arrangement in this phase is given in Figure 4.1. The CrB phase exhibits long range positional order in all the three dimensions. In fact, through high resolution Xray diffraction studies [1] it has been demonstrated that in the compound n-(4-n-butyloxybenzylidene)-4-n-octylaniline (BBOA), a prototype material exhibiting the CrB phase and also employed in this study, the in-plane ordering extends over at least 1400 nm and is actually limited by the resolution of the setup, thus establishing the crystalline nature of the phase. This phase supports a shear both within and between its layers. It must be mentioned that the Cr B phase is not truly crystalline but a soft solid or a plastic crystal; although possessing a three dimensional (3D) positional order the molecules still retain the rotational degree of freedom. The rotational feature is clearly seen in the dielectric spectroscopy measurements exhibiting the dynamics associated with the director modes [2-5]. Stated otherwise this means that the smectic layers can slide past each other.

Recently, investigations on binary mixtures of liquid crystal and a low-molecular weight non-liquid crystal organic material are getting increasing attention with the view that the latter substance can alter the intermolecular potential responsible for the LC order [6-11]. All these studies have focussed on

(i) the low ordered LC phases such as the nematic (N), which is simply an orientationally ordered fluid or the smectic or columnar phases having only one/two dimensional positional order,

(ii) the influence on the LC order.

Situations at the other end of the spectrum, viz., the influence of a rod-like unit with anisometric segments on the rotator phases of alkanes does not seem to have been investigated. Although the alkane moieties are quite stretched and thus behave like rods, enough number of gauche segments is known to be present. The gauche segments, being regions of disorder, reduce the ordering in the medium. Therefore one can expect the order to improve upon the addition of the anisometric molecules. On the other hand, owing to the chemical dissimilarity between the alkane and the LC molecule, the latter could act like an impurity and therefore try to destabilize the system.

In this Chapter we describe calorimetric and X-ray investigations on a binary system of n-tetracosane and a liquid crystal exhibiting the CrB phase performed to explore the effect of the LC molecule consisting of both the aromatic and aliphatic parts on the phases of the pure alkane made of entirely the aliphatic part. It was found that the nature of the structural change depends on which of the constituents is the minority component: if the alkane is the minor one, a nanophase segregation phenomenon is seen, while small amounts of the LC material result in a roughening of the alkane layer. More importantly, the induction of a rotator phase with a new phase sequence has been observed.

4.2. Materials

N-tetracosane which was employed work described in Chapters 2 and 3 was also used for the experiments described here. The liquid crystalline compound employed, butyloxybenzilidene-octylaniline (BBOA for short, purity-GC: 98%) was purchased from Frinton Chemicals, USA, and used without further purification. The structure and the phase sequence of BBOA along with the transition temperatures are shown in figure 4.2. In this chapter X represents the concentration (in weight %) of BBOA in the mixture. BBOA exhibits two LC phases, viz., nematic (N) and smectic A (SmA) phases above the plastic phase referred to as the crystal B (CrB) phase.

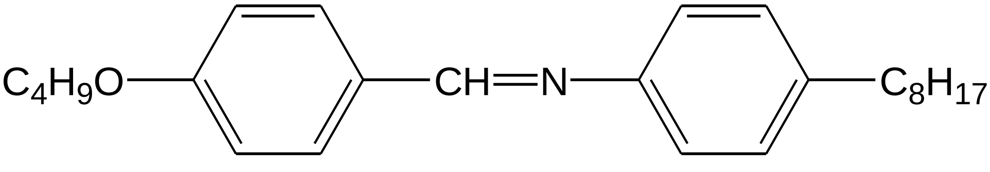

Iso 78.8 °C **N** 63.7 °C **SmA** 49.5 °C **CrB** 38.1 °C **Cr**

Figure 4.2: Molecular structure, phases and transition temperatures of BBOA

4.3 Methods

Calorimetric measurements were performed using a power-compensating differential scanning calorimeter (Perkin Elmer- DSC 8000), having the same operational principle as the instrument already described in Chapter-2. X-ray diffraction measurements were carried out using two different detectors: an image plate (IP) and a solid state detector. In the apparatus with the former type of detector, Cu K_α (λ = 0. 15418 nm) radiation from a source (GeniX^{3D}, Xenocs) operating at 50 kV and 0.6 mA in conjunction with a multilayer mirror was used to illuminate the sample contained in a glass capillary tube (Capillary Tube Supplies Ltd). The temperature of the sample was varied using a Mettler hot stage/programmer (FP82HT/FP90) and could be controlled to a precision of 100 mK. The diffraction patterns were collected on a 2D IP detector of 345 mm diameter and 0.1 mm pixel size (Mar345, Mar Research). The schematic diagram of the X-ray setup is shown in figure 4.3.

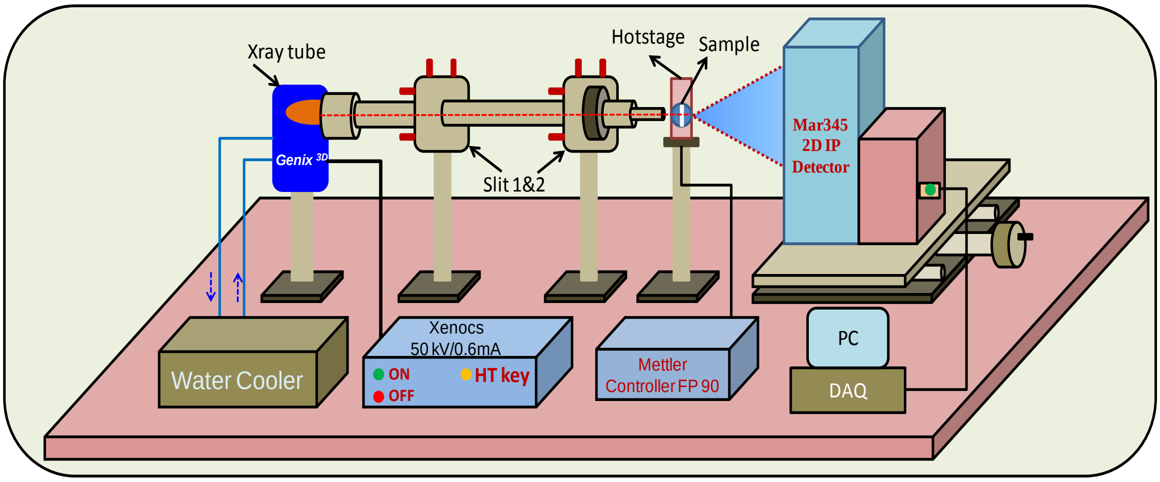

Figure 4.3: Schematic diagram of the X-ray setup with Image Plate detector.

The experiments were always conducted while cooling the sample from the isotropic phase. Although no orienting external field was employed, the interaction of the sample with the walls of the capillary tube resulted in a partial alignment of the molecules, especially for the mixtures. For the extensive temperature-dependent measurements the PANalytical X'Pert PRO MP X-ray diffractometer [12] was employed; the details of this apparatus are given in

Chapter-2. The profiles collected using this apparatus were analyzed using Fityk profile fitting software [13].

4.4 Results and Discussion

4.4.1 Differential scanning calorimetry

The differential scanning calorimetry (DSC) scans taken at a rate of 1°C/min for the pure compound and four mixtures X =2, 5, 10 and 20 are shown in Figure 4.4. The first feature to be noted is the weakening of both the Iso-R2 and the crystallization transitions, as X increases.

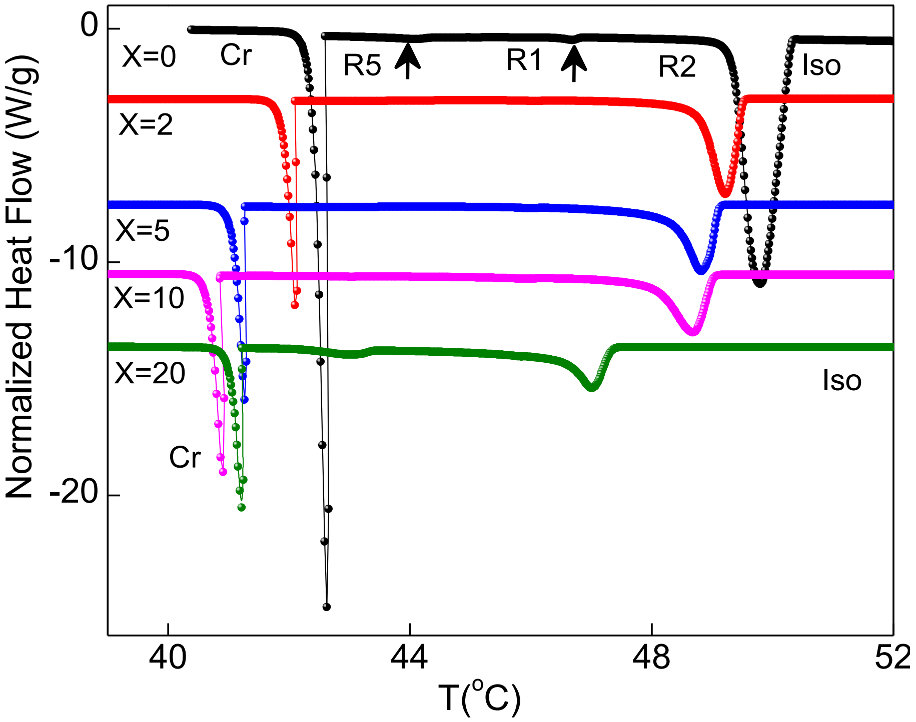

Figure 4.4: Differential scanning calorimetry profiles obtained at a rate of 1 °C/min for the pure C24 (X=0) and mixtures with different concentrations of BBOA (X= 2 to 20, X being the wt% of BBOA in the mixture). The phase labelling shown near the top applies only for X=0. The phase sequence for the mixtures occurring between the isotropic (Iso) and the true crystalline (Cr) phase are depicted in Figure 4.6 presenting an enlarged view of the intermediate temperature range.

Figure 4.4 presents the transition temperature and transition enthalpy (ΔH) for the two transitions in pure C24 and the mixtures. Addition of the LC component appears to have the largest effect on the Iso-R2 transition, with its ΔH value even getting halved for the X=2 mixture, whereas crystallization, another strong first order transition of the system has its transition enthalpy reduced by ~ 25%. Secondly, and surprisingly, the presence of the perturbing LC solute leads to only a small depression of the transition temperature, with the Iso-R2 temperature for X=10 mixture reduced by 1^{o}C compared to that of the pure alkane (see Fig. 4.5a). This is in stark contrast to the behaviour observed for mixtures of LC and organic solvents, wherein the LC forms the major component. For a rod-like LC addition of 3% benzene suppresses the nematic-isotropic temperature by ~ 15 ^{o}C [14], 10% hexane reduces it by ~ 9 ^{o}C [15]. With a bent-core LC host, even a small concentration of an alkane or Xylene as the second component reduces the clearing point (isotropic-LC phase transition temperature) by about 10 ^{o}C [10,16]. A large decrease in the clearing point was again seen for mixtures of a discotic compound with dodecane [17]. These values are about an order of magnitude larger than seen here. (For the presently studied systems, even when the concentration of BBOA is 20%, the reduction in the Iso-R2 temperature is only 3^{o}C.) As we shall see later this is caused by the different type of organization of the minority component in the alkane-majority (presently studied) and the LC-majority cases.

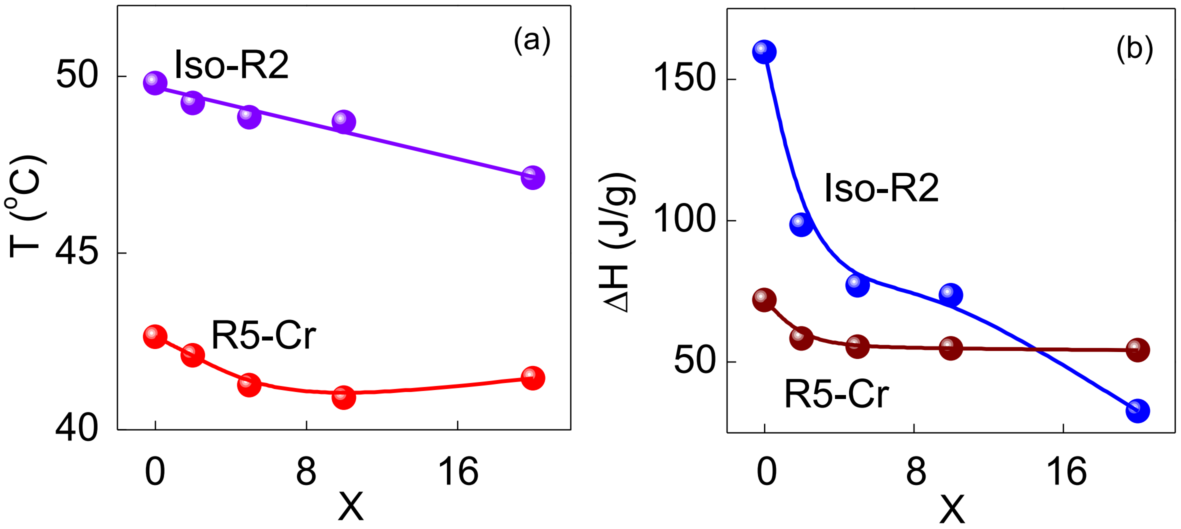

Figure 4.5: (a) Transition temperature and (b) transition enthalpy dependence as a function of X for the two strong first order transitions, Iso-R2 and R5-Cr. In all the cases the lines are merely guide to the eye.

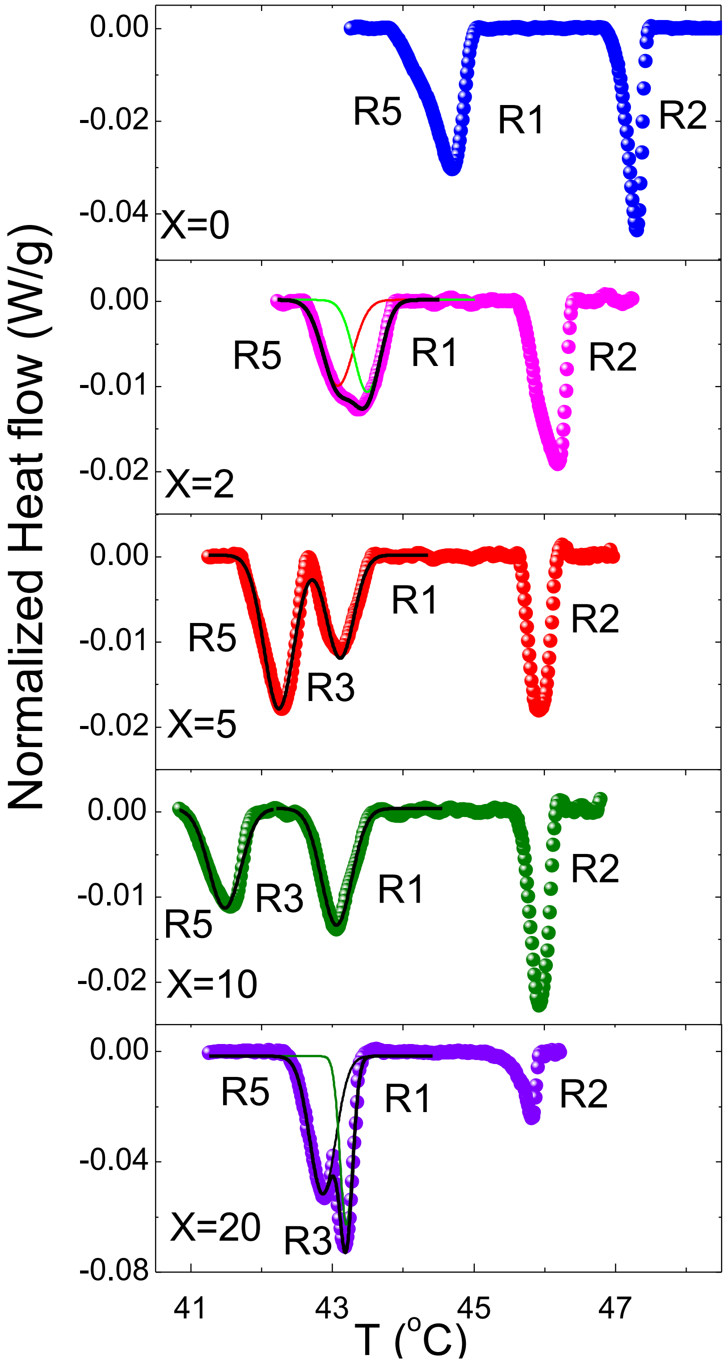

Figure 4.6: Enlarged view of the DSC scans in the temperature region between the Iso and Cr phases, showing the much weaker transitions between the different rotator phases, and more importantly the induction of the R3 phase. The thick lines through the data for the mixtures represent fit to a sum of Gaussian expressions (the individual contributions being shown as thin lines) observed below the R1 phase.

The data over the temperature range between the Iso-R2 transition and crystallization are shown on an expanded scale in Figure 4.6. The thermal profile for the X=2 mixture appears to be qualitatively the same as for pure C24, except that the low temperature peak is significantly broadened. Assigning the highest temperature profile in this diagram to be due to R2-R1 transition (a feature confirmed with the Xray results to be described below), it is noticed that the enthalpy of the transition is reduced by ~ 12% as compared to that for tetracosane. The behaviour of the higher concentration mixtures is drastically different from that of pure C24: A clear additional peak is seen in the temperature range intermediate between the R1 and the lowest temperature rotator phase, which is R5 for all the mixtures studied here. In fact, the low temperature broad thermal signature for X=2 can be resolved into two peaks. For the X=5 and 10 mixtures we observe: (i) the induced peak become better defined and stronger, and (ii) the thermal range between the lowest temperature peak (pertaining to the appearance of R5) and the induced peak increases. These features prompt us to propose the induction of a phase, which we shall see from the Xray data is R3, the rotator phase with triclinic symmetry. It is also interesting to see that the range of the intermediate phase diminishes for X=20, indicating that the induced R3 phase is very sensitive to intermolecular interactions. We shall discuss about this feature in section 4.4.4, and about the enthalpy behaviour in the Theory section.

4.4.2 Xray diffraction

The raw Xray diffraction scans obtained in the low angle region of the different rotator phases of pure C24, and a representative mixture (X = 10), are shown in Figure 4.7 (a) and (b). The strong and sharp multiple peaks seen in the low angle region, with their spacings corresponding to a lamellar structure, characteristic of the rotator phases are retained in the mixture also. However, I_2/I_1, the ratio of the intensities of the second harmonic to the fundamental, decreases upon adding BBOA, as seen in the inset of Figure 4.7(a). The presence and strength of the harmonic peaks is a measure of how well the layers are organized. As we shall see later in this section, a subtle change to the molecular arrangement is responsible for this behaviour.

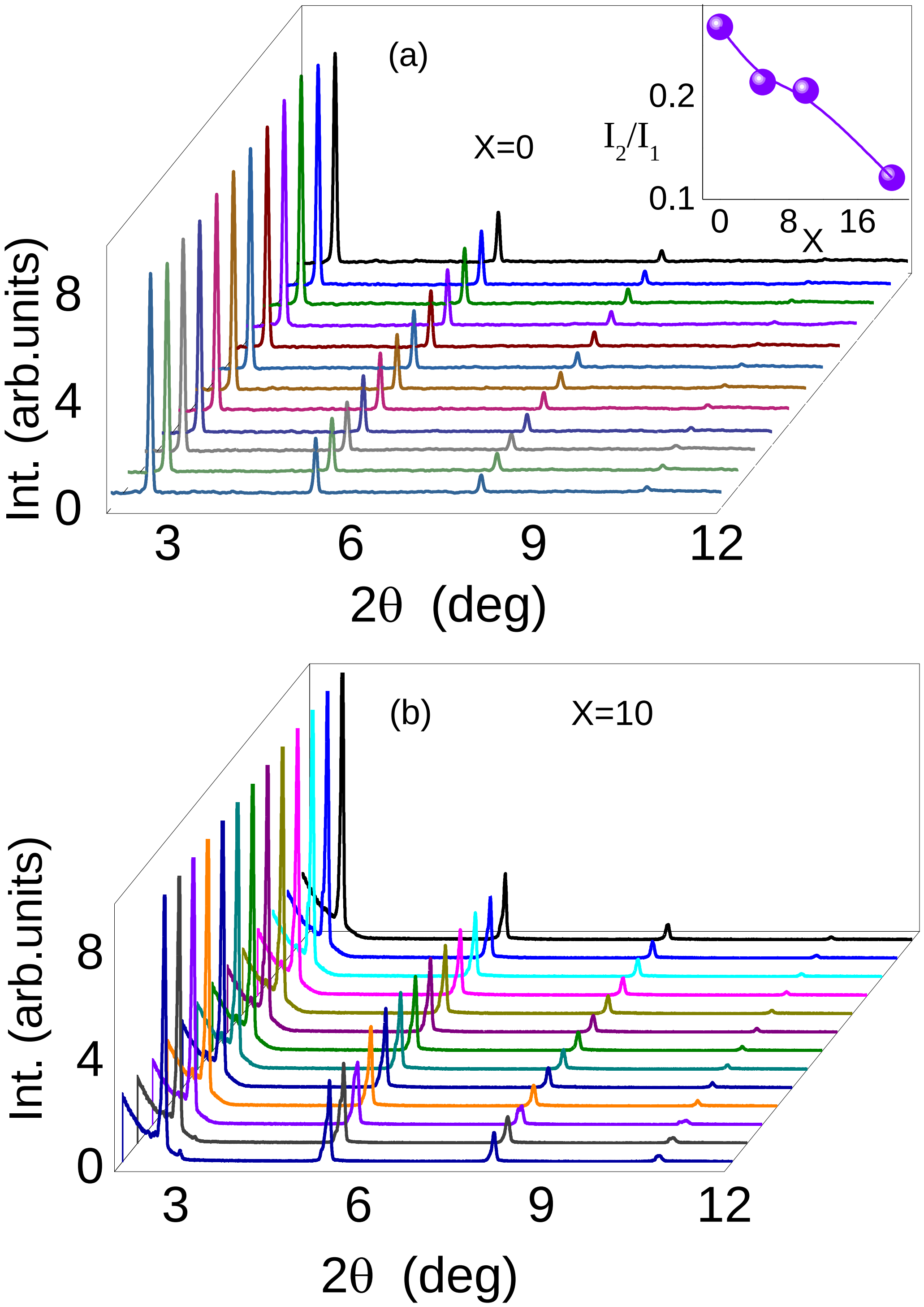

Figure 4.7: Raw Xray diffraction profiles in the low angle region for C24 and the X=10 mixtures, for various temperatures covering the range from the R2 to the R5 phase (the temperature interval is 0.4^{o}C between each scan, decreasing from 48 ^{o}C for the profile shown at the farthest back of the panel). The strong higher harmonics characteristic of the rotator phases of n-alkanes are seen for the mixture showing that the essential phase structure is kept intact even with the addition of the anisometric component BBOA. However, I_2/I_1, the ratio of the intensities for the second harmonic to the fundamental decreasing with increasing X (see inset) shows that the extent of the layering order diminishes with increasing presence of BBOA.

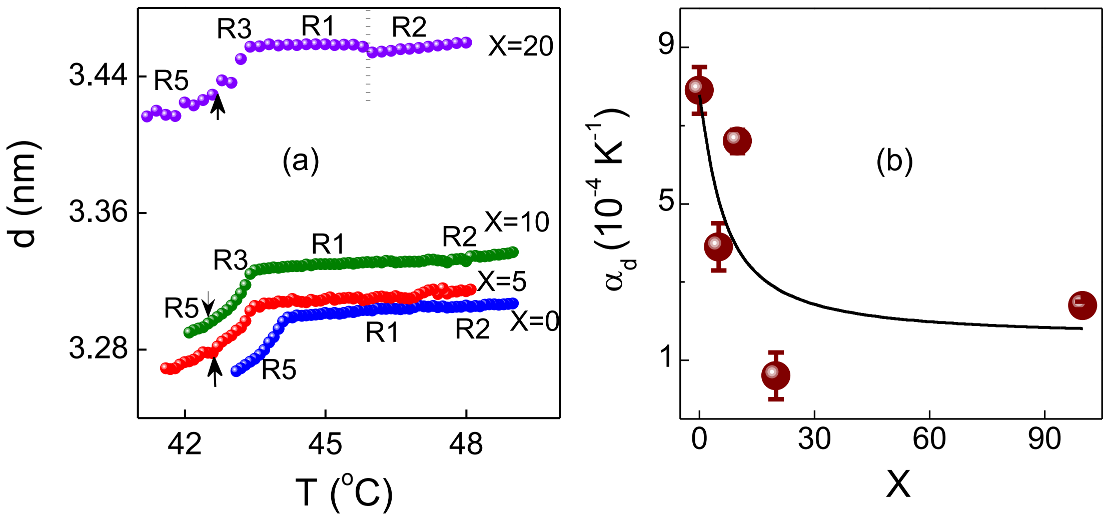

Figure 4.8: (a) Thermal variation of the layer spacing d for the pure C24 and the mixtures in the different rotator phases. While the lower concentration mixtures show a small increase in the layer spacing with respect to that for C24, the X=20 mixture exhibits a drastic increase in d, a feature that can be attributed to the nature of arrangement of the alkane and BBOA molecules. For each set, the abrupt decrease of d at lower temperatures marks the appearance of the tilted phase — R5 for X=0, and the induced phase R3, for the mixtures. The arrows indicate the R3-R5 transition as found from other measurements. The dashed line on the X=20 data indicates that R2-R1 transition with a stronger variation in d than for other materials. (b) Thermal expansion obtained in the R1 phase using the first derivative of d with temperature displaying a drastic reduction with increasing BBOA concentration.

Figure 4.8(a) shows the thermal evolution of the layer spacing for pure C24 and the three mixtures. The first feature seen is that qualitatively the behaviour is the same in the R2, R1 and R5 phases of all the four materials, although the d value in the orthogonal phases increases with increasing X. For example, the mean value of the spacing in the R1 phase has a small increase of ~ 0.3% for X=5, but becomes higher by 1% for X=10. Considering that BBOA has a shorter molecular length than C24 (ℓ_{BBOA} ~ 2.8 nm, ℓ_{C24} ~ 3.3 nm), the increase in ‘d’ upon adding BBOA is surprising, and cannot be explained from a simple linear variation between those for the two pure compounds. However, such a dilatation of the smectic layer upon addition of a small concentration of an alkane to a LC has been reported in a few cases [10, 18]. Found in systems which have a photoisomerizable component also [19, 20], this feature has been attributed to a phenomenon referred to as *nanophase segregation* [10, 21, 22].

In some of these cases [10, 18, 21], the extent of increase is very large (>10%) and is attributed to the incompatibility between the anisometric structure of the liquid crystal and the non-anisometric one of the alkane leading to a segregation of the two kinds of molecules with the minority alkane molecules moving out of the host layers to occupy a region between two neighbouring layers (see Figure 4.9(a)).

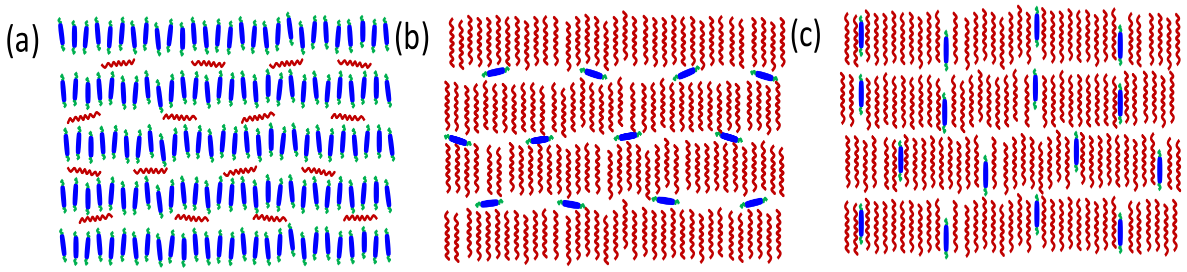

Figure 4.9: Schematic illustration of the possible arrangements of the alkane (red wiggles) and BBOA (blue entities) molecules exhibiting nanophase segregation of the minority component for the (a) LC-rich and (b) alkane-rich cases. The scenario when the system prefers a roughening of the layers instead of the nanophase segregation is shown in (c).

The minimum value of increase in the layer thickness (Δd) in such nanosegregation situations should correspond to the diameter of the minority component molecules which are expelled from the layers and occupy the interfacial regions. This expectation is indeed valid in the cases where the alkane is the minority component, unlike in the present case, in which the LC molecules (of BBOA) are the minority ones. As seen from Figure 4.8, Δd, instead of being in the range of 0.3 to 0.4 nm, is actually an order of magnitude smaller up to X=10. The molecular simulation results to understand the photoinduced enhancement of layer spacing by Lansac et al [22] invoked the argument that not all the minority concentration molecules get phase segregated, and thus their thermal distribution would result in a smaller Δd. Owing to the difference in the shape and dimension of the *trans* and *cis* conformers of the photoactive molecules, this explanation may work for the photoinduced case. However, it is difficult to imagine its application to cases such as the present one, wherein the presence of a second component cannot be expected to alter the conformers. It should also be pointed out that in the cases where such a demixing is observed, a substantial difference exists in at least one molecular factor between the two constituents. The difference could be in the polarity (strongly polar LC, non-polar alkane, Ref. 23) or the shape of the molecules (bent shaped LC and nearly linear alkane, Ref. 10, or rod-like LC and bent *cis* isomer as in Ref. 19, 20 and 22).The present system hardly has such differences between its two constituents. Both C24 and BBOA are linear molecules and with negligibly small polarity. Thus, in the present system with similar features of the constituents demixing is not a favoured situation.

A second possibility that was suggested [19] for the photodriven case, namely, dimer formation due to the large dipole moment of the cis isomers is also not applicable here. Hence one can conclude that although the presence of an anisometric molecule (BBOA) does perturb the formation of rotator phases, these plastic structures are more robust compared to the liquid crystalline phases to permit the nanophase segregation. The robustness could arise owing to the strong orientational ordering (as well as the 3-dimensional positional order) of the alkane system which does not allow the LC molecule to dictate terms for drastic structural changes. However, in the situation where the LC molecules are in majority and the alkanes are the minority constituents, the already liquid like arrangement of the LC phases, provides much leeway for the alkane to tend towards its natural (in a fluid like environment) random coil configuration, thus providing a larger perturbation to the environment. In view of these, the small increase in the spacing must be due to some other factor. Instead of a nanophase segregation wherein the minority LC molecules are driven between the layers of alkanes (Figure 4.9(b)), we would like to propose a possibility (Figure 4.9(c)) in which the positive vertical disorder in the stacking of the alkane molecules, known even in the pure alkanes [24], is responsible for the observed behaviour: The minority LC molecules stick out of the layer plane. Enhancement of such a disorder is possible by the addition of BBOA type molecules possessing anisometric segments, which are absent in the alkane molecules. The positive vertical disorder is like a dynamic excursion of the molecules between layers, and thus should roughen the layer interface. As a consequence, the higher harmonic reflections from the layer should weaken, i.e., the intensity ratio of I_2/I_1 should diminish. Indeed a decrease of about 55 % of this ratio was observed for the X= 10 mixture in comparison to the value for pure C24 (see inset of Figure 4.7(a)). For much higher concentrations of BBOA, layer roughening may cost more energy and also destabilize the layer structure itself, and therefore the intercalation of the LC molecules between the layers (nanophase segregation) may become favourable. This is indicated by the much larger (5%) Δd value for the X=20 mixture. A similar feature is seen for the X=90 mixture, i.e., on the BBOA rich side (Δd=0.14nm), confirming our argument that the LC-rich materials tend to have the nanophase segregation as suggested in Figure 4.9(a). For the X=20 mixture, unlike in the case of lower concentration mixtures, the transition enthalpy for the transition to the true crystalline phase is higher than for the lowest temperature rotator transition. This could also be an indication of a changed scenario of molecular arrangement in the X=20 mixture.

4.4.3 Thermal expansion

The temperature dependence of the layer thickness can be used to calculate the thermal expansion α_d along the layer normal using $\alpha_\mathrm{d} = \frac{1}{\mathrm{d}}\frac{d(\mathrm{d})}{dT}$. From a least-squares fit of the data in the R1 phase, α_d is found to be 6.5 x 10^{-4} K^{-1} for pure C24, a value comparable to that reported [25] for the lower homologue, C23. α_d decreases by about an order of magnitude for the X=20 mixture (See Figure 4.8(b)). The concentration dependence of α_d does suggest that the value reaches a minimum around this composition, which could be related to competition between the two components to dictate the overall behaviour. It may be recalled here that the fluid layered phases of liquid crystals often exhibit a negative thermal expansion that is attributed to the stretching of the terminal alkyl chains. Owing to the positionally ordered situation of rotator phases (or the crystal B phase of BBOA), such stretching becomes difficult, if not already complete. However, the bulky middle region of the BBOA molecules could provide additional free volume which may favour disorders like chain-end melting, i.e., presence of finite number of gauche bonds. This type of disorder would then lower the positive thermal expansion of the system with entirely stretched alkane molecules. The slight reduction in the ordering of the medium is also reflected in the transition enthalpy of the Iso-R2 transformation: The X=20 mixture have five times smaller value as that of the pure C24 compound (see Figures 4.4 and 4.5b).

4.4.4 Induction of a phase

The transition from the R2 to the R1 phase is marked by a small change in the layer spacing with the change becoming clearer for higher values of X. In fact, the wide angle diffraction profiles provide a better evidence for the appearance of the R1 phase with the single peak of the hexagonal R2 phase splitting into two, characteristic of the orthorhombic structure of the R1 phase. For pure C24, the onset of a marked decrease in the layer spacing (Figure 4.8a) associated with the appearance of the R5 phase, does not change the wide angle profile which continues to have the two-peak signature right till crystallization of the sample. The behaviour of the three mixtures, X= 5, 10 and 20, is different in this region. Just below the R1 phase, d exhibits a decrease and the twin-peak profile changes to a three-peak one (see Figure 4.10a). Further lowering of temperature results in the profile reverting to a two-peak one (in the R5 phase), before multiple peaks, indicating solidification of the sample, appear. Thus a phase that also has characteristics of a rotator phase, but different from R2, R1 or R5, is induced between the R1 and R5 phases. To rule out domain-formation to be causing the presence of a third peak, 2-D diffraction images were collected at selected temperatures over the entire rotator phase range. Figures 4.10 (b) and (c) present intensity vs. Bragg angle profiles (realized from azimuthal averaging of the patterns) along with the images in the relevant wide angle region, obtained using the image plate apparatus confirmed with the pattern seen in the one-dimensional scans from the PANalytical system (Figure 4.10a).

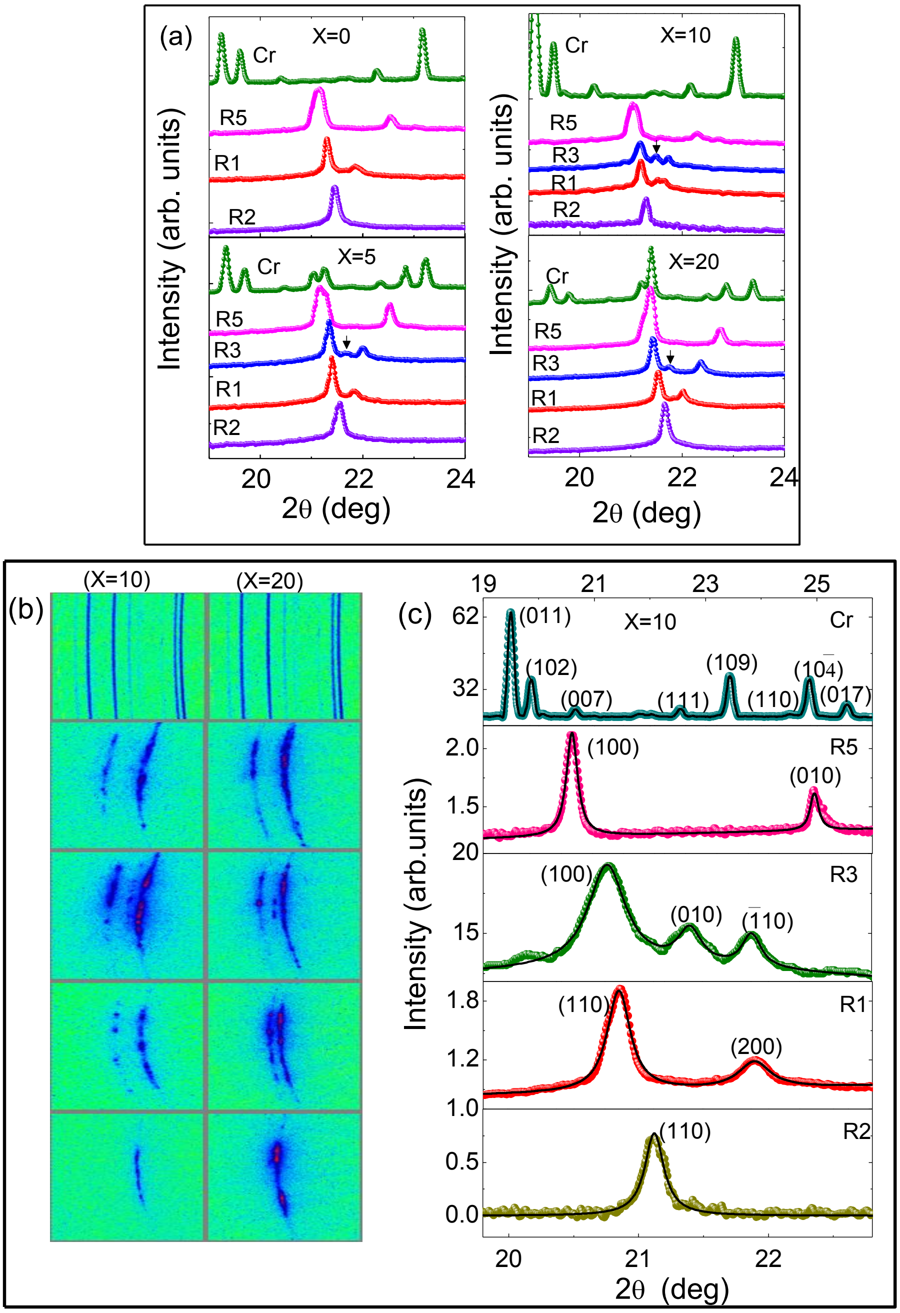

Figure 4.10: (a) Wide angle diffraction patterns obtained with the PANalytical apparatus in the different rotator phases, and the crystalline phase of pure C24 and the three mixtures. The single peak in the R2 phase, splits into two in the orthorhombic R1 phase. Interestingly, an additional peak appears at a slightly lower temperature, before the two peak profile is restored in the R5 phase. The region with 3 peaks (indicated by an arrow) is identified as the R3 phase. (b) Such a 1-2-3-2 peak profile with temperature becomes evident in the 2-d patterns from the image plate for the X=10 and 20 mixtures. (c) For the representative mixture X=10, the azimuthal-averaged intensity profiles are shown with the lines depicting the fitting of the data to a sum of Lorentzian expressions.

To identify the nature of this induced phase, consider the structural features mentioned above: (i) the molecules are tilted within the layer, as indicated by substantial lowering of d in comparison with the values in the upright R1 phase, and (ii) the wide angle region exhibits three strong reflections. From the literature, it is seen that the latter feature is unique for the R3 phase with its triclinic structure [24, 26, 27], which we assign to the induced phase (In the case of 1-alcohols another phase RV', having essentially the same features has been identified). (iii) The indexing of the three reflections with (100), (010) and ($\bar{1}$10) as the Miller indices is in agreement with the assignment given by Doucet et al., [28].

It may be noted that according to Sirota [24] an important difference between R3 and R5 phases is ξ, the magnitude of distortion (with respect to the hexagonal lattice); the distortion being quite small in the R3 phase. Figure 4.11 shows the spacings D of the wide angle reflections as a function of temperature, from which ξ is calculated (using the standard expression as given in Ref. 24) and is shown in Figure 4.12(a). The distortion shows a monotonic increase from the R2 –R1 transition point over the entire rotator phase region for the pure alkane as well as the mixtures, thus being high in the R3 phase of the currently studied system. However, as per earlier studies, the R3 phase with $\xi \sim 0$ always occurs above the R2 phase. In the present case, however, the R3 phase appears between the R1 and R5 phases, both having large distortion. Therefore the system may find it difficult to get rid of the large distortion, and prefer to retain it in the R3 phase. A further point is that in pure alkanes, the R3 phase is seen only when the number of carbon atoms (C) in the chain is >26, the longer chain facilitating the creation of more gauche linkages at the termini of the molecule. The host in the present study has, however C=24. Thus a possible reason for the appearance of the R3 phase here could be that the addition of BBOA, and the consequent layer roughening (discussed above) creates additional gauche bonds at the terminal positions of the alkane molecules, perhaps creating a favourable situation for the appearance of the R3 phase. Also to be recalled is the fact that the enthalpy associated with both (R1-R3 and R3-R5) transitions is quite large, unlike very weak thermal signatures for R3-R4 transition involving the R3 phase, reported in the literature [25].

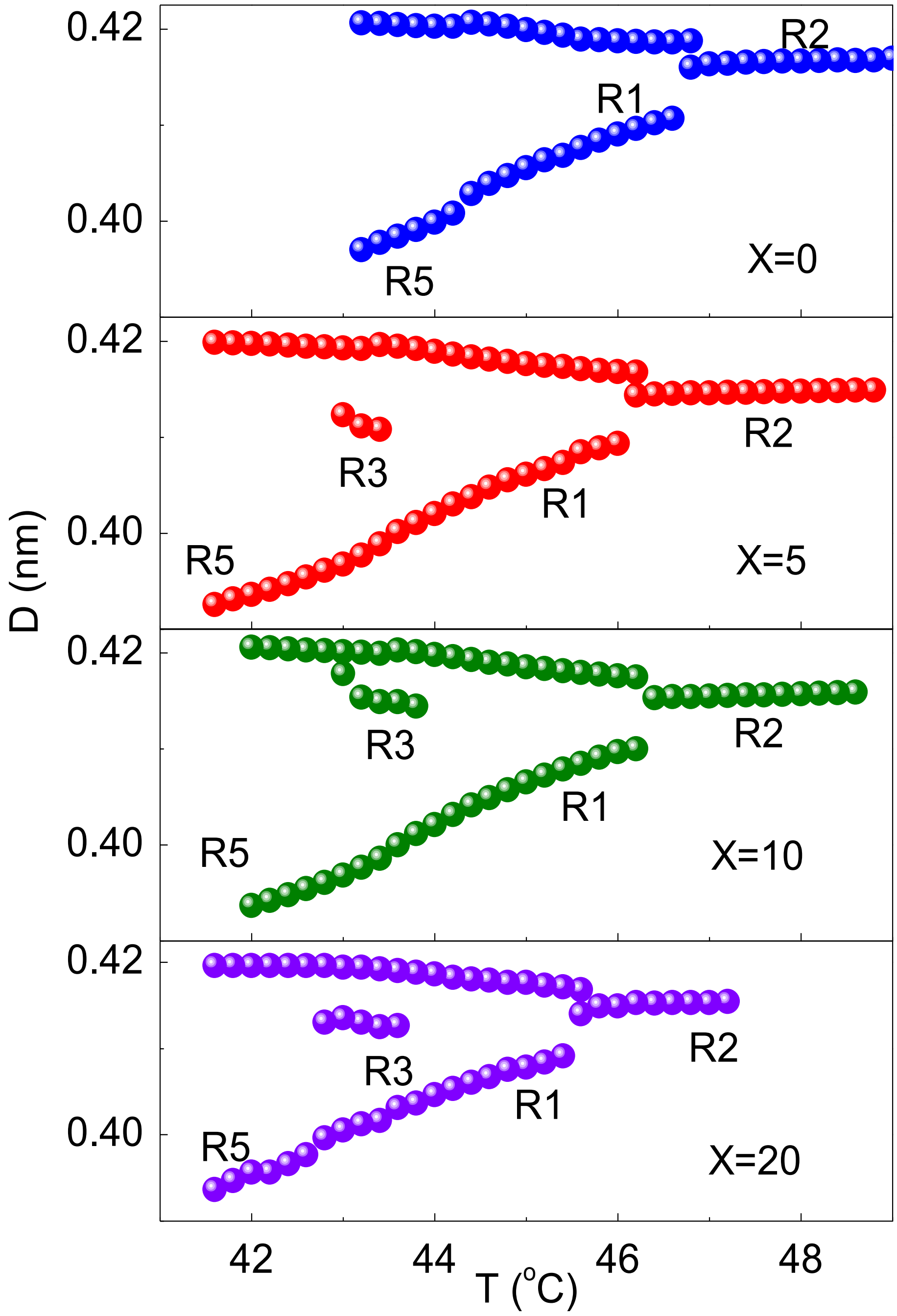

Figure 4.11: Thermal variation of the intermolecular spacing D in the plane of the layers, obtained from the wide-angle scans for C24 and the mixtures, indicating marked changes across the R2-R1, R1-R3 and R3-R5 transitions.

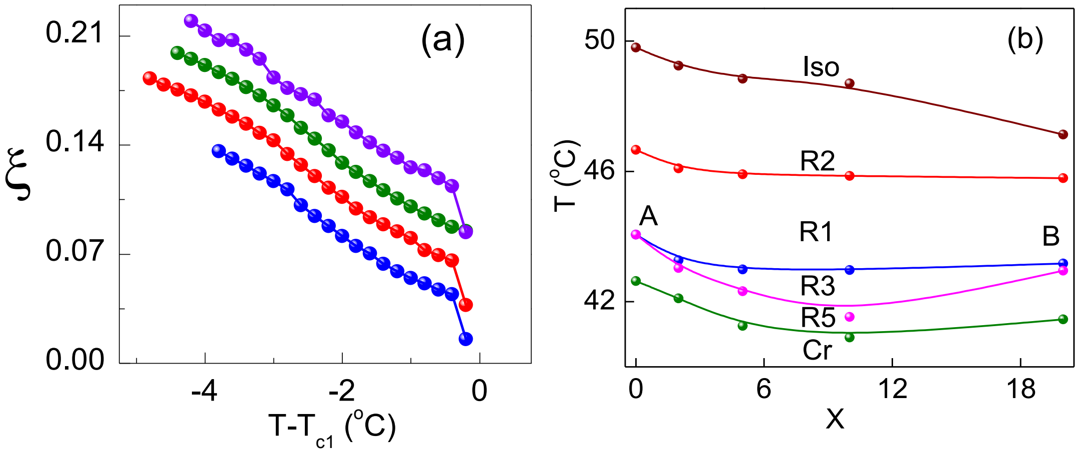

Figure 4.12: (a) The extracted lattice distortion ξ as a function of reduced temperature, with T_{c1} being the R2-R1 transition temperature. The data sets are given an arbitrary shift for the sake of presentation, and represent the materials X= 0, 5, 10 and 20 from bottom to top. (b) C24-BBOA partial phase diagram in the temperature-concentration (X indicates wt% of BBOA) plane showing the interesting feature that the R3 phase gets induced for a small concentration of BBOA and is bounded for a higher concentration. This results in two three-phase points, in the vicinity of the concentrations marked A and B.

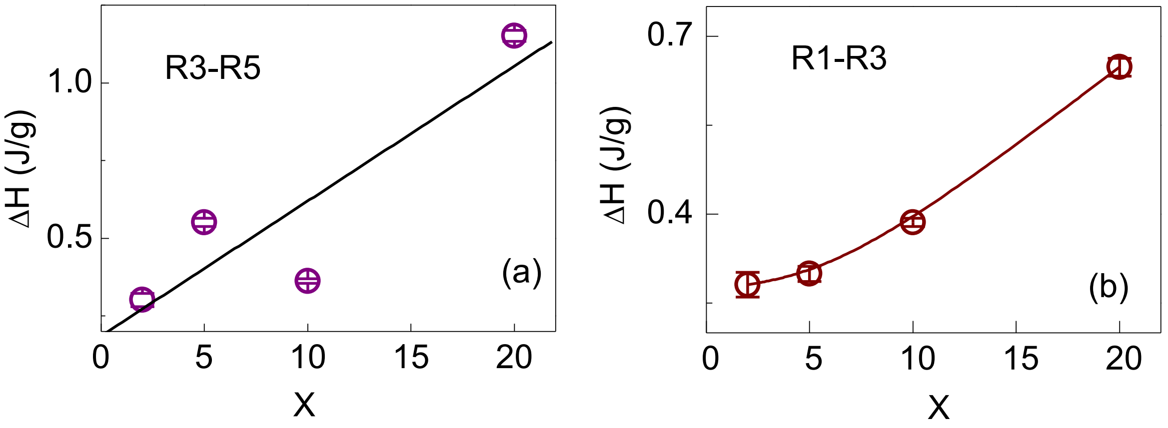

Figure 4.13: Concentration dependence of the transition enthalpy ΔH for the (a) R3-R5 and (b) R1-R3 transitions. The data suggest that on approaching the three-phase meeting at low concentrations (Point A in Figure 4.12(b)) ΔH goes to very small values for both the transitions. The lines are merely empirical fits.

This could again be due to the difference in the magnitude of distortion in the R3 phase observed here and those in the literature. A point that must be mentioned here is that the absolute magnitude of the distortion ξ increases by about 8% between X=0 and X=20. Whether such an increase in ξ (i) is the result of the presence of the anisometric component, and (ii) is responsible for the induction of the R3 phase, are features which should be explored in the future from experimental as well as theoretical aspects. Taking into account all these features we present in Figure 4.12(b) the partial phase diagram for the binary system of C24-BBOA, the high point of which is that the R3 phase, which gets induced on adding the anisometric compound is bounded on the lower as well as the higher concentration side, resulting in two R1-R3-R5 three-phase meetings points. Further, the R3 phase is below the R1 phase, unlike what the literature suggests. Whether the anisometry of the second compound is indeed responsible for the observed inverted sequence of the R3 phase, i.e., occurring below the R1 phase, is a feature that needs to be confirmed from experiments with other similar anisometric molecules. The reason for another feature, namely, with increasing concentration of BBOA, the transition temperature for the R1-R3 transition hardly changes while that for the R3-R5 transformation varies significantly, is also a topic for future investigations.

4.4.5 Theory

In this section, the Landau theory of phase transition, which has been quite successful [29, 30] in explaining many features of the rotator phases in alkanes, is applied to analyze the R3-R5 and R1-R3 transitions. Before doing so let us look at the concentration dependence of the transition enthalpy ΔH for these two transformations (see Figure 4.13 (a) and (b)). For both cases, ΔH decreases towards zero on approaching the lower concentration three-phase meeting point (i.e., as X decreases). If the value does indeed become zero in the vicinity of the point then it would be a bicritical point (BP) whereas if one of them remains finite, it would be a critical end point (CEP). Because ΔH increases with X as the higher three-phase point is approached, it would be a simple triple point. For the BP case since both transitions have to be second order, are explored in the following theoretical summary, conditions under which the second order nature can be observed. It may be recalled here that as per the only case (for C27 alkane) in the literature, no thermal signature was obtained for the R3-R5 transition, but Xray studies suggest it to be a continuous transition [25].

In the theoretical analysis, for simplicity the interaction between the stacking layers in the rotator phases is neglected so that the problem becomes two dimensional. As mentioned earlier, the R5 phase has NNN tilt and finite distortion, while the R3 phase differs from the R5 phase by the distortion azimuth and the tilt azimuth. Explicitly, we consider ordering of the 2D hexagonal crystal. Thus the tilt angle and the distortion are described by two-component order parameters. The tilt components can be expressed through a polar tilt angle θ and the tilt azimuth δ. The distortion components are expressed through the distortion amplitude ξ and the azimuth 2ω. The multiplier 2 comes from the fact that the distortion is a symmetric traceless tensor. Both the azimuths δ and ω are non-zero in the R3 phase and zero in the R5 phase. Thus two order parameters ξ and θ are employed to describe the R3 – R5 and R1 – R3 transitions. Then the Landau free energy should be invariant under the transformation $\delta \rightarrow \delta + \pi/3$ and $\omega \rightarrow \omega + \pi/3$.

Expanding the total free energy F in terms of the above mentioned order parameters yields,

$$
\begin{aligned}
F = F_o &+ \frac{1}{2}\alpha\theta^2 + \frac{1}{4}\beta\theta^4 - \frac{1}{6}\gamma\theta^6\cos 6\delta - \frac{1}{12}\eta\theta^{12}\cos 12\delta + \frac{1}{2}a\xi^2 - \frac{1}{3}b\xi^3\cos 6\omega + \frac{1}{4}c\xi^4 \\
&- \frac{1}{6}d\xi^6\cos 12\omega - J\theta^2\xi\cos 2(\delta-\omega) \qquad (4.1)
\end{aligned}
$$

Here F_0 is the nonsingular part of the free energy. The coefficients *a* and α are temperature and concentration dependent. The other coefficients are assumed to be temperature independent but functions of concentration. J is the coupling constant. The second and third terms on the right hand side of with Eq. (4.1) describe the tilt angle variation. The terms corresponding to the coefficients γ and η determine the tilt azimuth δ. For $\eta = 0$ and $\gamma > 0$, the only minimum of *F* is at $\delta = n\pi/3$ (n being an integer) the tilt occurs in NN direction. For $\gamma <$

0, the minimum is achieved at $\delta = \pi/6 + n\pi/3$ i.e. for tilt towards NNN direction. Since in the R5 phase tilt occurs towards NNN direction, it was assumed $\beta > 0$ and $\gamma < 0$. When γ is small, then the next higher order term corresponding to the coefficient η is nonzero and important. Then the transition from NN to NNN tilt takes place, with a possible R3 phase appearing in between. The terms corresponding to the coefficients b and d determine the distortion azimuth ω. The minimum free energy corresponding to the coefficient b occurs at $\omega = 0$ for b > 0 and d = 0 and at $\omega = \pi/2$ for b < 0 and d = 0. If b is small then the next higher order term corresponding to the coefficient d should be taken into account. According to the earlier experimental observations, $\omega = 0$ and $\delta = 0$ for R5 phase. However, for the R3 phase $\omega \neq 0$ and $\delta \neq 0$. The $\theta\xi$ coupling term gives $\omega = \delta$ for J > 0 and $\omega = \delta + \pi/2$ for J < 0. Since in the R5 phase $\delta = \omega = 0$, J is taken > 0 for the description of the R3 – R5 transition. The higher order terms like $\xi^2\theta^2\cos(2\delta + 4\omega)$ and $\xi\theta^4\cos(4\delta + 2\omega)$ can be added, when necessary.

The R3 phase has an intermediate tilt where the tilt azimuth δ varies from 0^o to 30^o. The case in the literature is considered wherein the distortion ξ is relatively small in the R3 phase, and thus unique determination of δ and ω is difficult. Hence for the R3 phase, we assume $\delta = \omega \neq 0$. The distortion induced by tilt is therefore taken to be $\xi \approx \theta^2$. As already pointed out the lowest-order angle-dependent term for the $\xi\theta$ coupling gives $\omega = \delta$ for J > 0. Therefore J is constant and positive values of η and γ favour the phase below R1 to be R3 than R5, as found in the current experiments. On the other hand, positive η and negative γ favours the R5 phase. For $\alpha > 0$, $\eta = 0$ and $\gamma = 0$ describes the R1 phase. In order of increasing concentration of the anisometric component (in the vicinity of the lower three-phase point), the relevant stable solutions of Eq. (4.1) are as follows (i) R2 phase: $\theta = 0$, $\xi = 0$; (ii) R1 phase: $\theta = 0$, $\xi \neq 0$. (iii) R3 phase: $\theta \neq 0$, $\xi \neq 0$ with tilt and distortion azimuths varying from 0 to 30^o. Here obviously distortion azimuth is directed along the tilt azimuth, and (iv) R5 phase: $\theta \neq 0$, $\xi \neq 0$.

R3 – R5 transition

As already mentioned ξ depends on the concentration X. Therefore the coefficient b can be expected to be a function of X, thus determining the order of the transition; (in a similar fashion if γ depends on X, it can govern the behaviour of the R1-R3 transition). The second order character of the R3 – R5 transition can easily be explained by taking into account the term $\sim -d\xi^6\cos 12\omega$ into the free energy expansion (Eq. 4.1). Assuming d to be positive, then for $b = -2d\xi^3$ i.e. for $b < 0$, the only minimum is at $\omega = 0^o$. Then the system is in the R5 phase. When $b = 2d\xi^3$ i.e. $b > 0$, the minimum at $\omega = 0^o$ passes through 0^o to 30^o, giving rise to a second order transition from the R3 to the R5 phase. As b increases from $-2d\xi^3$ to $2d\xi^3$, the minimum in the R3 phase shifts from 0^o to 30^o. Again assuming, η to be positive, then for $\gamma = -2\eta\theta^6$ i.e. for $\gamma < 0$, the only minimum is at $\delta = 0^o$, with the system in the R5 phase. When $\gamma = 2\eta\theta^6$ i.e. $\gamma > 0$, the minimum at $\delta = 0^o$ passes through 0^o to 30^o, leading again to a second order R3-R5 transition, but now at $\gamma = 2\eta\theta^6$. As γ increases from $-2\eta\theta^6$ to $2\eta\theta^6$, the minimum in the R3 phase shifts from 0^o to 30^o.

R1 – R3 transition

By substituting $\omega = \delta$ in Eq. (4.1), the free energy near the R1 – R3 transition reads

$$F = F_I(\xi) + \frac{1}{2}\alpha\theta^2 + \frac{1}{4}(\beta - 4J)\theta^4 - \frac{1}{6}\gamma\theta^6\cos 6\delta - \frac{1}{12}\eta\theta^{12}\cos 12\delta \qquad (4.2)$$

where $F_I(\xi)$ is the free energy of the R1 phase. Minimization of Eq. (4.2) over δ gives

$$\delta = \frac{1}{6}\cos^{-1}\left(\frac{-\gamma}{2\eta\theta^6}\right) \qquad (4.3)$$

Suppose that η is fixed at a negative value and γ decreases from positive to negative value.

When $\gamma = 2\eta\theta^6$ i.e. for $\gamma > 0$, the only minimum is at $\delta = 0^o$. Then the system is in the R1 phase. When $\gamma = -2\eta\theta^6$ i.e. for $\gamma < 0$, the minimum at $\delta = 0^o$ passes through 0^o to 30^o. Since in the R3 phase, δ changes through 0 to 30^o, we have the R3 phase for $\gamma < 0$, with a second order R1-R3 transition at $\gamma = -2\eta\theta^6$. As γ decreases from $2\eta\theta^6$ to $-2\eta\theta^6$, the minimum in the R3 phase shifts from 0 to 30^o. The variation of the tilt azimuth δ with temperature in the R3 phase can be obtained by the expansion of $\cos 6\delta$ and $\cos 12\delta$ over the powers of δ.

Our experiments also suggest a second order tilting transition from the R1 to the R3 phase. Near this transition the free energy reads

$$F = F_I(\xi) + \frac{1}{2}a_1\xi^2 + \frac{1}{2}\alpha\theta^2 + \frac{1}{4}\beta\theta^4 - J\theta^2\xi\cos 2(\delta - \omega) \qquad (4.4)$$

Here the tilt causes an induced distortion $\xi \sim \theta^2$. Then renormalized free energy reads

$$F = F_\xi + \frac{1}{2}\alpha\theta^2 + \frac{1}{4}\beta_1\theta^4 \qquad (4.5)$$

with $\beta_1 = \beta - 2J^2/a_1$ and $\alpha = \alpha_0 (T - T_C)$. Hence the tilt $\theta = 0$ for $T > T_C$ and $\theta \neq 0$ for $T < T_C$ resulting in a second order tilting transition between R1 and R3 phases.

4.5 Summary

Calorimetric and Xray diffraction measurements on a binary system composed of n-tetracosane exhibiting rotator phases, and an anisometric liquid crystalline compound showing, in addition to the fluid LC phases, a plastic phase, bring out a novel feature, namely the occurrence of an induced rotator phase in an inverted sequence. The features seen in the diffraction measurements suggest the induced phase to be the one argued to have a triclinic symmetry. The possibility that the phase induction could be owing to the creation of additional gauche bonds at the terminals of the alkane molecule, has been proposed. The fact that an anisometric molecule can induce a rotator phase with high disorder perhaps indicates that this route can be employed to increase the richness of features seen in alkane systems, e.g., observation of the condis phase [31-34]. The richness, however, can be augmented by a proper selection of a wide variety of LC compounds available, to bring different dimensionalities such as dipolar interaction, steric interactions, hydrogen bonding, etc. We have also provided Landau theory arguments for the experimentally observed possibility that the R1-R3 and R3-R5 transitions could be second order in the vicinity of a three-phase meeting point.

4.6 References

1. P.S.Pershan, G.Aeppli, J.D.Litster and R.J.Birgeneau, *Mol. Cryst. Liq. Cryst.,* **67**, 205 (1981).
2. L. Bata and A. Buka, *Mol.Cryst.Liq.Cryst.,* **63**, 307 (1981).
3. L. Benguigui, *Phys. Rev A* **28**, 1852 (1983).
4. C. Nagabhushan, Geetha.G.Nair, B.R. Rathna, R. Shashidhar and J.W. Goodby, *Liq. Cryst.,* **3**, 175 (1988).
5. K.L. Sandhya, Geetha G. Nair, S. Krishna Prasad and Anjuli Khandelwal, *Liq. cryst.,* **28**, 1847 (2001).
6. S. Chandrasekhar, B.K. Sadashiva, K.A. Suresh, N. V. Madhusudana, S. Kumar, R. Shashidhar and G.Venkatesh, *J. de Physique C3*, **40**, 120 (1979).
7. T.P. Rieker, *Liq. Cryst*. **19**, 497 (1995).
8. K. Denolf, G. Cordoyiannis, C. Glorienx and J. Thoen, *Phys. Rev. E*, **76**, 051702 (2007).
9. H. Sawade, I.D. Olenik, D. Kruerke, and G. Heppke, *Mol. Cryst. Liq. Cryst*. **367**, 529 (2001).
10. M.Y.M. Huang, A.M. Pedreira, O.G. Martins, A.M. Figueiredo Neto and A. Jakli. *Phys. Rev. E.,* **66**, 031708 (2002).
11. K.P. Sigdel and G.S. Iannacchione, *J. Chem. Phys.* **133**, 174501 (2010).
12. S. Krishna Prasad, D.S. Shankar Rao, S. Sridevi, C.V. Lobo, B.R. Ratna, J. Naciri and R. Shashidhar, *Phys. Rev. Lett.,* **102**, 147802 (2009).
13. M. Wojdyr, Fityk: a general-purpose peak fitting program. *J. Appl. Cryst.,* **43**, 1126 (2010).

14. S.K. Kundu, S. Okudaira, M. Kosuge, N. Shinyashiki and S. Yagihara, *J. Phys. Chem. B,* **113**, 11109 (2009).
15. K.P. Sigdel and G. Iannacchione, *Phys. Rev. E,* **82**, 051702 (2010).
16. A. Jákli, W. Cao, Y. Huang, C.K. Lee and L.C. Chien, *Liq. Cryst.,* **28**, 1279 (2001).
17. D. Kruerke, P. Rudquist, S.T. Lagerwall, H. Sawade and G. Heppke, *Ferroelectrics*, **243**, 207 (2000).
18. H. Heuer, H. Kneppe, and F. Schneider, *Ber. Bunsen. Phys. Chem.,* **93**, 923 (1989).
19. W.R. Folks, S. Keast, T.A. Krentzel B. Zalar, B.H Zeng, Yu.A. Reznikov, M. Neubert, S. Kumar, D. Finotello and O.D. Lavrentovich, *Mol.Cryst.Liq.Cryst*, **320**, 77 (1998).
20. S.K Prasad, and G.G Nair, *Adv. Mater.,* **13**, 40 (2001).
21. C.A. Guymon, E.N. Hoggan, N.A. Clark, T.P. Rieker, D.M. Walba, and C.N. Bowman, *Science,* **275**, 57 (1997).
22. Y. Lansac, M.A. Glaser, N.A. Clark and O.D. Lavrentovich, *Nature*, **398**, 54 (1999).
23. S. Tristram-Nagle, Y. Liu, J. Legleiter and J.F. Nagle, *Bio. Phys. J.* **83**, 3324 (2002).
24. E.B. Sirota, H.E. King, D.M Singer and H.H. Shao, *J. Chem. Phys.*, **98**, 5809 (1993).
25. E.B. Sirota and D.M. Singer, *J. Chem. Phys.,* **101**, 10873 (1994).
26. V.M. Kaganer, I.R. Peterson, R.M. Kenn, M.C. Shih, M. Durbin and P. Dutta, *J. Chem. Phys*., **102**, 9412 (1995).
27. E.B. Sirota, *Langmuir*, **13**, 3849 (1997).
28. J. Doucet, I. Denicola, A.F. Craievich and C. Germain, *J. Chem. Phys.,* **80**, 1647 (1984).
29. P.K. Mukherjee and M. Deutsch, *Phys. Rev. B,* **60**, 3154 (**1999**).
30. P.K. Mukherjee, *J. Chem. Phys*., **129**, 021101 (2008); *J. Phys. Chem. B,* **114,** 5700 (2010); *J. Chem. Phys*., **134**, 224502 (2011); *J. Phys. Chem. B,* **116**, 1517 (2012).
31. F.J.M. Casado, M.R. Riesco, M.I.R. Yelamos, A.S. Arenas and J.A.R. Cheda, *J. Therm Anal Calorim.,* **108**, 399 (2012).
32. H.P. Grossmann and W.R. Pechhold, *Coll. and Polym. Sc.* **264**, 415 (1986).
33. B. Wunderlich, M. Moller, J. Grebowicz and H. Baur, Conformational Motion and Disorder in Low and High Molecular Mass Crystals, Series: *Advances in Polymer Science*, vol. **87**, London: Springer–Verlag (1988).
34. B. Wunderlich, *J. Therm. Anal. Calorim.* **102**, 413 (2010).

Chapter-5

Comparative Studies of the Nano-Composites of Strongly/Weakly Polar Liquid Lrystals Doped with Carbon Nanotubes

Overview

This chapter describes the results of dielectric and conductivity measurements on a composite of carbon nanotubes and a liquid crystal possessing dual frequency switching characteristics. The conductivity increases by two orders of magnitude with respect to that for the host liquid crystal, and achieves negligible temperature dependence. The frequency dependence of the ac conductivity is explained by the extended pair approximation model, although the exponent is slightly higher than generally seen. We demonstrate that the current through the sample can be field-driven between the two anisotropic values (170:1) by simply changing the frequency of the applied voltage, and exhibiting at least a millisecond response. The chapter also presents a comparison in the dielectric and conductivity behaviour when the polarity of the host LC is substantially changed.

The results are published in:

1. S. Krishna Prasad, **M. Vijay Kumar** and C.V. Yelamaggad, Dual frequency conductivity switching in a carbon nanotube/liquid crystal composite, *Carbon*, **59**, 512-517 (2013).

2. **M. Vijay Kumar**, and S. Krishna Prasad, Composites of single walled carbon nanotubes and liquid crystals as switchable conductors, *Nanosystems: Physics, Chemistry, Mathematics,* **4,** 425–429 (2013).

5.1 Introduction

The research and development of nano materials in science and technology have received significant interest in the past decade [1]. From different dimensions carbon nanotubes (CNT) and liquid crystals (LC) have established their own niche world owing to many interesting properties, and a few similarities. Composites of the two materials are being actively investigated for their extraordinary combination of high electrical conductivity of CNTs and fluid, yet anisotropic properties of LCs [2-14]. The main property of LC one wants to exploit in such hybrid systems is their ability to get oriented by surface forces or moderate external fields [3, 9]. The further advantage of LC as a fluid medium would be that the external stimuli need not exert any direct influence on the CNTs at all: the LC molecules cooperatively orient the CNTs. A proper realization of such a feature has the potential to result in devices in which macroscopic properties can be switched between their anisotropic values along, say, parallel to perpendicular direction with respect to an internal reference axis. In fact, reorientation of the nematic director from the equilibrium direction to that dictated by the field, and the concomitant change in the parameters such as electrical conductivity caused by the presence of CNTs, have been well demonstrated [3,9,15]. The drawback in these systems, however, lies in the fact that the return to the equilibrium value, achieved by switching the external field off, is controlled by the viscosity of the medium and thus quite slow. The aim of the present study was to realize CNT/LC composites in which the return to the equilibrium state is also field-driven and thus eliminating the influence of viscosity.

5.2 Brief summary of carbon nanotube

Carbon nanotubes (CNTs) are allotropes of carbon with a cylindrical nanostructure. CNTs are normally produced by the techniques of arc-discharge, chemical vapor deposition, or laser ablation [16-18]. CNTs can have extremely large shape anisotropy: For example, a length-to-diameter ratio of up to 132,000,000:1 has been realized [19], which is significantly larger than for any other material. CNTs are valuable for nanotechnology, electronics, optics and other fields of materials science and technology, owing to certain unusual properties that they exhibit. Their extraordinary thermal conductivity, mechanical and electrical properties, makes them suitable as additives to various structural materials. For instance, nanotubes form a tiny portion of the material(s) in some (primarily carbon fiber) baseball bats, golf clubs, or car parts [20]. Single-walled nanotubes (SWNT) are likely candidates for miniaturizing electronics. SWNTs with diameters of an order of a nanometer can be excellent conductors [21] and thus appropriate for nano-sized wires. An interesting application is the development of the first intermolecular field-effect transistors (FET). The first intermolecular logic gate using SWCNT FETs was made in 2001 [22a]. Super-stretchy lithium-ion battery based on carbon nanotube fiber [22b] and carbon nanotube flow sensors [22c] are other potential devices.

For many applications a uniform alignment of CNTs is essential, and in general the ability of providing nanotubes a predetermined direction is of great importance. Additionally, it is desirable to be able to manipulate this direction, for example, by the application of external fields, such as electric, magnetic, or mechanical. The phenomenon of reorientation when achieved with an electric field, known as the Freedericksz transition [23], is exploited in all common LCD applications. Attempts have been made [3-14] to employ liquid crystals for imposing alignment on dispersed CNTs, and to use the Freedericksz transition for manipulating the alignment direction through elastic interactions with the LC director field. This approach opens the possibility to dynamically and collectively change the orientation direction of ensembles of nanotubes and thus their direction of mechanical and especially electrical anisotropy.

We have carried out studies on a composite system in which the director of the host nematic LC has the property of getting switched between two states by a mere change in the frequency of the applied field. The studies show that for the composite with a small concentration (0.05%) of CNTs the electrical conductivity increases by two orders of magnitude as measured by a very small probing field. The thermal variation of the conductivity points to the composite being above the percolation threshold. The advantage of employing a small concentration is that the dual frequency property of the host LC is hardly affected by the presence of CNTs. The frequency dependent conductivity exhibits behaviour similar to the well known feature in disordered solids and qualitatively agreeing with the expectations of the extended pair approximation model. The most salient feature of the study is the demonstration of the dual frequency switching of the conductivity between its low and high values driven by frequencies of the applied field lying above and below a crossover value.

5.3 Materials

The liquid crystalline host material is 4-pentylphenyl 2-chloro-4-(4-pentylbenzoyloxy) benzoate (PCPBB for short). This compound prepared in our laboratory using the methods reported [24] is weakly polar as seen from the molecular structure shown in Figure 5.1. It exhibits the isotropic-nematic (Iso-N) transition at 121.8^{o}C and the N phase can be supercooled to 0^{o}C; these values are in agreement with those reported [24]. An important feature of this compound, from the viewpoint of present studies, is that it belongs to the class of substances termed as dual frequency materials exhibiting a crossover in the sign of the dielectric anisotropy at a certain frequency; this feature is explained in the following section. For comparative studies, another nematogen, 4-Cyano-4'-pentylbiphenyl (5CB) was employed. The structural formula and the transition temperature for this compound exhibiting a room temperature nematic phase are also shown in figure 5.1. It may be noted that 5CB possesses a CN group along the longitudinal direction. This large dipole (4.2D) imparts a strong polar character to the molecule; hence, we refer to this compound as a strongly polar liquid crystal (SPLC), and PCPBB, which in contrast has a much weaker polar character as the weakly polar liquid crystal (WPLC). The CNTs employed are single-wall carbon nanotubes (SWCNT, Heji, Hongkong) with a nominal purity of >90%, diameter of about 2 nm with a peak length of 500 nm [25] and doped at a low concentration of 0.05wt% in the LC material [9]; it may be mentioned here that the dispersion of CNTs in the liquid crystal was much less satisfactory at higher CNT concentrations.

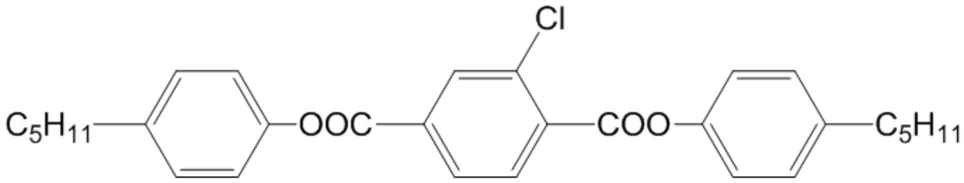

PCPBB Isotropic 121 °C Nematic

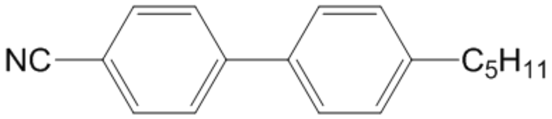

5CB Isotropic 35 °C Nematic

Figure 5.1: The molecular structure and the isotropic-nematic transition temperature for the two LC compounds used as hosts.

Preparation of the composites

The LC-CNT dispersion was prepared using the following procedure. Weighed amounts of the two components contained in a glass vial were heated to 100 °C and subjected to magnetic stirring for ~ 15 hours. Then the mixture was cooled to room temperature and the stirring was continued till the samples were filled into the cell. It may be mentioned here that the employed procedure yielded very uniform dispersion, which was stable over long durations of time. The visibly seen uniformity of the dispersions (shown in Figure 5.2(a)) was further confirmed by observation of a sharp nematic-isotropic (N-Iso) transition having a peak width of 0.8 °C in the differential scanning calorimetric scans. Microphotographs taken of the sample filled in glass cells of a nominal thickness of 10 μm and with a polyimide surface layer to promote planar orientation of the molecules, indicated that the dispersion of the particles hardly changed with time, at least over a period of one week (see figures 5.2(b) and (c)).

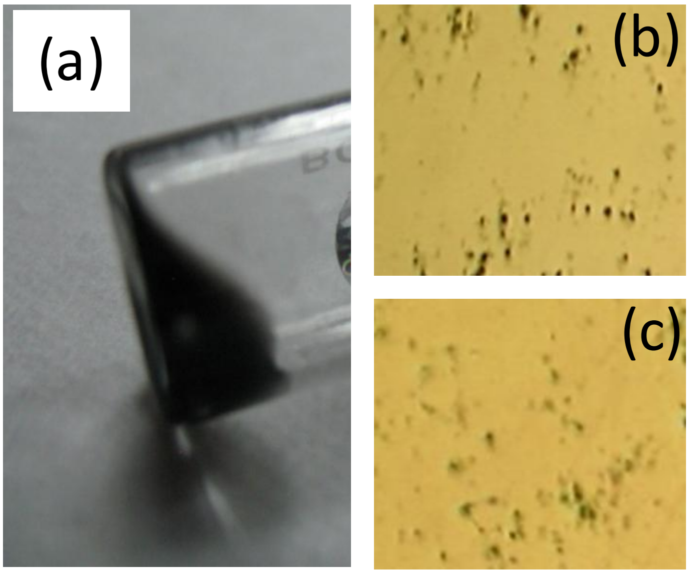

Figure 5.2: (a) Photograph of the CNT/ WPLC composite in a vial, taken two-months after the preparation to illustrate the long-term homogenous stability of the composite. Microphotographs of the field of view under a polarizing optical microscope taken (b) immediately after loading the composite into a glass cell, (c) and after a week.

5.4 Experimental techniques

For the conductivity (σ) and dielectric constant (ε) measurements the samples were sandwiched between two indium tin oxide (ITO) coated glass plates with very low sheet resistance (< 10 Ω); the ITO layer is transparent to light, thus permitting optical observations of the sample alignment. The desired alignment necessary to measure the anisotropic values, $\varepsilon_{||}, \sigma_{||}$ (parallel to the director) and $\varepsilon_{\perp}, \sigma_{\perp}$ (perpendicular to the director), can be achieved by applying the electric or magnetic field and also by surface coating. For the switching experiments a surface coating to promote planar alignment of the molecules was employed. To achieve such an orientation uniformly over the entire active area of the cell, defined by pattern-etching the ITO surface, the glass substrates were first thoroughly cleaned using a standard protocol, followed by a spin-coating of a pre-polymer solution (PI-Kit, E-Merck).

The glass plates were then kept at 300^{o}C to have the on-surface polymerization of the prepolymer. The polymer surface was then rubbed unidirectionally using a velvet cloth roll. The gap between the two glass plates was defined using polyethylene terephthalate (PET, Goodfellow) films of known thickness. The glass plates along with the PET strips were heated to a temperature slightly above the softening temperature of PET (~ 250^{o}C) and pressed evenly to get a cell of uniform thickness. The actual thickness of the fabricated cell was determined by an interferometric technique using a UV-visible spectrometer (Lambda 20, Perkin Elmer). The cell gap was chosen to be quite large – in the range of 25-30 μm – for three different reasons: (i) To facilitate effective control of the orientation molecules by the externally applied magnetic field, (ii) to realize a high enough (> a few MHz) cell relaxation frequency, arising due to the finite sheet resistance of the ITO plates, (iii) and also to avoid any possibility, however remote, of electrical shorting of the cell by the reorienting CNTs of 500 nm length. The ε and σ measurements were done using an Impedance Analyzer (HP4194A) with a small probing field of ~ 16mV/μm; the experimental setup is shown in figure 5.3. For the dual frequency conductivity-switching studies the glass plates were surface treated to achieve planar orientation of the molecules.

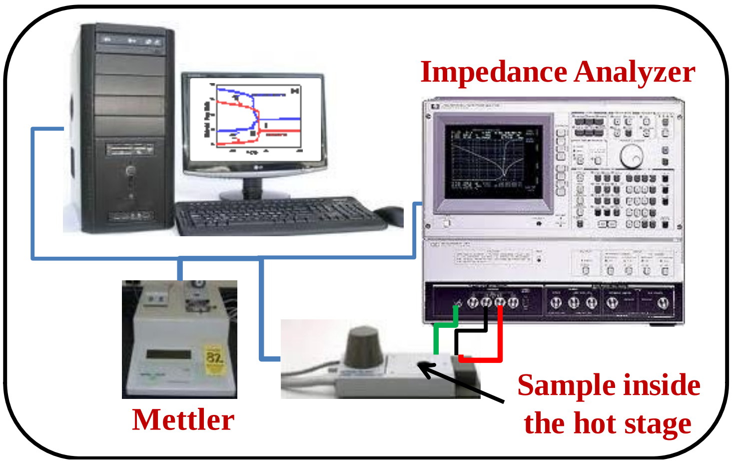

Figure 5.3: Schematic diagram of the apparatus used for the dielectric/conductivity experiments.

5.5 Results and Discussion

PART A: Dual frequency switching system

5.5.1 Dielectric permittivity

The temperature dependence of the low frequency (100 Hz) anisotropic dielectric constants in the planar ($\varepsilon_\perp$) and homeotropic ($\varepsilon_{||}$) configurations are given in Figure 5.4 for the pure WPLC as well as the CNT composite. The two configurations were realized by placing the sample in a magnetic field of 1 Tesla, a value much higher than the Freedericksz threshold of WPLC. The essential anisotropic aspect of the host LC is retained in the composite also showing that even in the presence of CNTs, the applied magnetic field is capable of orienting the LC molecules. Also to be noticed is that T_{NI}, the N-Iso transition temperature is hardly altered for the composite (T_{NI} is defined as the temperature where ε shows a discontinuous change while entering the isotropic phase). But the interesting feature is the large enhancement in the value of the permittivity in both the N and Iso phases. Such an increase seen earlier also [26], could be due to the larger dielectric constant of the aggregated CNTs causing, even at very low concentrations as that used here, a substantial increment of ε for the CNT/LC composite. However what is surprising is that despite the increase in the absolute values, the dielectric anisotropy ε_a (= $\varepsilon_{||}$–$\varepsilon_\perp$) decreases for the composite. For example, at T = 42 ^{o}C, a temperature at which the switching measurements (to be discussed later) are done, it reduces by about 10%.

A simple additive rule for a binary mixture of two different dielectric constants shows that there must be an increase in the value when CNTs are added. Indeed, if the host liquid crystal used is a strongly polar one (such as nCB) with a large dipole moment along the long axis of the molecule, ε_a shows an increase upon addition of CNTs, a feature corroborated by the results of Basu and Iannacchione [26] also. Therefore, we suggest that the interaction of CNTs with the weakly polar WPLC molecule is different from that with nCB molecules: In the case of the WPLC molecule, the interaction with CNTs would perhaps be dominated by hydrophobic forces due to the alkyl chains on both the termini of the molecule. Therefore the WPLC molecules would prefer to be perpendicular to the long axis of CNTs, at least in its vicinity. Such an arrangement would reduce locally the orientational order parameter of the LC medium, thus lowering the ε_a value.

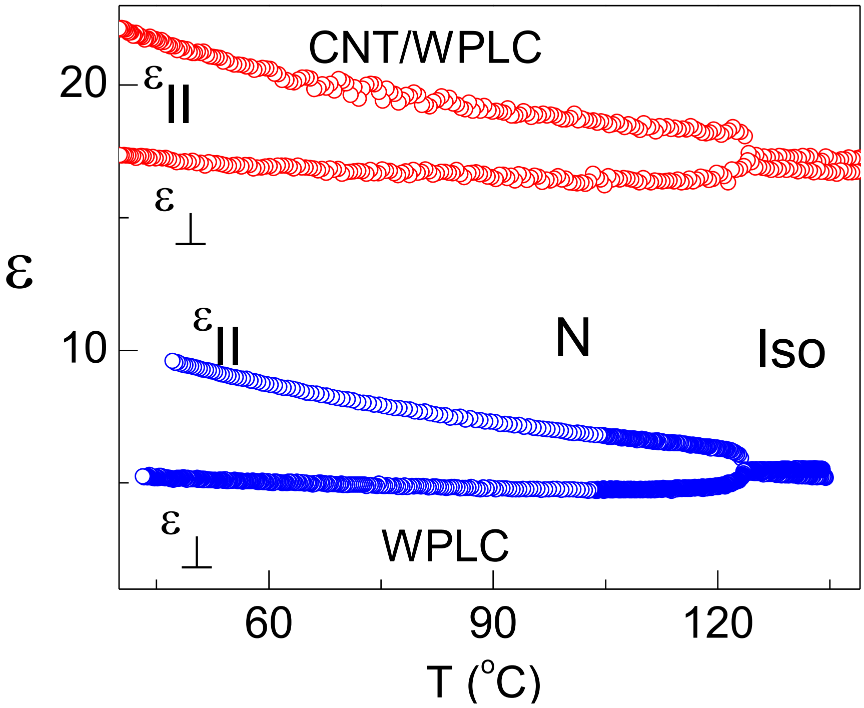

Figure 5.4: Thermal variation of the dielectric constant parallel ($\varepsilon_{||}$) and perpendicular ($\varepsilon_{\perp}$) to the director for the pure LC compound and the CNTs composite, with the latter exhibiting much higher values in the nematic (N) as well as isotropic (Iso) phases.

The results of the dielectric relaxation spectroscopy (DRS) measurements in the homeotropic configuration at a representative temperature of T = 42 ^{o}C are shown in Figures 5.5 and 5.6 for WPLC and the CNT composite respectively. The increase in ε' the real part of permittivity for the composite is possibly due to the creation of an increased number of CNT-LC-CNT capacitors. On the other hand, enhancement of ε'' the imaginary part of permittivity could be either due to an increased electrical conductivity (described below) or associated with CNT-LC interfacial regions. More than the absolute values of the permittivity, it is the presence of a relaxation – clearly visible in the ε' data for both the pure LC and composite samples – that is important.

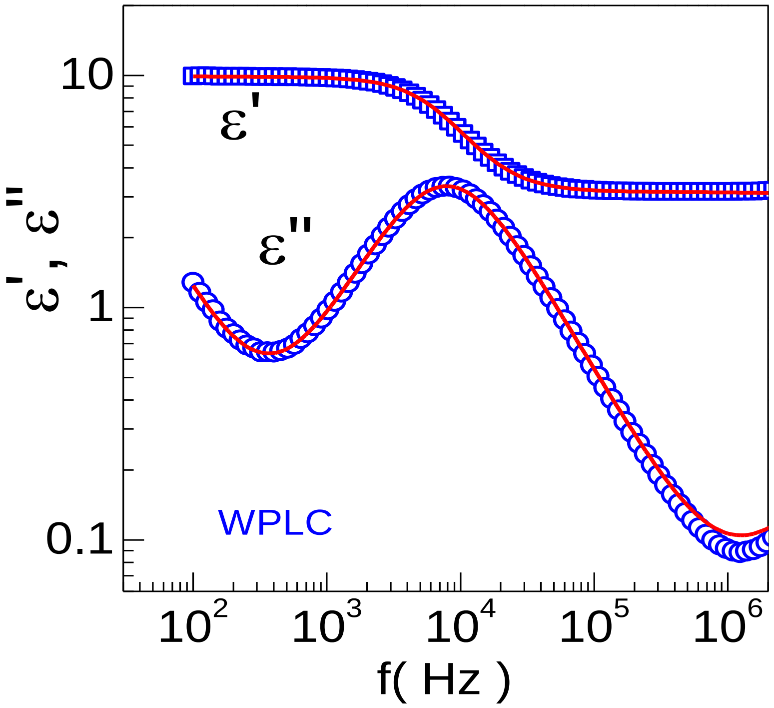

Figure 5.5: Frequency dependence of the real (ε') and imaginary (ε") parts of the permittivity for WPLC, showing a single relaxation. The solid lines represent the fit to eq. (5.1).

In the imaginary component ($\varepsilon''_{||}$), the data around the relaxation for the composite are partially masked by the large frequency dependence of ionic current contribution extending from the lowest frequency. However, quantitative description of the data using a standard Havriliak-Negami (HN) expression [27], given below, clearly brings out the relaxation phenomenon in the composite also.

$$\varepsilon^*(\mathrm{f}) = \varepsilon_\infty + \frac{\Delta\varepsilon}{\left[1 + (i\mathrm{f}/\mathrm{f_R})^\alpha\right]^\beta} + i\frac{\sigma_o}{f^N} + Af^m \tag{5.1}$$

Here ε*(f) is the complex capacitance at a frequency f, ε_∞ is associated with the dielectric strengths of all the high frequency modes other than the one under consideration. Δε and f_R are the strength and frequency of the relaxation mode.

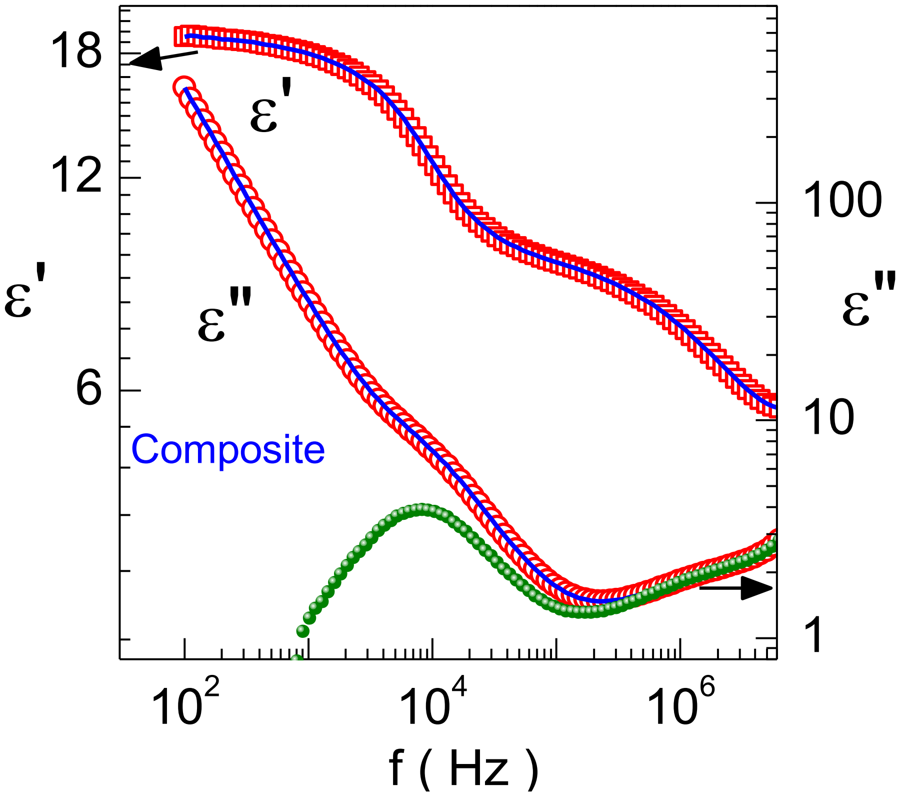

Figure 5.6: Frequency dependence of the real (ε') and imaginary (ε'') parts of the permittivity for CNTs composite. The presence of two relaxations is clearly seen in the raw data of ε', but is masked in the ε'' data owing to the large conductivity background. However, subtraction of the conductivity contribution determined from the fit (solid lines) to eq. (5.1), brings out the existence of the relaxation feature even in the ε'' data, as shown by the set depicted as solid circles.

The parameter α characterizes the distribution of the relaxation times while β is a measure of the asymmetry of the distribution. The RHS of eq. (5.1) contains, in addition to the first two HN terms, a term to account for the DC conductivity (σ_o) contribution to the imaginary part of the capacitance, and a part (the last term in eq. 5.1) to explain the cell relaxation time arising from the finite sheet resistance of the ITO-coated glass plates used. For both the pure LC and the mixture the frequency-dependent data are well described by eq. (5.1). The HN parameter β was found to be equal to 1 for the pure LC as well as the composite, indicating the symmetry of the relaxation profile. The other parameter, α, also turned out to be equal to 1 for the pure LC indicating a Debye relaxation; for the LC-CNT dispersion, however, α was 0.93 indicating a slight distribution of the relaxation times.

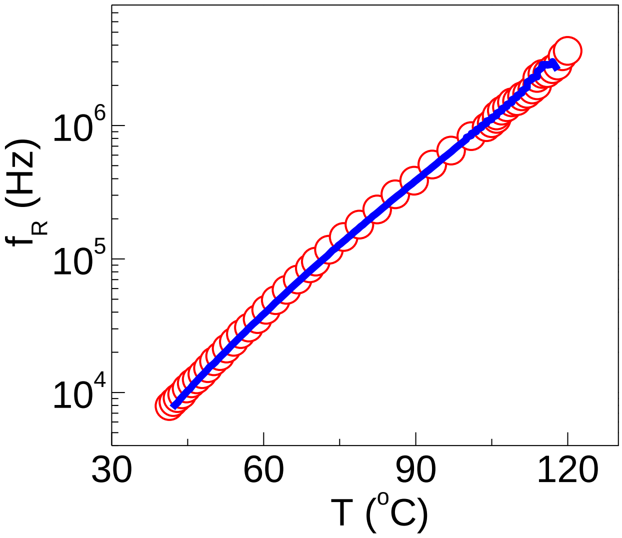

Figure 5.7: The temperature dependence of the relaxation frequency for the pure LC (solid line) and the CNT composite (open circles, representing the low frequency mode) exhibiting essentially no difference in the values for the two materials over the entire temperature range.

As stated earlier, the large conductivity masks the existence of the relaxation for the composite. But the subtraction of the conductivity contribution estimated from the third term of eq. (5.1) brings out the dielectric features in the imaginary part of the permittivity also (see data set shown as solid circles in Figure 5.6). In fact the observed features in ε'' are in conformity with those seen for the ε' vs. frequency data. The extracted relaxation frequency values are 7957 ±10 Hz and 7853 ± 20 Hz for the pure LC and the composite respectively. We identify this mode, well established for the pure LC, to correspond to the director relaxation for the pure material as well as the composite. Thus the fact that the f_R values are not different for the two materials indicates that the dynamics of the director relaxation is hardly affected by the presence of CNTs. In fact, the f_R values are practically the same for the two systems over the entire temperature range of the nematic phase (see Figure 5.7). An additional feature seen for the composite is that the DRS data also exhibits the presence of another relaxation at a higher frequency (~ 1 MHz), which is not present in the pure LC sample. The origin of this relaxation has to be found by more investigations, but currently we speculate that it could be due to the LC molecules anchored on to the surface of CNTs; the anchoring makes the relaxation faster.

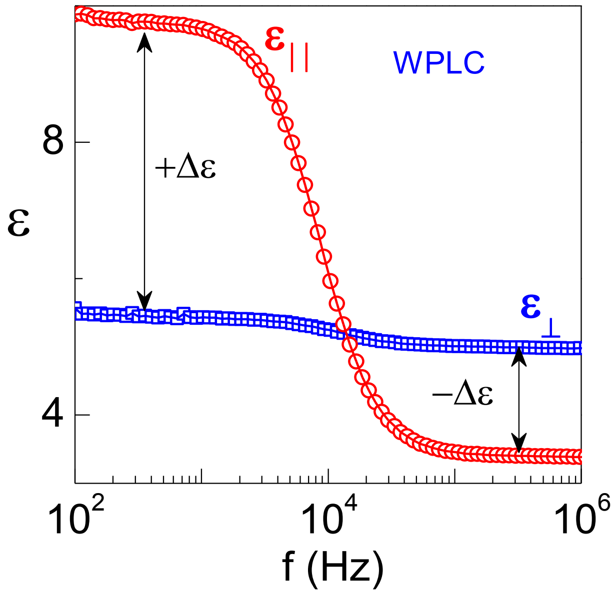

Figure 5.8: Frequency dependence of the dielectric constant in the homeotropic ($\varepsilon_{||}$) and planar ($\varepsilon_{\perp}$) configurations measured at room temperature. Notice that while $\varepsilon_{||}$ shows a relaxation, $\varepsilon_{\perp}$ remains practically same the over the entire frequency range. The dual frequency characteristic for the materials is evident from the fact that the director anisotropy $\Delta\varepsilon$ is positive below a certain frequency f_{cr} but is negative above it.

In the frequency range studied $\varepsilon_{\perp}$, the permittivity in the plane perpendicular to the nematic director, has hardly any frequency dependence, while $\varepsilon_{||}$ exhibits a relaxation. For the material under study, the relaxation creates a situation wherein at a particular frequency, referred to as the crossover frequency (f_{cr}), $\varepsilon_{\perp}$ cuts through the $\varepsilon'_{||}$ data. This causes ε_a to be positive, and negative, below and above f_{cr} (see figure 5.8). Invariably, f_{cr} lies in the close proximity of f_R. These features enable the possibility of realizing the conductivity switch that will be described later.

5.6 Electrical conductivity

5.6.1 Thermal variation

The thermal variation of the low frequency (100 Hz) anisotropic electrical conductivities, parallel ($\sigma_{||}$) and perpendicular ($\sigma_{\perp}$) to the nematic director, measured using a small probing voltage is shown for pure WPLC and the CNT composite in Figure 5.9. Upon addition of CNTs there is an increase in conductivity by about 2 orders of magnitude.

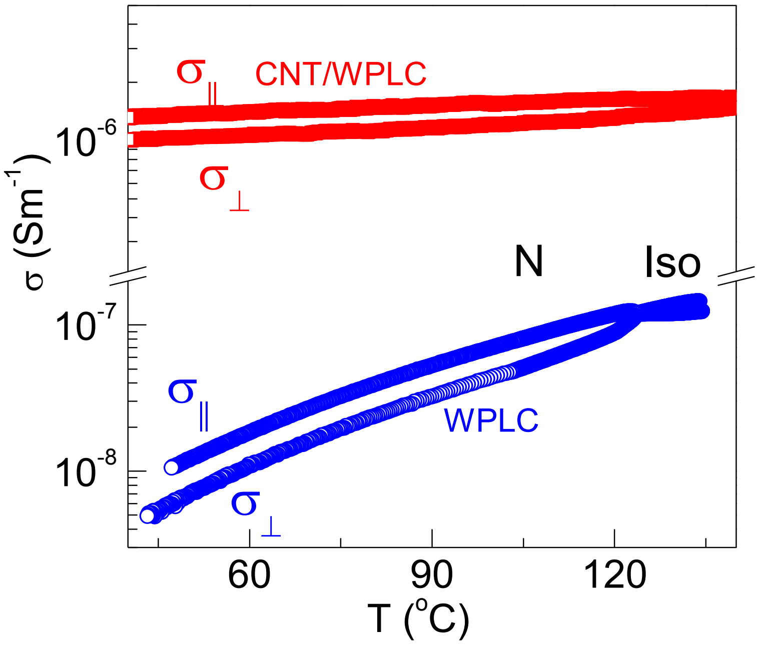

Figure 5.9: Thermal variation of the electrical conductivity at 100Hz for WPLC and its composite with CNT showing that the composite has not only two orders of magnitude higher conductivity, but also has negligible temperature dependence of the values.

More interestingly, the thermal dependences of σ are quite different for the pure LC and the composite. Describing the thermal variation using the Arrhenius equation, $\sigma \propto \exp(-\Delta E/kT)$, it is found that the activation energy, ΔE, decreases from 34.4 ± 0.05 kJ/mol for the pure LC (which is typical for LC materials), to a very small value of 2.68 ± 0.02 kJ/mol for the composite. Similar behaviour observed earlier by Lebovka et al [32] was explained on the basis of a percolation model, with the LC and the CNT/LC composite materials lying below and above the percolation threshold respectively. As per this model, the conductivity behaviour of the LC is dominated by ionic transport mechanism, with the material acting like a semiconductor for which thermally assisted hopping or charge tunnelling between the conducting particles is important. On the other hand, for the composite, the electronic conductivity of CNTs becomes important, which is represented by weak thermal dependence. Also to be appreciated is that whereas for the MBBA + CNT system studied by Lebovka et al [28] low ΔE values were found for significantly high concentration of CNTs, in the case studied here, even for 0.05% of CNTs, ΔE is quite low suggesting that the present system is better suited to achieve the electronic conducting regime.

5.6.2 Frequency dependence of conductivity

When conductivity measurements are made as a function of frequency (ω) it was found that up to a certain frequency ω_c, the value is essentially independent of ω and starts to increase at higher frequencies. Figure 5.10 show that the frequency dependence of $\sigma_{||}$ obtained with a small probing voltage is similar to profiles seen in disordered solids for which universal behaviour has been proposed [29]. In such materials the frequency dependent conductivity σ (ω) is expressed as $\sigma(\omega) = \sigma_{DC} + \sigma_{AC}$ where σ_{DC} is the zero-frequency DC component of the conductivity. Various expressions have been employed to analyze the ω–dependence of σ_{AC} with one of the earliest being the empirical equation $\sigma_{AC} \propto \omega^n$, used by Jonscher [30] considering a distribution of hopping probabilities between sites distributed randomly in space and in energy. In disordered solids, a *universal dynamic response* [30] is observed with the value of n being < 1. As stated earlier, considering the large increase in conductivity between the pure LC and the composite, and the weak temperature dependence for the latter, it may safely be assumed that the concentration of the CNTs is above the percolation threshold. However, since the concentration of CNTs is still low, the junction resistances between CNTs dispersed in the LC medium can, in the general case, be taken to be larger than the resistance of the CNTs themselves, and thus any possible network of CNTs could be imagined to have randomly distributed barriers for electrical transport. For such systems Kilbride et al [31] employed an extended pair approximation model to relate σ (ω) and ω as

$$\sigma(\omega) = \sigma_{DC}\left(1 + k(\omega/\omega_c)^s\right) \tag{5.2}$$

Where, k is a constant and s is expected to be < 1, and generally ~ 0.8. The solid line depicted in Figure 5.10 shows that eq. (5.2) describes the data well. The fitted value of the exponent s = 1.05 ±0.003, suggests that the dependence is practically linear. The exact value of the exponent, if taken very seriously, fails the expectation that it should be <1. The reason for this discrepancy is not clear to us, although it must be mentioned that the model, which is meant for disordered solids does not obviously consider thermal fluctuations, a feature that is invariably present in the nematic phase, and cannot be ignored.

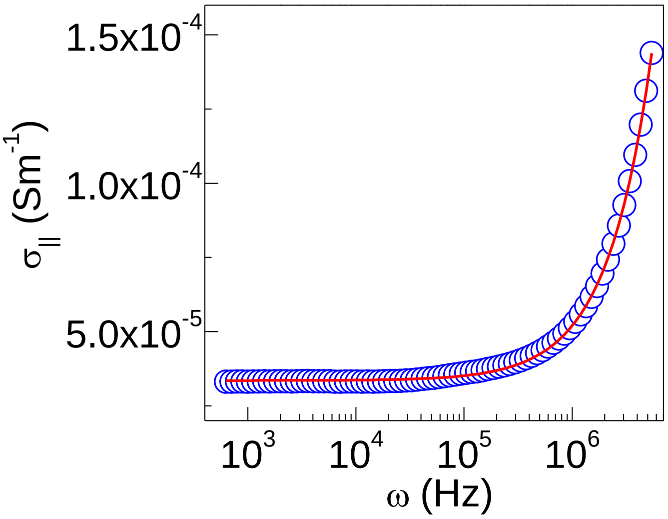

Figure 5.10: The frequency dependence of $\sigma_{||}$ of CNT composite with the solid line depicting the fit to eq. (5.2).

5.6.3 Dual frequency switching

In this closing section for Part A, we describe the dual frequency switching capability of the CNT/WPLC composite used here. As dicussed above, the dielectric anisotropy of the system switches from being positive below a crossover frequency f_{cr} to become negative above it. Thus for an applied electric field E (above the Freedericksz threshold), the dielectric torque $\varepsilon_a E^2$ on the nematic director which is positive for $f<f_{cr}$ thus driving the molecules parallel to E, becomes negative for $f>f_{cr}$, requiring the molecules to be perpendicular to E. Such a molecular reorientation driven simply by altering the frequency of the applied field should also result in the conductivity changing from $\sigma_{||}$ to $\sigma_{\perp}$.

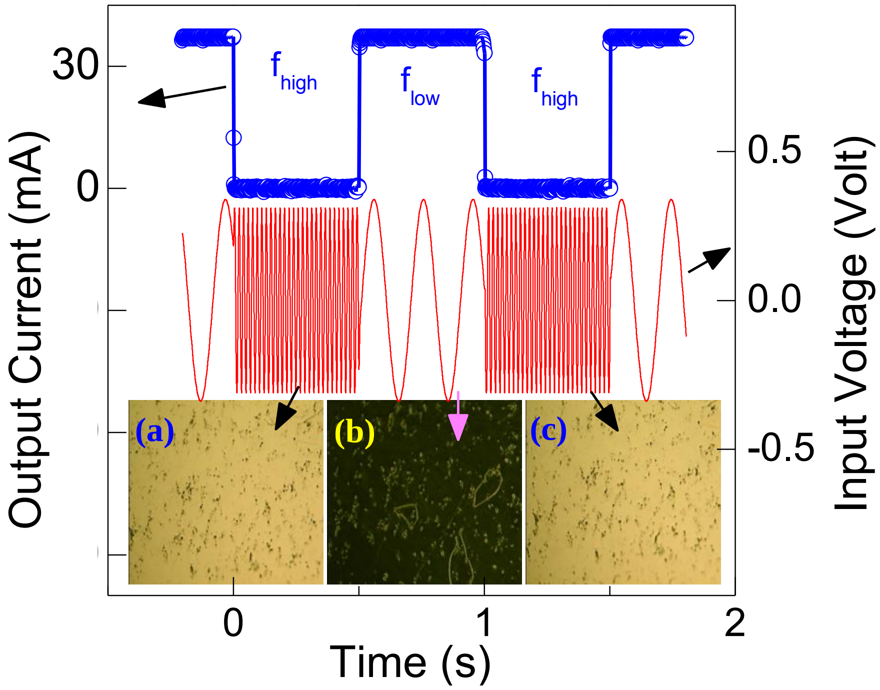

Figure 5.11: Demonstration of the CNT composite exhibiting the dual frequency character of the conductivity switching. The current through the sample kept at a temperature of 42 °C switches between high and low values, when the frequency of the driving voltage of 10 V is changed from f_{low} = 500 Hz to f_{high} = 600 kHz; the driving profile is shown schematically as a red line. The fact that the change in the current values is due to the reorientation of the WPLC molecules is illustrated in terms of the birefringent texture (a,c) at high frequency changing over to a dark field of view (b) at low frequency.

Figure 5.11 demonstrates this feature realized by applying a voltage of 10 V and alternating the frequency of the field between 500 Hz (<<f_{cr}) and 600 kHz (>>f_{cr}). The data are represented in terms of the amplitude of the current through the sample measured as a voltage drop across a 50 Ω resistor in series with the sample maintained at a temperature of 40 °C. The reorientation of the molecules from the no-field birefringent state (as shown by the polarizing microscopy texture in the inset (a) of Figure 5.11 having $\sigma_{\perp}$ to the homeotropic condition (inset (b)) with $\sigma_{||}$ is achieved with the low frequency (500 Hz) field. The return to the equilibrium planar state (inset (c)) with $\sigma_{\perp}$ is obtained by merely increasing the frequency of the field to 600 kHz. Although the return to the planar state could have been simply achieved by turning the field off completely, employing the high frequency component has the advantage of two orders of magnitude faster switching. The alternation between high and low conducting states (with a current ratio of 170:1) can be achieved within a millisecond. By enhancing the conductivity anisotropy through proper choice of the host material as well as the LC phase it should be possible to achieve the ultimate goal of switching between insulating and good semiconducting states.

PART B: Comparison of CNT doped SPLC and WPLC composites

In this part we describe dielectric and conductivity measurements on CNT composites with either SPLC or WPLC as the host, performed to find out whether the polarity of the host LC has any influence on permittivity as well charge transport. For the comparison, composites in which the content of CNT was the same – 0.05 wt % – were employed. Figures 5.9 and 5.12 depict the temperature dependence of conductivity obtained at a frequency of 100Hz along and perpendicular directions for the pure host LCs as well as their composites with CNT. Both the composites exhibit a significant enhancement of the conductivity in comparison to their host LCs. The magnitude of the enhancement is about an order of magnitude for SPLC whereas it is a further one order higher with WPLC compound.

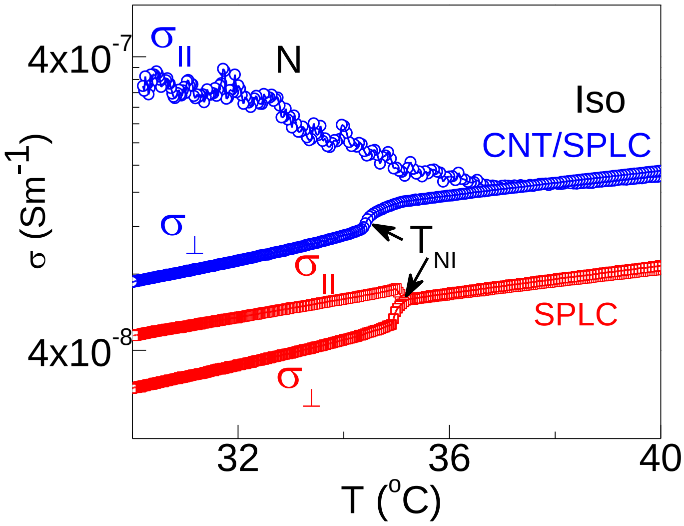

Figure 5.12: Electrical conductivity at 100Hz as a function of temperature parallel and perpendicular to the nematic director for SPLC and its composite with CNT.

The anisotropy in conductivity is still retained in the composites. Further for the SPLC composite there is a factor of 2.5 increase in the ratio $\sigma_a = \sigma_{\|}/\sigma_{\perp}$ with respect to that for the pure material. The WPLC case has the opposite behavior with the ratio σ_a decreasing by about 20% for the composite [For purposes of better comparison the data in the isotropic phase obtained with the two orientations have been matched]. In fact, σ_a becoming smaller for the composite is a feature known to be associated with the appearance of smectic ordering. Since it is clear from microscopy observation that the system remains in the nematic phase, this feature suggests that the additional ordering is only short range.

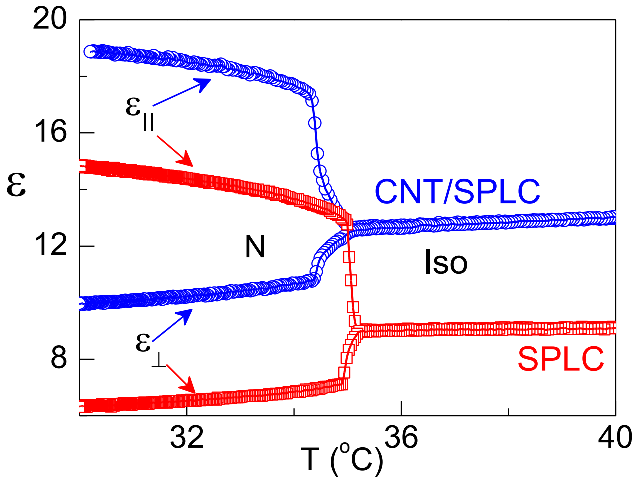

Figure 5.13: Thermal variation of the dielectric permittivity at 100Hz along (∥) *and perpendicular* (⊥) *to the director for SPLC and its composite with CNT.*

Figures 5.4 and 5.13 present the thermal behavior of $\varepsilon_{\|}$ and $\varepsilon_{\perp}$ for the two pure compounds and their composites. In both the cases the addition of CNT results in a significant increase in both $\varepsilon_{\|}$ and $\varepsilon_{\perp}$ as well as in the permittivity of the isotropic phase. However, the magnitudes of the increase are definitely dependent on the polar character of the host material: for SPLC the increase in, for example the isotropic permittivity is ~ 25%, but for WPLC case it is much larger: a factor of 3. Another interesting aspect observed is the temperature dependent permittivity behaviour at 1 kHz in the isotropic phase of the strongly polar material (shown in figure 5.14). The pure material exhibits a convex shaped anomaly (CSA) that has been argued to be associated with the antiparallel arrangement of the molecules even in the Iso phase [32,33], but in the vicinity of T_{NI}. It is observed that the temperatures at which the anomaly has a maximum and the highest ε value obtained are larger for the SPLC composite than for the pure SPLC compound. Such behaviour is not observed even pure WPLC. These features obviously suggest that the antiparallel correlations in the case of SPLC host can be enhanced by the presence of CNT.

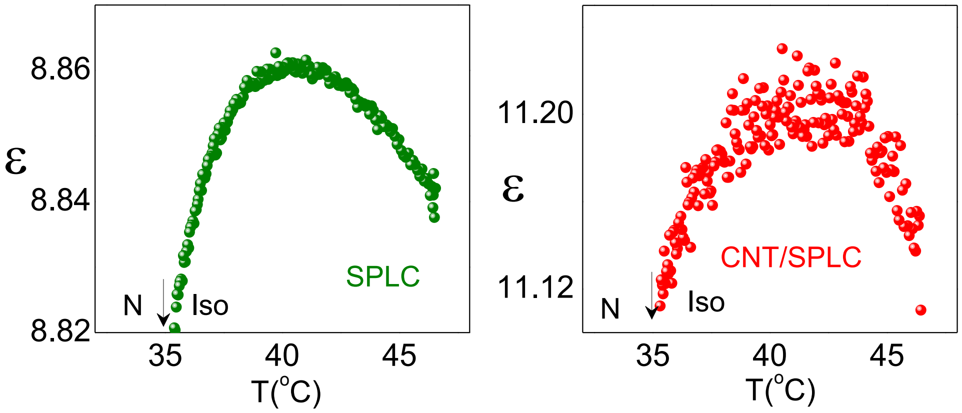

Figure 5.14: Thermal variation of the permittivity at 1 kHz in the isotropic phase for the composites with SPLC (Left) and the CNT composite (Right). Note that the maximum in ε, with respect to that at T_{NI} (indicated by arrow), is much higher for the composite than for pure SPLC.

5.7 Summary

We have performed dielectric and conductivity measurements on a composite of carbon nanotubes and a liquid crystal possessing dual frequency switching characteristics. In comparison to that for the pure liquid crystal, the conductivity is two orders of magnitude higher for the composite, in addition to being essentially temperature independent. The dependence of ac conductivity on the probing frequency can be described by the often employed extended pair approximation model, although the exponent value obtained is higher than usually seen. The composite retains the same director relaxation frequency as that of the pure liquid crystal, a feature that enabled us to realize the dual frequency switching capability of the system wherein by altering the frequency of the applied voltage, the current through the sample can be varied between anisotropic values that are two-orders of magnitude different. In addition to above study two liquid crystals are chosen such that one of them is strongly polar having its dipole moment parallel to the long axis of the molecule whereas the other one is weakly polar with its dipole in the transverse direction. Both conductivity and permittivity retain their anisotropic nature even in the composites. More importantly the conductivity exhibits large increase as much as 2 orders of magnitude – for the composite with the weakly polar material. The qualitative behavior of the permittivity is also quite different upon inclusion of CNT. Along with the mentioned electrical switchable character which imparts a field-switchable conductivity value, these materials are quite promising for devices.

5.8 References

1. P.J.F. Harris, Carbon Nanotubes and Related Structures, *Cambridge University Press*, Cambridge (1999); R. Saito, G. Dresselhaus and M.S. Dresselhaus, Physical Properties of Carbon Nanotubes, *Imperial College Press*, London (2001); C.N.R. Rao, B.C. Tatishkumar, A. Govindaraj and M. Nath, *Chem Phys Chem*, **2**, 78 (2001); H.S. Nalwa, Encyclopedia of Nanoscience and Nanotechnology, American Scientific Publishers, **15**, 11 (2011).
2. L. Dolgov, O. Kovalchuk, N. Lebovka, S. Tomylko and O. Yaroshchuk, *Carbon nanotubes*, Croatia: InTech Europe, 451 (2010); Z. Zalevsky, I. Abdulhalim, *Integrated Nanophotonic Devices*, Elsevier, Burlington (2014).
3. I. Dierking, G. Scalia, P. Morales and D. LeClere, *Adv. Mat.*, **16**, 865 (2004*)*.
4. J.P.F. Lagerwall, G. Scalia, M. Haluska, U. Dettlaff, S. Roth and F. Giesselmann, *Adv. Mat*, **19**, 359 (2004*)*.
5. R. Basu and G. Iannacchione, *Appl. Phys. Lett*., **93**, 183105 (2008).
6. P. Van der Schoot, V. Popa-Nita and S.J. Kralj, *Phys. Chem. B*, **112,** 4512 (2008).
7. J. Prakash, A. Choudhary, D.S. Mehta and A.M. Biradar, *Phys. Rev. E*, **80**, 012701 (2009).
8. W. Lee, H.Y. Chen and Y.C. Shih, *J. Soc. Info. Display.,* **16**, 733 (2008).
9. V. Jayalakshmi and S. Krishna Prasad, *Appl. Phys. Lett.*, **94,** 202106 (2009).
10. H.J. Shah, H. Pan, and C. Hsieh, *Jpn. J. Appl. Phys.*, **45**, 6392 (2006).

11. A.K. Srivastava, E.P. Pozhidaev, V.G. Chigrinov, and R. Manohar, *Appl. Phys. Lett.*, **99**, 201106 (2011).
12. R. Dhar, A.S. Pandey, M.B. Pandey, S. Kumar, and R. Dabrowski, *Appl. Phys. Exp*. **1**, 121501 (2008).
13. Y. Reznikov, O. Buchnev, O. Tereshchenko, V. Reshetnyak, A. Glushchenko, and J. West, *Appl. Phys. Lett*. **82**, 1917 (2003).
14. P. Blake, P. Brimicombe, R. Nair, T. Booth, D. Jiang, F. Schedin, L. Ponomarenko, S. Morozov, H. Gleeson, E. Hill, A. Geim, and K. Novose , Nano Lett., **8**, 100206-3, (2008).
15. I. Dierking, G. Scalia and P. Morales, *J. Appl. Phys*., **97,** 044309 (2005).
16. S. Iijima, *Nature London*, **354**, 56 (1991).
17. M. Endo, K. Takeuchi, S. Igarashi, K. Kobori, M. Shiraishi, and H.W. Kroto, *J. Phys. Chem. Solids,* **54**, 1841 (1993).
18. A. Thess, R. Lee, P. Nikdaev, H. Dai, P. Petit, J. Robert, C. Xu, Y.H. Lee, S.G. Kim, A.G. Rinzler, D.T. Colbert, G.E. Scuseria, D. Tomanek, J.E. Fischer, and R.E. Smalley, *Science*, **273**, 483 (1996).
19. X. Wang, L. Qunqing, X. Jing, J. Zhong, W. Jinyong, L.Yan, J. Kaili and F. Shoushan, *Nano Letters*, **9**, 3137 (2009).
20. http://news.nationalgeographic.com/news/2006/11/061116-nanotech-swords.html; S. Gullapalli and M.S. Wong, *Chemical Engineering Progress*, **107**, 28 (2011).
21. J.W. Mintmire, B.I. Dunlap and C.T. White, *Phys. Rev. Lett.*, **68**, 631 (1992); C. Dekker, *Physics Today*, **52**, 22 (1999).
22. (a) R. Martel, V. Derycke, C. Lavoie, J. Appenzeller, K. Chan, J. Tersoff and Ph. Avouris, *Phys. Rev. Lett.* **87**, 256805 (2001); (b) Y. Zhang, W. Bai, J. Ren, W. Weng, H. Lin, Z. Zhang and H. Peng *J. Mater. Chem. A,* **2**, 11054 (2014); (c) S. Ghosh, A. K. Sood, N. Kumar, *Science***, 299,** 1042 (2003).
23. V. Freedericksz and V. Tsvetkov, *Phys. Z.*, **6**, 490 (1934).
24. J. P. Van Meter and B.H. Klanderman, *Mol. Cryst. Liq. Cryst.*, **22**, 285 (1973)
25. The SWNTs used here were kindly provided free of cost by *M/s HeJi* (Hong Kong) Company Limited.
26. R. Basu and G. Iannacchione. *Phys. Rev. E,* **81**, 051705 (2010).
27. S. Havriliak and S. Negami, *Polymer*, **8**, 161 (1967).

28. N. Lebovka, T. Dadakova, L. Lysetskiy, O. Melezhyk, G. Puchkovska, T. Gavrilko, J. Baran, and M. Drozd, *J. Mol. Struct.,* **877**, 135 (2008).
29. J. Dyre, C. Jeppe and T. Schrøder, *Rev. Mod. Phys.,* **72**, 873 (2000).
30. A.K. Jonscher, *J. Non-cryst. Solids.* **8,** 293 (1972).
31. B.E. Kilbride, J.N. Coleman, J. Fraysse, P. Fournet, M. Cadek, A. Drury. *J. Appl. Phys.,* **92**, 4024 (2002).
32. M.J. Bradshaw and E.P. Raynes, *Mol. Cryst. Liq. Cryst. Lett.,* **72**, 73 (1981).
33. S. Sridevi, S. Krishna Prasad, D.S. Shankar Rao and C.V. Yelamaggad, *J. Phys. Condens. Matter,* **20**, 465106 (2008).

Chapter-6

Experimental Studies on Composites of Gold Nanoparticle/Weakly Polar Nematic Liquid Crystal in bulk and confined forms

Overview

This chapter deals with calorimetric and dielectric investigations on a pure nematic liquid crystal (LC) and its composites comprising Gold nanoparticles (GNPs). Calorimetric measurements show that the inclusion of GNP has a strong influence on the isotropic − nematic transition temperature as well its first order character in terms of the transition entropy. The absolute value of conductivity increases by two-three orders of magnitude with respect to that for the host liquid crystal and its concentration dependence is demonstrated to be described by the percolation scaling law generally observed in composites of metal particles and polymers. The frequency dependence of the ac conductivity exhibits a critical frequency that is concentration-dependent, but the exponents obtained defy Jonscher's Universal Response principle. A surprising feature is the observation of a substantial increase in permittivity and their anisotropy values with faster director relaxation in the presence GNP. We provide an explanation for this antagonistic behaviour in terms of the alignment of the liquid crystal molecules in the vicinity of GNP, and the importance of the weak polarity of the liquid crystal used. The second part of the Chapter looks at the influence of embedding the LC-GNP composite in a restricted geometry created by aerosil particles. The inclusion of aerosil particles creating a gel network, albeit being non-conducting, surprisingly enhances the already high conductivity of the LC-GNP material. The nature of the aerosil corona (hydrophobic/hydrophilic) also controls the behavior. We argue that these features are caused by the amelioration of the percolation network of GNPs through the primary gel network of the hydrogen bonding aerosil particles. The concept can be generalized for a variety of systems wherein metal nanoparticles are imbibed in an insulating matrix.

The results are published in:

1. S. Krishna Prasad, **M. Vijay Kumar**, T. Shilpa and C.V. Yelamaggad, Enhancement of electrical conductivity, dielectric anisotropy and director relaxation frequency in composites of gold nanoparticle and a weakly polar nematic liquid crystal, *RSC Advances*, **4**, 4453-4462 (2014).

2. K. Bhavesh, **M. Vijay Kumar**, C.V. Yelamaggad and S. Krishna Prasad, Enhancement of electrical conductivity of a liquid crystal-gold nanoparticle composite by a gel network of aerosil particles, *Appl. Phys. Lett.*, **106**, 083110-5 (2015).

6.1 Introduction

Nanocomposites have been attracting substantial attention since the first reports three decades ago [1]. The interest is especially due to the technological importance of percolative composites for the demanding applications requiring high electrical/thermal conductivity or high dielectric constant. Blending the processability of insulating organic materials with high conductivity values of metal particles has been in the forefront of this field [2,3]. Perhaps one of the best examples of these composites are those of liquid crystals (LC) and nanoparticles (NP) showcasing the importance of the judicial combination of soft matter and nanoscience, based on the soft elasticity and field tunability of liquid crystals. Several recent reports exist which demonstrate the importance of the combination of LC and NP [4-16]. Proper realization of the field tunability has been depicted at least in two cases [17,18] with the potential to result in devices in which macroscopic properties can be switched between their anisotropic values along, say, parallel to perpendicular direction with respect to an internal reference axis. In the case of mixtures with carbon nano particles, the frequency dependent conductivity exhibits (see Chapter-5) behaviour similar to the well known feature in disordered solids, qualitatively agreeing with the expectations of the extended pair approximation model [19]. Based on these aspects, investigations have been carried out on the composites in their bulk form as well as in the confined situation. The results are described in Part A and B of this chapter, respectively.

Part A: Composites of Gold Nano Particle-Liquid Crystal in bulk form

This part contains the results of dielectric and Differential Scanning Calorimeter (DSC) measurements on the bulk form of the composites of gold nano-particles (GNP) with a weakly polar nematic liquid crystal (LC) as the host. In fact, the weak polarity of this host and the absence of any strong longitudinal dipole moment reduce the possibility of build-up of short range ordering in the vicinity of the metal particles, and thus enhance the disordering imparted by the particles. Calorimetric studies show that there is a significant influence of the presence of the particles on the isotropic-nematic (I-N) transition of the host, with both the transition temperature and the transition entropy diminishing significantly. With increasing GNP concentration, while the anisotropic conductivities parallel as well as perpendicular to the director increase exhibiting percolation threshold behaviour, the rate of increase determined using a scaling law, exhibits an exponent that is below the dimension-related universal value. The anisotropy of the conductivity, taken as the ratio of the values in the two orthogonal directions, reduces slightly with increasing GNP concentration. The fact that the host material exhibits a low frequency director relaxation has enabled the first thermal investigations of the mode for the LC-metal particle composites which show strong influence of the concentration of GNP on the relaxation frequency of the mode.

6.2 Materials

6.2.1 Host liquid crystalline material

The liquid crystalline host used for the present study is 4-pentylphenyl 2-chloro-4-(4-pentylbenzoyloxy) benzoate (PCPBB for short), whose structure and phase sequence have already been given in the previous chapter. Structural feature of this compound that is of importance here is that it does not possess any strong dipole moment along the long axis of the molecule, but a weak one along the transverse direction. This feature was the criterion to select it so that the results could be compared with the data available in the literature collected mostly on alkyl/alkoxy cyanobiphenyl (with a strong longitudinal dipole moment) as the host. Also to be recalled is that PCPBB exhibits a low frequency director relaxation.

6.2.2 Preparation of nanoparticles

The Brust procedure [20], in which GNPs are prepared and capped with alkanethiols in a non-polar organic phase is a popular method, and has been found [9] to be suitable for the type of studies performed here; Dodecane-1-thiol, whose structure is shown in Figure 6.1, is used as the capping entity in the present studies. The starting materials, hydrogen tetrachloroaurate (III) trihydrate, sodium borohydride, tetraoctylammonium bromide and 1-dodecanethiol were procured from Aldrich Chemical Company and used as received. Ethanol and toluene obtained from a local source were purified following standard procedures. High purity (18MΩ) water was obtained from Milli-Q ultrapure water system (from Millipore).

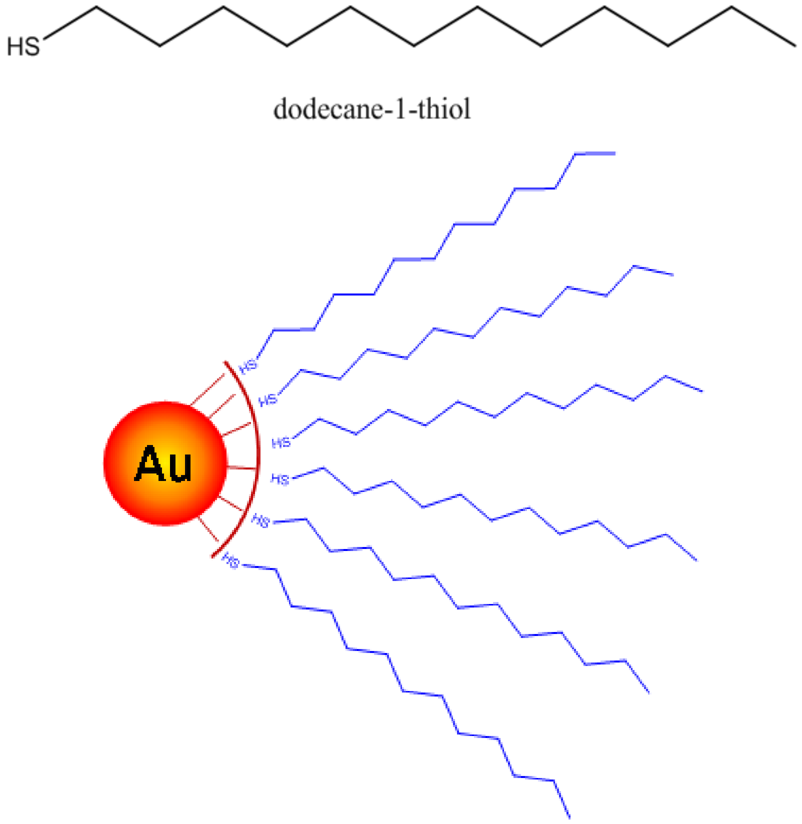

Figure 6.1: Top: Molecular structure of dodecane-1-thiol. Bottom: Schematic representation of a spherical gold nano particle capped with dodecane 1-thiol to achieve steric stabilization in the liquid crystal environment.

The deep brown dodecylthio-capped GNPs realized from the Brust procedure were repeatedly (5 times) washed with ethanol. The crude product collected by filtration was quickly dissolved in toluene and again precipitated with ethanol. This process was repeated several times and the pure GNPs were collected by filtration and preserved in the form of a solution in toluene (30 %). The general characteristics of the prepared material were found to be consistent with the literature reports [21].

6.3 Characterization of nanoparticles

6.3.1. ^{1}H NMR study

The chemical purity of the prepared nanoparticles was confirmed by ^{1}H NMR. The spectra given in figures 6.2 and 6.3, showed no indication of any free thiols left over. ^{1}H NMR spectrum of the GNP, prepared by modified Brust protocol, has been recorded using Bruker-AMX 400 instrument and analyzed. As shown in Figure 6.2, the spectral pattern suggests the stabilization of gold colloids by ligand, dodecane-1-thiol. Most importantly, in ^{1}H NMR spectrum of the GNP the signals due to ligands are almost negligible. That is, the quartet arising due to methylene moiety [–CH_2-SH] of lignad (see circled area in Figure 6.2 and compare with same region in Figure 6.3) is quite minute implying that the GNP is mostly free from un-bound ligands.

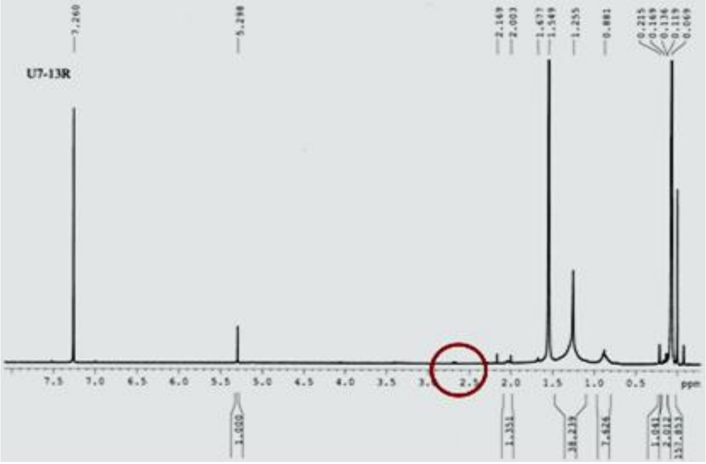

Figure 6.2: ^{1}H NMR spectrum of GNP ($CDCl_3$, 400 MHz)

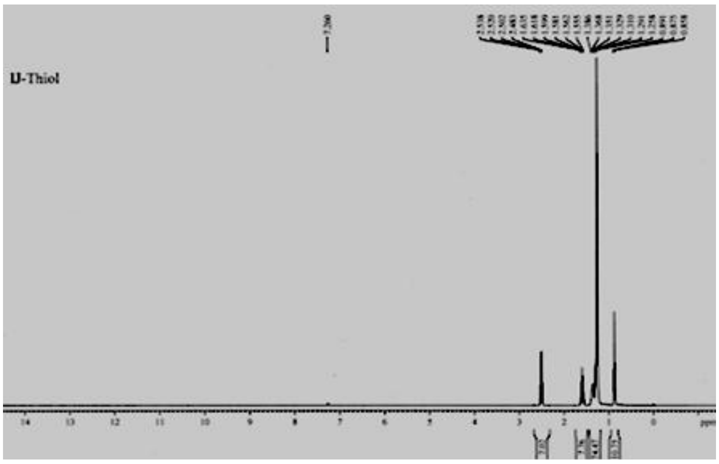

Figure 6.3: ^{1}H NMR spectrum of dodecane-1-thiol ($CDCl_3$, 400 MHz)

6.3.2. Transmission Electron Microscopy

TEM measurements were carried out to determine the shape as well as the size of the particles. The images were obtained on a JEOL 3010 TEM scanning/transmission electron microscope operating at 300 kV. Samples were prepared by casting a droplet of functionalized GNPs in DCM solvent onto carbon-coated copper TEM grids followed by drying for 20 min. The image, given in figure 6.4, which showed essentially spherical particles, was analyzed using a digital image analyzer (ImageJ, NIH) and yielded a mean particle size of 3.6 ± 0.6 nm; the histogram of the particle size distribution is also shown in fig 6.4.

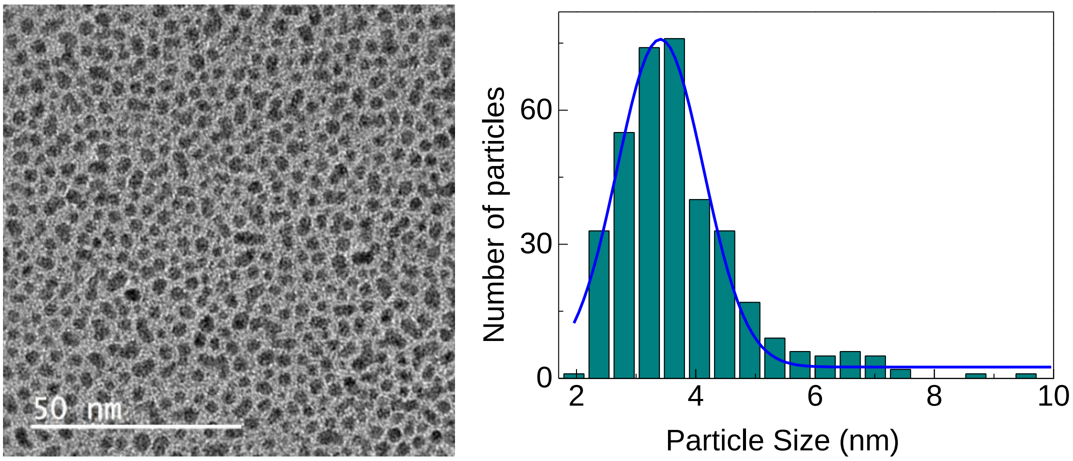

Figure 6.4: Left: Transmission electron microscopy image of the GNPs. Right: Histogram showing the particle size distribution.

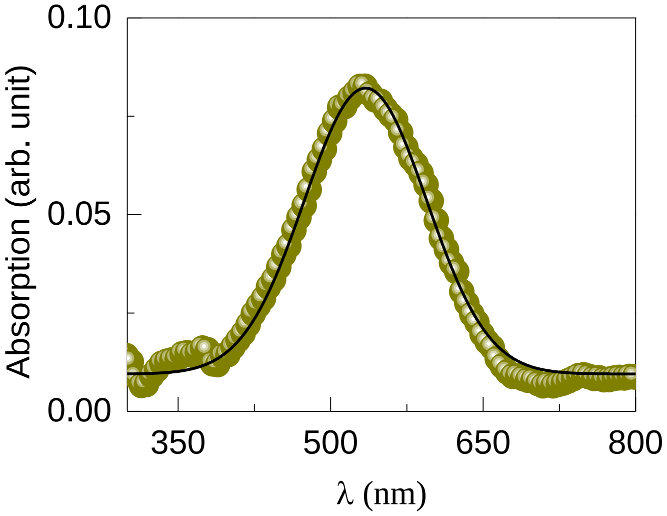

Figure 6.5: UV-Vis spectrum of GNPs with dichloro methane after subtraction of the background. The solid line depicts the fit of the data to a Gaussian expression.

6.3.3. UV-Vis spectrum

In order to observe the surface plasmon resonance (SPR), UV-Vis absorption spectra were recorded in transmission mode in the range 200 to 850 nm with a Perkin Elmer Lambda 20 spectrometer. A clear, single SPR peak at 517 nm (see figure 6.5) supported the spherical nature of the particles.

6.3.4. Xray diffraction

The size of the particles was estimated from the powder Xray diffraction pattern (Panalytical X'Pert Pro equipped with PIXEL detector, Cu K_α radiation, λ = 0.15481 nm). The two reflections seen conform to the (111) and (200) reflections of metal with face centred cubic structure (see figure 6.9).

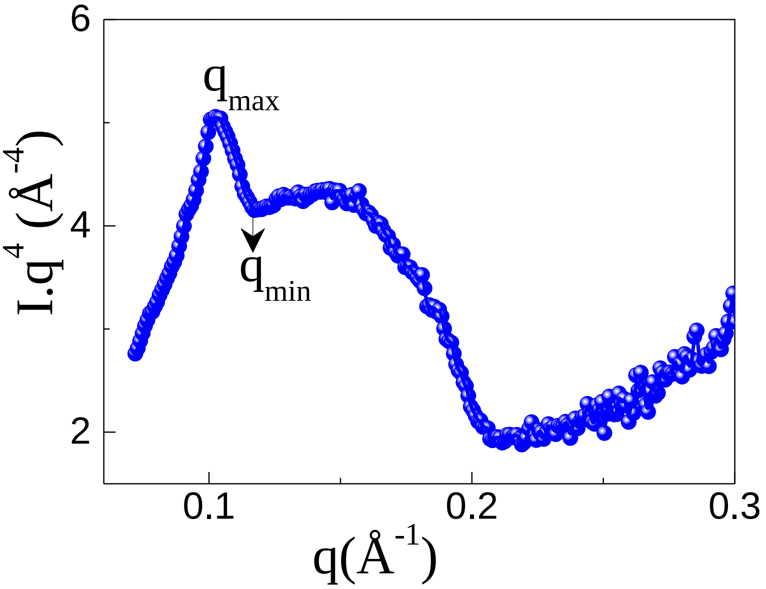

Figure 6.6: Wavevector dependence of the product I.q^4 ("Porod plot") obtained from low angle raw Xray scan of GNPs.

The lattice constant determined from XRD pattern, 0.409 ± 0.001 nm, is in good agreement with the standard diffraction pattern of gold metal (JCPDS Pattern 4-784). The nanoparticles, as one may expect, lack the extended order of usual crystals. This is evident from the fact that the peaks are much broader than one gets for the bulk metal. As is often done, the average GNP size ξ was calculated using the Debye–Scherrer formula, $\xi = K\lambda/(\beta\cos\theta)$. Here β is the full width at half maximum, λ and θ are the wavelength of the radiation and the Bragg angle, respectively. The coefficient K is a correction factor that depends on the shape of the domains. For fairly regular shapes it usually varies between 0.8 and 1.0, and is taken to be 0.89 for spherical particles. Using the experimental values for the different parameters the particle size turns out to be 5.4 ± 1 nm, a value comparable to that obtained from TEM. A further support comes from the Porod representation of the low angle Xray data (see Figure 6.6), which yields the particle size to be 5.3 nm.

6.4 Preparation of the LC-GNP composites

To prepare the composites, a colloidal solution of GNP in toluene was added to a previously weighed PCPBB placed in a 5 ml vial. The contents of the vial were subjected mechanical shaking to achieve uniform dispersion. Subsequently the solvent was evaporated and the mixture was dried under reduced pressure.

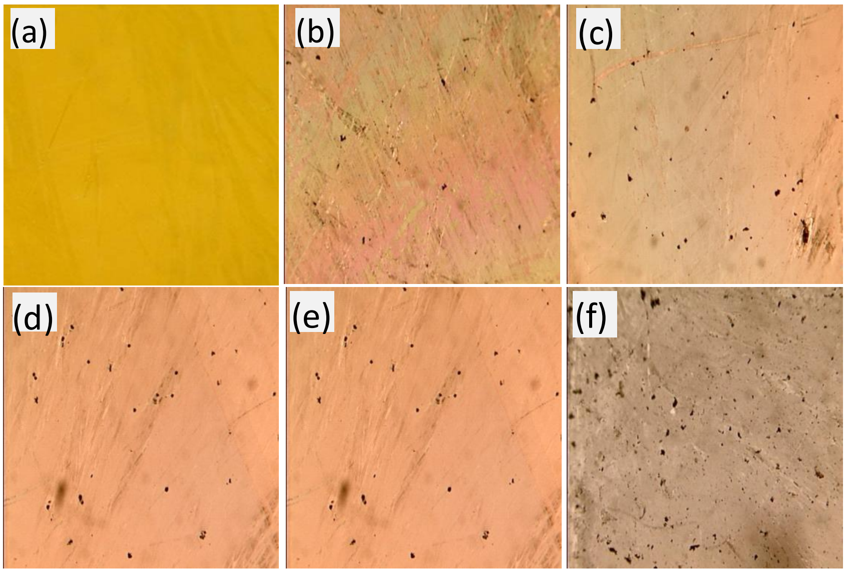

Figure 6.7: Polarizing microscopy photographs in the nematic phase for different concentrations of GNP with (a) X=0, (b) X=0.005, (c) X=0.01, (d) X=0.02, (e) X=0.025 and (f) X=0.05. In each case it is observed that the GNPs are quite well dispersed without any aggregation.

The concentration of GNP in the composite is denoted by X in weight fraction, taken as the ratio of weight of GNP to that of LC. Five different compositions were prepared with X=

0.005, 0.01, 0.02, 0.025 and 0.05. Texture photographs obtained with a polarizing optical microscope (Leica DMRXP fitted with Optronics digital camera) in the nematic phase for different concentrations of GNP showed that for all composites the GNPs are quite well dispersed without any aggregation as shown in Figure 6.7.

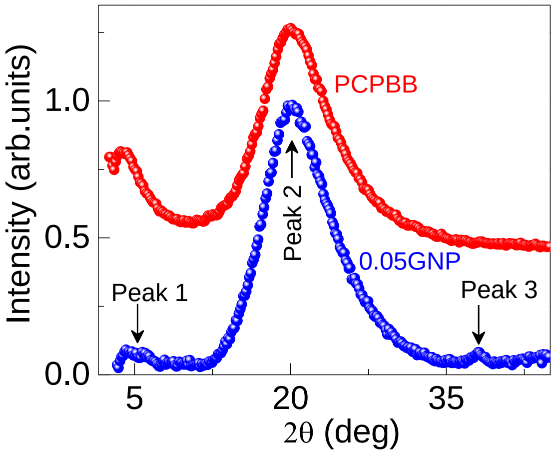

Figure 6.8: Xray diffraction profiles for the pure NLC (PCPBB) and the X = 0.05 GNP composite in the nematic phase exhibiting two diffuse reflections, Peak1 and Peak2, corresponding to the intermolecular spacing along and perpendicular to the director direction. The composite as well exhibits a low-intensity peak at wide angles (Peak3) due to the reflections from the gold nanoparticles.

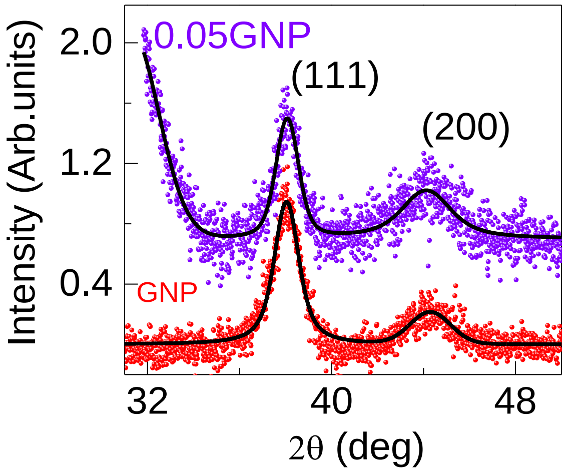

Figure 6.9: Wide angle Xray diffraction profiles for the nanoparticles as prepared and the LC/GNP (X = 0.05) composite, showing the (111) and (200) peaks characteristic of metallic Gold. The solid line depicts the fit of the data to the Lorenzian expression.

The Xray diffraction patterns obtained for the pure LC and a representative composite with X=0.05 are shown in Figure 6.8. The two diffuse peaks below $2\theta < 30^{o}$ are characteristic of the nematic scattering, with the low angle peak suggesting the presence of a slight local positional order; the wide angle represents scattering due to the intermolecular distance perpendicular to the nematic director. The presence of the peaks at $2\theta \sim 38^o$ and 44^o (shown on an enlarged scale in the Fig 6.9) due to the (111) and (200) reflections arising from gold establishes the presence of GNP in the nematic medium. Although the low concentration of GNP, together with the fact that the dispersing medium is essentially a fluid are responsible for the lowered S/N ratio of these peaks, it is clearly seen that peak positions and widths remain unaltered.

6.5 Methods of calorimetric and dielectric measurements

The differential scanning calorimetric measurements were performed with the power-compensating DSC system described in Chapter-2. The permittivity and electrical conductivity data were obtained with samples sandwiched between two indium-tin-oxide coated glass plates, having very low sheet resistance ($< 10\ \Omega/\square$). Thin Mylar strips, placed outside the electrically-active area, defined the thickness of the cell. The sample cells were placed inside a home-made copper block heater, which in turn was kept between the pole-pieces of an electromagnet (Bruker B-20) that provided a uniform magnetic field of 0.8 Tesla over the entire sample region. Owing to the positive diamagnetic nature of the sample, this field, which is much above the Freedericksz threshold, was used to orient the LC molecules, and fix the probing direction to be parallel or perpendicular to the nematic director. The electrical conductivity data were obtained using an Impedance analyser (HP 4194A) at a frequency of 1 kHz with a probing voltage of 0.5V.

6.6. Results and Discussion

6.6.1. Differential scanning calorimetry

Figure 6.10 presents the differential scanning calorimeter (DSC) scans taken at a cooling rate of 5 ^{o}C/min for pure PCPBB and five composites. A qualitatively significant change observed is the weakening of the I-N transition for the composites; the effect becomes more as the concentration of GNP is increased. Additionally the peak also gets broadened for the composites. Both these features can be considered to be arising as an impurity effect, especially since the second constituent (GNP) in the mixtures is a non-LC component.

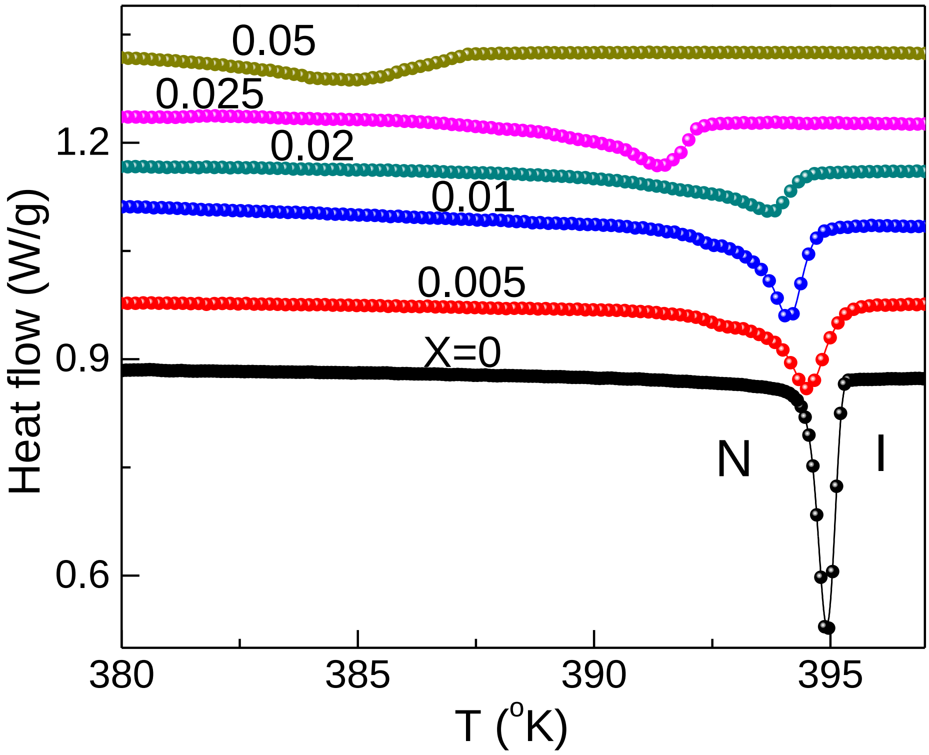

Figure 6.10: Differential scanning calorimeter profiles in the vicinity of the isotropic-nematic (I-N) transition for the pure LC (X = 0) and the different composites, with the concentration of GNP indicated against each curve. The drastic reduction in the thermal strength with increasing X is clearly visible.

Figure 6.11 shows the influence of X, the GNP concentration, on the thermal parameters, viz., transition temperature (T_{IN}) and transition entropy (ΔS_{IN}). When X changes from 0 to 0.05, while the transition temperature diminishes by 10 K, the transition entropy reduces by ~ 45%. Gorkunov and Osipov [22] have worked out a molecular mean field theory for the composites of nanoparticles with liquid crystals. A special case they consider is that of spherical particles, for which according to the theory the influence on the I-N transition is given by $T_{IN} = (1-\nu)T_{INO}$, where T_{INO} and T_{IN} are the transition temperature for the pure LC and the composites, respectively and $(1-\nu)$ represents the contribution of the *dilution* effect.

The term *dilution* here refers to the feature that inclusion of nanoparticles into the nematic medium diminishes the interaction between the LC molecules, thus diluting the order parameter of the system.

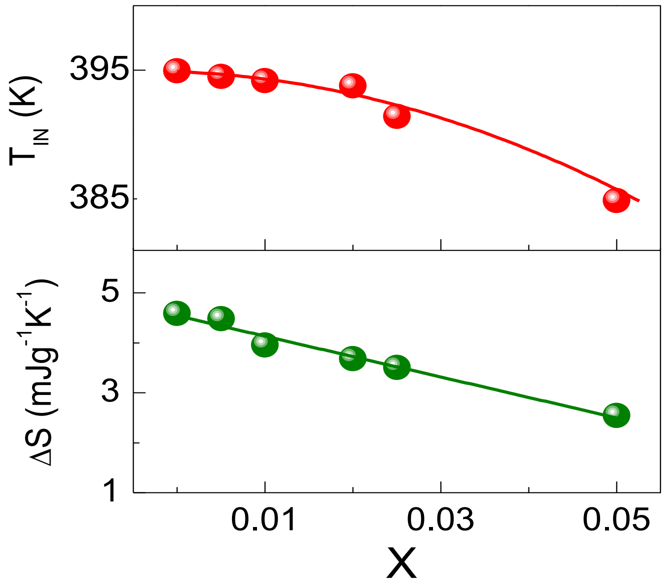

Figure 6.11: The concentration dependence of the transition temperature (T_{IN}) and the associated entropy (ΔS_{IN}). *The line through the former set is a fit to eq. 6.1, and that through the latter is a straight line through the data.*

In the absence of any explicit expression for the concentration dependence of the parameter ν in the theory, and keeping in view the trend observed in the experiments, we fitted the data of Figure 6.11 to eq. (6.1)

$$T_{IN} = T_{INO} - AX^2 \tag{6.1}$$

and find the fitting to be quite good, which shows that the dilution effect is quite strong for the present system. The weakening of the thermal signature of the transition with increasing GNP concentration is evident from the DSC scans. To quantify the weakening, we determined the entropy (ΔS) associated with the transition using the area under the peak. Figure 6.11 shows that ΔS decreases significantly with X, a feature in general agreement with the dilution theory [22]. A further argument can be made by keeping in mind that the I-N transition for the pure LC is a weak first order transition with a jump in the order parameter.

The observed behavior of ΔS suggests that the presence of the particles drives the transition to the second order transition region through a tricritical point [23]. Another feature that was observed for X= 0.005 and 0.01 composites is the existence of a small peak just below the main peak (seen clearly on an enlarged scale of Figure 6.12 for X=0.005).

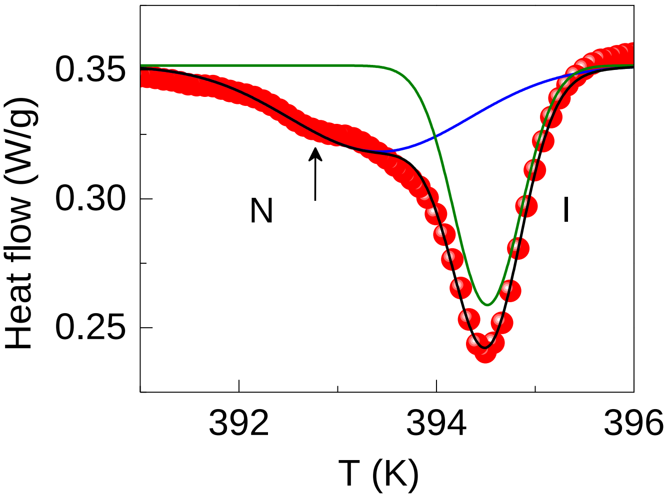

Figure 6.12: DSC profile in the vicinity of the I-N transition on enlarged scale exhibiting a double peak profile for the X = 0.005 composite, with the position of the weaker peak indicated by the arrow corresponding to the surface I-N transition, discussed in the text. The profile is fitted with a sum of two Gaussian expressions (black line), the individual contributions being resolved as shown by coloured lines.

Optical microscopy observations show that there is no textural change across the small peak, with the material remaining in the nematic phase. The separation between the twin peaks decreases for X=0.01 composite, and for higher concentration materials it is difficult to discern such a feature, even if present owing to the fact that the overall strength diminishes. A twin peak profile for the isotropic-nematic transition, absent in the pure LC material, has been observed in both specific heat and DSC profiles for composites of LC with aerosil [24, 25; also see Chapter-3]. Analyzing high resolution calorimetric, light scattering and microscopy techniques, Caggioni et al [25], propose that in the LC-aerosil systems the nematic order develops from the isotropic phase through a two-step process and explain in terms of a system exhibiting temperature dependent disorder strength, and due to a crossover from a random-dilution regime where the silica gel couples to the scalar part of the nematic order parameter, to a low-temperature random-field regime where the coupling induces distortions in the director field. A similar crossover phenomenon has been found in disordered antiferromagnets [26].

As it happens in these systems also, the presently studied materials show that the high-temperature peak is much sharper compared to the low-temperature peak. While the random field crossover phenomenon mentioned above is possible in the present case also, the observed double peak profile here can also be viewed in terms of a surface transition separated from a bulk transition. The bulk transition is caused by molecules which are away from the GNP surfaces and are not influenced by the particles. The second transition is due to the molecules which are attached to, or in the immediate vicinity of GNP. Such "*surface"* LC molecules bind to GNP (through chain-chain interaction of the hydrophobic chain on the LC molecule and the capping agent of the particle) with an orientation that is locally perpendicular to the particle surface creating a region of higher disorder in comparison to the *bulk* region. The reduced order of the surface molecules would also lower their transition temperature. If the surface effects become strong, then there can be a bifurcation of the temperature at which the bulk and the surface molecules undergo the transition resulting in doubling of the peaks. With increasing concentration of GNP, the proximity of the particles reduces the unaffected bulk regions thus weakening the thermal signal at the transition, and consequently diminishing the ability to detect the surface transition.

6.7 Electrical conductivity

Figures 6.13(a) and (b) show the conductivity along ($\sigma_{\|}$) and perpendicular ($\sigma_{\perp}$) to the nematic director ($\vec{n}$) obtained at 1 kHz by having a small probing voltage (0.5V) parallel and normal to $\vec{n}$, respectively, whose direction is fixed by imposing an orienting magnetic field of magnitude 1 T. In order to avoid the effects of the sample pre-history and any transient processes, the samples were first heated to the isotropic phase and the data were collected in the cooling mode.

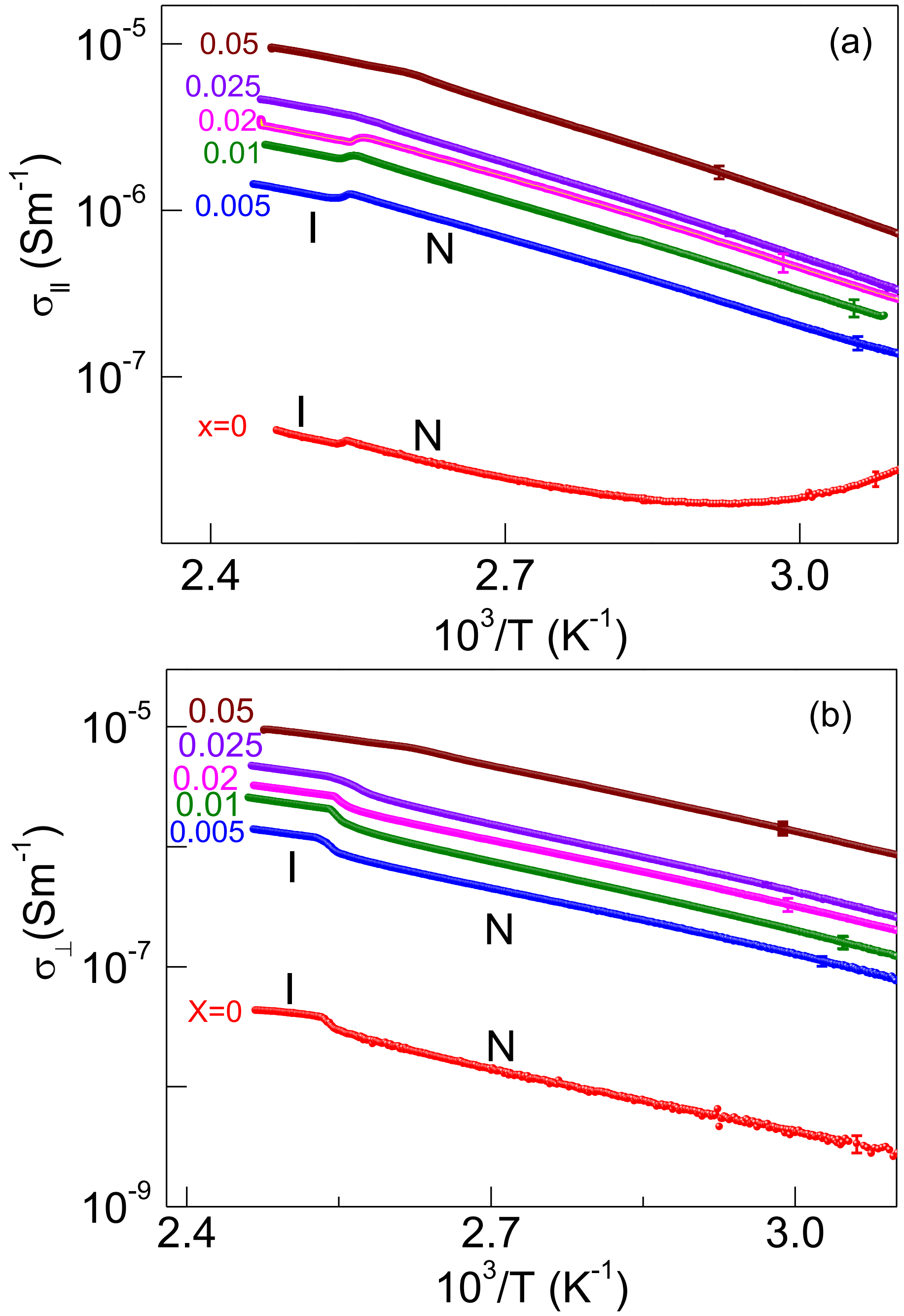

Figure 6.13: Thermal dependence of the electrical conductivity at 1 kHz on a semi-logarithmic scale (a) along, and (b) perpendicular to the nematic director direction for the pure LC and the different composites, with the concentration of GNP indicated against each data set. The step like change seen in each set corresponds to the I-N transition.

Even at a cursory level, the data presented are consistent with the percolation model, i.e., the σ values, which for the pure LC are typical of insulators, increase by more than an order of magnitude even for the lowest concentration studied, viz., X = 0.005. With further increase in concentration there is a steady increase in the value resulting in an overall increase of ~ two orders of magnitude for X =0.05. Two other features seen in figures 6.13(a) and (b) are: (i) $\sigma_{||}$ for pure LC exhibits an anomalous increase at low temperatures (high 1/T). As we shall see later this is an artefact resulting from the dielectric relaxation of the medium. (ii) For all concentrations, the I-N transition is marked by a step or change in the slope of the temperature dependence of σ, although the effect gets smoothened for higher concentrations.

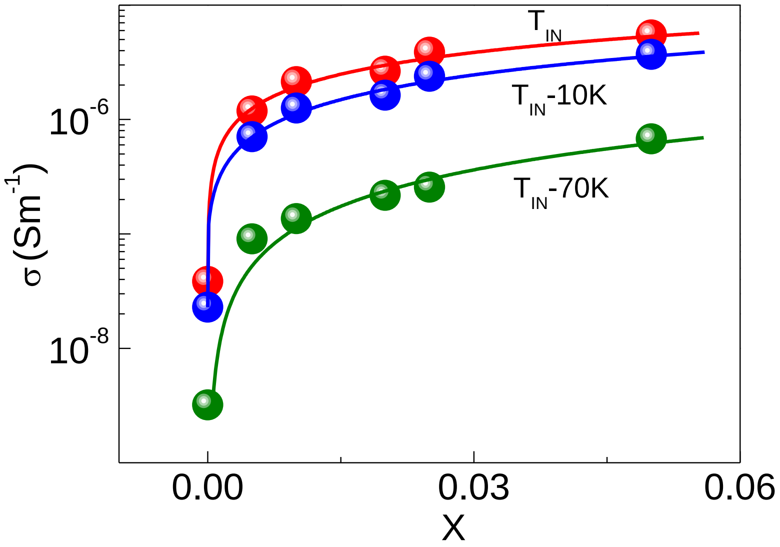

Figure 6.14: GNP concentration dependence of σ at the isotropic-nematic transition (T_{IN} set), and $\sigma_{\perp}$ in the nematic phase, not too far from the transition (T_{IN} -10K set) and deep in the nematic phase (T_{IN} -70K set). The lines represent the fit to the percolation model (eq. 6.2). Error bars are smaller than the symbol size used.

The concentration dependence of the σ value at the I-N transition, and $\sigma_{\perp}$ in the nematic phase taken at two fixed relative temperatures of T_{IN}–T =10K and T_{IN}–T =70K are shown in Figure 6.14. The data sets exhibit transition to a reasonably high conducting state at concentrations of GNP exceeding X = 0.005, and the behaviour is again typical of systems showing a percolation threshold [27], which can be explained as follows. With increase in the content of GNP in the composite, the interactions between individual GNPs become important, and at the percolation threshold, defined as content of GNP necessary for building a continuous conductive path inside the isolative matrix, a transition from the nonconductive to the conductive state occurs [28]. After the drastic increase at the threshold, σ develops a much weaker dependence on further increase in the concentration of GNP. The abrupt increase at the threshold followed by a weaker increase can be described by a percolation scaling law of the type

$$\sigma \propto (X - X_c)^t \qquad (6.2)$$

Here X_c is the threshold concentration and t is a characteristic exponent. Fitting the data presented in Figure 6.14 to eq. (6.2) yields exponent values which are essentially the same, being t=0.63± 0.03 and 0.71± 0.05 in the nematic (at T_{IN}–10K) and at T_{IN} respectively. It should however be noted that these values are much lower than found in a large number of insulating systems [29], in which the conducting state is induced by the addition of particles such as carbon nanotubes (CNTs). In such polymer-CNT complexes, the value of the exponent t is dependent on the dimensionality d of the system: t =1.1-1.3 for d = 2, and 1.6-2.0 for d=3. Thus the exponent values for the currently studied composites, are much lower than these expectations. The experimental values are rather closer to those expected in the pre-percolation regime, which definitely is not true in the present scenario. But it may be recalled that deviations are often found in conductive composites containing dispersed fillers, and attributed [30] to many peculiarities associated with such systems, such as, host–filler interaction and existence of contact phenomena on the particle–particle boundary. In the case of liquid crystal hosts, a further parameter that may have to be included is the influence of thermal fluctuations on the fluid environment, and consequently on the connectivity of the metal particles with their organic capping unable to maintain a time-independent contact. This requirement is perhaps supported by our observation that the exponent increases from 0.63 to 0.99 when the lowest temperature data (at T_{IN}–70K) in the nematic phase are considered. In part B we discuss how the duration of the contact may be enhanced by embedding the material in get matrix.

For an anisotropic system, the behaviour in different directions is an important feature. Figure 6.15 shows the concentration-dependence of the conductivity anisotropy, defined as $\sigma_a = \sigma_{||}/\sigma_{\perp}$, exhibiting a gentle decrease of about 15% from X=0 to X=0.05 and suggesting that the charge transport becomes more isotropic. This could be arguably due to the network becoming more 3D-like, as the GNP concentration is increased. Employment of anisotropic metal particles perhaps reduces this tendency to form a 3D network, and thus help to retain the conductivity anisotropy ratio unaltered [10].

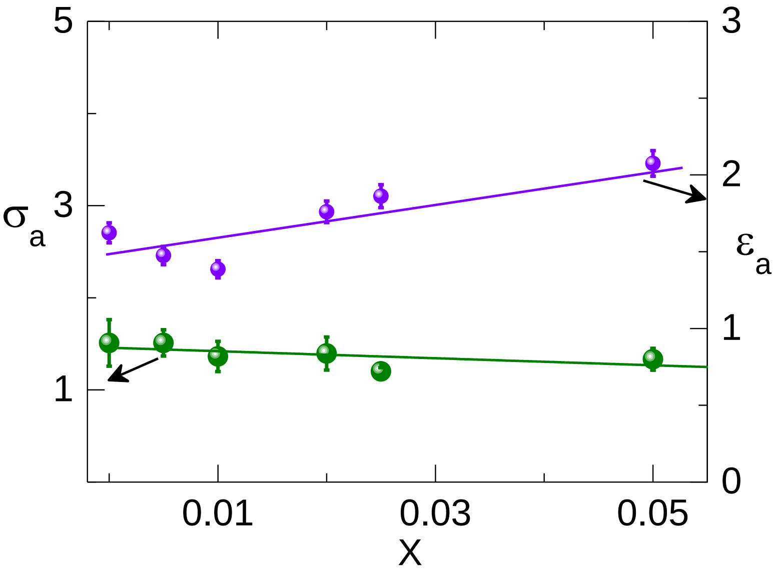

Figure 6.15: Concentration dependence of the conductivity anisotropy σ_a *(=* $\sigma_{//}/\sigma_{\perp}$*) and permittivity* ε_a *(=* $\varepsilon_{//} - \varepsilon_{\perp}$*) at a relative temperature of* T_{IN} *-10 K. The lines are just guides to the eye.*

6.8 Arrhenius behaviour of conductivity

Both the anisotropic conductivities, $\sigma_{||}$ and $\sigma_{\perp}$ (in the nematic phase), and σ at T_{IN} exhibit significant temperature dependence. Owing to the influence of the low frequency director relaxation on $\sigma_{||}$, mentioned above, we use the $\sigma_{\perp}$ data for analysis in the nematic phase. In the semi-logarithmic depiction in Figure 6.13(b), σ is seen to vary linearly with inverse temperature. Therefore we fitted the data in the two phases (except in the vicinity of the transition) to the Arrhenius law

$$\sigma = \sigma_o \exp\left(\frac{-E_s}{k_B T}\right) \qquad (6.3)$$

This equation is derived to describe the change of the electrical conductivity with temperature for the general case of non-metallic thermally-driven conductors, with E_s denoting the thermal activation energy of electrical conduction that depends on the nature of the conductor, the prefactor (σ_0) being the conductivity when the reciprocal temperature approaches zero and k_B, the Boltzmann constant. It should however be mentioned that the quality of fitting improves slightly if instead of the Arrhenius law, the Vogel–Fulcher–Tammann (VFT) expression, $\sigma(T) = \sigma_o \exp[-B/(T - T_g)]$ with T_g as the glass transition temperature, is employed. However, since experiments could not be carried out at temperatures which are close to the possible T_g we limited the analysis to the Arrhenius law. The E_s values obtained by a least-squares fit of the data to eq. (6.3) for the different concentrations in the nematic and isotropic phases are presented in Figure 6.16 and also listed in Table 6.1.

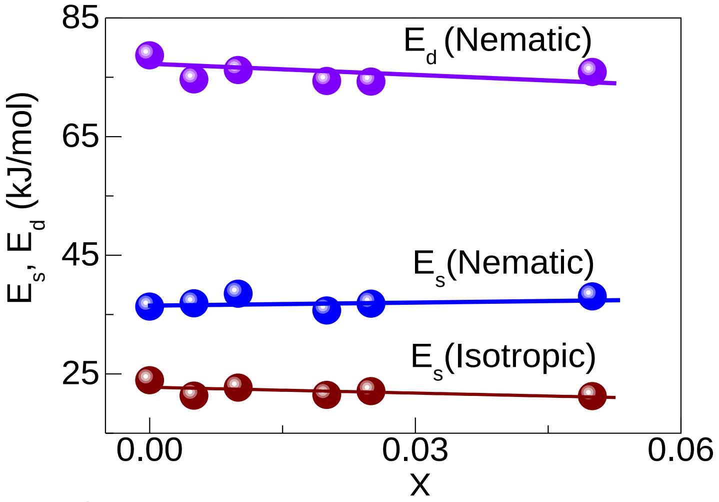

Figure 6.16: Influence of GNP concentration on the activation energy values associated with the thermal dependence of conductivity (E_s) and the dielectric relaxation frequency (E_d). The lines are merely guides to the eye. The error bars are contained inside the symbols used, as can be seen from Table 6.1.

Interestingly, the activation energy values in the isotropic phases are about half of those in the nematic phases indicating that the charge transport is influenced by the underlying orientational order, although the conducting particles are themselves isotropic. It may be mentioned that the activation energy values obtained from the $\sigma_{||}$ data set (by considering the region away from the relaxation frequency artefact mentioned above) is marginally different from those for the $\sigma_{\perp}$ data.

Table 6.1: Activation energies (in kJ/mol) for the thermal behaviour of the conductivity (E_s) and dielectric relaxation frequency (E_d) as a function of GNP concentration in the composite

X	**E_s**		**E_d**
	Nematic	**Isotropic**	**Nematic**
0	36.3 ± 0.05	23.9 ± 0.07	78.7 ± 0.20
0.005	36.9 ± 0.05	21.3 ± 0.06	74.6 ± 0.08
0.01	38.5 ± 0.02	22.7 ± 0.02	76.2 ± 0.10
0.02	35.7 ± 0.02	21.5 ± 0.02	74.4 ± 0.08
0.025	35.7 ± 0.03	21.5 ± 0.02	74.4 ± 0.08
0.05	36.8 ± 0.04	22.1 ± 0.03	74.3 ± 0.08

6.9 Frequency dependence of conductivity

The frequency-dispersion of conductivity is an important characteristic of conductors formed by particle-doped insulators. A wide variety of materials including glasses, polycrystalline semiconductors, polymers, transition metal oxides, organic-inorganic composites, ceramics, etc., exhibit a similar frequency dependent conductivity, often termed Jonscher's *Universal Response* [31]. In such materials, at low frequencies, one observes a constant conductivity while at higher frequencies the conductivity becomes strongly frequency-dependent. Therefore it is customary to express the conductivity σ (f) measured at a finite frequency f as $\sigma(\mathrm{f}) = \sigma_{DC} + \sigma_{AC}$ where σ_{DC} and σ_{AC} are the zero-frequency DC component, and AC contributions, respectively. The Jonscher's universal description considers a distribution of hopping probabilities between sites distributed randomly in space and in energy and uses the following explicit expression for σ (f)

$$\sigma(\mathrm{f}) = \sigma_{DC}\left(1 + k\left(f / f_c\right)^n\right) \tag{6.4}$$

where k is a constant and in disordered solids, $0 < n < 1$. The critical frequency f_c marks the onset of the conductivity relaxation, and the transformation from long range hopping to the short range motions. Figure 6.17 presents the frequency-dependent $\sigma_\perp$ data for pure LC and composites, with X= 0.02, with the observed behaviour consistent with other such conducting systems. The solid lines depict the fitting to eq. (6.4) showing that the expression describes the data well.

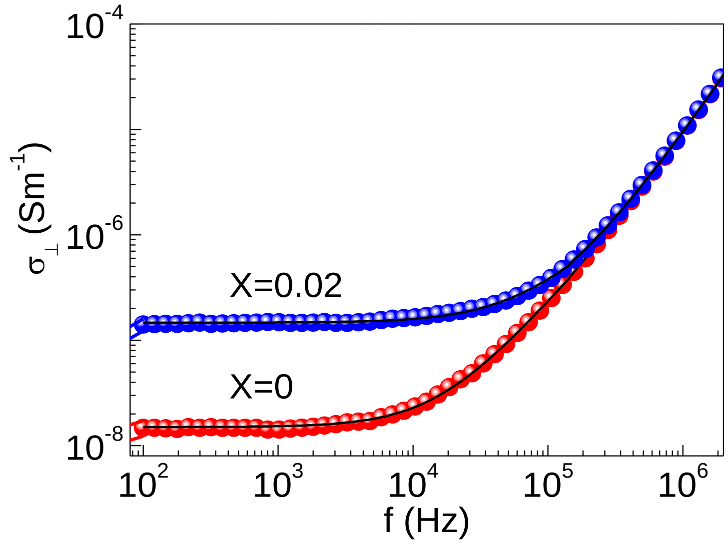

Figure 6.17: Probing frequency dependence of the conductivity for the pure LC and the X = 0.02 composite at a relative temperature of T_{IN}-70K. The lines represent the fit to eq. (6.4).

For both the two materials the fitted values of the exponent, n = 1.45 ± 0.01 and 1.26 ± 0.02 for X = 0, 0.02 composites respectively, fail the universal expectation that the exponent should be <1. The reason for this discrepancy is not clear to us, although it must be mentioned that the model, which is meant for disordered solids does not obviously consider thermal fluctuations, a feature that is invariably present in the nematic phase, and cannot be ignored. It may, however, be pointed out that discussing a jump relaxation model Funke [32] suggested that a value of n >1 could actually be suggesting a physical situation wherein the motion involved is a short hopping of the species localized to the neighbourhood. More recently Papathanassiou et al, [33] highlighted the experimental observations in certain glassy materials [34] and proposed a model stating that there is no physical argument to restrict the value of n below 1. According to them while a qualitative universal behaviour of the AC conductivity in disordered media is envisaged, there need not be a universal fractional power law. More liquid crystalline systems have to be investigated to test the application of this idea in soft systems. The critical frequency f_c is seen to increase with increasing concentration, behaviour consistent with that seen for insulating polymers incorporated with conducting particles [35].

6.10 Dielectric permittivity

The temperature dependence of the permittivity along ($\varepsilon_{||}$) and perpendicular ($\varepsilon_{\perp}$) to the nematic director determined at a fixed frequency of 1 kHz for the pure LC and three composites, X=0.01,0.02 and 0.05 are shown in Figure 6.18.

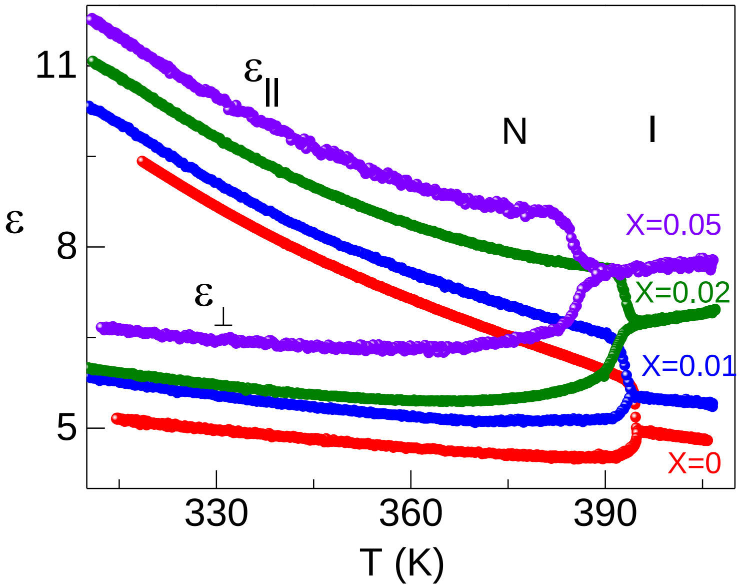

Figure 6.18: Thermal variation of the permittivity in the isotropic and nematic phases measured at 1 kHz along ($\varepsilon_{||}$), and perpendicular ($\varepsilon_{\perp}$), to the director for the pure LC and composites. In each case the temperature at which there is a step-like change marks the transition between the two phases. The significant increase in the values with increasing concentration of GNP is evident.

In all the three sets the abrupt change in the data marks the I-N transition. Several interesting features are seen: (i) the composites retain the positive dielectric anisotropy of the pure LC, (ii) both the anisotropic permittivities ($\varepsilon_{||}$ and $\varepsilon_{\perp}$), as well as the value in the isotropic phase (ε_{iso}) increase with increasing GNP concentration, (iii) the difference between $\varepsilon_{||}$ and $\varepsilon_{\perp}$ appears to increase as X increases. These features suggest that there is an additional dipolar contribution from the metal particle network to the overall permittivity of the medium, which increases with the concentration of GNP. The increase in ε for the composite is also possibly due to the creation of an increased number of GNP-LC-GNP capacitors. A better explanation perhaps is the following. An increase in dielectric constant in polymeric systems with metal nanoparticles has been attributed to the phenomenon of Coulombic blockade [36]. This phenomenon, which has found applications in single electron transistors [37] and thermometers [38] etc., occurs in systems having tunnel barriers separating conducting islands from one another and the electrodes, resulting in an enhancement of the permittivity. Such a blockade also leads to a lowering of the dielectric dissipation factor. This could not be checked in the present system owing to the presence of a low frequency relaxation, to be discussed below.

The anisotropy ε_a (= $\varepsilon_{||} - \varepsilon_{\perp}$) at T_{IN}–10K, shown in Figure 6.15, exhibits a marked increase of 28%. It may be recalled here that the qualitative behaviour of ε_a seen for the present system is quite similar to that for composites with a strongly polar nematic liquid crystal having spherical [9] as well as rod-like GNP [10], and thus is perhaps a general feature of GNP/LC systems. In liquid crystalline materials an enhancement in ε_a is associated with an increase in the orientational order. However, the lowering of σ_a discussed earlier, and the director relaxation behaviour (vide infra), indicate the opposite, i.e., a reduction in nematic order with increasing GNP concentration. In view of this antagonistic requirement we tend to think that the increase in the dielectric anisotropy to be arising from the polarisability of the GNPs.

6.11 Dielectric relaxation spectroscopy

Figure 6.19 (a) and (b) show spectra for the real (ε′) and imaginary (ε″) parts of the permittivity for the pure LC and composites with X = 0.05 at a fixed relative temperature of T_{IN}−70 K. While the increase in ε′ could be because of reasons mentioned above, the enhancement of ε″ could be either due to an increased electrical conductivity (described below) or associated with GNP-LC interfacial regions. More than the absolute values of the LC and composite samples (the governing relaxation frequency of the mode being approximately the midpoint of the step in ε′ and peak point in ε″ data) – that is important.

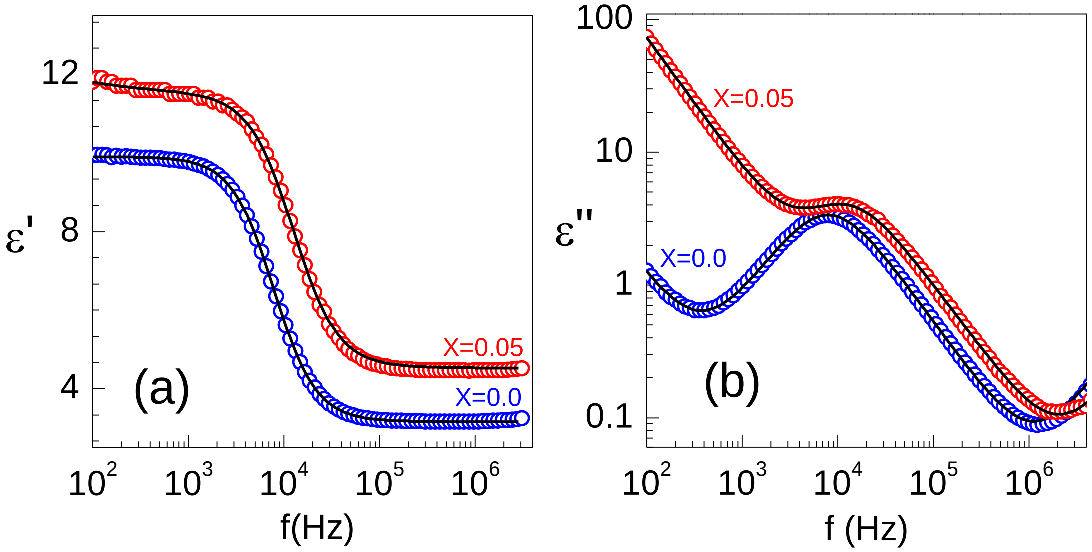

Figure 6.19: Dielectric relaxation spectra in the nematic phase (T_{IN} -70K) for the pure LC and a representative composite X = 0.05 exhibiting a clear relaxation process in both the (a) real and (b) imaginary components of the permittivity. The large increase in ε" at low frequencies is due to the conductivity of the system, by subtracting which the relaxation curves stand out as shown in the figure 6.20. The lines represent the fit of the data to eq. (5.1).

The single relaxation is associated with the director relaxation, and it is notable that the relaxation frequency appears to be shifting to higher values with increasing X; nearly doubling in the value from X=0 to 0.05. We will discuss this feature below. Especially for the composite in the vicinity of the relaxation, the data of the imaginary component (ε''), is partially masked by the large frequency dependence of ionic current contribution extending from the lowest frequency. However, quantitative description of the data using a standard Havriliak-Negami (HN) expression [39], already described in Chapter-5 (eq.5.1), clearly brings about the relaxation phenomenon in the composite also. For both the pure LC and the mixtures the frequency-dependent data are well described by the HN equation. The HN parameter β was found to be equal to 1 for the pure LC as well as the mixtures, indicating a symmetric relaxation profile. The other parameter, α, also turned out to be equal to 1 for the pure LC indicating a Debye relaxation; for the LC-GNP dispersion, however, $0.93 < \alpha < 1$ indicating a slight distribution of the relaxation times.

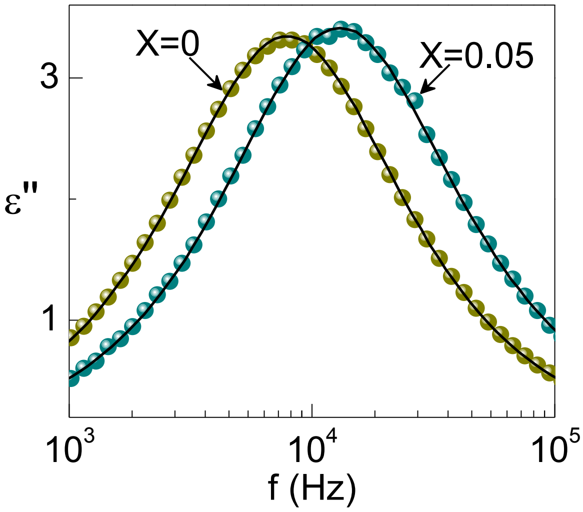

Figure 6.20: ε'' vs frequency for X=0 and X=0.05, obtained after subtraction of the conductivity contribution. The lines stand for the fit of the data to eq. (5.1).

As stated earlier, the large conductivity masks the existence of the relaxation for the composite. But the subtraction of the conductivity contribution estimated from the third term of eq. (5.1) brings out the dielectric features in the imaginary part of the permittivity also (see Figure 6.20). In fact, the observed features in ε'' are in conformity with those seen for ε'. In the frequency range studied $\varepsilon_{\perp}$, the permittivity in the plane perpendicular to the nematic director, has hardly any frequency dependence, while $\varepsilon_{||}$ exhibits a relaxation. For the material under study, the relaxation creates a situation wherein at a particular frequency, referred to as the crossover frequency (f_{cr}), $\varepsilon_{\perp}$ cuts through the $\varepsilon'_{\parallel}$ data. This causes ε_a to be positive below f_{cr}, and negative, above f_{cr}; invariably, f_{cr} lies in the close proximity of f_R. Figure 6.21 shows the GNP concentration (X) dependence of the dielectric anisotropy below ($+\varepsilon_a$) and above ($-\varepsilon_a$) f_{cr}, and it is seen that both the parameters have a very weak dependence on X.

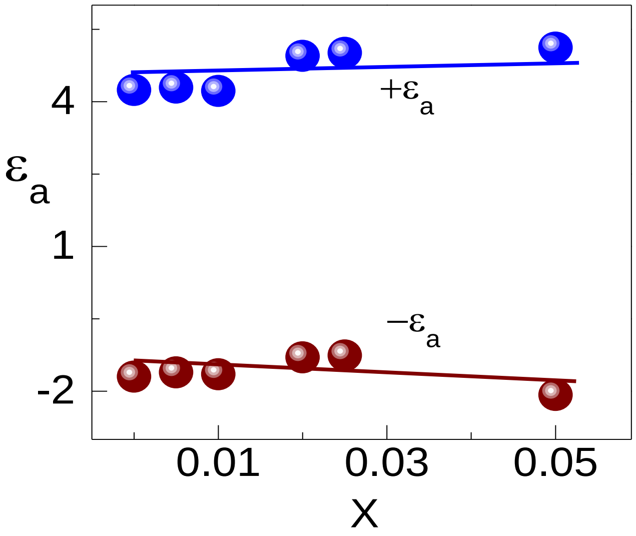

Figure 6.21: Permittivity anisotropy below (+ε_a) and above (-ε_a) the crossover frequency that lies very close to the relaxation frequency. The error bars are smaller than the symbol size used.

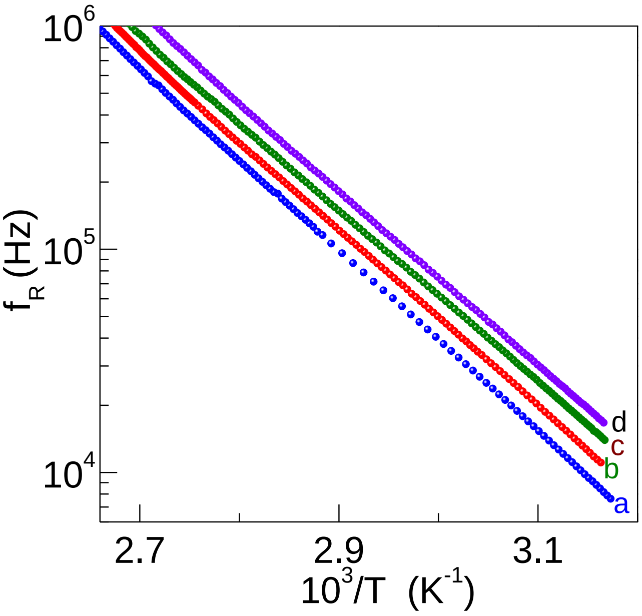

Figure 6.22: Temperature dependence of the dielectric relaxation process in the nematic phase of the pure LC (a), and the composites X = 0.01, 0.02 and 0.05 (b,c,d) exhibiting Arrhenius behaviour, the activation energy (E_d) of which is shown in Figure 6.16.

The temperature dependence of the relaxation frequency f_R for the pure LC and different composites are shown in Figure 6.22. The presence of the nanoparticles is seen to have a substantial influence on the magnitude of relaxation frequency: f_R increases with increasing X, as shown in Figure 6.23 presenting the concentration dependence of the relaxation frequency at a constant temperature of $T = 50\ ^oC$.

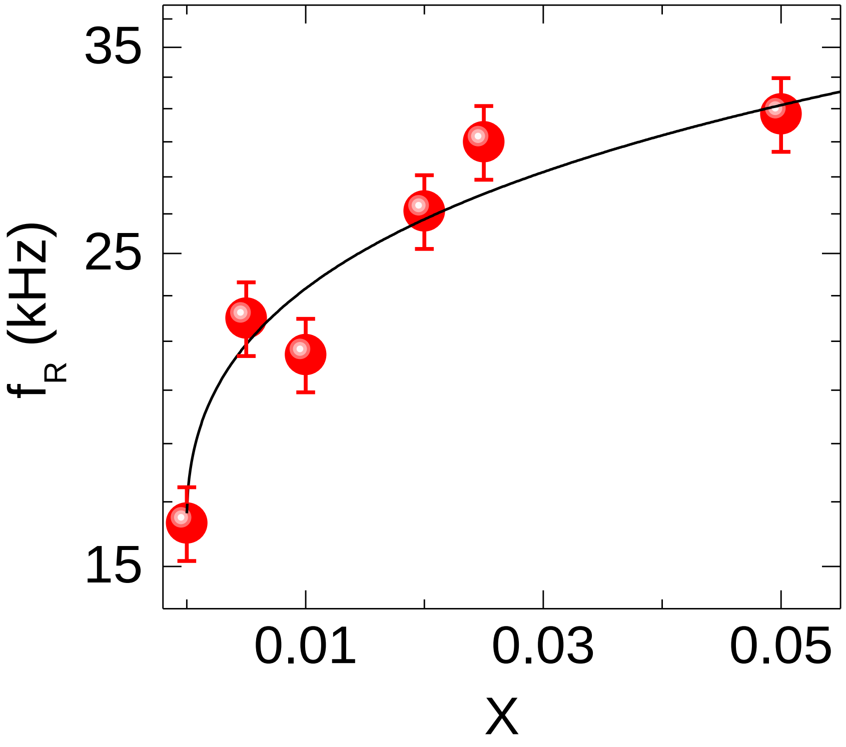

Figure 6.23: Plot to show the strong influence of GNP concentration on the relaxation frequency at $T = 50^oC$ *(Note that the data is presented on a semilogarithmic scale). The line is merely a guide to the eye.*

An increase in f_R for the observed director relaxation mode can be associated with a reduction in the orientational order. In fact, such an increase in the relaxation frequency is also seen in a non-conducting nanoparticle/LC system [24], such as, for example, in composites of nematic with aerosil particles. However, the effect is much weaker in the case of aerosil systems. For example, with the same host LC and a particle concentration of 5%, the increase in f_R is only ~ 20% for the aerosil composites, whereas the presently studied GNP composites exhibit a doubling of the value. This is indicative of the stronger reduction in the order parameter for the GNP composites than for the aerosil mixtures. Of course, a feature of the aerosil system that should be borne in mind is that the hydroxyl groups decorating the particles create a hydrogen bonded network that perhaps is responsible for diminishing the influence of the particles on the order parameter of the system. For the pure LC and the composites as well f_R has a linear dependence (except in the vicinity of T_{IN}) with reciprocal temperature in the semi-logarithmic representation shown in Figure 6.22. As mentioned in the conductivity case, such a feature indicates Arrhenius behaviour. Accordingly we fitted the data to

$$f_R = f_o \exp\left(\frac{-E_d}{k_B T}\right) \qquad (6.5)$$

The E_d values obtained by a least-squares fit of the data for the different concentrations in the nematic phase are given in Table 6.1 and also graphically represented in Figure 6.16. Unlike the concentration-independence of E_s, the activation energy for the conducting process, E_d exhibits a small decrease with X. These two features suggest that despite the large changes in the magnitude to the parameters of σ and f_R, the activation energies are not altered much by the presence of the metal particles. Further E_d values are much higher than the corresponding E_s values indicating that different mechanisms control the two processes.

To conclude part A, we consider the importance of the host PCPBB LC molecule used in the present study. As already stated the molecule does not possess a strong dipole moment along the long axis of the molecule, but has a weak one (*Cl*) along the transverse direction. Since there is no basis to expect the interaction between the PCPBB molecule and the metal particle surface (the dodecane thiol shell rather than the bare particle) to be dipolar in nature, we consider such an interaction to be hydrophobic – between the terminal chains of PCPBB and the dodecane chain of GNP. Maximizing such an interaction would then make the LC molecular arrangement in the vicinity of GNP to radiate out resembling a pin-cushion, and lowering the order parameter of the region. However, the resulting elastic deformation of the director profile would not allow the radiating pattern to extend over long distances away from GNP. With an increasing concentration of GNP the regions around the particles also start interacting diminishing the overall order parameter of the medium. These features are schematically shown in Figure 6.24.

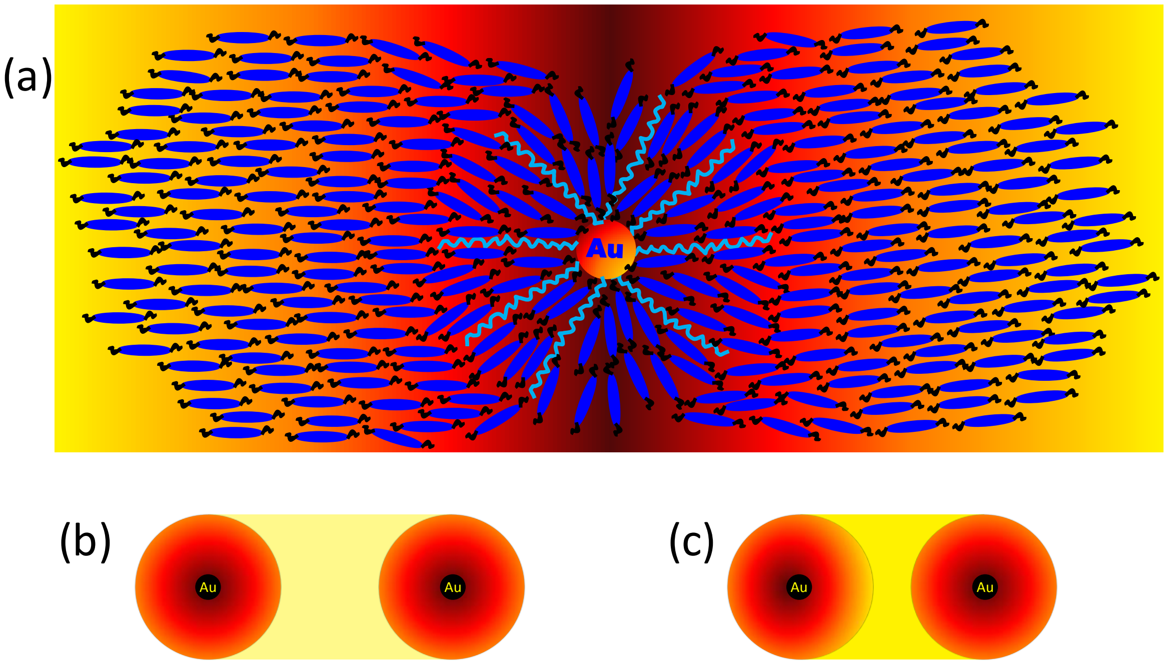

Figure 6.24: Schematic illustration to show the disruption of the oreientational ordering of the liquid crystal molecules in the vicinity of GNP: The dodecane thiol chains involved in the capping of the particle are shown in wiggles in cyan, and the LC molecules as blue ellipses with two hydrocarbon chains (shown as black wiggles) on either side the molecule. Moving away from the centre of the particle, the orientational ordering increases towards the value dictated by the surrounding nematic. This feature is colour coded such that lighter the colouring, higher is the orientational ordering. When the particles are far apart the ordering of the intervening region is comparable (light yellow) to that of the bulk nematic, as shown in (b). When the particles come nearer as would happen with higher concentration of GNP, the disordering increases shown with deeper yellow in (c).

Part B: Composites of Gold Nano Particle-Liquid Crystal in a Restricted Geometry Created Aerosil Particles

As discussed in the Introduction for Chapter-3, understanding the theoretical as well as experimental aspects of the influence of geometrical restrictions on properties of LC has been quite attractive in recent years [40]. In this direction, composites of LC with silica composites (aerogels/aerosils) are considered to be interesting model systems [41]. While several properties of the LC-aerosil composites have been studied, the influence of QRD on the electrical conductivity of LC, or more importantly of metal NP doped LC systems has not been investigated. In this part, we describe thermal and probing frequency dependence of electrical conductivity of a nematic composite incorporating gold NP as well as aerosil particles displaying the surprising result that a network of non-conducting particles enhances substantially the conductivity of the LC-GNP composite. Further, the inclusion of aerosil as well moves the system towards classical disordered solids as seen by the power-law behaviour of the high frequency conductivity. The influence of the nature of the aerosil corona (hydrophobic/hydrophilic) is also described.

6.12 Materials

The liquid crystalline host material is the same as that used in part A of the investigations. However, unlike the work on the bulk form, here we employed commercially obtained GNPs, the details of which are given below. The spherical Gold nanoparticles, capped with 1-dodecanethiol and having a diameter of 3 nm, were purchased from Nanopartz^{TM}. The details of the particle characterization, provided by the manufacturer along with the Certificate of analysis are: Particle size as obtained from DLS and TEM: 3 nm; UV-Vis Peak: 516 nm and Concentration of suspension in toulene: 2.49×10^{14} nps/mL. For the creation of aerosil network, two types of nanosilica particles of 7 nm diameter were employed. One of them is hydrophilic (Aerosil A-300), and the other hydrophobic (Aerosil R812) with the specific surface area being 300 ± 30 and 260 ± 30 m^2/g respectively. Both hydrophilic and hydrophobic nanosilica particles (Aerosil®) were from Degussa Corporation, provided as a gift by Mr. Vikas Rane of d-hindia Ltd, Mumbai. Toluene, obtained from a local source, was used as a solvent for dispersing nanoparticles in LC. Details of these types of aerosil particles are already discussed in Chapter-3.

6.13. Preparation of the composites of GNP-LC-Phob/Phil

The procedures for preparing the composites with the different nanoparticles are similar to those described in Part A as well as in Chapter-3, and will not be repeated here. The thermal treatment of keeping the vial containing the constituent materials in a hot air oven at 110^0C for two hours and subsequently subjecting to vacuum drying for about 14 hours ensured a proper composite. The concentration of the Gold NPs was 3 wt%, and aerosil NPs was 1.5wt% in the appropriate composites. Hereafter we refer to the single NP composites as LCPhil (LC with 1.5 wt% hydrophilic aerosil particles) and LCG (LC with 3 wt% GNP). The two-nanoparticle composites, LCGPhob and LCGPhil, contain LCG mixture with the aerosil particles (at 1.5 wt%) being of the hydrophobic/hydrophilic variety respectively. Polarizing Optical Microscopy images display the uniform distribution of the nanoparticles throughout the host material in all the four composites (See figure 6.25).

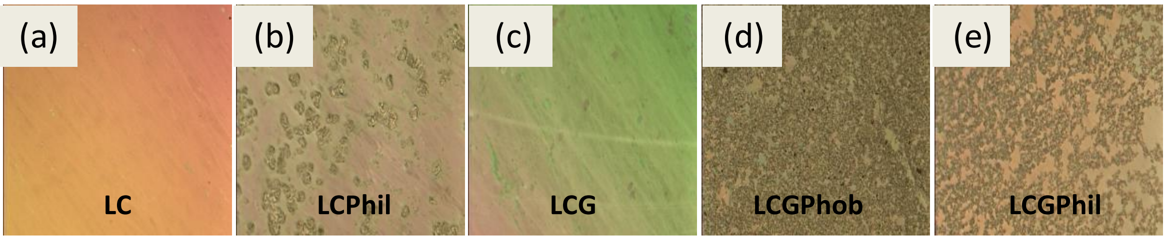

Figure 6.25: Polarizing optical microscopy images of (a) pure LC, (b) LCPhil, (c) LCG, (d) LCGPhob and (e) LCGPhil. Note that in all the four composites GNPs and aerosil particles are dispersed quite uniformly through the host material.

6.14 Results and Discussion

6.14.1 Differential Scanning Calorimeter results

Differential Scanning Calorimeter (DSC) scans (Figure 6.26) showed the existence of a clear thermal signature across nematic-isotropic transition for the pure LC and all the composites. While the peaks are quite strong for pure LC and LCPhil materials the thermal signatures become much weaker for the other composites.

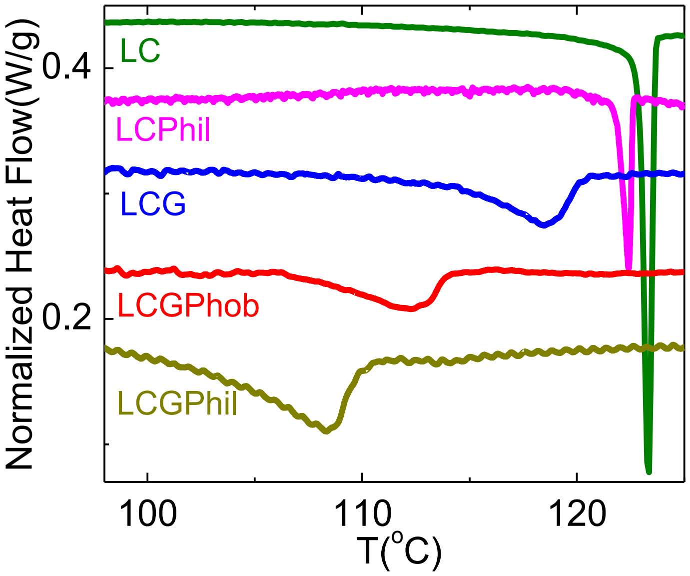

Figure 2.26: Differential scanning calorimeter scans for the pure LC and the different composites across the isotropic-nematic transition at a cooling rate of 5K/min.

6.14.2 Thermal variation of conductivity

The temperature-dependence of $\sigma_{\perp,}$ the conductivity perpendicular to the nematic director, for the pure LC as well as the different composites, is shown in Figure 6.27. In all the cases the isotropic-nematic transition is clearly indicated by a marked change in conductivity. The transition temperatures obtained with these data agree with the information from DSC. The σ values marginally increase between LC and LCphil materials, but exhibit more than three orders of magnitude enhancement on adding GNP (LCG) to the LC material. Such a behavior must be expected, as discussed in part A. However, addition of the insulating aerosil particles leads to the surprising feature of a further increase in conductivity by factor of 4-5. The extent of increase is clearly dependent on the nature of the corona with the hydrophilic composite (LCGPhil) being more conducting than the hydrophobic one (LCGPhob). It must be noted that upon addition of aerosil (i) the enhancement in the conductivity is observed in the nematic as well as the isotropic phases, and (ii) the anisotropy in the nematic phase is still retained, as confirmed from additional measurements of $\sigma_{\|,}$ i.e., σ along the director. In fact, the magnitude of the anisotropy appears to be essentially the same for the pure compound as well as the composites. We shall explore possible reasons for the enhancement of σ later.

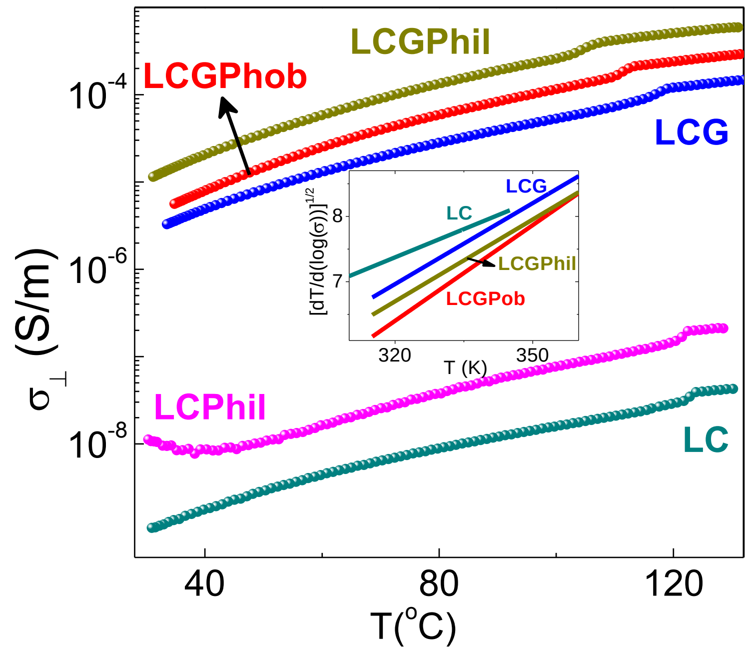

Figure 6.27: Temperature dependence of electrical conductivity perpendicular to the nematic director for the pure LC and the different composites with nanoparticles. Data in the inset represent the derivatized form of eq. (6.7), also known as the Stickel plot. The slope and intercept of this linear form yields the fragility strength and VFT estimate of the glass transition temperature.

Before discussing the detailed thermal variation of σ we would like to point out that the dataset for LCPhil exhibits a reversal in the thermal trend at low temperature, a feature that can be explained considering the interaction of the LC molecules with the virtual surfaces at the interfaces with aerosil particles. The hydrophilic aerosil particles which are entirely decorated with siloyl groups provide a strong anchoring of the LC molecules at the particle surfaces. Thus, the spherical shape of the particles would lead to a 3-dimensional “powder-like” alignment of the LC molecules present in the vicinity of the aerosil surface despite the fact that the bulk of the LC molecules have the orientation dictated by the substrate surface or applied field. This results in a certain number of molecules being in the homeotropic orientation and thus being influenced by the director relaxation. This feature is not seen for pure LC sample because there is no opposing influence for the surface-dictated orientation. The absence of the step for the LCG composite shows that the anchoring at the GNP surfaces (with alkyl thiol capping) is much weaker than at the aerosil surfaces. The GNP influence could perhaps be dominating when both (GNP and aerosil) kinds of nanoparticles are present, as seen for the LCGPhil and LCGPhob composites.

The inclusion of the nanoparticles alters the quantitative thermal behaviour of σ. For example, whereas the two insulating materials (LC and LCPhil) exhibit Arrhenius behaviour, log(σ) versus inverse temperature being strictly linear, the three GNP containing composites present a significant deviation. Deviation from the Arrhenius behaviour is often taken to be indication of a glass transition at low temperatures. The *super-Arrhenius* behaviour, commonly seen in glass-forming molecular liquids and polymeric systems, is often portrayed by the Vogel–Fulcher–Tammann (VFT) expression. The VFT equation is similar in form to that of the Arrhenius equation, but with the important exception that the value diverges exponentially at a finite temperature. For the temperature dependence of σ it is expressed as

$$\sigma(T) = \sigma_o \exp\left(\frac{DT_o}{T - T_o}\right) \tag{6.6}$$

Here D is the fragility strength coefficient and T_o is the VFT estimate of the glass transition temperature. Considering the non-linear nature of this expression, it is derivitazed with respect to T to get a linear form. This representation, known as the "Stickel plot" [42] is given as

$$y = \left(\frac{d\log(\sigma)}{dT}\right)^{-1/2} = \left(DT_o\right)^{-1/2}(T - T_o) \tag{6.7}$$

The parameters D and T_o can be directly obtained from the slope and intercept of this equation. Inset of figure 6.27 inset shows the data for the different composites represented in this fashion. The D and T_o values extracted from the fits to eq.(6.7) are given in Table 6.2. To be noted is the fact that the D value for the three composites are much smaller than 10 and significantly lower than for pure LC. This is important since the magnitude of D, a measure of the deviation of σ (T) curve from thermally activated behaviour, has been employed to classify a large number of glass formers [42]: Materials labelled *fragile* glass formers exhibiting large deviations have small values of D (typically D < 10) whereas *strong* glass formers (D > 10) follow the Arrhenius law. Thus all the three GNP composites studied here can be classified as fragile glass formers. In contrast, the host LC shows a strict Arrhenius behaviour and therefore should be regarded as a strong glass. The much weaker temperature dependence of the behavior for the pure LC material, characterized by a high value of D =17, indeed supports this premise. Owing to a possible influence of the relaxation discussed above, the data for LCPhil composite are not considered here, although it is apparent that this material also has an Arrhenius behavior.

6.14.3 Frequency dependence of the conductivity

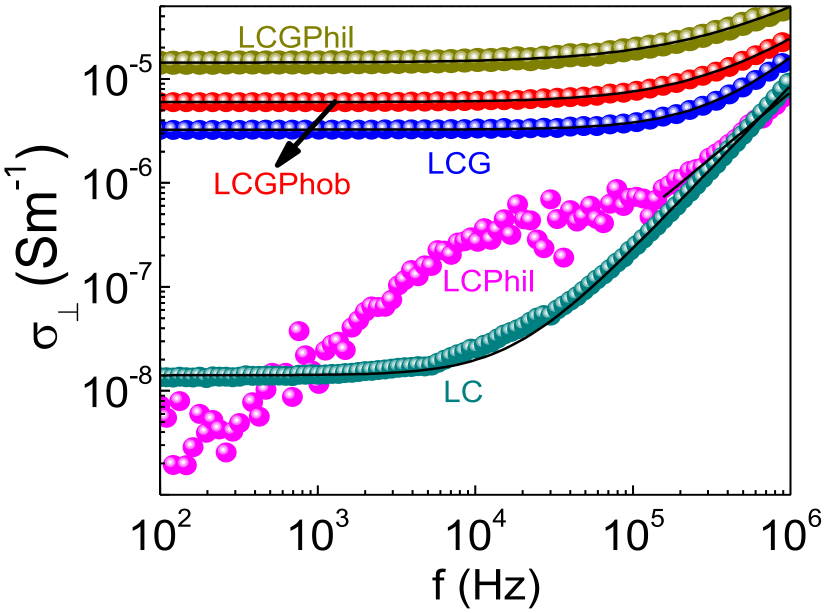

Figure 6.28: Frequency spectrum of the conductivity for the pure LC and the different composites at room temperature. The lines show the fit to eq. (6.8) and yield the exponent n.

The fit was not performed on the data for LCPhil composite owing to the possible influence of the director relaxation discussed in the text.

To describe the observed frequency dependence of conductivity we use Jonscher's universal principle which considers a distribution of hopping probabilities between sites distributed randomly in space and in energy, and employs the following explicit expression for σ (f)

$$\sigma(\mathrm{f}) = \sigma_{DC} + kf^{n} \qquad (6.8)$$

Where, *k* is constant and the exponent n is known to be in the limits $0 < n < 1$ for disordered solids. The frequency spectra for the pure LC and the different composites studied here (see Figure 6.28) are in qualitative agreement with the expectation of the universal behaviour. The step-like feature seen in the intermediate frequency ranges for the LCPhil composite is due to the director relaxation combined with antagonistic orientation condition of certain molecules, as explained in section 6.14.2. The good description of the high frequency data by eq. (6.8), as indicated by the solid lines in Figure 6.28, suggest the applicability of universality for all the samples investigated here. The evaluated exponent n, however, shows a surprise (see Table 6.2). For the pure LC the value is very high, $n = 1.59 \pm 0.025$, and falls outside the Jonscher limits as seen in part A also. With the addition of nanoparticles, *n* reduces to such an extent that the two-particle system LCGPhil composite has values which are in the ambit of the Jonscher limit (see Table 6.2). The value of *n* being in this limit is characteristic of a situation in which the hopping charge carriers are subject to energy barriers that randomly vary in space. Thus, in the case of the LCGPhil composite, although the confined LC is still a fluid, the overall material behaves like a disordered solid. For all the materials, the critical frequency f_o, marking the transformation from long range hopping to the short range motions, was taken to be the frequency at which the conductivity reached 110% of its low frequency value. With this convention it is seen that f_o increases by about an order of magnitude changing from 5.8 kHz for pure LC to 65 kHz for LCG composite, but gets lowered slightly upon adding the second type nanoparticles, indicating that the presence of the nanoparticles extends the long range hopping to a wider frequency range.

Table 6.2: Parameters obtained by fitting the experimental data for different materials to equations (6.7) and (6.8).

	LC	**LCG**	**LCGPhob**	**LCGPhil**
T_o (K)	71	156	193	164
D	17	3.7	2.2	3.5
n	1.59	1.36	1.07	0.87
f_o (kHz)	5.8	65	33	25

Now we propose a possible physical scenario involving network dynamics, for the observed enhancement of conductivity of the LCG composite upon addition of aerosil particles. The feature that the underlying phenomenon of conductivity in the studied materials is percolation dominated [28] forms the basis of this reasoning. Percolation theory expects that a random assembly of nanoparticles has a critical surface coverage, labelled percolation threshold (P_t), above which the network is connected across the sample resulting in classical conduction. The pure LC represents a system far below P_t having essentially no connectivity resulting in insulating characteristics. This is true for the LCPhil composite also since the added particles are also insulating. The situation changes when GNP is added to LC; at the concentration employed here the system is located [see part A of this Chapter] above P_t and thus there is a dramatic increase in conductivity. A large number of connections are available for the charge transport, and thus the behaviour should be like that of filler particles in a disordered insulating system. The significantly large conductivity, which exists over a wide range of frequencies for the LCG composite, is in conformity with the expectations for the filler/matrix system. However, differences do exist, especially in the form of the exponent *n* obtained for the high frequency behaviour. The *n* value, although below that for pure LC, is still substantially higher than the model expectations [31]. An obvious reason is that the percolation models are meant to describe disordered solids, and definitely do not consider thermal fluctuations. Such fluctuations, inherently present in the nematic phase, cannot be ignored for the fluid-like LC and LCG cases. The scenario is changed by the addition of aerosil particles. The presence of siloyl groups on the surface and the consequent capability for H-bonding makes the aerosil particles to gelate a large number of organic liquids, including liquid crystals [41]. From visual inspection of the sample vials it is evident that this feature is true for the host LC used here as well; there is a drastic increase in the viscosity of the system upon addition of aerosil. At the microscopic level, to begin with, three to four lightly fused nano sized (7 nm diameter) primary aerosil particles attach to each other giving rise to H-bonded silica chains with branched fractal structures [43]. These aggregates in turn form a gel by diffusion-limited aggregation process. The LC molecules get contained in cavities of the quite fragile gel network. Such containment brings in finite size effects into the problem, and therefore restricts the range of thermal fluctuations. Applying it to the case of percolation network metal particles, it can be envisaged that in the absence of aerosil, the thermal fluctuations are strong enough to sustain quite a few “dead bonds”, i.e., connections which are broken (see Figure 6.29a). The strengthening of the system by H-bonding would reduce the thermal fluctuations of the GNPs resulting in resurrection of the dead bonds (Figure 6.29b). This results in a longer path for the charge transport.

Indeed in a recent experiment on conducting molecular crystals reduction of the H-bonding of the system was observed to lower the electrical conductivity [44]. Another way of looking at it is to consider that the aerosil chains provide a solid-like connection through the system (at least through the broken percolation network regions). The improved percolation network thus leads to higher electrical conductivity. In this simple picture, the strength of the H-bonded network can be expected to tune the magnitude of σ. Indeed we see such a feature, when we compare the σ values for LCGPhil and LCGPhob. While in the former type of particles, the decoration is entirely of siloyl groups, in the latter type some of the siloyl groups are replaced by alkyl chains. The reduced number of hydrogen bonds available per particle still creates a network (gel), albeit much weaker. The weaker network results in a smaller increase in conductivity for the LCGPhob system in comparison to that for the LCGPhil composite. These features are in agreement with the values of the evaluated exponent *n* for the two systems. It is worthwhile recalling here that employing molecular simulations, Nigro et al demonstrated that formation of a gel by conducting colloidal particles leads to enhancement in bulk conductivity, and ascribed it to the interparticle electron tunnelling [45].

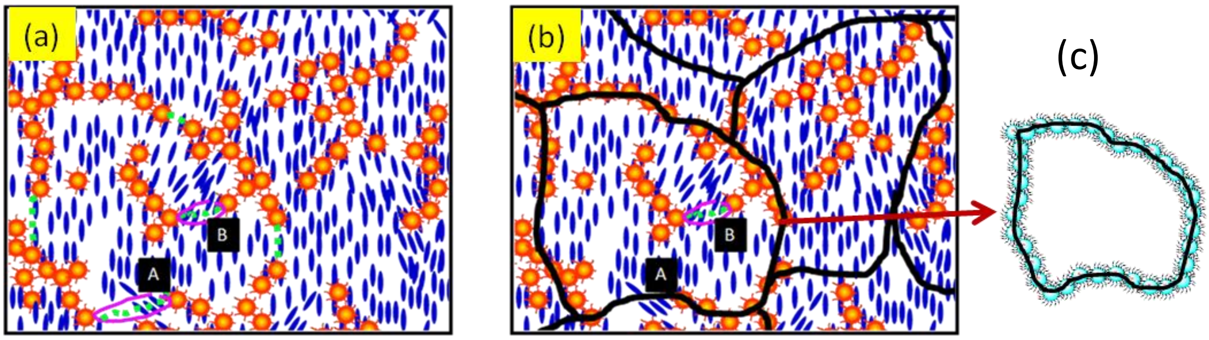

Figure 6.29: Schematic illustration of a possible model for the enhancement of conductivity due to the gel network. The percolation networks due to GNPs (Orange circles) are randomly spread around in the sea of nematic liquid crystals (Blue lines). (a) The non-ideal nature of this network results in several "dead-bonds" (Green dashed lines); two representative dead-bond regions labelled A and B are shown encircled. (b) The imposition of the gel hydrogen-bonded network (Black contours) created by the aerosil particles (shown as cyan circles in (c)) heals some of the dead-bonds (for example, in the region A) providing a longer path for the charge transport, thus enhancing the conductivity of the LCGPhil composite.

In fact, it is possible that tunnelling between Gold nanoparticles could be augmented if they are trapped inside the H-bonded aerosil network, causing the conductivity to increase. Detailed experiments by varying the concentration of GNPs and aerosil particles should throw more light on these attractive metal nanoparticle nematic gels. Designing materials with combinations of local fluidity and global mechanical robustness through the unprecedented route suggested in the present work can yield highly conducting materials amenable for easy moulding owing to their semisolid nature. Such materials are potential candidates for improved energy storage and transport applications.

6.15. Summary

We have performed detailed calorimetric, frequency-dependent anisotropic conductivity and permittivity measurements in composites of gold nanoparticles (GNP) and a weakly-polar nematic liquid crystal possessing a low frequency director relaxation in its bulk form, and by confining the composite in a network of aerosil particles. The presence of the nanoparticles substantially lowers the nematic-isotropic transition temperature and also the associated transition entropy. The conductivity of the composites is enhanced by two orders of magnitude, with a concentration dependence described by a percolation scaling law usually observed in mixtures of metal particles and polymers. The exponent determined is much smaller, which could be due to the presence of thermal fluctuations characteristic of the fluid-like nematic medium. The frequency dependence of the AC conductivity exhibits a critical frequency that increases with concentration of GNP; the high frequency response is not in agreement with Jonscher's *Universal Response principle*. The low frequency of the director relaxation mode enabled detailed dielectric relaxation spectroscopy studies, the first of its kind. While the value of the relaxation frequency depends strongly on the concentration of GNP, the activation energy remains essentially the same. We compare the observations with those predicted by the dilution theory, and find a general agreement. Experiments by replacing the spherical particles used here with anisotropic particles would further test the predictions of the theory.

In the second part of the Chapter, we have demonstrated that a network of insulating aerosil particles can have a strong influence on the magnitude of the electrical conductivity of a nematic liquid crystal composite comprising GNPs, increasing it beyond the values achieved by the metal particles. The gel network which results in a large bulk viscosity of the medium also forces the frequency behavior of the system to conform to the expectations for disordered solids, despite the presence of the confined liquid. It is also seen that the nature of the aerosil corona (hydrophobic/hydrophilic) which provides tunability factor for the H-bonding influences the magnitude as well as the frequency dependence of conductivity. We propose an argument that these features are caused by the repair of the "dead bonds" in the percolation network by the imposed gel network of aerosil particles, extending the path for the charge transport. Such a possibility opens up an avenue to tune the conductivity by controlling the strength of the gel. The methodology is easily amenable to generalization for a variety of systems involving metal particles embedded in an insulating matrix. Since these types of gels have the capability to be self-supporting, free standing conducting systems as well as patternable motifs can be realized.

6.16. References

1. K.I. Winey and R.A. Vaia, *MRS Bulletin*, **32**, 314 (2007).
2. A. Heilmann, *Polymer Films with Embedded Metal Nanoparticles*, (Springer-Verlag, Berlin) (2003).
3. D. Bloor, A. Graham, E.J. Williams, P.J. Laughlin, and D. Lussey, *Appl. Phys. Lett.* , **88**, 102103 (2006).
4. O. Stamatoiu, J. Mirzaei, X. Feng, and T. Hegmann, in *Liquid Crystals Materials Design and Self-Assembly*, Ed. C. Tschierske (Springer-Verlag, Heidelberg) *Top. Curr. Chem,* **318**, 331 (2012); Q. Li (Ed.), *Nanoscience with Liquid Crystals*, Springer Cham (2014)
5. Yu. M. Yevdokimov, V.I. Salyanov, E.I. Katz, S. Skuridin, *Acta nature,* **4**, 78 (2012).
6. K.K. Vardanyan, D.M. Sita, R.D. Walton, W.M. Saidel, K.M. Jones, *RSC Advances*, **3**, 259 (2013).
7. P. Goel, G. Singh, R.P. Pant, and A.M. Biradar, *Liq. Cryst.*, **39**, 927 (2012).
8. M. Draper, I.M. Saez, S.J. Cowling, P. Gai, B. Heinrich, B. Donnio, D. Guillon and J. W. Goodby, *Adv. Func. Mater*, **21**, 1260 (2011).
9. S.K. Prasad, K.L. Sandhya, G.G. Nair, U.S. Hiremath, C.V. Yelamaggad and S. Sampath, *Liq. Cryst.*, **33**, 1121 (2006).

10. S. Sridevi, S. Krishna Prasad, G.G. Nair, V. D'Britto, and B.L.V. Prasad, *Appl. Phys. Lett.*, **97**, 151913 (2010).
11. Neeraj and K.K. Raina, *Optical Materials (Amsterdam, Netherlands),* **35**, 531 (2013).
12. J. Mirzaei, R. Sawatzky, A. Sharma, M. Urbanski, K. Yu, H.S. Kitzerow, and T. Hegmann, *Proc. SPIE 8279, Emerging Liquid Crystal Technologies VII*, **8279**, 827913 (2012); Y.A. Garbovskiy and A.V. Gluscchenko in Solid State Physics Vol. **62**, Eds. R. E. Camley and R. L. Stamps, Academic Press (2011).
13. U.B. Singh, R. Dhar, R. Dabrowski and M. B. Pandey, *Liq. Cryst.*, **40**, 774 (2012).
14. P.K. Tripathi, A.K. Misra, S. Manohar, S.K. Gupta, R. Manohar, *J. Mol. Struc.* **1035**, 371 (2013).
15. W. Haase, A. Lapanik and M. Ottinger, *Proceedings of SPIE 8114, Liquid Crystals XV*, 81140H (2011).
16. J.P.F. Lagerwall and F. Scalia, *Curr. Appl. Phys.* **12**, 1387 (2012); E R. Soulé, J. Milette, L. Reven and A. D. Rey, *Soft Matter*, **8**, 2860 (2012).
17. H. Qi, B. Kinkead and T. Hegmann, *Adv. Funct. Mater.*, **18**, 212 (2008).
18. For a recent review see G. Si, Y. Zhao, E. Leong and Y. Liu, *Materials*, **7**, 1296 (2014) and references therein; Y. Zhao, Q. Hao, Y. Ma, M. Lu, B. Zhang, M. Lapsley, I.C. Khoo, and T.J. Huang, *Appl. Phy. Lett.*, **100**, 053119-1 (2012); Q.K. Liu, Y.X. Cui, D. Gardner, X. Li, S.L. He, I.I. Smalyukh, *Nano Lett.*, **10**, 1347 (2010); A. N. Grigorenko, H. F. Gleeson, Y. Zhang, N. W. Roberts, A. R. Sidorov, and A. A. Panteleev, *Appl. Phys. Lett.*, **88**, 124103 (2006).
19. B.E. Kilbride, J.N Coleman, J. Fraysse, P. Fournet, M. Cadek, A. Drury, S. Hutzler, S. Roth, W.J. Blau, *J Appl Phys.*, **92**, 4024 (2002).
20. M. Brust, M. Walker, D. Bethell, D.J. Schiffrin and R. Whyman, *J. Chem. Soc., Chem. Commun.*, 801 (1994).
21. M.J. Hostetler, J.E. Wingate, C.J. Zhong, J.E. Harris, R.W. Vachet, M.R. Clark, J.D. Londono, S.J. Green, J.J. Stokes, G.D. Wignall, G.L. Glish, M.D. Porter, N.D. Evans and R.W. Murray, *Langmuir*, **14**, 17 (1998).
22. M.V. Gorkunov and M.A. Osipov, *Soft Matter,* **7**, 4348 (2011); M.V. Gorkunov, G.A. Shandryuk, M.S. Alina, Y.K. Irina, S.M. Alexey, V.K. Yaroslav, V.T. Raisa and A.O. Mikhail, *Soft Matter,* **9**, 3578 (2013).
23. P.K. Mukherjee, *Int. J. Mod. Phys. B,* **12**, 1589 (1998); V.M. Lenart, S.L.Gómez, I.H. Bechtold, A.M. Figueiredo Neto, S.R.Salinas. *Eur. Phys. J E Soft Matter*. **35**, 4 (2012);

J.S. Rzoska, A. Drozd-Rzoska, *Nato Science Series II*: A.R. Imre, H.J. Maris, P.R. Williams, (Eds.), **84,** 117 (2002); M.S. Ishtiaque, P. Virgi, G.P. Rolfe and C. Rosenblatt, *Phys. Rev. E*, **67**, 011704 (2003).

24. V. Jayalakshmi, Geetha G. Nair and S Krishna Prasad, *J. Phys.: Condens. Matter*, **19**, 226213 (2007).
25. M. Caggioni, A. Roshi, S. Barjami, F. Mantegazza, G.S. Iannacchione, T. Bellini, *Phys. Rev. Lett*., **93**, 127801-1 (2004).
26. See e.g., D.P. Belanger, *Brazilian J. of Phys*., **30**, 682 (2000).
27. See e.g., Y. Pan, G.J. Weng, S.A. Meguid, W.S. Bao, Z.-H. Zhu and A.M.S. Hamouda, *J. Appl. Phys*. **110**, 123715 (2011).
28. D. Stauffer, A. Aharony, *Introduction to Percolation Theory,* Taylor & Francis, London (1994).
29. See e.g., C.-W. Nan,Y. Shen, and Jing Ma, *Annu. Rev. Mater. Res.* **40**, 131 (2010).
30. Ye.P. Mamunya, V.V. Davydenko, P. Pissis, E.V. Lebedev, *Euro. Poly. J.,* **38**, 1887 (2002).
31. A.K. Jonscher, *Nature (London),* **267**, 673 (1977); J.C. Dyre and T.B. Schrbder, *Rev. Mod. Phys*., **72** 873 (2000); D.L. Sidebottom, B. Roling and K. Funke, *Phys. Rev., B*, **63**, 5068 (2001).
32. K. Funke, *Prog. Solid State Chem*., **22**, 111 (1993).
33. A.N. Papathanassiou, I. Sakellis, and J. Grammatikakis, *Appl. Phys. Lett*., **91**, 122911 (2007).
34. C. Cramer, S. Brunklaus, E. Ratai, and Y. Gao, *Phys. Rev. Lett*., **91**, 266601 (2003).
35. S. Barrau, P. Demont, A. Peigney, C. Laurent, and C. Lacabanne, *Macromolecules,* **36**, 5187 (2003).
36. See e.g., Jiongxin Lu, Kyoung-Sik Moon, Jianwen Xu and C. P. Wong, *J. Mat. Chem.,* **16**, 1543 (2006).
37. M.A. Kastner, *Rev. Mod, Phys.,* **64**, 849 (1992).
38. J.P. Pekola, K.P. Hirvi, J.P. Kauppinen, and M.A. Paalanen, *Phys. Rev., Lett*, **73**, 2903 (1994).
39. S. Havriliak, S. Negami., *Polymer,* **8**, 161 (1967).
40. M. Steinhart, S. Zimmermann, P. Göring, A.K. Schaper, U. Gösele, C. Weder and J.H. Wendorff, *Nano Lett.,* **5**, 429 (2005); S. Krishna Prasad, D.S. Shankar Rao and Geetha G. Nair, *J. Indian Inst. Sci.,* **89**, 211 (2009); C. Krause and A. Schönhals, *J. Phys. Chem.*

C, **117**, 19712 (2013); A. Acreman, M. Kaczmarek, and G. D'Alessandro, *Phys. Rev. E,* **90**, 012504 (2014).

41. S. Iannacchione, *Fluid Phase Equilibria.*, **177**, 222 (2004).
42. F. Stickel, E.W. Fischer and R. Richert, *J. Chem. Phys.*, **102**, 6251 (1995); P. Lunkenheimer, U. Schneider, R. Brand and A. Loid, *Contem. Phys.,* **41**, 15 (2000).
43. F.J. Galindo-Rosales, F.J.Rubio-Hernández, J.F. Velázquez-Navarro, *Rheologica Acta*, **48**, 699 (2009).
44. A. Ueda, S. Yamada, T. Isono, H. Kamo, A. Nakao, R. Kumai, H. Nakao, Y. Murakami, K. Yamamoto, Y. Nishio, and H. Mori, *J. Am. Chem. Soc.*, **136**, 12184 (2014).
45. B. Nigro, C. Grimaldi, P. Ryser, F. Varrato, G. Foffi, and P. J. Lu, *Phys. Rev. E*, **87**, 062312 (2013).

Chapter-7

Confinement Studies on a Room Temperature Ferroelectric Liquid Crystal

Overview

This chapter describes the results of Xray, linear and non-linear dielectric constant measurements on a room temperature ferroelectric liquid crystalline phase in its bulk form and upon confinement in an Anopore membrane. The used material exhibits smectic C (SmC*) helical pitch of p ∼ 200 nm, which is comparable to the pore dimension of the membrane. Xray measurements show several interesting results including unusually strong harmonic reflections, substantial broadening of the peak profile, correlation length smaller than the pore diameter etc. The data suggest that the smectic A–SmC* transition could be very close to a tricritical point in the bulk and moving away from it upon confinement. The dielectric studies show that confinement accelerates the relaxation dynamics of both the soft and the Goldstone modes, although with a reduced strength. The non-linear component of the dielectric constant exhibits qualitatively different thermal behaviour in the bulk and Anopore samples.*

The results are published in:

M. Vijay Kumar, S. Krishna Prasad, D.S. Shankar Rao and E.P. Pozhidaev, Confinement driven effects in a room temperature ferroelectric liquid crystal: X-ray, linear and non-linear dielectric investigations, *Phase Transitions*,. **86**, 323–338 (2013).

7.1 Introduction

Smectic A (SmA) and smectic C (SmC) liquid crystals are layered structures possessing quasi long-range positional order in one dimension represented by a mass density wave [1]. In the smectic A (SmA) phase, the director $\vec{n}$ is parallel to the layer normal while in the smectic C (SmC) phase it is tilted with respect to it. However, the arrangement of the molecules within the layer is liquid-like in both the cases. The chiral version of these two smectics, labelled SmA* (or sometimes simply SmA) and SmC*, exhibit certain interesting properties, and have attracted much attention [2]. Phase transitions involving these ferroelectric liquid crystals (FLCs) have been of significant interest, owing to the presence multiple order parameters, and coupling between them etc. The advent of bistable fast responding and high contrast displays have made FLCs technologically important.

7.1.1. Origin of ferroelectricity in Liquid crystals

Since the director $\vec{n}$ is apolar (except under very special circumstances [3] we need to consider only the possibility of spontaneous polarisation in a direction normal to the local director. In the achiral and chiral versions of the nematic and Sm A phases, the symmetry is so high that the occurrence of ferroelectricity is prevented due to (i) free rotation around the long molecular axis (cylindrical symmetry about the director axis), (ii) a weak dipole-dipole interaction such that the thermal energy is larger than the interaction energy and/or (iii) cancellation of the effective dipole moment by the formation of antiparallel arrangement of the molecules. Now, let us consider the symmetry arguments, which allow for the existence of ferroelectricity in the chiral SmC* phase [4]. For spontaneous polarisation to exist in a given phase, the polarisation $\vec{P} = (P_x, P_y, P_z)$, which is a polar vector, must be invariant under symmetry operations that are allowed in the structure under consideration. In the achiral SmC phase with a point group symmetry C_{2h} (see figure 7.1) as well as the chiral SmC* phase, having point group symmetry C_2, a 2-fold rotation around the Y-axis (axis perpendicular to the tilt plane) is an allowed symmetry operation.

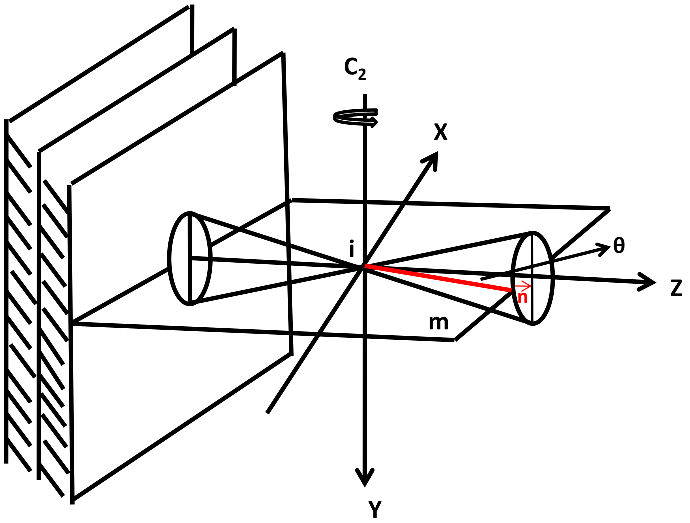

Figure 7.1: Symmetry elements in the Smectic C phase : a two-fold symmetry axis C2 parallel to the layer and along y-axis, a mirror plane m perpendicular to this two-fold axis and the centre of inversion 'i'.

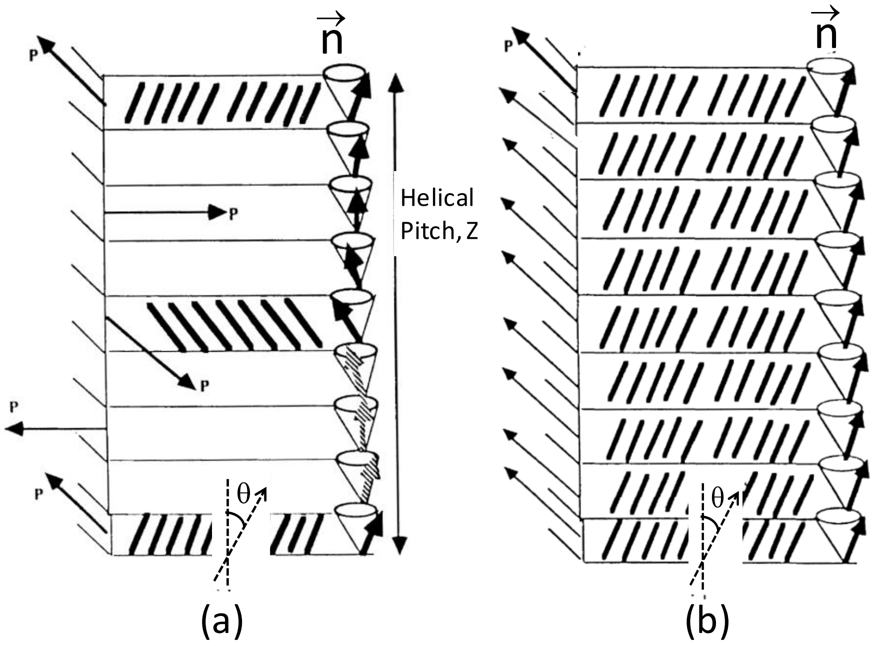

Fig 7.2: (a) Twisted smectic C structure, in which the director precesses around the layer normal forming a helix causing the net polarization to get cancelled out (b) Unwound smectic C* structure - helical structure when unwound with the application of a field will result in a net polarization P_s.*

Under this transformation, the polarisation vector transforms according to $\vec{P} = (P_x, P_y, P_z) \Rightarrow (-P_x, P_y, -P_z)$. Since these two expressions must be identical, the possibility of a spontaneous polarisation only in the direction of the two-fold axis, i.e, $\vec{P} = (0, P_y, 0)$ is allowed. In the achiral SmC phase, the XZ plane (the tilt plane) is a mirror plane, which changes $(0, P_y, 0)$ into $(0, -P_y, 0)$. Again, since these two expressions must be identical, $\vec{P}$ must be zero and thus ferroelectricity is not allowed in the achiral SmC phase. On the other hand, in the SmC* phase the molecules, being chiral, are not mirror images of themselves and therefore due to chirality the reflection operation is not allowed. Thus, the absence of the XZ mirror plane leads to the SmC* phase becoming ferroelectric, whereas the achiral SmC phase is not. The spontaneous polarization in the SmC* phase points in the direction of the Y-axis, i.e., perpendicular to the plane of the tilt. But the presence of chirality makes the director to precess around the layer normal on going from one layer to the another giving rise to a helicoidal structure whose pitch values are in the range (~μm) [2, 5-10]. Thus the spontaneous polarization of each layer, tightly coupled to the tilt direction also precesses around the layer normal averaging out the macroscopic polarization to zero in the undistributed state (see figure 7.2(a)). The helical structure can be unwound by the application of an external force, e.g., electric field. The resulting uniform state (see figure 7.2(b)) shows a non-zero value of P_s, whose magnitude goes to zero in the SmA phase.

7.1.2 Overview of literature on ferroelectric liquid crystals under confinement

In contrast to reports on the nematic-isotropic and nematic-smectic A transitions, the effect of confinement in more complex mesophases like the ferroelectric SmC* has been investigated only scarcely [11-17]. In the following we will not be mentioning those cases wherein the thickness of the smectic film is found to considerably influence the SmA to SmC* phase transition [18, 19] by competing with the length scale of the helix. Aliev and Kelly [12] studied the dynamics in the vicinity of the SmC*-SmA transition of a FLC confined in porous glass. They found that in macropores (pore size ~ 100 nm) the rotational viscosities associated with the two collective modes are about 10 times higher than in the bulk. In micropores (pore sizes ~10 nm), neither of the collective modes was detected. Investigating the influence of aerogel confinement on a FLC Xu et al [13] reported a significant broadening of the second order SmA to SmC* transition. Further it was seen that upon confinement a single relaxation process in the SmA phase splits in to three processes at the transition to the SmC* phase. The process occurring at frequency ranges intermediate to the two processes observed in the bulk was attributed to an interfacial liquid crystal layer at the large inner surfaces of the porous matrix.

In the case of a FLC compound having small spontaneous polarisation P_s, confinement in Synpor membranes led [15] to the complete disappearance of collective dynamic processes for all the pore sizes studied – 0.23 to 0.85 μm – which were smaller than the helical pitch. With another material having a higher Ps, and a shorter pitch, these authors found that the mode connected with azimuthal fluctuation could be observed, although its strength was reduced by almost two orders of magnitude, broadened with respect to the bulk and shifted to higher frequencies by more than one decade. Kutnjak et.al [20] studied the influence of the dispersed aerosil particle concentration on dielectric relaxation. Both the collective modes were found to be strongly suppressed with increasing x, the concentration of aerosil. The critical coefficient γ, which reveals the character of the AC transition, approaches the value characterizing the three-dimensional XY universality class. At the transition, the gap in the relaxation frequency of the two modes increases as x increased. Confining a FLC compound with a large P_s in Anopore membranes Sandhya et al [16] observed that the temperature dependence of the x-ray layer spacing shows a qualitatively different behavior, the relaxation frequency of the collective mode increases by a factor of 2.5 in the smectic-A phase, whereas in the smectic C* phase the increase is much larger: factor of 400. Thus, it can be concluded that the relaxation parameters can be expected to depend on the matrix structure and surface interactions. This chapter describes X-ray, linear and non-linear dielectric constant measurements on a room temperature ferroelectric liquid crystalline phase in its bulk form and upon confinement in an Anopore membrane. To be emphasized is the fact that the used material exhibits smectic C* (SmC*) helical pitch of p ~ 200 nm, which is comparable to the pore dimension of the membrane.

7.2 Materials

The room temperature FLC mixture, labeled FLC-576, was developed at the P. N. Lebedev Physical Institute of Russian Academy of Sciences, Moscow [21]. Its constituents, phase sequence and transition temperatures are given in figure 7.3. A point concerning this material, is that the helical pitch in the SmC* phase is very short ~ 200 nm [21c], and thus in the same range as the nominal pore diameter of the matrix used to restrict the length scale of the medium.

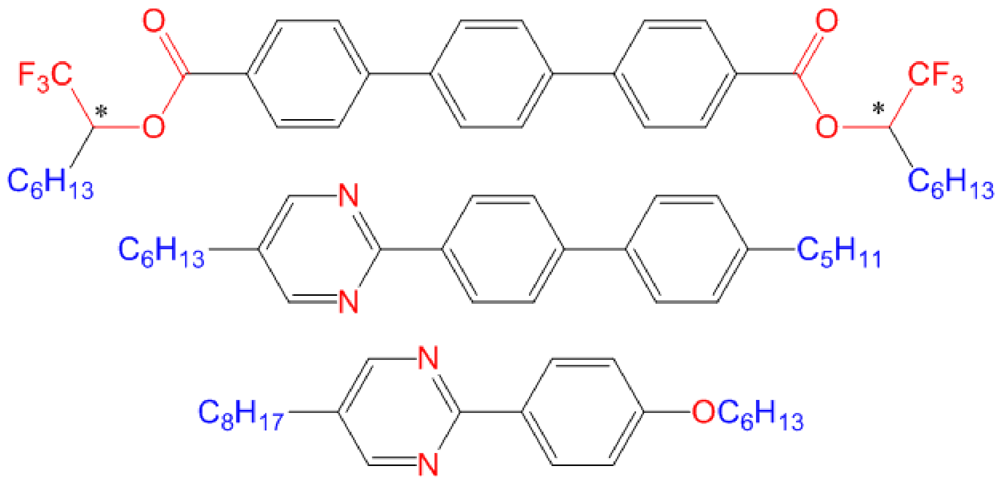

Isotropic 90°C Smectic A 74.3°C Smectic C*

Figure 7.3: Molecular structure of the constituents, the phase sequence and transition temperatures of FLC-576 mixture.

The Anopore membranes (Anodisc, Whatman) with a pore size of 200 nm, thickness of 60 μm, 50% porosity and a pore density of 10^9 cm^{-2} are employed to impose the required geometric restriction on the sample (Further details of this membrane are already given in

Chapter-2). The aspect ratio (pore diameter/membrane thickness) of the channels is over two orders of magnitude and therefore alludes a low dimensionality (quasi 1D) to the system. The as-supplied membranes have a strong tendency to orient the LC molecules to be orthogonal to the membrane plane or along the pore normal. To obtain the molecular orientation in the plane of the membrane, the cavity surfaces were treated with palmitic acid, before filling the liquid crystal for promoting the LC molecules to lie in the plane. The details about sample filling etc. are similar to those given in Chapter-2.

7.3 Methods

Xray measurements were performed using the PANalytical X'Pert PRO MP Xray diffractometer, described in Chapter-2. A wide-frequency range impedance analyzer (Solatron model 1260) along with a broadband dielectric converter (BDC-N, Novocontrol), controlled by WINDETA software (Novocontrol) was used to carry out the linear dielectric experiments (Experimental set up already given in Chapter-5). The non-linear dielectric measurements were performed using Lock in Amplifier (EG&G Instruments, DSP7260). A schematic diagram of the set up used for non-linear dielectric measurements is given in figure 7.13 and the details are discussed in section 7.4.4. For dielectric measurements in the bulk configuration, the sample filled in a 40 μm thick cell made up of unidirectionally rubbed, polyimide coated ITO glass plates was used. For measurements in the confined geometry, the Anopore membrane filled with the sample (procedure given in Chapter-2) was sandwiched between two ITO-coated glass plates serving as electrodes. With the director perpendicular to the pore wall (membrane normal), which is also the probing electric field direction, this geometry allows us to study the behaviour of the dielectric constant perpendicular to the director. Since the calculation of the empty cell capacitance is not trivial in Anopore membranes, we present the dielectric data for the confined sample in terms of the capacitance normalized with respect to the value deep in the SmA phase.

7.4. Results and Discussion

7.4.1. Xray diffraction

7.4.1.1 Harmonic peaks

Figure 7.4a shows the raw Xray diffraction profiles obtained for the bulk and Anopore samples in the SmC* phase at room temperature. The most significant feature to be noticed is that the bulk as well as the confined sample exhibit, more than one reflection in the low angle region (see Fig. 7.4b and 7.4c). The peak 2θ values determined by fitting the raw data to a Lorentzian expression are such that the values for the higher angle reflections are exact integer multiples of the lowest angle peak, indicating that they are the higher-order harmonic reflections of the fundamental. The observation of even the second harmonic peak is rather surprising, owing to the fact that smectic layering is argued to be represented by a pure sinusoidal wave. Such a representation necessitates the higher-order harmonic reflections from the layer order, even if present, to be extremely weak. High resolution experiments were in fact used to show that the second harmonic peak is at least four orders of magnitude weak in intensity than the fundamental peak. This was found to be true immaterial of whether the substance is composed of strongly polar molecules or not [22-25]. These studies were indeed used to quash the simple picture of layering in the smectic phase wherein the molecules stack like planks of wood (In the jargon of mass density wave, such a perfect stacking would mean a square wave profile for the periodicity). At the molecular level, the formation of the smectic phase is caused by microphase separation of the rigid core and paraffinic tail portions of the molecules. Therefore the extent of such segregation should be the control factor in deciding any deviation from the pure sinusoidal modulation. It may be recalled that in the case of lipid bilayers [26], sugar terminated molecules [27], polymers [28] multiple harmonic peaks have been reported (in the case of lipids where a sheet of water separates the lipid bilayers up to 9 harmonic peaks were seen).

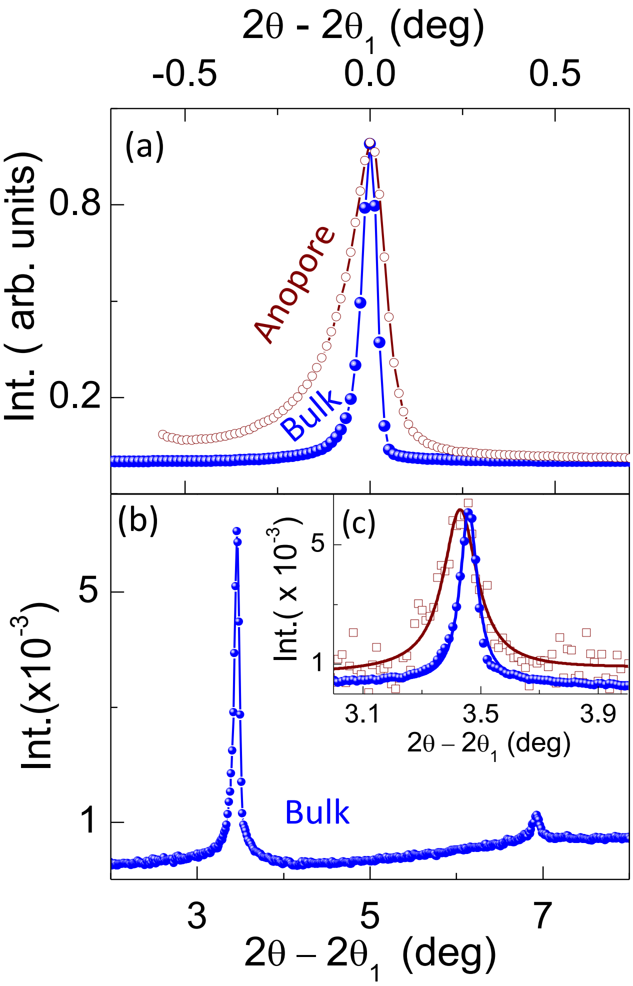

Figure 7.4: Xray diffraction profiles in the low angle region for the bulk (filled symbol) and confined (open symbol) samples, shown in terms of reduced diffraction angle. (a) The lowest angle peak, with a Bragg angle $2\theta_1$, corresponds to the layer thickness of the smectic phase. Notice that upon confinement the profile is broadened. (b) The second and third harmonic peaks are seen for the bulk sample. The panel (c) shows that the second harmonic is significantly strong, and that its intensity is comparable for the bulk and Anopore sample. For comparison, the intensity of the peaks has been normalized with respect to the peak intensity of the first low angle peak.

In the light of these observations let us look at the results for the present system, which is a low molecular weight thermotropic material without any hydrogen bonding. For the bulk sample, the ratio of the second harmonic intensity to that of the fundamental is 1/177, a value which is about two orders of magnitude higher than that observed for the archetypal alkyl cyanobiphenyl (nCB) material [24]. Even the third harmonic is an order of magnitude stronger than the second harmonic seen for the nCB compounds. In the lipid bilayer, sugar molecule and the polymeric system mentioned above, the reason for the strong layering (intense harmonic peaks) is the well defined layer separation driven by strong dislike of different parts of the molecules. In the present case it is probably caused by the trifluoro groups located near the terminals of one of the constituents of the studied mixture. It has been noted in the past that in the case of a single component material wherein one of the terminal chains has fluoro groups, and the other hydrocarbon groups, the dislike between the two parts can even give rise to a segregated ordering within the layer, as reflected in two diffuse reflections in the wide angle region [29]. Since for FLC-576 only one of the constituents has the fluoro groups, such segregation may not be very strong, but still effective in improving the layering order. We speculate that the dislike between the fluoro and the hydrocarbons perhaps reduces the extent of excursion of molecules between layers in the smectic phase, thereby increasing the layering order. It should be possible to test this idea by measuring the layer compression modulus of such systems, which should be higher than that for, say, nCBs. Surprisingly, confinement of the material in the Anopore membrane hardly affects the relative strength of the second harmonic (see Figure 7.4c) although the background noise increases [the increase in the background intensity is due to scattering from the Anopore matrix]. The strong background scattering in combination with the smaller sample thickness of only 60 μm (thickness of the membrane), is responsible for the non-observation of the third-harmonic reflection. Thus the finite size effects do not seem to be influencing the extent of layering order.

7.4.1.2 Width of the profile

As mentioned earlier, the raw Xray profiles were fit to a Lorentzian expression, in addition to a background term. Figure 7.5 shows β, the full-width-at-half-maximum (FWHM) of the fundamental peak at a few temperatures: confinement widens the peak by a factor of about 4. From the line broadening the average length scale of the structure (ξ_s) can be calculated by using the Debye-Scherrer expression, $\xi_s = 0.89\lambda/(\beta \cos \theta_{peak})$, where λ is the wavelength of the Xray beam.

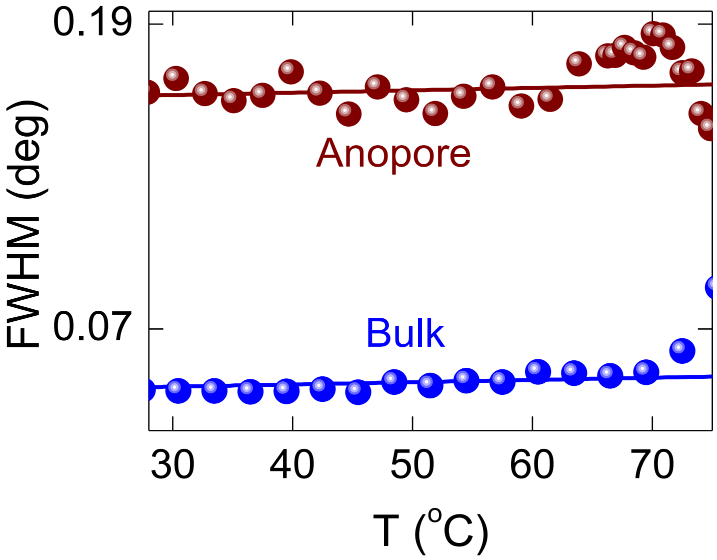

Figure 7.5: Temperature dependence of the width (FWHM) of the lowest angle peak, showing that confinement increases the value by a factor of ~ 4

The calculated ξ_s values is 350 nm for the bulk but much lower – 98 nm – for the Anopore sample [30], clearly showing the effect of confinement. Let us recall that in these experiments the molecules (and therefore the layer normal) lie in the plane of the membrane. Therefore the pore diameter of 200 nm and the layer thickness of ~ 3 nm mean that there can be only about 70 layers within a pore. Hence, finite size effects can be expected to be dominant in restricting the correlation length to which the smectic ordering can grow. However, for the confining case, ξ_s being much smaller than the pore diameter of 200 nm suggests a diminished ordering in the system more than that dictated by finite size effects. Further, in the geometry employed wherein the molecules are forced to lie in the plane of the membrane, the layers should be forming concentric circles, like for example, the layers of an onion slice [31]. The orientation of the molecules would thus be radial planar, leading to a topological defect at the centre point of every pore. This feature can be the limiting factor for the maximum achievable correlation length.

7.4.1.3 Thermal variation of the layer spacing

Figures 7.6 (a) and (b) show the temperature dependence of the layer thickness (*d*) for the bulk and confined geometries respectively. Firstly, it is noted that the Anopore sample has a slightly higher (0.6%) layer spacing, caused perhaps due to the slight stretching of the alkyl chains of the liquid crystal molecules owing to the stronger surface interaction in the confined space.

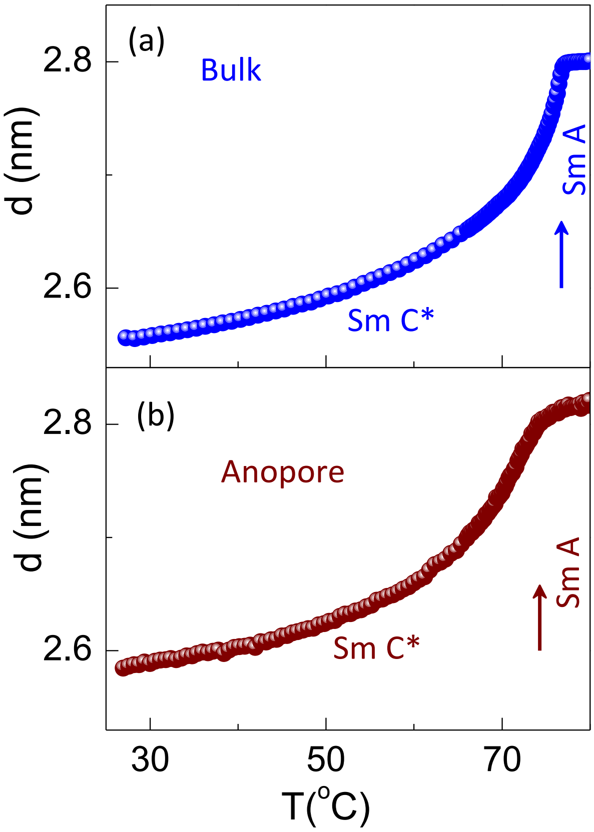

Figure 7.6: The thermal variation of the smectic layer thickness across the SmA and SmC phases for the bulk and (b) Anopore samples. The arrow indicates the transition temperature between the two phases.*

Second and more importantly, there is a qualitative difference in the thermal behaviour in the SmA phase: whereas in the bulk material the value has a very weak dependence on temperature, the Anopore sample exhibits surprisingly a significant positive thermal expansion. Fitting the data in the SmA phase to a straight line, it is found that the slope for the bulk situation is very small $(6 \pm 0.5) \times 10^{-3}$ Å/K, and a factor of 5 smaller than that for the Anopore sample $(30 \pm 1 \times 10^{-3})$ Å /K. Generally, a negative thermal expansion of *d* is not an uncommon feature in the SmA phase, and has been understood to be due to the stretching of the terminal alkyl chains of the molecules. Therefore, the stronger positive thermal expansion seen in the Anopore case here could actually be owing to the presence of a small tilt in the SmA phase itself. Such a feature could be arising due to a tilted anchoring provided by the palmitic acid molecules being anchored at an angle with respect to the pore wall. At the transition to the SmC* phase the system undergoes a transformation to a state wherein the tilt gets dictated by the structure of the phase.

A convenient method of determining the molecular tilt angle θ in the SmC* is to assume that the molecules tilt like rigid rods, and using the expression $\theta = \cos^{-1}(d_{SmC*}/d_{SmA})$, where d_{SmC*} and d_{SmA} are the layer thickness values in the SmC* phase and at the transition to the SmA phase respectively. Figure 7.7 presents the temperature variation of the tilt angle obtained in this manner. The Anopore sample behaves essentially similar to that of the bulk except that the saturated θ value is slightly lower. In the past, the temperature variation of θ has been analyzed in terms of an extended mean field model [32] whose free energy is written as

$$F = F_0 + \frac{1}{2}at\theta^2 + \frac{1}{4}b\theta^2 + \frac{1}{6}c\theta^6 \qquad (7.1)$$

Here *a*, b and c are the usual Landau coefficients and the reduced temperature $t = (T_c - T)$, T_c is SmA-SmC* transition temperature. The presence of the 6th order term in θ is to suggest that the transition could be in the vicinity of a tricritical point. Minimization of eq. (7.1) yields

$$\theta = \theta_o\left[\left(1+\frac{t}{t_0}\right)^{0.5} - 1\right]^{0.5} \quad \text{for } T < T_C \qquad (7.2)$$

The parameter $t_0 = (T_c - T_{co})$, where T_{co} is the crossover temperature at which the behaviour changes from mean field-like to tricritical-like; the nearer the value is to zero, closer it is to the tricritical point (TCP) and $t_0 = 0$ occurs at the TCP. It must be pointed out here that in the

Anopore case, the thermal variation of *d* in the vicinity of T_c, was rounded having a somewhat S-shaped variation across the transition, reminiscent of the supercritical behaviour of the order parameter in, for example, gas-liquid transition.

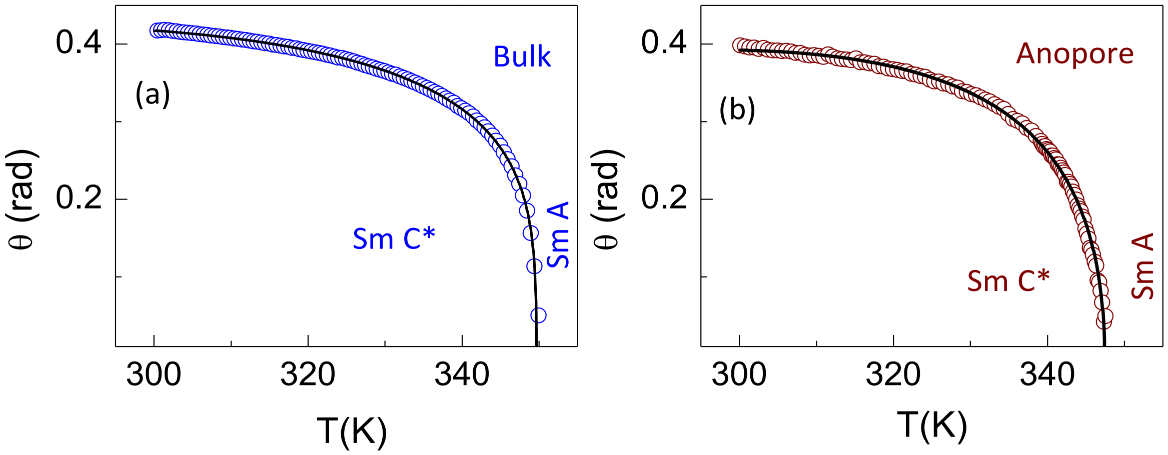

Figure 7.7: The temperature dependence of the molecular tilt angle extracted from the layer thickness data for the (a) bulk and (b) confined cases. The solid line corresponds to fit to eq. (7.3).

Also possible is the fact that the surface field mentioned above acts in a fashion similar to an electric field which smoothens the tilt angle variation in the vicinity of the SmA-SmC* transition. The positive thermal expansion discussed above could in fact be the influence of such a surface field on the layer thickness. Such a rounding of *d* affects the temperature dependence of θ in the proximity of T_c. To avoid the influence of this rounding, we did not include for the fitting to be described below, the data within 0.2°C of the temperature at which there is a turn-around in the layer spacing for the Anopore sample. For both the bulk and Anopore cases it was found that eq. (7.2) describes the data well only over a limited temperature region close to the transition region (down to T_c-10°C); inclusion of the data down to room temperature yielded poorer fits. However, very good fit over the entire temperature range studied, shown in Figure 7.7 as solid line, was obtained when a term linear in *t*, the reduced temperature, was added to eq. (7.2),

$$\theta = \theta_o\left[\left(1+\frac{t}{t_0}\right)^{0.5}-1\right]^{0.5}+At \tag{7.3}$$

Table 7.1: Best-fit parameters from the fit to eq. (7.3)

Parameter	**Bulk**	**Anopore**
T_c (K)	349.91 ± 0.006	347.42 ± 0.01
T_{co} (K)	349.77 ± 0.007	342.30 ± 0.45
t_0 (K)	$140 \pm 0.001 \times 10^{-3}$	5.12 ± 0.35
θ_o	$15.4 \pm 0.6 \times 10^{-3}$	$148 \pm 11 \times 10^{-3}$
A	$-2.17 \pm 0.03 \times 10^{-3}$	$-3.75 \pm 0.14 \times 10^{-3}$

The necessity for the linear term is the strong positive thermal expansion seen in the SmA phase. The best fit values, obtained by floating all the four parameters θ_o, T_c, T_{co}, A, and t_0 are given in Table 7.1 for the Anopore as well as the bulk case. It is noticed that $t_0 = (T_c\text{-}T_{co})$ which is very small for the bulk sample, increases to a large value of 5K for the Anopore sample. As pointed out already a small t_o indicates that the transition is closer to TCP, which in the present case is true for the bulk sample. It is rather surprising that confinement of the sample increases t_0 by a factor of 36 and moves the crossover temperature T_{co} quite away from the transition. A further support of this reduced influence of the TCP on the transition is seen in the value of the parameter θ_o, which is given by the ratio of the Landau coefficients b and c; larger the ratio, more away is the system from TCP. This ratio is an order of magnitude higher for the confined sample, and hence substantiates the argument that the finite size of the system moves the transition away from the TCP. Finally, while justifying the need for a linear term in eq. (7.3) it was mentioned that the positive thermal expansion seen in the SmA phase perhaps is responsible for it. In fact, the best-fit value of the coefficient of the linear term is seen to be higher by a factor of 2 for the Anopore sample, which perhaps is in line with the fact that the temperature variation of *d* is higher in the confined system.

7.4.2 Dielectric behaviour

The importance of confinement studies in ferroelectric liquid crystalline materials lies in the fact that it relates macroscopic properties like spontaneous polarization to microscopic parameters like the dipole moment of the molecule. Even though the behaviour of $\varepsilon_{\|}$, the dielectric constant parallel to the director, is very similar in both chiral and achiral systems, transverse dielectric constant $\varepsilon_{\perp}$ exhibits drastically different behaviour in chiral systems. It has one dispersion due to molecular rotations around long axis (frequency range 10^8-10^{10} Hz) and other due to intra-molecular rotation at still higher frequency range. At lower frequencies (frequency range of 10^2-10^6 Hz) the spectra contains two collective relaxation modes. These are referred to as soft mode (SM) and the Goldstone (GM) mode relaxations. While both modes are present in SmC* phase only SM is observed in the SmA phase. Before discussing the dielectric results, we shall give a brief description of these modes.

Goldstone mode

According to the Goldstone theorem [33], spontaneous breaking of a continuous symmetry results in a massless Boson. Consequently, a gapless branch of collective excitations exists that tries to restore the lost symmetry. A transformation between the SmA phase in which the molecules are along the layer normal and the SmC* phase having the molecules tilted with respect to the layer normal involves the breaking of a continuous symmetry group. It may also be noted that whereas the SmA phase is uniaxial, the SmC* phase is biaxial. However, in the SmC* phase the azimuthal precession of the tilt direction (figure 7.2a) and the consequent appearance of the helix recover, on a macroscopic scale, the uniaxial symmetry. Hence a symmetry recovering or Goldstone mode (GM) related to the helicoidal structure arises [see

Figure 7.8a]. Since the pitch of the helix is of the order of μm the relaxation frequency of the GM lies in the range of 10-1000 Hz.

Soft mode

The existence of soft modes in the vicinity of structural phase transitions was first observed by Raman and Nedungadi [34], although the term ‘soft mode’ was introduced by Cochran [35] to describe the inelastic neutron scattering results in $BaTiO_3$. Employing Raman scattering, Raman and Nedungandi [34] found that the frequency of a totally symmetric optical phonon decreases as the α→β transition in quartz is approached. The reason for the presence of the soft mode in the Sm A phase occurring above the tilted Sm C* phase is the following. In the Sm A phase the stability of the molecules to be aligned along the layer normal, is governed by an elastic constant.

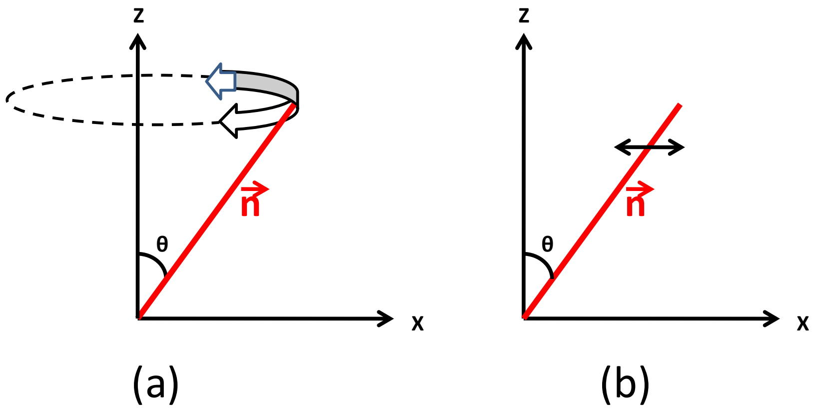

Figure 7.8: Schematic diagram illustrating the mechanism of the two collective modes: (a) Goldstone mode and (b) soft mode.

However, fluctuations of the director due to the finite temperature (thermal energy ~ kT) lead to, on a local scale, an instantaneous tilt angle between the director and the layer normal (figure 7.8b). As the system approaches T_C, the SmA-SmC* transition temperature, the elastic constant controlling the tilt fluctuation softens. Thus the fluctuation amplitude increases drastically with the susceptibility diverging at T_C and the associated frequency tending to zero. Hence this tilt amplitude fluctuation mode is called the soft mode (SM). The softening of this elastic constant means that the phase will lose its stability gradually until it becomes unstable at $T_{C.}$ Such a mode exists in non-chiral liquid crystalline system also, but cannot be detected by dielectric methods. However, it can be studied by light scattering techniques [36].

7.4.3 Linear dielectric measurements

The temperature variation of the dielectric constant perpendicular to the director (ε') obtained at two different fixed frequencies for the bulk sample is shown in Figure 7.9 (a). For the measuring frequency of 1 kHz, the onset of the SmA–SmC* transition is marked by a large increase in the ε' value. The large value of ε' in the SmC* phase is expected because for the material studied the spontaneous polarization is quite high (saturated polarization is ~ 2.5 mC/m^2) and that the Goldstone mode (GM) is present. When the frequency is increased to 100 kHz, the behaviour changes, and a peak-like profile is seen at the transition, characteristic of the presence of the soft mode (SM) relaxation arising out of tilt fluctuations. Application of a small DC bias field of 0.67 V/μm significantly diminishes the contribution due to GM near the transition, but hardly has any influences near room temperature. Obviously, the data at 100 kHz, with no contribution from GM is essentially the same with and without the bias field.

The results for the Anopore sample are shown in Figure 7.9 (b). Note that since the calculation of the empty cell capacitance is not trivial in Anopore membrane we present here data in terms of the capacitance C normalized with respect to the 100 kHz value deep in the SmA phase. It is interesting to note that although the value increases on transformation from the SmA to the SmC* phase, the magnitude of increase is quite small, suggesting that GM is suppressed, at least partially. Further, the absence of any peak-type behaviour in the 100 kHz data set, points to the possibility of SM being moved to much higher frequencies than in the bulk, or strong suppression in the immediate neighbourhood of the transition on the SmC* side.

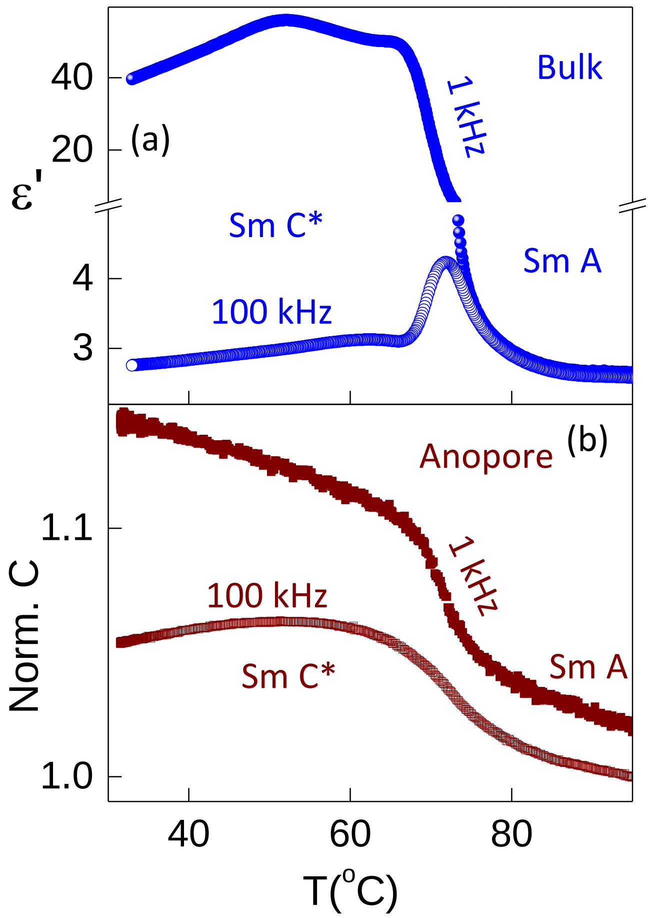

Figure7.9: (a) Fixed frequency dielectric constant variation across the SmA-SmC transition at two different frequency values, with a planar alignment of the bulk sample. (b) shows similar data as in (a) for the Anopore sample, except that it is presented in terms of the capacitance C normalized with respect to the 100 kHz value deep in the SmA phase.*

The dielectric spectra for the bulk and confined geometries in the SmA and SmC* phases are shown in Figures 7.10 (a) and (b). For the Anopore case, the imaginary (C″) part of the measured complex capacitance was employed instead of ε″. In each case, a single peak, and a conductivity-dominated process at lower frequencies are seen. For the bulk sample, the peak in the SmC* phase has a much larger strength and occurs at a much lower frequency than in the SmA phase. In contrast, for the Anopore sample, the strength of the SmC* phase is slightly larger than that in the SmA, but the frequencies hardly change. To extract the values of the relaxation frequency f_R and the strength of the mode ε_R, the ε^* (f) data were analyzed using a Havriliak-Negami function [37] in a form simpler than the mentioned in eq. 5.1,

$$\varepsilon^*(f) = \varepsilon_\infty + \frac{\varepsilon_R}{\left[1+\left(\frac{if}{f_R}\right)^{\alpha}\right]^{\beta}} + i\frac{\sigma}{2\pi\varepsilon_0 f} \tag{7.4}$$

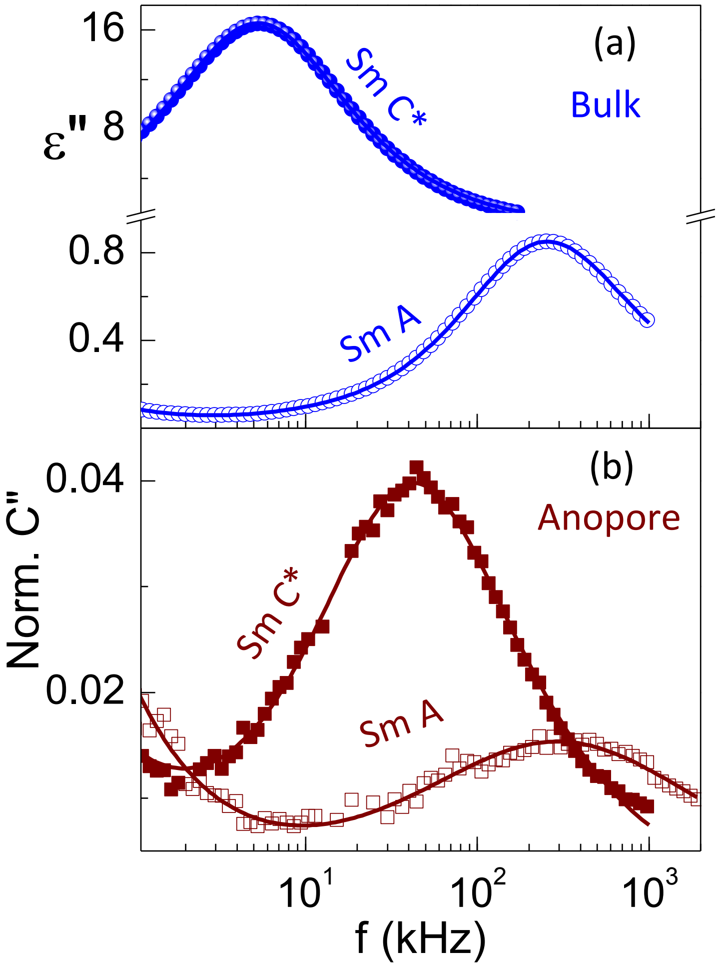

Figure 7.10: Dielectric absorption profiles in the SmA and SmC phases represented in terms of the imaginary part of the dielectric constant (capacitance) for the bulk (a) (Anopore (b)) samples. The lines depict the fit to the Havriliak-Negami equation (eq. 7.4).*

As indicated in Chapter-5, f is the measuring frequency, ε_∞ is the sum of the dielectric strengths of all the high frequency modes other than the one under consideration. The width of the peak, and its asymmetry, if any, are taken care of by the parameters α and β. The last term on the right side of eq. (7.4) accounts for the DC conductivity (σ) contribution to the imaginary part of ε^*. For the bulk sample, the two profile parameters, α and β, were both close to 1, suggesting a near-Debye symmetric relaxation profile with a single relaxation time. For the Anopore sample, although α was close to 1, β was slightly lower, indicating asymmetry in the profile shape. As mentioned earlier, for ferroelectric liquid crystals the collective relaxation is analyzed in terms of the fluctuations of the two component tilt order parameter: the amplitude part of the tilt gives rise to SM, and softens on approaching the transition from either of the phases. The azimuthal angle part responsible for GM, is active only in the SmC* phase. With this background we look at the temperature dependences of f_R and the dielectric strength for the bulk (in terms of ε_G) as well as the confined (in terms of C_G) situations shown in Figures 7.11 (a) and (b) respectively.

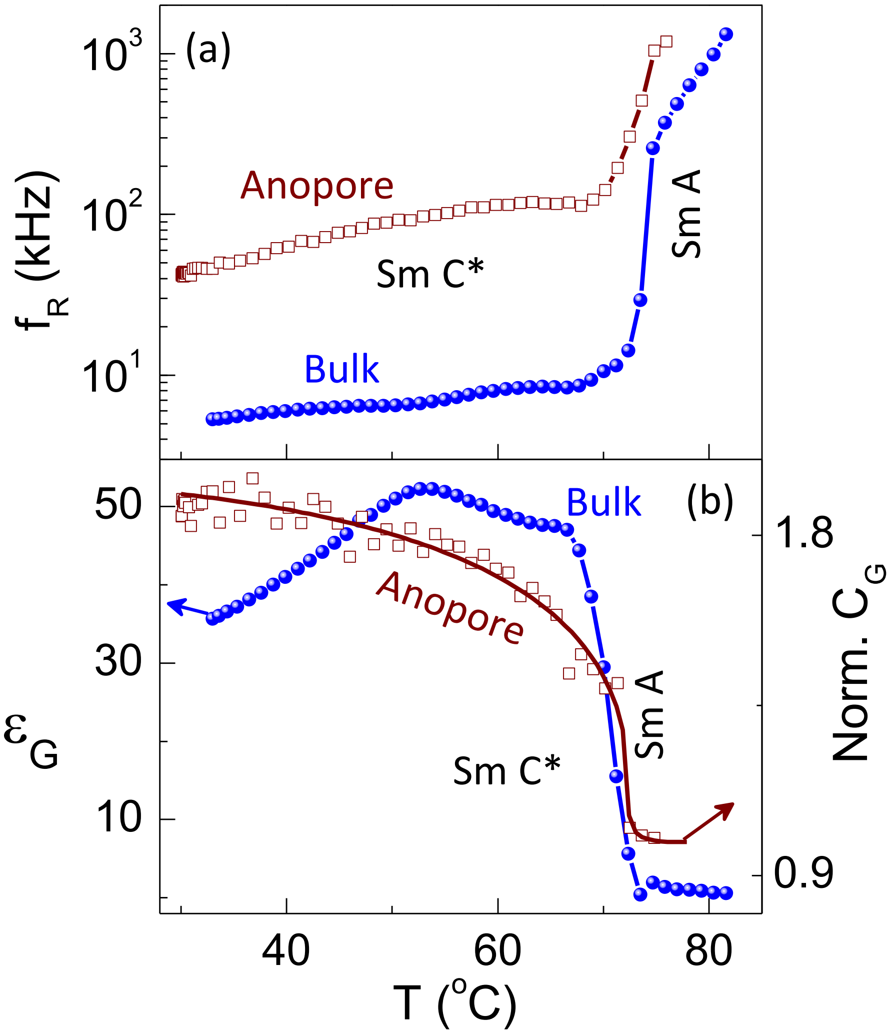

Figure 7.11: Temperature dependence of (a) the relaxation frequency and (b) the strength of the mode (in terms of the dielectric constant and capacitance for the bulk and Anopore samples, respectively) in the SmA and SmC phases. The lines are merely guides to the eye.*

We could manage to get only a few data points in the SmA phase of the Anopore sample owing to two reasons: (a) the amplitude of the corresponding mode decreases with temperature and therefore the signal level decreases with increasing temperature and (b) the presence of the ITO relaxation. However, the signature behaviour of the mode softening, viz., decrease in f_R and the concomitant increase in the strength, are clearly seen in the confined case also, although the enhancement in the strength across the transition is much smaller in the Anopore case. Interestingly, the slope with which the relaxation frequency diminishes in the SmA phase is different for the two cases: while for the bulk the slope value is 134 ± 7 kHz/^{o}C, it gets nearly doubled to 239 ± 59 kHz/^{o}C for the Anopore sample. More importantly, the absolute value of the soft mode relaxation frequency increases upon confinement. For example, at a reduced temperature of $T-T_c = 1$ ^{o}C, the Anopore sample has a factor of 2 higher f_R value than the bulk case. At the transition, the GM appears and due to its overwhelming dielectric strength the soft mode is hardly observed in the SmC* phase, as suggested by the fixed frequency data also (Fig.7.9). The GM frequency is also enhanced when the sample is confined, and the extent of enhancement which, with respect to bulk is a factor of 16 near the transition reduces to about 8 near room temperature. The reduced correlation length of the medium in the pores, as seen from the Xray data, is responsible for such an acceleration. It may be mentioned that the dynamics getting accelerated in nanoconfined liquids has been well studied [38]. But it should be borne in mind that the helical pitch of FLC-576 is ~ 200 nm, which is the same as the nominal pore diameter of 200 nm of the Anodisc membrane. Thus the very act of confining in the pore may, to a slight extent, unwind the helix a feature that could also affect both the frequency and the strength of GM.

A second possible reason for the observed features can be reckoned by considering the expressions of a Landau model for the GM relaxation frequency f_G and its strength ε_G,

$$f_G = \frac{Kq^2}{2\pi\gamma} \tag{7.5}$$

$$\varepsilon_G = \frac{(P/\theta)^2}{2\varepsilon_o Kq^2} \tag{7.6}$$

Here K and γ denote the effective elastic constant and the Goldstone rotational viscosity of the system, respectively, θ is the tilt angle and P is the polarization. $q_o = 2\pi/p$, where p, considered to be constant, is the helical pitch of the ferroelectric liquid crystal. Now, we make an assumption that the influence of the pore diameter is negligible and pitch remains the same in the bulk as well as the confined cases. Thus, the value of f_G can be taken to be dependent on the ratio K/γ. Therefore an order of magnitude higher f_G for the Anopore case must mean a similar higher value for the K/γ ratio, with a higher K or a lower γ responsible for it. γ alone may not be responsible for the higher f_G since it cannot account from the normalized strength which is lower by a factor of 30 for the Anopore sample. It is to be noted that ε_G is proportional to the factor $(P/\theta)^2$. Xray measurements presented earlier show that the saturated tilt angle θ is only slightly lower in the Anopore case. In the absence of the polarization data on the Anopore sample, we make a further assumption that just like θ, P may have comparable values in the bulk and confined cases. Therefore the large reduction in the strength for the Anopore sample must be due to the increase in the elastic constant. As a further check we looked at the product of ε_G and f_G, which from eqs. (7.5) and (7.6) yields

$$y = \frac{1}{\varepsilon_G f_G} = \frac{4\pi\varepsilon_o\gamma}{(P/\theta)^2} \tag{7.7}$$

in which the elastic constant term is absent. Figure 7.12 presents the parameter $1/\varepsilon_G f_G$ as a function of temperature for the bulk and the Anopore sample, from which it is seen that the value for the Anopore case is higher by a factor of 3 suggesting increase in γ upon confinement.

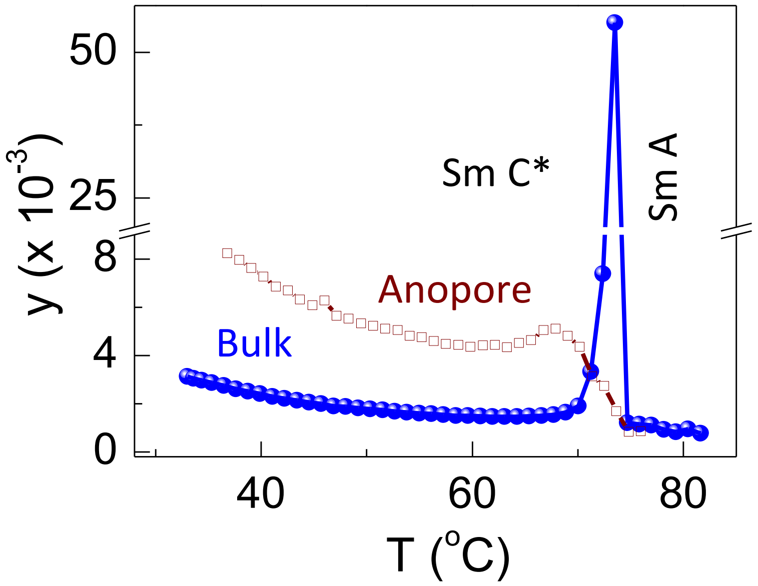

Figure.7.12: Temperature dependence of y, the inverse of the product of relaxation frequency and strength of the dielectric relaxation mode (see eq. 7.7 for details).

This feature in combination with eq. (7.3) therefore indicates that the increase in f_G when the sample is confined is certainly due to substantial increase in the effective elastic constant term Kq^2, which in turn supports the large decrease in the GM strength. It may be recalled here that in a polymer stabilized ferroelectric liquid crystal (PSFLC) system which involves confining the liquid crystal in a polymeric fibrillar environment, very similar features of increase in f_G and decrease in ε_G have been observed [39] with increasing polymer concentration. Thus, a universal feature of the confined systems, irrespective of the type of confinement, is the acceleration of the dynamics, a behaviour that has been found in nematic liquid crystal confined in a gel network also [40]. Just as in this gel network or the polymer cases, the confinement in the Anopore provides virtual surfaces all through the sample, instead of just at the substrates as in the bulk sample. Such surface forces would then help accelerating the dynamics of the system. Specifically in the ferroelectric phase, having the helical structure, the helix can get pinned at the pore boundaries with anchoring energy that is in excess of the usual forces at the two surfaces of the bounding plates. The excess anchoring may even be dominating over the natural elastic energy of the helical twist elastic energy giving rise to a more rigid anchoring and thus responsible for the increased f_G with a concomitant lowered GM strength. In another study [41] on a PSFLC system, it was found the P/θ ratio changes by only about 4% between the pure FLC and the PSFLC material. If a similar feature is applicable to the present case of Anopore confined sample, then it lends justification to the assumption that was made in the above described analysis that P/θ ratio may not be responsible for the diminution of ε_G.

7.4.4 Non-linear dielectric measurements

In comparison to the large database available for linear dielectric investigations on FLC, there are only a handful of measurements on the non-linear response [42-44]. More importantly, FLCs confined to Anopore membranes do not seem have been investigated at all. The reasons for this are two-fold: (a) the signal due to the non-linear part is very small compared with that due to the linear part and therefore difficult to extract; (b) there is no commercially available equipment with which to perform these measurements. Before we discuss the results of the FLC studied here when the sample is confined in Anopore membranes, let us look at the background information available on this topic.

In liquid crystals the study of the nonlinear dielectric measurements was started perhaps by Ziolo et al. [45; also see Ref.46], who investigated the non-linear response across the nematic-isotropic phase. Based on a principle developed by Chelkowski [47] for general dielectric materials, they applied large pulsed voltages (in the range 200 to 1000 V) to the sample and probed the dielectric constant with a much smaller field. The difference in the values with and without the large pulsed voltage is taken to be a measure of the non-linear response. The disadvantages of the technique, especially for the study of FLC, are the need for application of high voltages, and the generally used high frequencies [46]. A second technique available overcomes this problem, and is based on Nakada's phenomenological theory [48] of multi-time after-effect functions. It involves applying a low amplitude sinusoidal field to the sample and measuring the electrical displacement at past multi-time point. In the frequency regime this is achieved by measuring the displacement response at the fundamental and harmonic frequencies of the applied field. For an applied field of amplitude E_o and angular frequency ω, the different components of the displacement can be written as

$$\begin{aligned} D_1 &= \varepsilon_1 E_o + \frac{3}{4}\varepsilon_3 E_o^3 + \ldots \\ D_2 &= \frac{1}{2}\varepsilon_2 E_o^2 + \frac{1}{2}\varepsilon_4 E_o^4 + \ldots \\ D_3 &= \frac{1}{4}\varepsilon_3 E_o^3 + \frac{5}{16}\varepsilon_5 E_o^5 + \ldots \end{aligned} \qquad (7.8)$$

and so forth. In the experiments described here the field amplitude was very low (0.05V/μm) and therefore we neglect the higher order terms on the right hand side of each of the expressions in equation (7.8) and retain only the first terms. This approximation is validated by the fact that the raw values obtained for the sub harmonics were found to be much weaker than the signal for the fundamental. In the light of this we can approximate D_l to be the linear response, D_2 and D_3 to be the second and third harmonic responses respectively, thereby allowing the determination of the linear dielectric constant ε_1 and the non-linear dielectric constants ε_2 and ε_3. This principle was exploited by Furukawa et al. [49] to study solid state ferroelectric samples. In their measurements, the field to be applied to the sample was digitally synthesized and the sample response collected using a charge amplifier. The output of the charge amplifier was passed through a Sample & Hold module and transferred to a PC through an A/D converter; the Fourier transform of the data was done on the PC to obtain the multiple frequency responses. Although cumbersome to implement, the technique provides high precision data. Kimura and Hayakawa [50] adapted this method by substituting a storage oscilloscope to perform the functions of the Sample & Hold module and the analogue-to-digital converter, and investigated ferroelectric liquid crystals. In the following we describe a much simpler method developed in our laboratory [51].

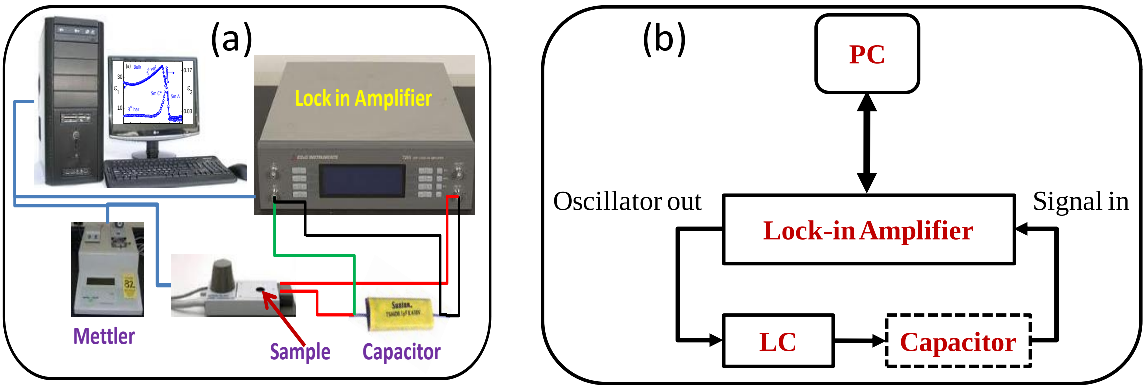

Figure 7.13: Diagram depicting (a) the experimental setup and (b) the circuit diagram employed for measurement of non-linear dielectric constant.

The diagram of the experimental set-up used is shown in Figure 7.13. While the charge-to-voltage conversion is accomplished by a very low loss, good high frequency performance capacitor (RS Electronics) calibrated using a standard frequency response analyser (Solartron1260), the remaining functions, namely, waveform generation, Sample & Hold, A/D conversion and FFT, are all realized through a digital lock-in amplifier (EG&G Instruments, DSP7260). The lock-in technique also helps in drastically improving the signal-to-noise ratio.

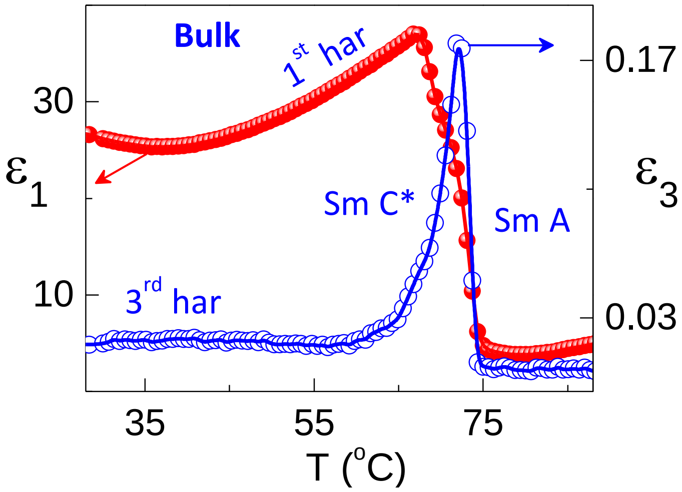

Figure 7.14: Thermal variation of the first and third harmonic dielectric response in the SmA and SmC phases for the bulk sample.*

If the sample thickness is more than the helical pitch, then the global symmetry of the SmC* phase will be the same as that of the SmA phase, and therefore the system possesses a centre of symmetry. Thus ε_2 and other even harmonics which can exist only in non-centrosymmetric systems will be absent. For these measurements, the amplitude of the applied voltage, kept at 500mV, was much smaller than the helix-unwinding or equivalently the polarization-reversal field in the SmC* phase.

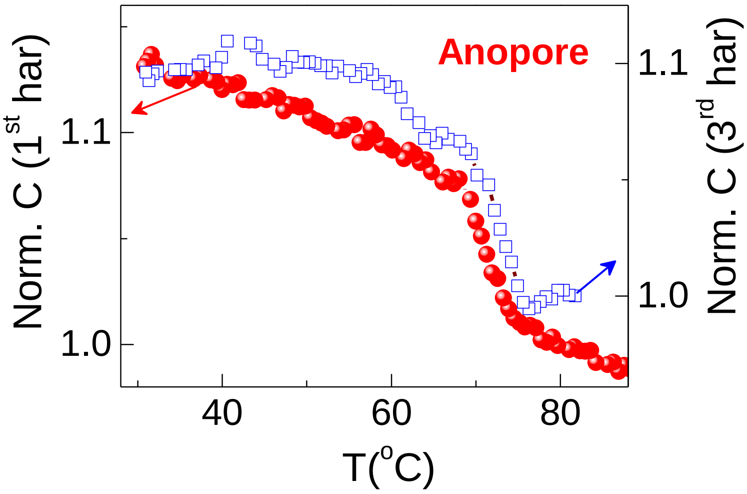

Figure 7.15: Thermal variation of the first and third harmonic dielectric response in the SmA and SmC phases for the confined sample normalized to have a value of 1 at the SmA-SmC* transition.*

Also, as stated earlier, since the “empty cell capacitance” is not precisely known for the Anopore case, we present all the data in terms of the ratio of the capacitance measured with respect to that in the SmA phase. Figures 7.14 and 7.15 show the data for the fundamental and third harmonic components obtained for the bulk and Anopore cases. For both situations, the second harmonic signal is practically comparable to the background noise. The absence of any improvement of the second harmonic signal can be taken to be an indication of the helix remaining intact in the confined case also. For the bulk sample the third harmonic signal is quite strong and its temperature dependence is quite similar to that seen for another room temperature FLC material [51] with a sharp peak at the transition. At room temperature the raw third harmonic signal is 3 orders of magnitude weaker than the fundamental, but at the peak, it is a little more than 2 orders lower. Further with respect to the value in the SmA phase, the peak is 2 orders of magnitude stronger. For the Anopore case, just like the fundamental, the 3rd harmonic is also weak, and has only a small step-like change at the SmA-SmC* transition. However, the 3rd harmonic is only a factor of two lower than the fundamental, but this could be solely due to the weakness of the fundamental itself, a behaviour which is corroborated by the fact that the maximum third harmonic component is only 20% higher than the value in the SmA phase, as against two orders of magnitude higher value for the bulk case.

7.5 Summary

In summary, we have performed Xray, linear and non-linear dielectric measurements on a room temperature ferroelectric liquid crystal mixture in the bulk and restricted geometry by confining the sample in Anopore membranes. The layering order is substantially better than the standard sinusoidal density modulation, as indicated by the presence of strong 2nd harmonic peak for the bulk as well as the Anopore sample. Confinement however brings in many features, some of which are caused purely due to the finite size of the system. It is observed that the Xray profiles are much broader in the confined case, and the determined correlation length is smaller than the pore size. The temperature dependence of the extracted tilt angle has a behaviour that suggests that the restricted geometry takes the system away from the tricritical point, deeper into the mean field regime. The fact that the pitch length of the smectic C* phase is comparable to the pore size of the membrane is reflected in an order of magnitude increase in the relaxation frequency and a concomitant reduction in the strength of the Goldstone mode upon confinement. This feature also causes the qualitatively different behaviour of the non-linear dielectric constant.

7.6 References

1. S. Chandrasekhar, *Liquid Crystals*, Cambridge University Press, Cambridge, U.K. 2nd ed. (1992).
2. S.T. Lagerwall, *Ferroelectric and Antiferroelectric Liquid Crystals*, John Wiley & Sons, New York (1999); I. Muševic, R. Blinc and B. Zekš, *The Physics of*

Ferroelectric and Antiferroelectric Liquid Crystals, World Scientific, Singapore (2000).

3. F. Tournilhac, L.M. Blinov, J. Simon and S.V. Yablonsky, *Nature*, **359**, 621 (1992).
4. R.B. Meyer, L. Liebert, L. Strzelecki and P. Keller, *J. Phys. (Paris)*, **36,** 69 (1975); R. B. Meyer, *Mol. Cryst. Liq. Cryst*., **40**, 33 (1977).
5. I. Musevic, B. Zeks, R. Blinc, L. Jansen, A. Seppen and P. Wyder, *Ferroelectrics*, **58**, 71 (1984); Z.M. Sun, Z.H. Wang, X. Zhang and D. Feng, *Phys. Lett. A*, **156**, 114 (1991); D.K. Rout and R. N.P. Choudhary, *Ferroelectrics*, **82**, 157 (1988).
6. E.P. Pozhidaev, L.A. Beresnev, L.M. Blinov and S.A. Pikin, *JETP Lett*. **37**, 88, (1983); K. Kondo, H. Takezoe, A. Fukuda and E. Kuze, *Jpn. J. Appl. Phys*, **21**, 224 (1982).
7. S. Krishna Prasad and G.G. Nair, *Mol. Cryst. Liq. Cryst.*, **202**, 91 (1991).
8. S. Rozanski, *Phys. Stat. Solidi*, **79**, 309 (1983).
9. L.A. Beresnev, L.M. Blinov, M.A. Osipov, S.A. Pikin, *Mol. Cryst. Liq. Cryst.* **158A**, 3 (1988).
10. A.M. Biradar, S.S. Bawa, S.B. Samanta and S. Chandra, *Phys. Stat. Solidi*, **97**, 427(1986).
11. G. Cordoyiannis, G. Nounesis, V. Bobnar, S. Kralj, and Z. Kutnjak, *Phys. Rev. Lett*. **94**, 027801 (2005).
12. F.M. Aliev and J. Kelly, *Ferroelectrics* **151**, 263 (1994).
13. H. Xu, J.K. Vij, A. Rappaport and N.A. Clark, *Phys. Rev. Lett.*, **79**, 249 (1997).
14. L. Naji, F. Kremer and R. Stannarius, *Liq. Cryst.*, **25**, 363 (1998).
15. S.A. Rozanski, R. Stannarius and F. Kremer, *Liq.Cryst*, **28**, 1071 (2001).
16. K.L. Sandhya, S. Krishna Prasad, D.S. Shankar Rao, and Ch. Bahr, *Phys. Rev. E*, **66**, 031710 (2002).
17. G. Cordoyiannis, S. Kralj, G. Nounesis, Z. Kutnjak, and S. Zumer, *Phys. Rev. E*, **75**, 021702, (2007).
18. See e.g., S. Heinekamp, Robert A. Pelcovits, E. Fontes, E. Yi Chen, R. Pindak, and R. B. Meyer, *Phys. Rev. Lett.*, **52**, 1017 (1984).
19. Ch. Bahr and D. Fleigner, *Phys. Rev. Lett.*, **70**, 1842 (1993).
20. Z. Kutnjak, S. Kralj and S. Zumer, *Phys. Rev. E*, **66**, 041702 (2002).
21. (a) E.P. Pozhidaev, S.I. Torgova, V.E. Molkin, M.V. Minchenko, V.V. Vashchenko,

A.I. Krivoshey, and A. Strigazzi, *Mol. Cryst. Liq. Cryst.*, **509**, 1042 (2009); (b) E.P. Pozhidaev, Gurumurthy Hegde, V.G. Chigrinov, A.A Murauski, H.S. Kwok, V.V. Vashchenko, and A. I. Krivoshey, *Mol. Cryst. Liq Cryst.*, **510** 12 (2009); (c) A.D. Kiselev, E.P. Pozhidaev, V.G. Chigrinov, and H.S. Kwok, *Phys. Rev. E.*, **83,** 031703 (2011).

22. P.E. Cladis, R.K. Bogardus, W.B. Daniels, and G.N. Taylor, *Phys. Rev. Lett.*, **39,** 720 (1977).
23. A.J. Leadbetter, J.C. Frost, J.P. Gaughan, G.W. Gray, and A.J. Mosley, *J. Phys. (France)* **40,** 375 (1979).
24. P.E. Cladis, J. Stamatoff, D. Guillon, M.C. Cross, T. Bilash, and P. Finn, in *Advances in Liquid Crystal Research and Applications*, edited by L. Bata, Pergamon, Oxford (1981).
25. B.M. Ocko, A.R. Kortan, R.J. Birgeneau, and J.W. Goodby, *J. Phys. (Paris)* **45**, 1139 (1984).
26. S. Tristram-Nagle, Y. Liu, J. Legleiter, and J.F Nagle, *Biophys. J.*, **83,** 3324 (2002); S. Tristram-Nagle and J. F. Nagle, *Chem. Phys. Lipids*, **3**, 127 (2004); G. S. Smith, C. R. Safinya, D. Roux, N. A. Clark, *Mol. Cryst. Liq. Cryst.*, 144, 235 (1987).
27. S. Das, N. Gopinathan, S. Abraham, N. Jayaraman, M.K. Singh, S. Krishna Prasad, and D.S. Shankar Rao, *Adv. Func. Mater.*, **18,** 1632 (2008); For the thermotropic sugar derivates used in this study they observed the second harmonic to be only a factor 1.5 weaker than the fundamental peak.
28. P. Davidson and A.M. Levelut, *Liq. Cryst.*, **11**, 469 (1992).
29. T. Murias, A.C. Ribero, D. Guillon, D. Shoosmith, and H.J. Coles, *Liq. Cryst*., **29**,627 (2002); L.Li, D.J. Christopher, M. Jakob, and P.L. Robert, *J. Mater. Chem*., **17**, 2313 (2007); S. Dielea, D. Losea, H. Krutha, G. Pelzla, F. Guittardb and A. Cambonb, *Liq. Cryst*., **21,** 603 (1996).
30. The ξ_s values quoted in the text are obtained from the width of the raw scans. If corrections for the instrumental resolution are applied the ξ_s values for the bulk become 480 nm, whereas that for the Anopore case changes marginally to 100 nm. Therefore we discuss the observations in terms of the correlation length values determined without these corrections.
31. S. Krishna Prasad, S. Sridevi, and D.S Shankar Rao, *J. Phys. Chem. B*, **114**, 7474 (2010).

32. C.C. Huang, and J.M. Viner, *Phys. Rev. A* **25**, 3385 (1982).
33. J. Goldstone, A. Salam and S. Weinberg, *Phys. Rev.*, **127**, 965 (1962).
34. C.V. Raman and T.M.K. Nedungadi, *Nature*, **145**, 147 (1940).
35. W. Cochran, *Phys. Rev. Lett.,* **3**, 412 (1959); W. Cochran, *Adv. Phys.,* **9**, 387 (1960).
36. M. Delaye and P. Keller, *Phys. Rev. Lett.,* **37**, 1065 (1976).
37. S. Havriliak, and S. Negami, *J. Polym. Sci., Part C: Polym. Symp.,* **14,** 99 (1966).
38. R. Richert, *Annu. Rev. Phys. Chem*. **62**, 65 (2011).
39. S. Kaur, I. Dierking, and H. F. Gleeson, *Eur. Phys. J. E* **30,** 265 (2009).
40. See e.g., Geetha G. Nair, S. Krishna Prasad, V. Jayalakshmi, G. Shanker, and C.V. Yelamaggad, *J. Phys. Chem. B* **113**, 6647 (2009).
41. M. Petit, A. Daoudi, M. Ismaili, and J.M. Buisine, *Eur. Phys. J. E,* **20**, 327 (2006).
42. Y. Kimura, S. Hara, and R. Hayakawa, *Phys. Rev. E* **62**, 5907 (2000).
43. Y. Kimura, Frequency-Domain Nonlinear Dielectric Relaxation Spectroscopy: Its applications to ferroelectric liquid crystals in Nonlinear Dielectric Phenomena in Complex Liquids, Nato Science Series, Rzoska, J. Sylwester, Vitaly and Zhelezny (Eds), Netherland, **157**, 221 (2005).
44. Y. Ishibashi, *J. Kor. Phys. Soc.,* **32**, 407 (1998).
45. J. Ziolo, J. Chrapec, S. J. Rzoska, and W. Pyzuk, *Mol.Cryst. Liq. Cryst*. **3**, 183 (1986)
46. Rzoska, J. Sylwester, Zhelezny, Nonlinear Dielectric Phenomena in Complex Liquids, Nato Science Series II, Jaszowiec-Ustron, Vitaly (Eds.), Poland, Vol. **157** (2003).
47. A. Chelkowski, Dielectrics Physics, PWN / Elsevier, Warsaw /Amsterdam (1980).
48. O. Nakada, *J. Phys. Soc. Japan,* **15**, 2280 (1960).
49. T. Furukawa, K. Nakajima, N. Koizumi and M. Date. *Jpn. J. Appl. Phys.,* **26**, 1039 (1987).
50. Y. Kimura and R. Hayakawa, *Jap. J. Appl. Phys.,* **32,** 427 (1993).
51. S. Krishna Prasad, Geetha G. Nair, and D.S. Shankar Rao, *Liq. Cryst.* **26**, 1587 (1999).